Advancements and applications of the microclimate model ENVI-met

Dissertation
zur Erlangung des Grades
"Doktor der Naturwissenschaften"
im Promotionsfach Geographie
am Fachbereich Chemie, Pharmazie,
Geographie und Geowissenschaften
der Johannes Gutenberg-Universität Mainz

Tim Sinsel
geb. in Göttingen

Mainz, 2021

1. Berichterstatter:
2. Berichterstatter:

Tag der mündlichen Prüfung: 19. Januar 2022

D77 (Dissertation Universität Mainz)

Summary

Urban heat stress leads to increased morbidity and mortality rates in vulnerable groups and will further exacerbate due to the ongoing processes of climate change, urbanization, and urban densification. Modeling tools are used to quickly and cost-effectively evaluate possible heat mitigation strategies, such as blue or green infrastructure, on both general scientific and distinct planning levels. While the established microclimate model ENVI-met represents the most commonly applied tool for such studies on the urban quarter level, validation studies reported modeling inaccuracies that have been tackled by works presented in this thesis. Advancements featuring the so-called Indexed View Sphere (IVS) scheme and Advanced Canopy Radiation Transfer (ACRT) module improved radiation modeling in general. IVS represents a ray-tracing approach that stores all objects which are visually and thus radiatively linked to a cell. Given this information, it is possible to account for the received radiation, which has been reflected or emitted by objects in a cell's field of view. ACRT features a calculation module that takes into account extinction of diffuse as well as scattering of direct shortwave radiation within plant canopies. Due to the newly implemented Lindenmeyer-system trees, leaf area densities and shapes are additionally resembled with higher accuracy. A model validation study in Hong Kong featuring different green infrastructure typologies and varying levels of detail for the ENVI-met simulation settings corroborated that the general model accuracy was improved by IVS and ACRT modules. However, modeled mean radiant temperature (MRT) still revealed discrepancies compared against values derived from six-directional radiation flux measurements. As MRT represents the most important parameter in thermal comfort analysis and hence urban heat stress studies, the reported shortcomings have subsequently been tackled by the implementation of the common six-directional radiation flux approach as well as three differing shortwave radiation projection factors into ENVI-met. Evaluation with measured data – originating from the Hong Kong field campaign as well as grey globe temperature-based values coming from a field campaign in Sao Paulo – demonstrated that the new MRT modeling schemes greatly improved modeling results and reduced error magnitudes at eight examined sites. Besides these implementations of IVS, ACRT, and MRT schemes in the ENVI-met core, a new post-processing tool called Lagrangian Stochastic Particle Trajectory Model was developed. It represents the first model of its kind

that enables flux footprint modeling and backwards-tracking of particle trajectories for complex urban environments.

Aside from these advancements, ENVI-met was applied in an air quality modeling study as well as an investigation on new specific heat stress mitigation measures. The air quality study examined increased particulate matter expositions at child height levels compared to adult height levels measured by low-cost sensors on urban route tracking along kindergartens and schools. Simulations could corroborate that the relative differences increased with overall higher absolute values and are thus found to be larger near streets with high traffic intensities. The contributions to heat mitigation strategy research considered newly developed super cool materials – featuring a very high albedo and emissivity – applied as roof coatings to examine their possible impact on air temperatures at pedestrian level. A sensitivity study featuring simplified building morphologies found super cool roofs (SCR) to have a slightly higher cooling effect on pedestrian-level air temperatures compared to traditional cool and green roofs. This effect, however, decreases with rising building heights. A consecutive study analyzed the SCR impact for realistic scenarios featuring complex urban environments in two contrasting cities: New York City and Phoenix. Simulations were not only conducted with ENVI-met but also with the regional Weather and Research Forecast model (WRF) in order to, as a first step, examine the impact of SCR application over entire metropolitan areas, as a second step, use WRF's model output as realistic meteorological boundary conditions for the ENVI-met simulations, and, as a third step, find similarities and discrepancies between both models. The better SCR performance in Phoenix compared to New York City in prediction of both models could primarily be explained by the hotter and drier climate, while the prevailing lower building heights turned out to be a minor factor. The present thesis hence demonstrates, on the one hand, advancements that will allow more accurate microclimate modeling in general and, on the other hand, a broad range of application studies to provide progress for the urban climate community and support sustainable urban planning in the future.

Zusammenfassung

Hitzestress in Städten führt zu gesundheitlichen Risiken und letztendlich zu einer erhöhten Sterberate in vulnerablen Gruppen. Durch das Fortschreiten des Klimawandels, der Urbanisierung und der Verdichtung von Städten wird dieser in Zukunft zudem weiter zunehmen. Daher werden Modelle entwickelt und angewendet um schnell und kostengünstig mögliche Strategien zur Vermeidung bzw. Minderung von Hitzestress zu untersuchen. Solche Strategien, wie beispielsweise der vermehrte Einsatz von grüner und blauer Infrastruktur, können mit Hilfe von Modellen sowohl grundlegend wissenschaftlich erforscht als auch in konkreten Planungsszenarien für Kosten-Nutzen-Analysen zu Rate gezogen werden. Das Mikroklimamodell ENVI-met stellt dabei das meistgenutzte Tool für Analysen auf städtischer Quartiersebene dar. Allerdings wurden in Modell-Evaluierungen Ungenauigkeiten aufgezeigt, die nun durch einige in dieser Arbeit präsentierte Weiterentwicklungen gemindert wurden. Diese Neuentwicklungen umfassen unter anderem das sogenannte Indexed View Sphere (IVS)-Modell sowie das Advanced Canopy Radiation Transfer (ACRT)-Modul, welche die Strahlungs-Modellierung präzisieren. Im IVS-Modell wird mit Hilfe von Ray-Tracing untersucht, welche Zellen mit welchen Objekten in einem direkten Sichtkontakt und damit Strahlungsaustausch stehen. Dadurch kann anschließend ermittelt werden, wieviel reflektierte oder emittierte Strahlung die jeweilige Zelle durch die Objekte in ihrem Sichtfeld erhält. ACRT stellt ein Modul dar, welches die Reduktion von diffuser sowie die Streuung von direkter kurzwelliger Strahlung in neue diffuse Strahlung innerhalb von Blattstrukturen wie z.B. Baumkronen berechnet. Zudem wurde dem Modell eine neue Art der Baumimplementierung basierend auf dem Lindenmeyer-System hinzugefügt, sodass Baumgeometrie sowie lokale Blattflächendichte realistischer modelliert werden können. Eine Validierung mit Messdaten in Hongkong, die für verschiedene Orte und Simulations-Einstellungen durchgeführt wurde, bestätigte die generellen Verbesserungen in der Modellierung. Allerdings offenbarte die Studie Ungenauigkeiten in den modellierten mittleren Strahlungstemperaturen (MRT) im Vergleich mit Werten, die aus der Messung von Strahlungsflüssen gewonnen wurden. Da MRT den wichtigsten Parameter für die Bestimmung des thermalen Komforts am Tag darstellt und damit essentiell für Studien zum Hitzestress in Städten ist, wurden diese Ungenauigkeiten in einer Folgestudie untersucht und durch die Implementierung einer allgemein anerkannten Strahlungsfluss-Berechnungsmethode sowie der Ergänzung von drei weiteren Faktoren zur Korrektur

der erhaltenen kurzwelligen Strahlung angegangen. Eine anschließende Evaluierung anhand der Messdaten aus Hongkong sowie weiteren MRT-Werten basierend auf Grey-Globe-Temperatur-Messungen aus Sao Paulo ergaben, dass die neue Modellierung eine deutliche Verbesserung bzgl. Korrelation und Abweichungen für alle acht untersuchten Messpunkte bewirken konnte. Neben diesen Implementierungen am Simulationskern von ENVI-met wurde zudem ein neues Post-Processing-Tool namens Lagrangian Stochastic Particle Trajectory Model entwickelt, welches die Verfolgung und Herkunft von Partikel-Flüssen für komplexe urbane Strukturen modellieren kann.

Abgesehen von den Neuentwicklungen wurde ENVI-met zum einen in seiner Funktion als Luftschadstoff-Modell und zum anderen als Tool zur Modellierung spezifischer Hitzestress-Vermeidungs-Strategien verwendet. Die Luftschadstoff-Studie ergab bei städtischen Messtouren entlang von Kindergärten und Schulen, dass auf der Kopfhöhe von Kindern höhere Feinstaub-Konzentrationen gemessen wurden als auf der Kopfhöhe Erwachsener. Diese relativen Differenzen zwischen den Höhen vergrößerten sich mit zunehmenden absoluten Werten und waren daher in der Nähe von Straßen hohen Verkehrsaufkommens besonders ausgeprägt. Die Modellierung der Hitzestress-Vermeidungs-Strategien befasste sich mit neuartigen Materialen, die eine extrem hohe Albedo und Emissivität aufweisen und als mögliche kühlende Dachmaterialien in Betracht gezogen werden. Eine Sensitivitätsstudie mit vereinfachten, standardisierten Gebäudestrukturen in ENVI-met zeigte, dass diese extrem reflektierenden Dächer eine etwas größere Temperaturreduktion auf Fußgänger-Niveau bewirken können als herkömmliche helle Dächer oder Dachbegrünungen und dass dieser Effekt mit zunehmender Gebäudehöhe deutlich abnimmt. Eine Anschlussstudie untersuchte den Einfluss dieser Dächer auf bodennahe Temperaturen für reale und entsprechend komplexere urbane Strukturen zweier unterschiedlicher Städte: New York City und Phoenix. Hierfür wurde neben dem Mikroklima-Modell ENVI-met auch das regionale Weather and Research Forecast (WRF)-Modell genutzt, um zum einen den Kühlungseffekt bei einer Applikation der Materialien auf Dächern einer ganzen Metropolregion zu untersuchen, zum zweiten die Ergebnisse der WRF-Simulationen als realistische meteorologische Randbedingungen für die ENVI-met-Simulationen verwenden zu können und zum dritten mögliche Unterschiede und Gemeinsamkeiten zwischen den beiden Modellen zu analysieren. Der von beiden Modellen simulierte stärkere Abkühlungseffekt in Phoenix im Vergleich zu New York City konnte auf die heißeren und trockeneren klimatischen Bedingungen

zurückgeführt werden, während die vorherrschenden niedrigeren Gebäudehöhen eine geringere Rolle spielten. Die vorliegende Arbeit stellt somit zum einen Weiterentwicklungen an der Modellierung des urbanen Mikroklimas dar und zeigt zum anderen die vielfältigen Anwendungsmöglichkeiten und Forschungspotentiale in diesem Bereich auf, mit dem Ziel die nachhaltige Stadtplanung der Zukunft positiv zu beeinflussen.

Acknowledgements

Not available online.

Table of Contents

1 Introduction

Climate change is arguably the greatest challenge of humankind. Future scenarios of the recently published Intergovernmental Panel on Climate Change's Sixth Assessment Report (AR6) on the physical science basis of climate change state that global temperatures will rise by around 2 to 4.6 K until 2100 with current greenhouse gas emission levels continuing until 2050 (IPCC, 2021). Even in scenarios that take the implementation of massive, not-yet planned counter-measures into account which yield net zero emissions by 2050, global warming is still projected to be around 1.5 K compared to pre-industrial times. With its multitude of relationships and effects, climate change represents a very complex topic that affects every human being in any kind of manner. Its most hazardous effects such as sea-level-rise, flooding, droughts, or an increasing strength and frequency of storms (IPCC, 2021) gained wide-spread publicity due to recent events. Urban heat stress, however, represents a rather occasionally discussed topic since it is usually not recognized as an imminent threat. Nonetheless, extreme heat waves such as 2003 in Western Europe significantly increased both morbidity and eventually mortality rates mostly induced by circum-vascular diseases, which are especially threatening the elderly (Habeeb et al., 2015; Kovats et al., 2004; Kravchenko et al., 2013; Robine et al., 2008; Schinasi et al., 2018; Wong et al., 2013). Due to demographic change in several civilizations like Europe, Japan, or China, the number of people that is thus affected by urban heat stress will increase in upcoming decades, raising the importance of this subject (Romanello et al., 2021; UN Human Settlements Programme, 2020). Furthermore, more than 55 % of the world's population already lives in cities and it is predicted that with continuing urbanization the amount will further increase up to 68 % until 2050, with particularly high urbanization rates in the most vulnerable regions in Asia and Africa (UN Department of Economic and Social Affairs, Population Division, 2019).

While the number of possibly endangered people hence progressively increases, urban heat stress itself intensifies as well: Due to climate change, rising global temperatures are assumed to exacerbate heat related health impacts in cities (Chapman et al., 2017). This phenomenon of higher temperatures within urban agglomerations compared to its rural surroundings is described by the commonly known and intensively studied Urban-Heat-Island-Effect (UHI). These temperature discrepancies are primarily caused by the evapotranspiration capabilities of urban areas and differences in the radiation scheme

(Mills, 2014). Evapotranspiration is usually lower compared to rural surroundings since built environments feature less pervious soils, open water bodies, and vegetation (Pyrgou et al., 2020). It though represents an important process as it is able to considerably reduce air temperatures due to transformation of sensible to latent heat (Gunawardena et al., 2017; Li et al., 2019).

A major driver of climatological processes in general is solar energy with its vast majority being received as shortwave radiation. This direct shortwave radiation component is subsequently reflected or absorbed depending on an object's albedo or can be scattered into diffuse solar radiation upon hitting objects such as aerosols. The amount of energy being absorbed by an object together with its specific thermal properties – such as heat capacity or conductivity – and convection as well as advection based on the surrounding conditions subsequently determine its resulting temperature. Depending on the object's emissivity, the amount of emitted longwave energy can then be approximated according to Stefan-Boltzmann-law. In urban environments, a larger number of buildings and sealed surfaces usually feature lower albedos and higher heat capacities compared to rural surroundings. Received solar energy is hence absorbed and stored during daytime and released during nighttime (Oke, 1987). However, bright materials or glass facades are contrastingly able to reflect large portions of shortwave radiation, which leads to large local differences of radiative fluxes and climatic conditions. Urban climate is hence very difficult to determine due to the high complexity and heterogeneity of a city's specific design regarding urban structure (dimension and spacing of buildings and streets), urban cover (pervious, impervious soils, vegetated areas, water bodies), urban fabric (building materials), and urban metabolism (production of heat and pollutants based on human activity) (Oke, 1997, 1988; Runnalls and Oke, 2006; Thomson and Newman, 2018; Zhang, 2013). Although large discrepancies in nighttime temperatures between rural and urban sites represent the major UHI aspect, tackling urban climate challenges by sustainable urban planning is particularly related to daytime heat stress being primarily caused by extreme air temperatures (Martilli et al., 2020; Schinasi et al., 2018). The so-called human thermal comfort (HTC) defines whether a distinct microclimatic situation is comfortable for a human being. One major driver of this impression is the thermal radiative heat load received by a standing human body that is defined by the parametrized temperature-dimension index Mean Radiant Temperature (MRT) (Johansson et al., 2014; Kántor and Unger, 2011; VDI, 2008). However, several additional parameters such as wind speed, air temperature,

and air humidity are important for an advanced evaluation of HTC. Multiple biometeorological indices such as Predicted Mean Vote PMV (Fanger, 1972), Standard Effective Temperature SET (Gagge et al., 1986), Physiologically Equivalent Temperature PET (Mayer and Höppe, 1987), and Universal Thermal Climate Index UTCI (Bröde et al., 2012) have thus been developed, taking all of these parameters into account.

In order to improve HTC to reduce dangerous health implications and allow sustainable living in climate-change-resilient cities, researchers investigated a multitude of heat mitigation measures in recent decades (Aflaki et al., 2017; Akbari et al., 2016; Fallmann and Emeis, 2020). A cheap and feasible solution to improve thermal comfort are shading structures that reduce the perceived shortwave radiation at pedestrian level (Elgheznawy and Eltarabily, 2021; Kántor et al., 2018). An alternative are high-albedo materials that reflect incoming shortwave radiation and are thus able to reduce material surface and hence ambient air temperatures (Santamouris and Fiorito, 2021). However, as reflected shortwave radiation at pedestrian level would increase the received radiative load and thus lower thermal comfort, most studies conclude that they should not be used as street or wall materials in cities with medium to wide street canyons (Falasca et al., 2019; Middel et al., 2020; Schrijvers et al., 2016). These materials are therefore often examined as a heat mitigation measure when applied on roofs. These so-called cool roofs lower the amount of energy stored in buildings and are thus able to reduce day- and nighttime outdoor air temperatures as well as building indoor temperatures (Akbari et al., 2005; Bozonnet et al., 2011; Santamouris et al., 2011; Synnefa et al., 2008). However, ageing and weathering is yet a drawback as it lowers cool roofs' albedo, which in turn requires maintenance to preserve their cooling performance (Dornelles et al., 2015; Mastrapostoli et al., 2016; Synnefa et al., 2007). An additional measure called blue infrastructure aims to lower sensible heat and increase latent heat by evaporation. Water bodies, fountains, or nozzles that create a fine mist of water droplets, are hence able to reduce air temperatures. Blue infrastructure, however, represents a rather expensive measure featuring both high water consumption and maintenance effort with comparatively small improvements in thermal comfort (Farnham et al., 2015; Jacobs et al., 2020; Lehnert et al., 2021; Liu et al., 2021; Theeuwes et al., 2013; Žuvela-Aloise et al., 2016). Furthermore, it is not applicable for humid conditions, making it a less valuable option for cities in subtropical and tropical climates. Lastly, the most important and already widely applied heat

mitigation tool is green infrastructure. Vegetation of any kind is able to lower air temperatures by evapotranspiration like blue infrastructure. Furthermore, trees, either along streets or accumulated in parks, additionally provide shading, thus lowering radiative heat load (Bartesaghi Koc et al., 2018; Gunawardena et al., 2017; Liu et al., 2021; Morakinyo et al., 2017b, 2020; Saaroni et al., 2018; Tsoka et al., 2018). It is, however, difficult to find the right urban tree fitting both the altering conditions caused by climate change as well as numerous additional requirements such as low toxicity, resistance against tree pests, low allergy potential from pollen, low isoprene emissions, or powerful roots to resist storms on the one hand and small roots to prevent damaging of streets and the urban underground on the other hand (Vogt et al., 2017). Furthermore, trees represent a possible threat for people during storm events and feature high maintenance costs for cutting back branches. Lastly, they are a very space-consuming measure, which yields the opposite desired outcome from urban planning nowadays trending towards urban densification to meet residential needs and keep pace with the progressing urbanization (Dembski et al., 2020; Lin et al., 2015; Roman et al., 2021). Although roof and façade greening offer a space-saving solution of green infrastructure compared to trees, they usually do not provide shade and only show a rather low impact on outdoor thermal comfort (Liu et al., 2021; Morakinyo et al., 2017a). While they are favored for their building indoor cooling performance, hence lowering building energy demands otherwise needed for air conditioning, they can in turn be even more expensive than trees in terms of application and maintenance (Heusinger et al., 2018; Manso and Castro-Gomes, 2015; Shafique et al., 2018). Both cool and green roof solutions also have to compete against photovoltaic panels that are assumed to negatively affect urban heat stress but represent a space-saving regenerative power supply (Berardi and Graham, 2020; Masson et al., 2014). However, recent studies suggest that green roofs are still a viable option to be applied below photovoltaic panels (Jahanfar et al., 2020; Movahhed et al., 2019; Scherba et al., 2011; Van Renterghem, 2018). As all measures feature strengths and weaknesses, a combination of mitigation tools is needed to tackle the challenge of urban heat stress (Hatvani-Kovacs et al., 2018; O'Malley et al., 2015; Wang et al., 2016). One example for a holistic approach yielding resilient cities could be the sponge city concept, which prevents urban flooding by saving the water of heavy rainfalls in large storage spaces and in open soils (Nguyen et al., 2019). During heat waves, this

stored water can be then used for blue and green infrastructure in order to cool the city by evapotranspiration.

Besides these heat mitigation strategies, future urban planning concentrates on reducing air pollution as it also yields strong health implications like neuronal, respiratory or cardiovascular diseases and eventually an increased mortality (Azarmi et al., 2016; Feng et al., 2016; Karagulian et al., 2015; Kumar et al., 2015; Lelieveld et al., 2019). Critical pollutants like particulate matter or NO_2 are mainly induced by traffic, industry, or residential combustion (Fann et al., 2011; Sofia et al., 2020). The possible range of air pollution mitigation strategies is hence plentiful: from (1) a general transformation of fossil-fuel-based to electricity-based traffic, industry as well as heating/cooling components, to (2) smart cities with extensive air pollution monitoring for regulating purposes, to (3) improved electrified public transport supported by low-emission traffic zones as well as bicycle renting systems and car sharing (Duque et al., 2016; Nieuwenhuijsen and Khreis, 2016; Rabl and de Nazelle, 2012; Rojas-Rueda et al., 2011; Sofia et al., 2020).

In order to examine the performance of measures, regardless whether mitigating heat or air pollution, models are needed to predict possible advantages and disadvantages before the implementation in reality. They thus represent quick and reliable tools to evaluate hypothetical scenarios at virtually no cost. For climatological analysis, most models predict parametrized interactions between parts of a defined model domain (grid cells) based on external drivers such as irradiation, wind, air temperature, air humidity, and air pressure. Such climate models are not only limited to urban climate analysis. They are typically classified into macroscale, mesoscale, and microscale models depending on their respective modeling objectives and the processes that hence have to be included or neglected. Macroscale models like the Coupled Model Intercomparison Project (CMIP) are used to examine climate change impacts on global or continental level for different global CO_2 emission scenarios in future decades (Meehl et al., 2000; Taylor et al., 2012). Macroscale models like GFS, ECMWF, or ICON are additionally able to predict large-scale weather developments on a contrastingly short timescale (Bassill, 2014; Giorgetta et al., 2018; Hagedorn et al., 2008; Hamill et al., 2008). Their global forecasts of predicted meteorological conditions can then be taken as input for mesoscale models like WRF or COSMO that are on the one hand used for more detailed weather forecasting on a regional scale (Baldauf et al., 2011; Coniglio et

al., 2010; Zheng et al., 2016). On the other hand, they are utilized to investigate regional climate change scenarios and adaptations, for example UHI intensities, the effects of land cover changes (Local Climate Zones), or the possible performance of greening modifications in an entire metropolitan area (Berardi et al., 2020; Brousse et al., 2016; Fallmann et al., 2013; Giannaros et al., 2018; Sharma et al., 2017, 2016; Vogel and Afshari, 2020). While macro- and mesoscale models feature coarse resolutions of kilometers down to hundreds of meters per grid cell of their model domain, microscale models are usually applied on urban quarter scope and thus work in resolutions of around 1-20 m. Representative objectives of microscale models are for example the impact of different building morphologies/materials or green/blue infrastructure on microclimate conditions (Liu et al., 2021). However, for each scale there are models that are concentrating on specific aspects and are thus capable of simulating particular aspects in great speed and detail, while others are rather following a holistic approach trying to capture the majority of possible interacting processes. On the microscale, models like RayMan, SOLWEIG, or CityComfort+ particularly focus on heat stress and thus mainly model radiation budgets, MRT, and thermal comfort based on energy balances (Huang et al., 2014; Lindberg et al., 2008; Liu et al., 2021; Matzarakis et al., 2010). Models based on Computational Fluid Dynamics (CFD) like OpenFOAM, are able to conduct wind and turbulence analysis in particular (Jasak, 2009). Holistic microclimate models like ENVI-met, SOLENE, or the not yet publicly available Palm4U, however, take all kinds of surface-plant-air interactions into account while additionally simulating three-dimensional wind fields, turbulence, air temperature and humidity, as well as radiative fluxes or even pollution dispersion (Bruse, 1999; Bruse and Fleer, 1998; Huttner, 2012; Liu et al., 2021; Maronga et al., 2018; Musy et al., 2015; Simon, 2016; Steuri et al., 2020; Tsoka et al., 2018).

ENVI-met is not only the most frequently used tool for urban heat stress analysis by scientists worldwide, it is also commercially and non-commercially applied by architects as well as urban and landscape planners (Crank et al., 2020; Jänicke et al., 2021; Liu et al., 2021). From its first development in the 1990s by Michael Bruse (Bruse, 1999; Bruse and Fleer, 1998), the application potential of ENVI-met increased significantly up to now, as the model benefited from rising supply of computational power like all models and was further improved by several major advancements such as Full Forcing of measured meteorological boundary conditions, the 7-node-wall model for a higher building modeling

accuracy, a vector editor for quick creation of large model areas, and the façade/roof greening module (Huttner, 2012; Simon, 2016). Due to its multitude of added calculation modules, it is not limited to urban heat stress analysis but can be used for all kinds of specific applications featuring for example the simulation of trees' transpiration rates (Simon et al., 2018c), air quality scenarios such as the creation and distribution of ozone originating from emitted biogenic volatile organic compounds (Simon et al., 2019), or the effect of façade greenery on air temperature at pedestrian level (Morakinyo et al., 2019).

What applies for ENVI-met and all other models accordingly is that their purpose is to uncover and examine trends, relationships, and approximations. In order to gain new knowledge about a topic by the usage of modeling studies, different scenarios are hence needed to compare impacts and outcomes between one another. Examples would be the climate change impact depending on different CO_2 emission scenarios based on several ensemble runs for macroscale modeling (Chen et al., 2020), the difference between a scenario of a Status Quo against a scenario where cool roofs have been applied to an entire metropolitan area for mesoscale (Li et al., 2014), or a comparison of thermal comfort between two planning scenarios featuring more or less trees on a public square for microscale modeling (Zölch et al., 2019). Depending on the magnitude of impact, modeling leads to distinct guidelines that have to be eventually evaluated by cost-benefit analysis. However, modeling is of course not only reliant on relative differences; the prediction of absolute values needs to be accurate as well. In order to examine modeling performances and check their predictions, evaluation studies comparing modeled against measured data are performed. In general, these studies found ENVI-met to be in good agreement with observations as recent review studies by Liu et al. (2021) and Tsoka et al. (2018) summarized. Yet, some studies addressed shortcomings or imprecise parametrizations that caused inaccuracies in modeling (Tsoka et al., 2018). In order to further improve ENVI-met's modeling of urban heat stress and thus the accuracy of heat mitigation studies in general, the most relevant shortcomings reported have been tackled in the present work.

Primarily, ENVI-met's radiation scheme was criticized for its inaccuracy which results in larger discrepancies regarding heat stress indicator MRT and hence thermal comfort calculation (Acero and Herranz-Pascual, 2015; Crank et al., 2020; Gál and Kántor, 2020; Lam et al., 2021; Roth and Lim, 2017; Sharmin et al., 2017; Tsoka et al., 2018; Wallenberg et al., 2020). Longwave emitted and shortwave

reflected radiation were not accurately modeled in particular as a grid cell did not receive such radiation from its surrounding environment but utilized averaged values for the radiation budget calculations. This shortcoming has now been addressed by the development of the so-called Indexed View Sphere (IVS) scheme presented in Section 2. This enhanced ray-tracing approach actually accounts for radiative contributions of objects that are seen by each grid cell. Its basic concept being developed by Michael Bruse in 2017 was significantly reworked by Helge Simon, who also added flexibility to the IVS calculation accuracy that can now additionally be adapted by the user depending on model area size. Proof-of-concept simulations investigated whether IVS simulations featured a higher accuracy in modeling secondary radiative fluxes, i.e., longwave emitted and shortwave reflected radiation, compared to simulations featuring the previously common Averaged View Factor (AVF) concept. The author could substantially support the IVS development and algorithm optimization, prepared, conducted and evaluated the proof-of-concept-simulations, and wrote the majority of the manuscript. The manuscript was published in *Applied Science* 11(12) in June 2021 (Simon et al., 2021b).

Radiation modeling was additionally tackled by the development of an Advanced Canopy Radiation Transfer (ACRT) module that accounts for extinction of diffuse as well as scattering of direct shortwave radiation into secondary diffuse radiation within plant canopies (Section 3). Furthermore, a new plant digitization technique developed by Michael Bruse following the Lindenmeyer-system (L-Trees) was presented, which allows complex plant skeleton structures to be defined with a more realistic position, size, and alignment of leaf clusters, thus resulting in a more accurate representation of plants in ENVI-met. Due to its skeleton with defined branches and twigs, this implementation represents the basis for upcoming developments that will feature the analysis of a tree's biomechanical response to storm events. Proof-of-concept simulations examined whether the combination of both new features – ACRT and L-trees – refined radiation modeling within and below canopies at street-level. The author contributed to this work by developing parts of the ACRT module, preparing and conducting the proof-of-concept simulations, as well as writing several sections of the manuscript. The manuscript was published in *Forests* 11(8) in August 2020 (Simon et al., 2020).

The advancements demonstrated in Section 2 and Section 3 improved ENVI-met's radiation modeling in general and thus positively affected MRT modeling. However, a detailed evaluation study comparing

measurements of air temperature, relative humidity, as well as six-directional radiation fluxes and the resulting calculated MRT with ENVI-met modeling results in Hong Kong found that there are still rather large inaccuracies in MRT modeling (Section 4). The study examined modeled and measured data for six locations that featured three different types of green infrastructure, i.e., a green roof, a green façade, and a tree as well as their three bare counterparts as measurement sites. Furthermore, the demand of both using localized materials and accurate meteorological boundary conditions for the simulations was analyzed. The author contributed by preparing and simulating the multitude of scenarios as well as adding ENVI-met modeling expertise and insights during conceptualization and proofreading of the manuscript. The manuscript will be published in *Building and Environment* 207 in January 2022 (Ouyang et al., 2022).

In order to overcome the reported MRT modeling inaccuracies and hence improve ENVI-met's thermal comfort analysis, new MRT schemes were implemented into the model (Section 5). A new MRT calculation method based on the six-directional radiation flux measurement approach that was used in the validation study in Section 4 as well as three differing projection factors, which are needed to approximate the direct shortwave radiation received by a standing human body's shape, were added to ENVI-met. Subsequent proof-of-concept simulations evaluated the performance of the implementations for eight measurement sites in Sao Paulo and Hong Kong. The author added the different MRT schemes to ENVI-met, prepared, conducted, and evaluated the proof-of-concept simulations, and wrote the manuscript. The manuscript is currently under Review in *Urban Climate*.

Besides these implementations of IVS, ACRT, and MRT schemes in the ENVI-met core, a new post-processing tool called Lagrangian Stochastic Particle Trajectory Model (LaStTraM) was developed (Section 6). While ENVI-met already featured a pollution and chemistry module that is also capable of simulating the effects of water spray, its particle distribution modeling is mainly based on local wind flow and in case of particulate matter on particle size and density (Wania et al., 2012). However, in order to validate and refine conducted eddy-covariance measurements that examine the surface-energy exchange of energy and matter, a more detailed analysis of particles' origins is needed. Therefore, the so-called flux footprint or flux source area is analyzed, which represents an estimation of the surface area influencing the signal measured at a detector location. In simplified models like analytical or Lagrangian

stochastic particle dispersion models, this approximation is based on a function featuring characteristics of the earth surface like roughness length or topography, the state of the atmosphere regarding stability, wind conditions and turbulence, as well as the distribution of sources and sinks (Horst and Weil, 1992; Kljun et al., 2015, 2002; Kormann and Meixner, 2001). While these simplified models cannot take into account the complex urban environment at the measurement site, large-eddy simulations and closure models are capable of simulating flux footprints for more heterogenous environments but feature a very high computational demand and are still not building-resolving (Hellsten et al., 2015; Sogachev et al., 2002). LaStTraM now enables the ability to analyze flux footprints for complex urban environments with distinct objects like buildings, trees, meadows, or green roofs, based on stochastics that are applied on ENVI-met's predicted microclimatological conditions. The author supported the development and coding of LaStTraM, conducted the comparison against other flux footprint models, prepared proof-of-concept simulations, and wrote parts of the manuscript. The manuscript was published in *Atmosphere* 12(8) in July 2021 (Simon et al., 2021a).

While the presented advancements in modeling could be made as developers of ENVI-met with specific model insights and code accessibility in particular, the author could also contribute to scientific progress by applying the model, e.g., as air quality modeling tool demonstrated in Section 7. The study investigated air pollution at child and adult height levels by using low-cost particulate matter measurements on walking routes along kindergartens and schools. To further investigate whether children are exposed to higher air pollution concentrations as they are nearer to the emissions sources of traffic, a simulation study was conducted featuring specific meteorological conditions of the measurement campaign as well as local traffic emission rates. The author contributed to this work by developing and coding a reanalysis, filtering and extrapolation tool fitting the measured data to an optimal route and to a higher temporal resolution, respectively, as well as preparing, conducting and evaluating the ENVI-met simulations, and proof-reading the manuscript. The manuscript is currently under Review in *Urban Climate*.

Aside from air quality modeling, ENVI-met was applied as research tool for new urban heat mitigation measures regarding passive daytime radiative cooling (PDRC). PDRC gained increasing interest over the last years, as new materials have been developed that combine a very high-albedo (>0.96) and very high emissivity (>0.98), which allows them to stay several degrees Celsius below ambient air

temperatures – even during high solar radiation conditions (Mandal et al., 2018). Due to their high reflectivity and thus negative impact on MRT, these materials are not considered as future street or wall materials but as possible coating for roofs. Previous studies found that they could be able to improve building indoor temperatures and hence lower building energy demands (Anand et al., 2021; Baniassadi et al., 2019; Chen et al., 2021; Chen and Lu, 2020; Mandal et al., 2020; Santamouris and Yun, 2020; Yang and Zhang, 2020). In order to evaluate their possible outdoor impact on air temperature at pedestrian level when applied on roofs on a larger scale, a sensitivity study using ENVI-met was conducted (Section 8). Performances of the new super cool roofs (SCR) were compared against the impacts of both traditional cool and green roofs. The study additionally featured varying building height scenarios of a uniformly built model area to examine a possible dependency of pedestrian-level air temperature cooling on building height. The author prepared, conducted, and evaluated the simulations, and wrote the manuscript. The manuscript was published in *Urban Climate* 38(85) in June 2021 (Sinsel et al., 2021a).

Lastly, following the sensitivity study with uniformly built model areas presented in Section 8, a consecutive study analyzed the SCR effect on pedestrian-level air temperature for realistic scenarios featuring complex urban environments in two contrasting cities: New York City and Phoenix (Section 9). Simulations were not only conducted with ENVI-met but also with the mesoscale model WRF in order to, in a first step, examine the impact of SCR application over entire metropolitan areas, in a second step, use WRF's model output as realistic meteorological boundary conditions for the ENVI-met simulations, and, in a third step, find similarities and discrepancies between both models. As SCR performances differed between NYC and Phoenix scenarios in the prediction of both models, it was additionally investigated whether the discrepancies were caused by the prevailing building morphologies or climatological conditions. The author prepared, conducted, and evaluated the ENVI-met simulations, and wrote the majority of the manuscript. The manuscript will be published in *Urban Climate* 40 in December 2021 (Sinsel et al., 2021b).

.

2 Advances in simulating radiative transfer in complex environments

Helge Simon[1], Tim Sinsel[1], Michael Bruse[1]

[1]*Department of Geography, Johannes Gutenberg University Mainz, 55099 Germany*

Summary:

Modeling microclimate conditions largely depends on the accurate modeling of radiative fluxes. However, ENVI-met's radiation scheme was criticized for its modeling of secondary radiative fluxes which results in inaccuracies regarding heat stress indicator MRT and hence thermal comfort calculation. Longwave emitted and shortwave reflected radiation were not accurately modeled in particular as a grid cell did not receive such radiation from its surrounding environment but utilized averaged values for the radiation budget calculations. This shortcoming has now been addressed by the development of the so-called Indexed View Sphere (IVS) scheme presented in the following work. This enhanced ray-tracing approach actually accounts for radiative contributions of objects that are seen by each grid cell. Its basic concept being developed by Michael Bruse in 2017 was significantly reworked by Helge Simon. The author could substantially support the development process and the implementations in the source code. Proof-of-concept simulations investigated whether IVS simulations featured a higher accuracy in modeling secondary radiative fluxes, i.e., longwave emitted and shortwave reflected radiation, compared to simulations featuring the previously common Averaged View Factor (AVF) concept. Aside from code developing support, the author prepared, conducted and evaluated the proof-of-concept-simulations, created the figures, and wrote the majority of the manuscript.

Applied Science 11(12), June 2021 – published

“

2.1 Introduction

Accurate modeling of radiative fluxes plays an important role in microclimatology. This is especially the case in urban areas, where large differences in radiative fluxes can be found due to complex structures, heterogeneous materials, and a multitude of different surface types (Arnfield, 1990, 1982; Oke, 1997; Rosenfeld et al., 1995; Santamouris, 2013). While primary radiative transfer, i.e., incoming shortwave and longwave radiation, can be simulated quite easily using ray tracing algorithms and local Sky View Factors, simulating secondary radiative fluxes which are emitted or reflected by objects of the environment (walls, roofs, the ground surface, or vegetation) are much more complicated to be modeled. The complexity in modeling these radiative fluxes lies in the multiple interactions between the different elements within the view range of the grid analyzed. For instance, radiation reflected by a surface will contribute to the incoming radiation received by other surfaces. These surfaces will again also re-reflect parts of this radiation and distribute in vicinity. Handling such complex conditions is a challenge that is common to all algorithms that involve simulating multiple reflections of radiation such as daylight simulation or image rendering in general (Brown et al., 2001; Cook and Torrance, 1981; Hämmerle et al., 2011; Hu and Qin, 2007; Mardaljevic, 1999).

Over the years, different approaches have been developed to tackle this problem using different kinds of numerical algorithms. The multiple reflections of shortwave radiation can for example be handled by tracing the reflected photons using a Monte-Carlo approach (Aguerre et al., 2017; Howell, 1998, 1969; Lee et al., 2011; Wang, 2014). For the analysis of more mono-directed rays originating from discrete light or radiation sources, raytracing algorithms can be used to follow the radiation on its path through the modeled environment, similar to the algorithms implemented in the microclimate model ENVI-met to calculate the shadow casting (Michael Bruse, 2004; Glassner, 1989; Meinzer et al., 1991; Shirley and Morley, 2008). Another group of algorithms approaches the problem from the other side, by not tracing the radiation itself, but analyzing the view relations between the different emitting and receiving elements in a scene or environment. These types of algorithms are generally categorized as Radiosity Approaches, with several sub-groups depending on the way the individual interactions between the elements are solved (e.g., Matrix Radiosity, Progressive Radiosity or Wavelet Radiosity) (Ayoub, 2020;

Chelle and Andrieu, 1998; Cohen et al., 1988; Fiala and Kadlecová, 2005; Gortler et al., 1993; Helbig et al., 2009; Recker et al., 1990; Wallace et al., 1989).

While these methods give good results in smaller environments like indoor spaces, they are hardly applicable for outdoor situations where an enormous number of elements and view relations between points in space need to be analyzed due to the larger and more complex geometries. Moreover, different to indoor environments, where the radiative fluxes are often calculated only once for a given setting, the situation in an outdoor environment is constantly changing due to movement of the sun and the resulting heating and cooling of surfaces. Hence, the radiative situation needs to be solved frequently - similar to the shadow casting which is typically updated every few minutes (Simon, 2016).

Modern microclimate models like the CFD-model ENVI-met, that considers turbulence and is based on solving Reynolds-Navier-Stokes equations (Bruse and Fleer, 1998; Crank et al., 2018; Simon, 2016; Tsoka et al., 2018), allow for a very precise representation of the urban environment: Besides the detailed plant model (Shinzato et al., 2019; Simon et al., 2018), ENVI-met recently introduced an Accurate In-Canopy Radiation Transfer scheme which accounts for scattering and attenuation of shortwave radiation within tree's canopies (Simon et al., 2020). Buildings cannot only be digitized with a variety of different materials but also individual facades of the same building can consist out of different materials (Forouzandeh, 2021; Simon, 2016; Simon et al., 2017). The same is possible with the ground surface, where different surface types can be assigned to every grid. Since the different objects, materials, and surface types carry their own physical parameters such as albedo, emissivity, heat transfer coefficient etc., the possibility to accurately replicate the variety of the urban environment drastically increases the accuracy of the model results. In previous versions of ENVI-met however, the effects of different materials and surfaces were only calculated explicitly for primary radiation (Huttner, 2012). The distribution of secondary radiative fluxes (reflected shortwave radiation and longwave radiation emitted from objects) was, due to lack of memory and to save computational effort, carried out using a simplification, where instead of the actual reflected shortwave radiation and longwave radiation emitted, averages over all facades and surfaces within the model area were used (Huttner, 2012). This simplification could in some instances lead to a rather low accuracy that has been reported in evaluation studies comparing modeled against measured values of radiation and mean radiant temperature (MRT) (Acero and

Arrizabalaga, 2018; Acero and Herranz-Pascual, 2015; Chen and Ng, 2013; Lee et al., 2016; Roth and Lim, 2017; Salata et al., 2016; Sharmin et al., 2017; Tsoka et al., 2018).

In this paper, a newly developed method is introduced to overcome these shortcomings. It enables the simulation of fluxes of reflected shortwave and emitted longwave radiation within the urban environment with a much higher level of detail, considering the actual objects, i.e., facades, surfaces, and trees "seen" by a grid cell. By simulating secondary radiation in greater detail, differences in local microclimates can be identified more clearly and influences of e.g., highly reflective surfaces or vegetation cover onto bio climate indices such as PET (physiological equivalent temperature) can be taken into account. In a large ENVI-met proof-of-concept simulation featuring a multitude of different surfaces and plants, the new method is compared against the previous approach. The comparison should evaluate the accuracy of the new radiation scheme and examine the impacts of the more accurate secondary radiation modeling on the simulated local microclimate.

2.2 Model description

In the following, the old Averaged View Factor concept used in ENVI-met is described (Section 2.2.1) and the advancements of the new Indexed View Sphere (IVS) algorithm are laid out in detail (Section 2.2.2). To evaluate the advantages of the new IVS module, a proof-of-concept simulation is conducted comparing the results of both concepts (Section 2.2.3).

2.2.1 The Averaged View Factor (AVF) Concept

To describe the radiative situation and solve the interactions between different elements, ENVI-met version 4.4.5 and prior used a generalized visibility concept based on Averaged View Factors (AVF). In the AVF concept, first, a three-dimensional ray tracing analysis is performed for every cell. Starting from a grid cell's center, rays are being shot for every 10° height and 10° azimuth angle creating a sphere consisting out of 18 x 36, thus 648 individual view facets. While calculating these 648 individual view facets for every grid cell can be very time consuming, it only needs to be performed once for a model simulation as the objects seen by a cell do not change over the course of a simulation. Based on the object type (sky, building, plant, ground surface) seen by the view facet / hit by the ray and the total number of view facets, averaged view factors of sky σ_{Sky}, vegetation σ_{Veg}, buildings σ_{Bldg} and ground

surfaces σ_{Grnd} were stored as single values for each grid cell. By only saving the view factors for the different object types instead of the actual façade elements, ground surfaces, and plant sections seen in the facets, a lot of memory can be saved. However, since no information is stored about which individual elements are in radiative exchange with the cell, the calculation of secondary radiative fluxes cannot take into account the radiation exchanges between actual objects seen but rather has to resort to an approximation. Instead of individual information about radiation received from particular objects, the secondary radiation is approximated by combining a grid cells' view factor for buildings, plants, and ground surfaces with averaged values of reflected and emitted longwave radiation for all buildings, plants, and ground surfaces over the entire model domain (Michael Bruse, 2004; Huttner, 2012; Helge Simon, 2016).

The received secondary radiation of a cell – in this case the received shortwave reflected radiation from buildings – is thus calculated by:

$$Q_{swrefl,in}(i,j,k) = \sigma_{Bldg}(i,j,k) \cdot Q_{Bldg,swrefl} \qquad \textit{Eq. 2-1}$$

with $\sigma_{Bldg}(x,y,z)$ as the building view factor (0 to 1) of cell i,j,k and $Q_{Bldg,swrefl}$ as the averaged reflected shortwave radiation from all buildings calculated by:

$$Q_{Bldg,swrefl} = \frac{1}{N}\sum_{a=1}^{N} \propto (a) \cdot Q_{sw}(a) \qquad \textit{Eq. 2-2}$$

with N being the total number of facades in the model, $\propto$ the albedo of façade a and Q_{sw} the shortwave radiation in front of façade a. The same calculations are carried out taking into account averaged surface temperature values of buildings, leaves, or ground surfaces for the estimation of received secondary longwave radiation.

To account for changes in the radiative situation, these calculations (Eq. 2-1, Eq. 2-2) and their respective counterparts for other object types and emitted longwave radiation need to be solved regularly, i.e., every 15 minutes by default in ENVI-met.

The consequence of this simplification is that every point with an identical view factor for buildings, ground surfaces, or vegetation will receive the exact same amount of reflected shortwave and emitted longwave radiation.

While this simplification does save memory, it also leads to very unrealistic results: Given the same view factors, a cell would receive the exact same amount of reflected shortwave and emitted longwave radiation independent of the actual radiative processes in its vicinity. This could lead to identical reflected shortwave fluxes in front of north and south facades or high-reflective façade materials or low-reflective façade materials.

2.2.2 The Indexed View Sphere (IVS) algorithm

To overcome this simplification, the Indexed View Sphere (IVS) algorithm was developed and implemented into ENVI-met. The main idea behind IVS is to save the results (i.e., the objects seen by a cell in a certain view angle) of the initial geometrical analysis so that it is possible to relate the calculated View Factors back to the contributing elements of the urban scene. Its fundamentals are comparable to Sky View Factor calculations based on fish-eye-imagery where the amount of sky pixels per annulus ring is analyzed (Figure 2-1a) (Chapman and Thornes, 2004; Middel et al., 2018; Steyn, 1980; Steyn et al., 1986). To reduce the memory needed, the new IVS does not calculate the same amount of view facets in all height angles of the view sphere (Figure 2-1b).

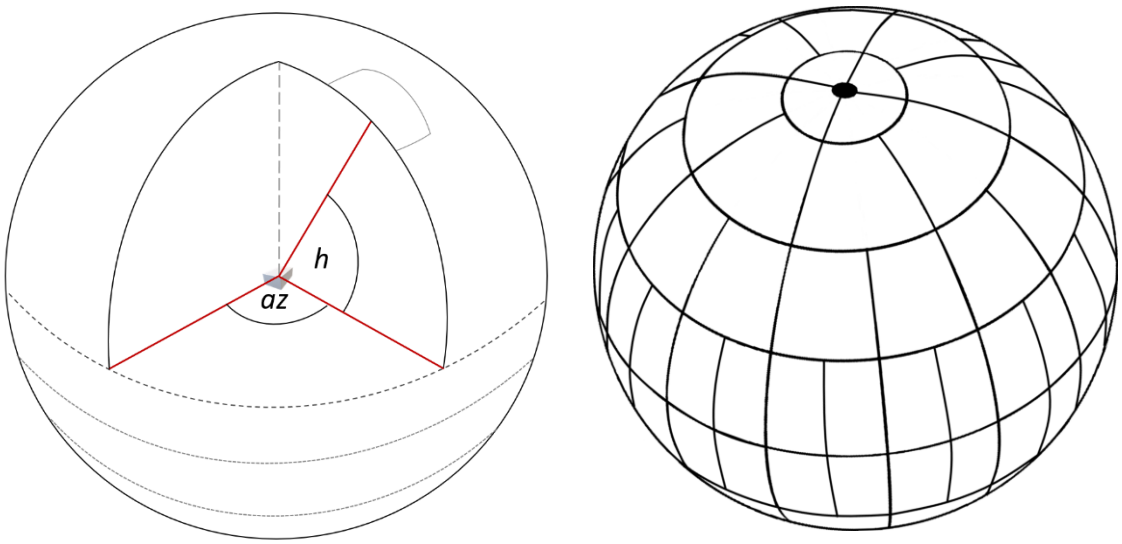

(**a**) (**b**)

*Figure 2-1: View sphere for an exemplary grid cell to be analyzed depicting azimuthal angle az and height angle h definition (**a**) and individual view facet distribution per height angle (**b**) showing that view facet count decreases with increased height angles.*

Since the resulting surface area for a given azimuthal angle decreases with increased height angles, the size of the azimuthal angle and thus of the view facets can be set larger with little to no information loss. The size of the azimuthal angles and thus the view facets is calculated by a function of the height angle.

The user only defines the resolution of the height angles and the azimuthal angles at the equator of the cell. The number of azimuthal angles, i.e., the number of distinct view facets for a given height angle is then calculated by:

$$\lambda(h) = \frac{360}{az_{eq}} \cdot \cos(h) \qquad \textit{Eq. 2-3}$$

with az_{eq} as the user defined size of azimuthal angle at the sphere's equator, and the height angle h. To ensure all cardinal directions are represented, a minimum of four azimuthal angles is set for height angles less than |90°|. For height angles of +- 90° only one view facet is obtained since azimuthal angles would be indifferent for these height angles.

By reducing the number of view facets per cell, an immense amount of memory can be saved without losing too much information about objects seen by a grid cell. Where a 10° height and azimuthal angle would previously result in 648 view facets, the same height and azimuthal resolution at the equator now results in 414 view facets. In combination with more efficient data structures, this decreases memory demand by around 40 % and enables the possibility to store pointers to the objects seen by cell in a particular direction. By storing a direct link to objects seen by a cell, the actual radiation reflected / emitted by these objects can now be used to calculate a cell's received reflected shortwave and longwave radiation instead of using averaged values. Taking into account this radiation received, the cell alters its own reflection of shortwave and emission of longwave radiation and in turn contributes to the radiation received of other cells.

To calculate the received reflected shortwave and emission of longwave radiation coming from buildings or ground surfaces, the individual contribution of the objects is weighted by the view angle of the facet and simply added up:

$$Q_{Build,Grnd,in}(i,j,k) = \sum_{a=1}^{F} \omega(a) \cdot \tau_{Veg}(a) \cdot Q_{Build,Grnd,out} \qquad \textit{Eq. 2-4}$$

with F being the total number of facets of the view sphere, $\omega(a)$ as the weight of the view facet a, $\tau_{Veg}(a)$ as the transmission factor accounting for reduction of the visibility due to vegetation between

the cell i, j, k and the objects seen, and $Q_{Build,Grnd,out}$ as the outgoing reflected shortwave or emitted longwave radiation by the seen objects.

Secondary radiation emitted by vegetation is accounted for by inverting the transmission factor:

$$Q_{Veg,in}(i,j,k) = \sum_{a=1}^{F} \omega(a) \cdot (1 - \tau_{Veg}(a)) \cdot Q_{Veg,out} \qquad \textit{Eq. 2-5}$$

with $Q_{Veg,out}$ as the outgoing reflected shortwave or emitted longwave radiation by the seen plants.

While the height angles are constant within a view sphere, the azimuthal angle and thus the number of view facets changes with increased height angles. This implies, that the weighing factor is not identical for all view facets, but depended on the number of view facets in a particular height ring. The individual weighting factor accounting for the contribution of a view facet is calculated by:

$$\omega = \frac{1}{\lambda(h)} \cdot \frac{1}{r_{cnt}} \qquad \textit{Eq. 2-6}$$

with $\lambda(h)$ as the number of view facets in a given height angle and r_{cnt} as the number of height rings for a particular view direction, e.g., downward view or upward view.

The transmission factor for vegetation τ_{Veg} is calculated within the raytracing and accounts for a partial obstruction of radiation due to vegetation in the ray's path. The calculation of transmission is carried out using the exponential extinction coefficient accounting for leaf orientation φ (currently set to 0.5), the local leaf area density (LAD) and the path length through the vegetation cells:

$$\tau_{Veg} = \mathrm{e}^{-(\varphi \cdot \mathrm{LAD} \cdot dRay)} \qquad \textit{Eq. 2-7}$$

Further advancements have been undertaken with regards to the ray tracing algorithm. While in previous versions, the segment length for the ray would be determined only once for a given angle, the new algorithm tries to find an appropriate length for the ray segments based on current grid dimensions as well as azimuthal and height angle. Determining a segment's length is not only critical for the calculation speed as short rays drastically increase computational effort but also for the quality of the resulting radiation calculation. With the discretization of space in models like ENVI-met an optimal ray length is very hard to determine. With typical cell dimensions of 2 to 5 meters in x, y, and z (Simon, 2016), too short ray segments might lead to an over-representation of cells which are only marginally clipped by a

ray since the whole cell would count as "hit" by the ray. Too large ray segments however might lead to not detecting / not taking into account objects in the path of a ray.

To determine an optimal vector length increment for the ray trace, given the azimuthal and height angle, the normalized contribution weight (dx_{nwght}, dy_{nwght} and dz_{nwght}) of the x, y, and z axis onto the resulting vector is calculated at first:

$$\begin{pmatrix} dx_{wght} \\ dy_{wght} \\ dz_{wght} \end{pmatrix} = \begin{pmatrix} |\cos(h) \cdot \cos(az)| \\ |\cos(h) \cdot \sin(az)| \\ |\sin(h)| \end{pmatrix}$$

$$dxyz_{Sum} = dx_{wght} + dy_{wght} + dz_{wght} \qquad \textit{Eq. 2-8}$$

$$\begin{pmatrix} dx_{nwght} \\ dy_{nwght} \\ dz_{nwght} \end{pmatrix} = \begin{pmatrix} dx_{wght}/dxyz_{Sum} \\ dy_{wght}/dxyz_{Sum} \\ dz_{wght}/dxyz_{Sum} \end{pmatrix}$$

By taking into account the cell dimensions of the current cell, the normalized weights for all axes are then used to scale the length of the three-dimensional vector:

$$dRay(i,j,k) = \vartheta \cdot \left(dx(i,j,k) \cdot dx_{nwght} + dy(i,j,k) \cdot dy_{nwght} + dz(i,j,k) \cdot dz_{nwght}\right) \qquad \textit{Eq. 2-9}$$

with ϑ as a scaling factor of the vector length. This scaling factor should ensure that cells are detected which only partially lie along the path of the vector, i. e. a segment of the ray ends within the cell's boundaries. While a small scaling factor ensures a very precise ray tracing detecting all cells hit by a ray, it also leads to increased calculation time. Even more importantly, cells that might only lie very marginally in the path of the ray, i.e., clipped only very slightly, may be overrepresented in the further calculation. Test simulations showed that a scaling factor between 0.25 and 0.5 led to a good compromise between accuracy of the ray tracing and representation of cells clipped by the ray.

To determine the increments in x, y and z direction the calculated vector length $dRay(i,j,k)$ is then again calculated by:

$$\begin{pmatrix} dx_{seg} \\ dy_{seg} \\ dz_{seg} \end{pmatrix} = \begin{pmatrix} dRay(i,j,k) \cdot \cos(h) \cdot \cos(az) \\ dRay(i,j,k) \cdot \cos(h) \cdot \sin(az) \\ dRay(i,j,k) \cdot \sin(h) \end{pmatrix} \qquad \textit{Eq. 2-10}$$

After each iteration, the ray length for the current grid cell is updated to account for non-equidistant gridding in the model.

The new IVS calculation method for calculating secondary radiation transfers can be enabled in the simulation settings of the SIMX file. By default, the module is switched off. If enabled, the user is able to adjust the height angles and azimuthal angles at the sphere's equator. To save memory, the simulation settings allow to define a high-resolution and a low-resolution angle pair. After a cut-off height defined, the model switches from the sphere definition of the high-resolution angles to the low-resolution angles. Similar to ENVI-met's vertical splitting (see Simon, 2016), radiation processes near surface can thus be modeled with higher accuracy while processes of secondary radiation transfer above are carried out in a coarser resolution. This not only saves memory but also computational power. In case the user does not want to use this option, the high-resolution and low-resolution angles can simply be entered identically.

2.2.3 Proof-of-Concept Simulation

The advancements of ENVI-met's new IVS module are evaluated by comparing the model results of a simulation featuring the old AVF concept against a simulation featuring the new IVS algorithm, respectively. The model results will first be compared against each other with regard to longwave and shortwave radiation patterns, MRT, and potential air temperatures for different heights and times during the day. Furthermore, the impact of simulating secondary radiative transfers using IVS is examined by comparing the thermal comfort index PET between the two simulations.

In order to find the expected large differences in radiation budgets – and thus in the resulting microclimate conditions – between varying surface and building materials, the modeled area was chosen based on a high spatial variability. The model area is located at the edge of Central Park in New York City, USA featuring an additional high recognition value because of its iconic urban morphology surrounding the Columbus Circle. Varying building heights, differing materials such as glass, concrete, or brick, and specific roof types such as roofs featuring greenery or cool (high-albedo) materials, which are common heat mitigation measures (He et al., 2020; Santamouris and Yun, 2020), already show the heterogeneity of the model area. Furthermore, the great differences in surface materials (meadows, rocks, sand pitches, streets, and pavements) together with the dense tree vegetation in Central Park located in model area's

lower right will enable to show the complexity in secondary radiative fluxes that can be modeled by the new IVS module. To show the large variety of building and surface materials, the different materials have been visualized by specific colors (Figure 2-2). Table 2-1 gives an overview on the parameters of these materials that are based on the Midrise Apartment Post 1980 Standard for American Housing in NYC (Deru et al., 2010). Building footprints and street tree locations were retrieved from the NYC open data portal (NYC Open Data, 2019). Surface and building materials as well park trees were digitized based on aerial imagery.

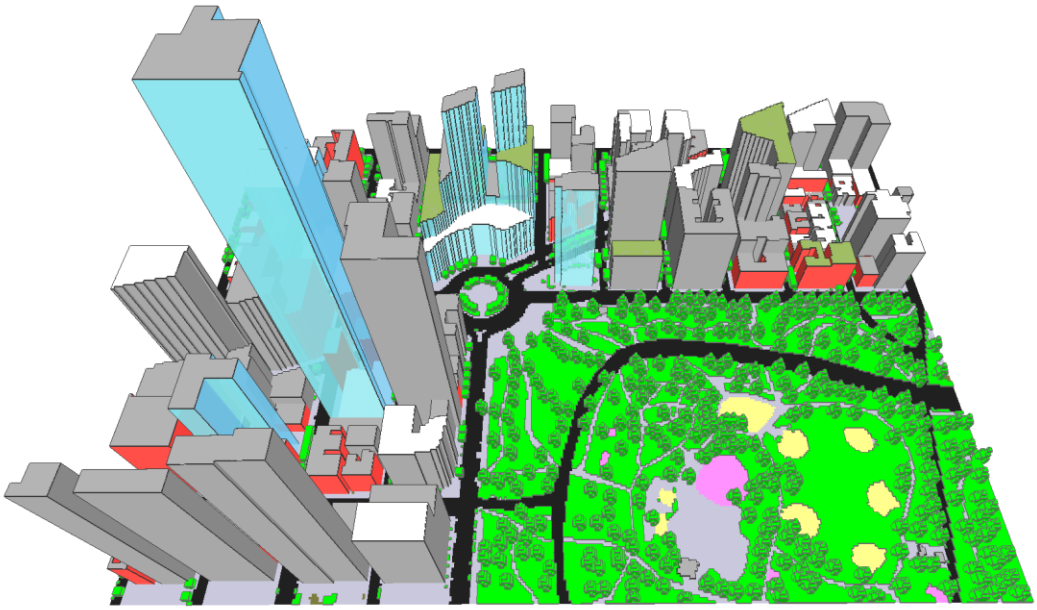

Figure 2-2: Example model area at the edge of the Central Park in NYC modeled for the proof-of-concept simulations. Different colors indicate different material properties. Non-default ENVI-met database item properties are defined in Table 2-1. Grey facades/roofs indicate Concrete Walls and Default Roofs, respectively; blue transmissive facades indicate Glass Walls; red facades indicate Brick Walls; white roofs indicate Cool Roofs; green facades indicate Default Roofs with default greenery 01NASS being applied; green surfaces indicate default open soil 0100SL and default grass 0100XX; black surfaces indicate default asphalt road 0100ST; grey surfaces indicate default pavement 0100PP; pink surfaces indicate basalt rock profile entirely filled with default 0000BA soil; yellow surfaces indicate default sand profile 0100SD.

Table 2-1: Summary of material properties in the proof-of-concept simulation (Deru et al., 2010).

	Layer	Name	Albedo	Absorptivity	Emissivity	Thickness [m]	Conductivity [W (m K)$^{-1}$]	Density [kg m^{-3}]	Specific Heat (J (kg K)$^{-1}$)
Concrete Wall	Outside	Concrete	0.2	0.8	0.9	0.2	1.311	2240	836.8
	Middle	Steel frame Insulation	0.2	0.8	0.9	0.08	0.049	265	837
	Inside	1/2IN Gypsum	0.2	0.8	0.9	0.01	0.16	785	830
Glass Wall	All	Glass	0.25	0.05	0.94	3 x 0.01	0.029	830	840
Brick Wall	All	Brick	0.15	0.85	0.9	3 x 0.08	0.66	1500	1000
Default Roof	Outside	Default membrane	0.2	0.8	0.9	0.01	0.16	1121	1460
	Middle	Insulation	0.2	0.8	0.9	0.14	0.049	265	837
	Inside	Metal Decking	0.2	0.8	0.9	0.01	45	7680	418
Cool Roof	Outside	Cool material	0.65	0.35	0.9	0.02	0.85	1200	1200
	Middle	Insulation	0.2	0.8	0.9	0.14	0.049	265	837
	Inside	Metal Decking	0.2	0.8	0.9	0.01	45	7680	418

The meteorological boundary conditions were taken from an Energy Plus Weather File of NYC (Wilcox and Marion, 2008). To resemble a hot summer day with clear sky conditions, July 21st was selected as simulation date. The simulation has been run for 24 hours. Figure 2-3 shows the meteorological conditions for the whole simulation period provided by the EPW-file.

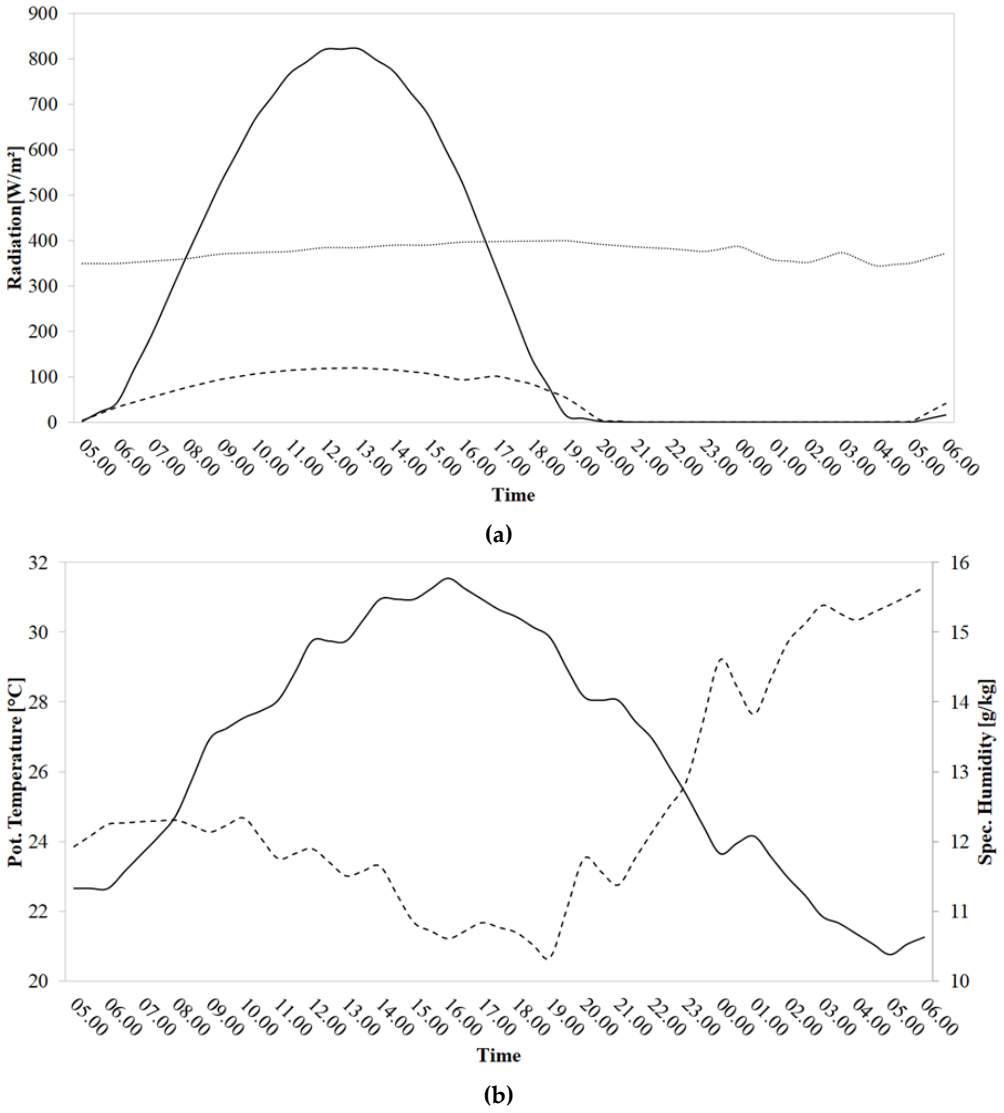

*Figure 2-3: Meteorological boundary conditions for the proof-of-concept simulation depicting direct shortwave (black line), diffuse shortwave (dashed line) and longwave radiation (dotted line) (**a**) as well as potential air temperature (black line) and specific air humidity (dashed line) (**b**).*

General simulation and model area properties are described in Table 2-2. Air temperature within buildings is held constant at 20 °C to account for the strong air conditioning cooling used in almost every building in NYC. Radiation scheme settings for the IVS simulations feature medium resolutions for lower cells at pedestrian level and low resolutions for higher cells above 8 m. Due to the large size of the model area featuring high-rise buildings and covering multiple different urban morphologies and typologies in a high spatial resolution, IVS settings could not feature higher view facet resolutions due to memory limitations. With these settings, the simulation yields around 50 GB of RAM for the IVS simulation.

Table 2-2: Parameters of the proof-of-concept simulations.

General properties of both simulations	
Start date and time (Local)	21.07.2017 05:00
Duration [h]	24
Wind Speed [m s^{-1}]	2
Wind Direction [°]	325
Meteorological Boundary Conditions	Full Forcing
Location Lat (Lower Left Corner)	40.76 °N
Location Lon (Lower Left Corner)	-73.98°E
Dimensions	360 x 260 x 52
Resolutions (X, Y, Z) [m]	2.5 x 2.5 x 5
Lowest Grid Cell Splitted	Yes
Telescoping: Factor & Starting Height	30 % above 180 m
Height of 3D Model Domain [m]	1434 m
Building Indoor Temperature Held Constant at	20 °C
View Factor Update Interval	30 days
Specific Radiation Scheme Settings for IVS simulation	
Height Angle High Resolution Near Ground	15°
Azimuthal Angle High Resolution Near Ground	15°
Height Angle Low Resolution Above Height Boundary	30°
Azimuthal Angle Low Above Height Boundary	30°
Height Boundary between High and Low Resolution	8 m

2.3 Results and Discussion

To give an overview on the differences between AVF and IVS, visualizations of the case study simulation results are presented. Radiation patterns as well as temperature distributions and impacts on thermal comfort are compared using absolute value maps of both scenarios to evaluate the advancements provided by the new IVS scheme.

After the theoretical explanations in Section 2.2.2, principles in IVS modeling are visually demonstrated by the 3D view of the model area. Figure 2-4 shows the rays that were traced for one specific grid cell at 138, 150, 6 amid the center of Columbus Circle. Each ray represents a view sphere segment of the grid cell to be analyzed. It is emitted from the grid cell center and searches for objects in each view sphere direction. When a building or soil surface is hit, the raytracing is aborted, and the object information is stored. With increasing height angle and especially above the highest object height, the length

of each raytracing segment is, to save computational time, drastically increased as the probability of hitting an object is diminishing.

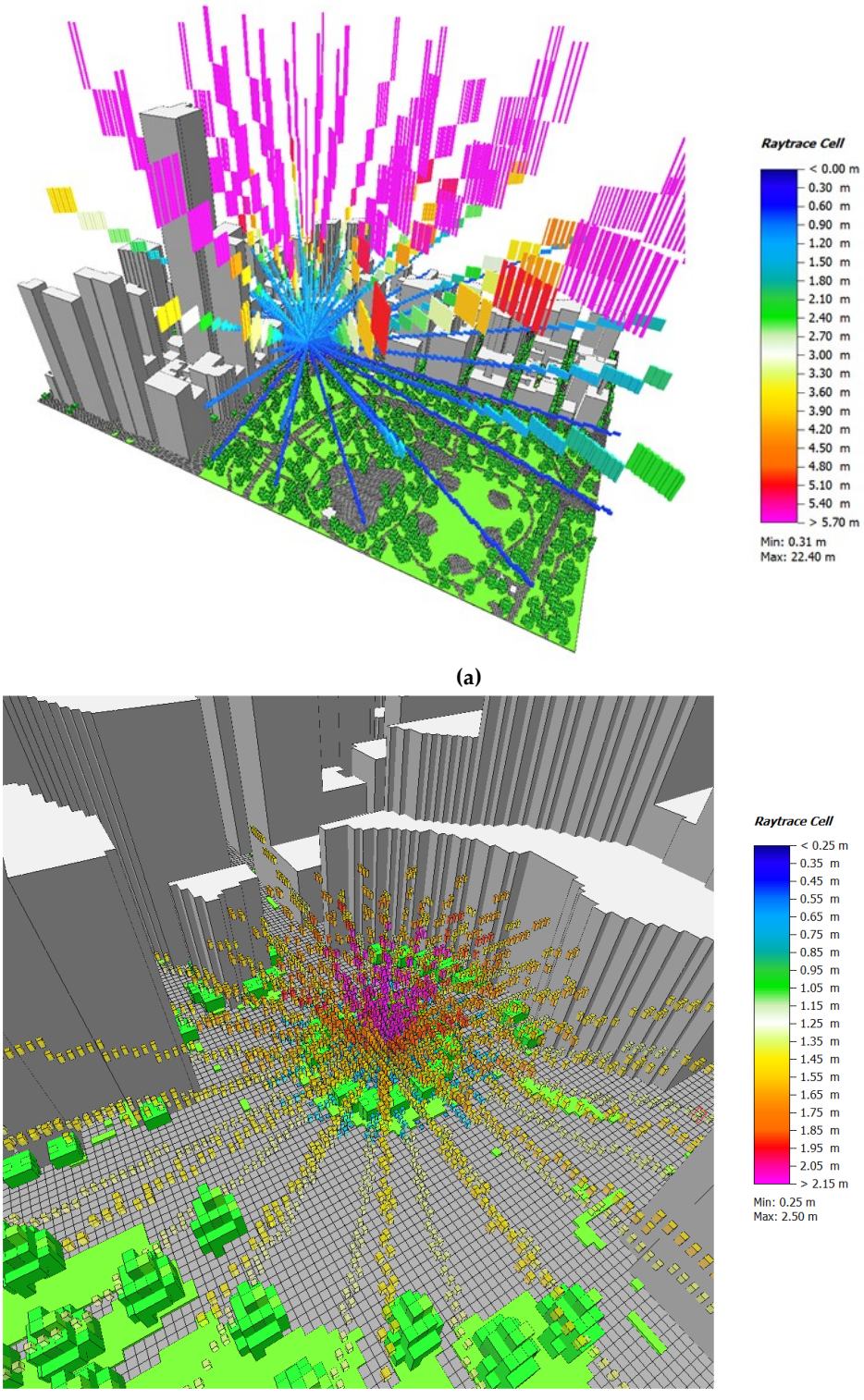

*Figure 2-4: This specifically generated simulation output depicts the length of raytracing segments for one observed grid cell above the center of Columbus Circle. The 3D output view shows these raytracing lengths from a far perspective demonstrating the long ray distance and the length increase with height in (**a**) and from a near-by perspective with a 50 % decreased data cube size, 50 % data cube transparency, and data*

*being filtered for height levels below k = 13 to visualize the high view sphere resolution and the resulting rays near the observed cell in (**b**).*

ENVI-met provides multiple output variables to allow the analysis of radiation patterns. Variables containing shortwave or longwave radiation values are distinguished between upper and lower hemisphere to allow a specification from which direction the radiation is received. Analyzing for example longwave radiation distribution received from lower hemisphere in a horizontal cut at 1.5 m height, most radiation input probably originates from soil surfaces, ground vegetation, and nearby façade elements. Figure 2-5a demonstrates that longwave radiation values cover a wider range and more distinct differences over the model at 13:00 in the IVS scenario compared against the AVF scenario. Especially the pattern of park streets can be recognized as they emit more longwave radiation than their surroundings. That is caused by their low-albedo surfaces that heated up more during the morning hours in contrast to the street canyons which have been shaded by buildings. In IVS, dotted patterns of lower longwave radiation values received by lower hemisphere can be found in the Central Park where trees cast shade and thus cool the ground below canopies leading to less longwave emission compared to the open surfaces in other park areas. These patterns are still visible in Figure 2-5b depicting the same results but for a horizontal cut in 82.5 m height. Furthermore, as the cut is performed in an intermediate height – above some low- and medium-rise buildings of the model area – differences in roof type effects can be examined. In IVS, the rather cold – and thereby not emitting much longwave radiation – cool and green roofs stand out against the traditional hotter low-albedo roofs that strongly contribute to the longwave radiation received in 82.5 m height. In AVF with its averaging approach, these different roof surface temperature differences while being simulated to not translate in differences of emitted longwave radiation as their contribution as specific object is not stored individually. Even differences in longwave radiation values caused by trees in Central Park are still recognized by IVS, even though spatial distances between the grid cells in 82.5 m height and the trees at ground level are quite large.

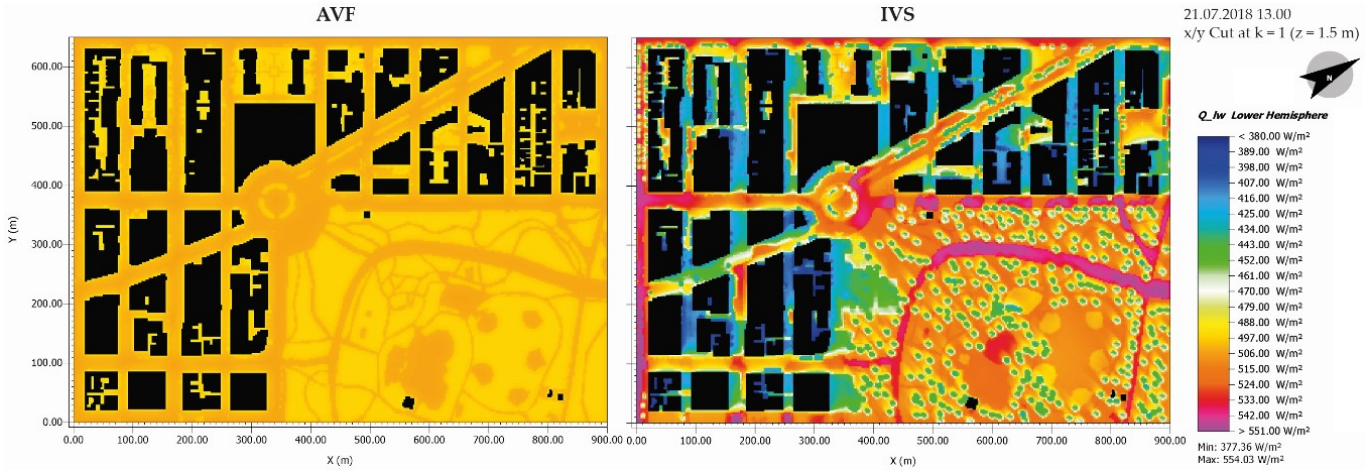

(a)

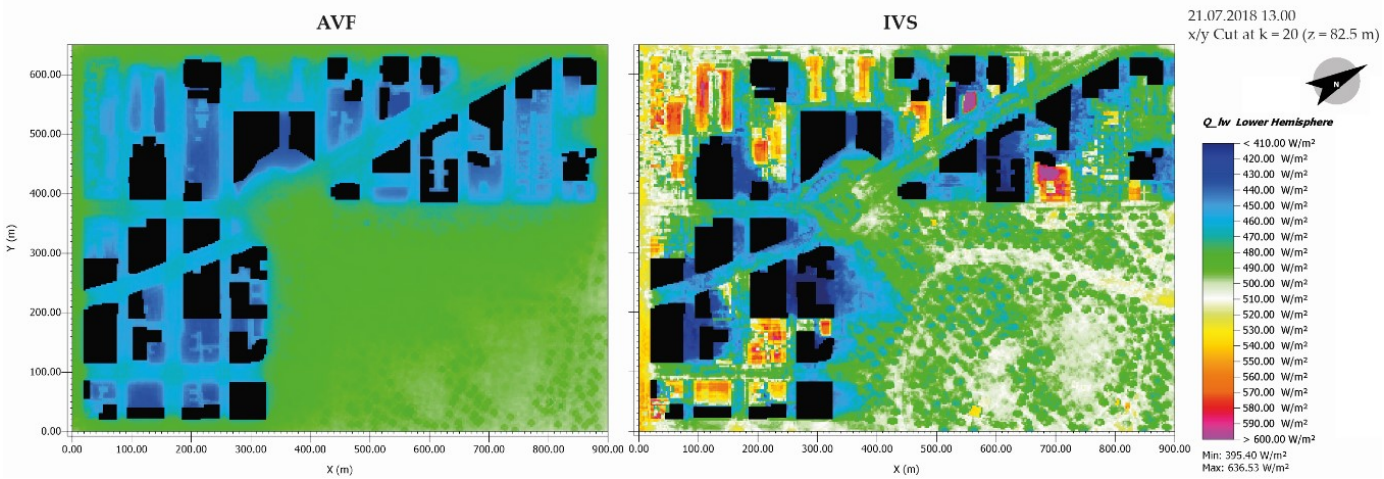

(b)

*Figure 2-5: Comparison of proof-of-concept simulation results between AVF and IVS for longwave radiation received from lower hemisphere at 13.00 in a height of 1.5 m (**a**) and in a height of 82.5 m (**b**), respectively.*

While surface temperature mainly drives the emitted longwave radiation patterns, reflected shortwave radiation is influenced by both albedo and shadowing. Figure 2-6a clearly demonstrates which areas are shaded during 13:00 when the sun's position is in the South - thus being at model area's left due to its rotation. Figure 2-6a and b again show less pronounced differences in AVF. Especially the very small range between 90 and 144 W/m² at pedestrian level in AVF shows that most parts of the model area are rather homogenously affected by reflected shortwave radiation. The IVS results however accurately account for spatial relationships between objects and thus models minimal reflected shortwave radiation of <5 W/m² for shaded areas but very large contributions of reflected radiation in high-albedo spots, for example above open sand at the ballpark in Central Park.

Furthermore, when performing a horizontal cut at 82.5 m height, we again find roofs in IVS to show higher values than other parts of the model area in contrast to AVF. However, with their higher albedo, green and especially cool roofs now show higher values as they reflect more shortwave radiation than the traditional low-albedo roofs. By examining these comparisons in Figure 2-5 and Figure 2-6, it becomes clear that both longwave and shortwave contributions to a cell's radiation budget are underestimated by AVF. Urban heating caused by traditional building materials as well as cooling performances of cool or green roof application hence probably have been underestimated in previous ENVI-met modeling studies (Tsoka et al., 2018).

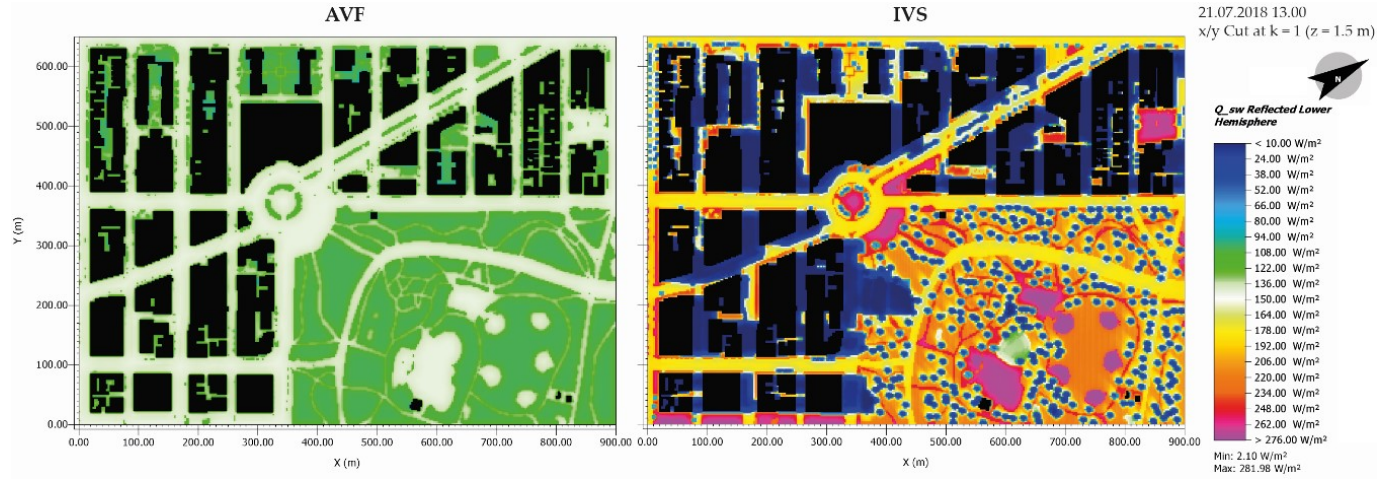

(a)

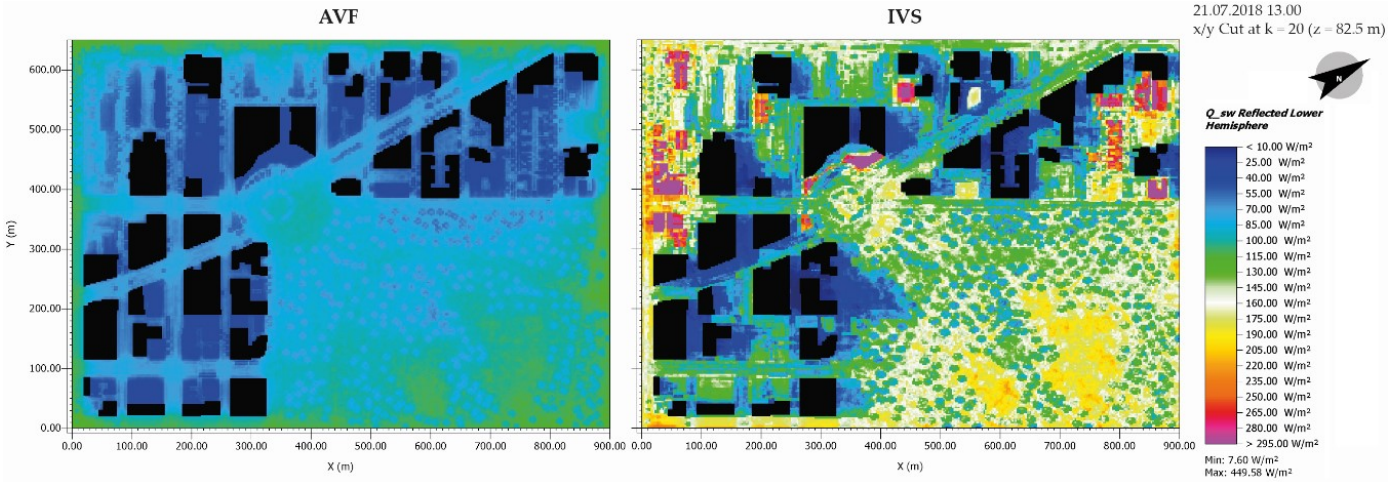

(b)

*Figure 2-6: Comparison of proof-of-concept simulation results between AVF and IVS for reflected shortwave radiation received from lower hemisphere at 13.00 in a height of 1.5 m (**a**) and in a height of 82.5 m (**b**), respectively.*

By using the model area average, AVF does not consider shortwave radiation reflections accurately in general which is proved by two additional examples. It is firstly shown by the comparison of reflected shortwave radiation patterns for the horizontal cut at 82.5 m at 09:00 where the sun's position is in the East coming from the bottom side of the model area (Figure 2-7a). Since the circular shaped building at the Columbus Circle features glass facades and thus works like a magnifying glass, shortwave radiation is reflected from all sides to the center which leads to a high accumulation in sum. By using IVS, these reflections are accounted for and values of up to 299 W/m² amid the circular-shaped building wall at the Columbus Circle are predicted by the model whereas AVF only shows very low values around 25 W/m² here.

Secondly, the pedestrian level horizontal cut of shortwave radiation reflections from the upper hemisphere also shows that, in contrast to AVF, IVS takes the reflection of glass facades into account (Figure 2-7b). As solar radiation at 13:00 originates from South being at the left-hand side of the model area, shortwave reflected radiation coming from upper wall parts is modeled to be received in urban canyons at pedestrian level on the left-hand side of glass-façade buildings. The total amount however is comparatively low as solar radiation is mostly reflected upwards from soil or roof surfaces and is thus included in lower hemisphere values. Besides the primary reflection from wall surfaces, secondary reflected radiation can be found in Central Park, where primary reflected solar radiation from soil surfaces and grass is secondarily reflected downwards by tree canopies.

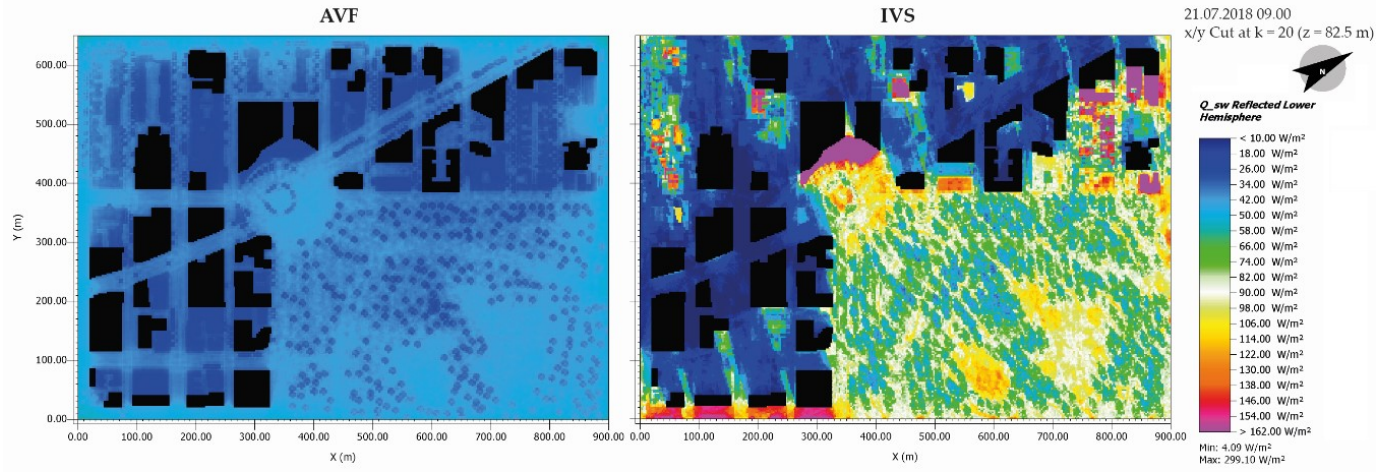

(a)

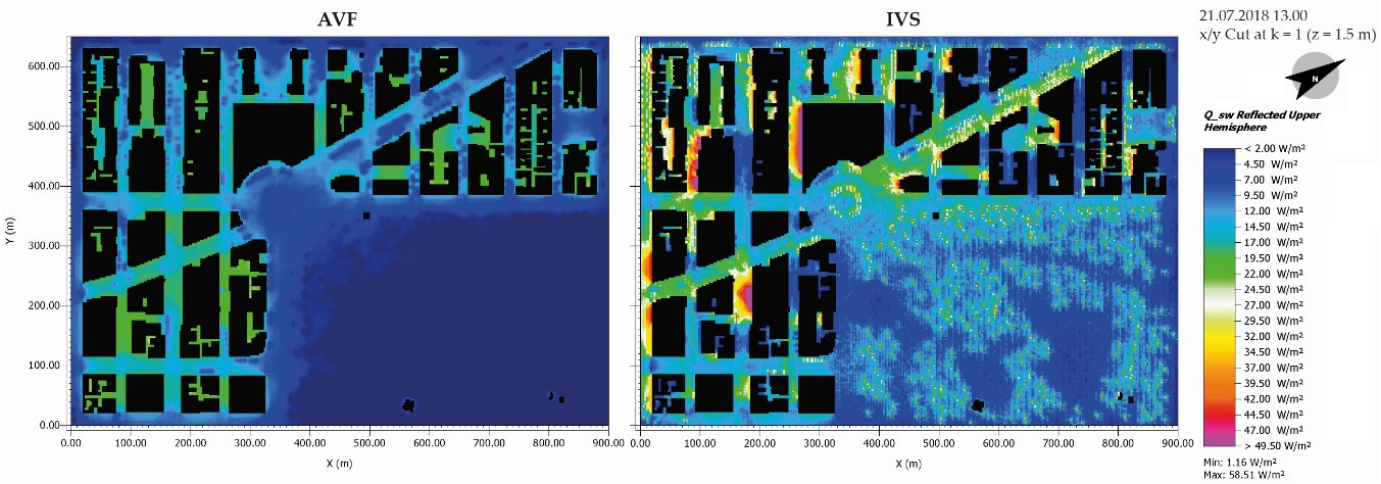

(b)

*Figure 2-7: Comparison of proof-of-concept simulation results between AVF and IVS for reflected shortwave radiation received from lower hemisphere at 09.00 in a height of 82.5 m (**a**) and for reflected shortwave radiation received from upper hemisphere at 13.00 in a height of 1.5 m (**b**), respectively.*

In contrast to the massively differing radiation patterns, at first glance we only find small discrepancies in potential air temperature results for a horizontal cut at pedestrian level at 13:00 between AVF and IVS (Figure 2-8a). In general, IVS features slightly lower values of around 0.2 – 0.4 K. However, we find distinct differences between AVF and IVS in parts where high discrepancies of secondary radiation fluxes were observed. Especially the cooler regions in the Southern/left part of the model area are more pronounced in IVS as they receive less emitted longwave and less reflected shortwave radiation due to the shadows of larger skyscrapers next to them.

Analysis of MRT corroborates that by showing even larger deviations between AVF and IVS for the same height and timestep (Figure 2-8b). According to the radiation patterns the MRT is based on, MRT also features a wider range of values in IVS. To address the magnitude of urban heat stress and the effects of mitigation strategies properly, thermal comforts indices are often used as holistic indicators in urban environments. These indices take several parameters such as air temperature, humidity, wind speed, and MRT into account (Höppe, 1999; Matzarakis et al., 1999). In this study, the thermal comfort index PET is used representing a commonly used index for outdoor environments of temperate climate zones (Gómez et al., 2013; He et al., 2015; Matzarakis and Amelung, 2008). When analyzing PET in Figure 2-8c, we find that major patterns are the same between AVF and IVS. However, the range is again wider and more differentiated in IVS simulation. As discrepancies in wind field and humidity are assumed to be marginal by the use of different radiation schemes and as temperatures are shown to be

only slightly different in Figure 2-8a, deviations are mainly based on the differences in MRT patterns which are in turn a key factor for thermal comfort and thus PET calculation.

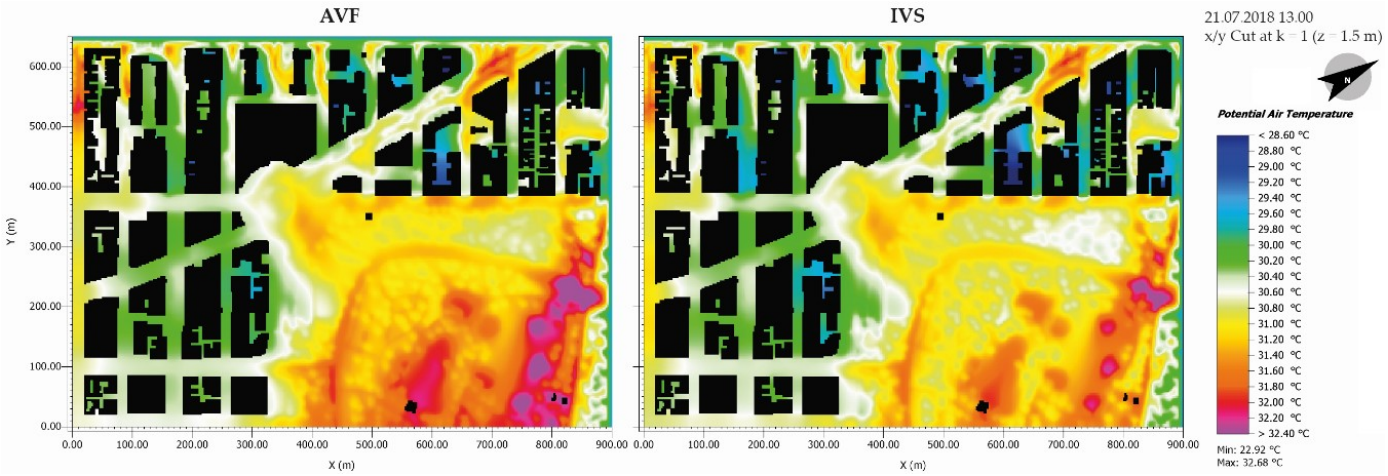

(a)

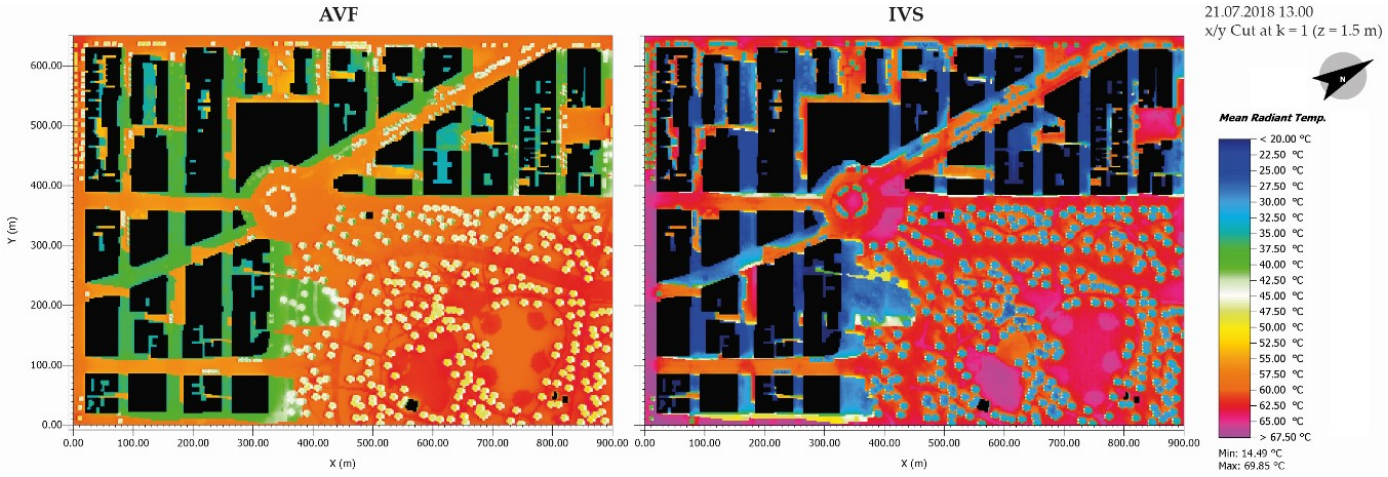

(b)

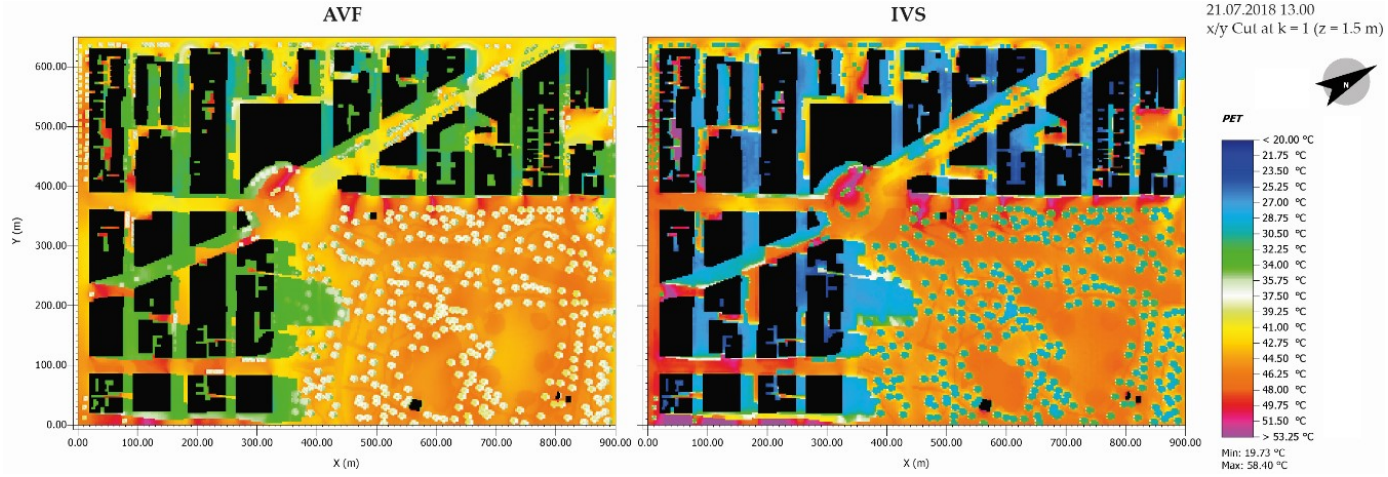

(c)

*Figure 2-8: Comparison of proof-of-concept simulation results between AVF and IVS at 13.00 in a height of 1.5 m for Potential Air Temperature (**a**), for Mean Radiant Temperature (**b**), and for PET (**c**), respectively.*

These findings agree with the analysis of nighttime results shown in Figure 2-9. Longwave radiation emissions are based on the object temperatures. During nighttime, these surface temperatures of soils, buildings, and plants are influenced by their thermal properties, which specify their behavior in storing and releasing heat, as well as the amount of solar radiation that has or has not been received during daytime. As both of these parameters vary massively over the model area, simulated surface temperatures and hence longwave radiation patterns should differ as such. However, only in IVS, these very fine and distinct patterns of emitted longwave radiation from lower hemisphere are recognized for both urban canyons as well as Central Park in the horizontal cut in 1.5 m height at 03:00 (Figure 2-9a). AVF, in contrast, shows a uniform distribution of values around 415 W/m² for all parts of the model area. As thermal comfort indices take MRT into account and MRT is solely based on longwave radiation during nighttime, the high accuracy in modeling longwave radiation budgets, when using IVS compared to AVF, improves the accuracy and reliability of thermal comfort indices. High accuracy for modeling nighttime urban heat stress is especially needed for metropolitan regions where thermal stress at nighttime can lead to health implications such as insomnia or cardio-vascular diseases (Schinasi et al., 2018). In the comparison of PET results at pedestrian level for 03:00 (Figure 2-9b), we indeed find some discrepancies in defining thermal hotspots between both scenarios. By including more precise MRT values into thermal comfort calculations, PET is refined and mostly decreased in almost all parts of the model area. Cooling influences of Central Park for the built-up areas, however, cannot be observed as the wind flows in from the top of the model area and leaves at the open park side at the bottom of the model area. Since the influence of both shortwave and longwave radiation patterns on thermal comfort proves to be very large, the new IVS scheme seems to be able to contribute to a more accurate analysis of urban thermal comfort in general.

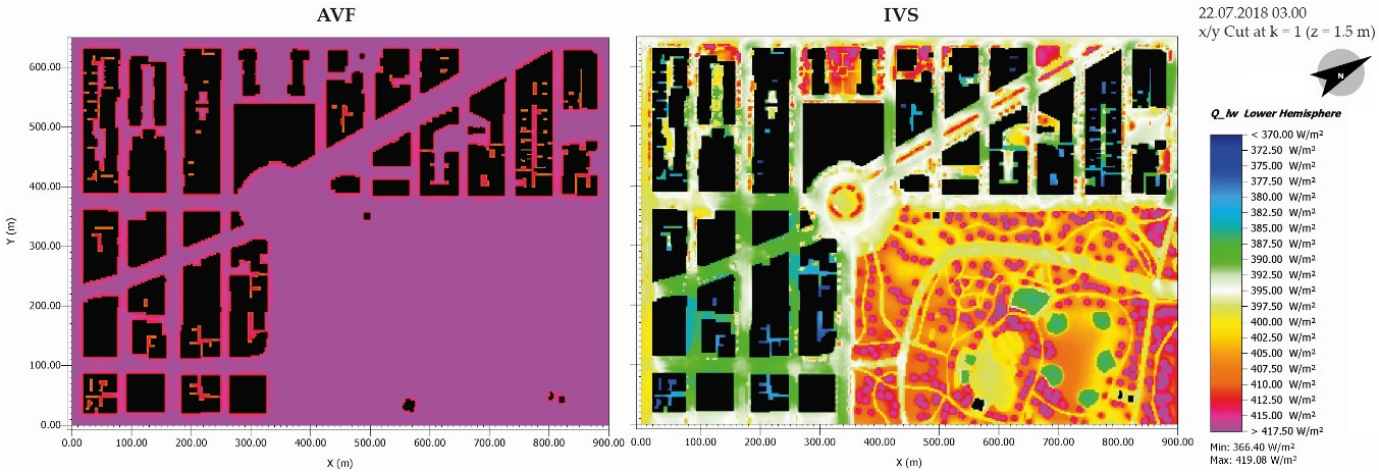

(a)

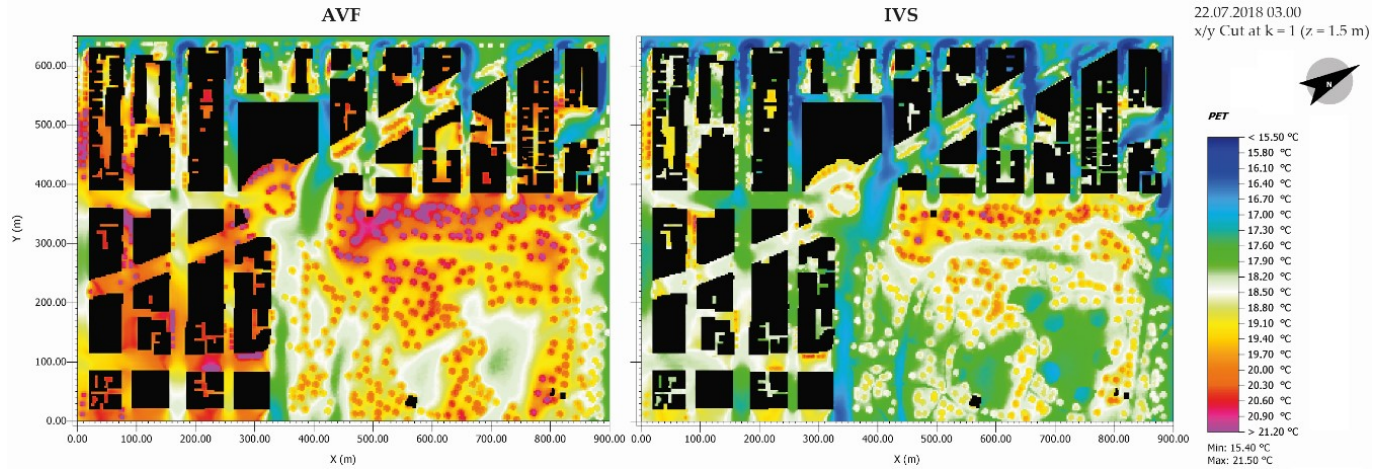

(b)

*Figure 2-9: Comparison of proof-of-concept simulation results between AVF and IVS at 03.00 in a height of 1.5 m for longwave radiation received from lower hemisphere (**a**) and for PET (**b**), respectively.*

2.4 Conclusions

In order to improve microclimatological analysis of complex urban environments, a new radiation scheme is introduced into the microclimate model ENVI-met. In contrast to the old AVF scheme, where view factors are averaged over the whole model area, the new IVS scheme is able to analyze the surrounding objects of each grid cell and calculate their contribution to the local radiation budget. The high accuracy of modeling secondary radiative fluxes such as emitted longwave radiation and reflected shortwave radiation by using IVS was demonstrated by a proof-of-concept simulation. By taking into account shading of surfaces or a higher reflection by high-albedo materials for example, fluxes of secondary shortwave and longwave radiation can be simulated in great detail. Several comparisons of different parameters, timesteps, and height levels between AVF and IVS showed that accurate surface properties and conditions affected the modeled microclimate conditions not only locally and for a

specific timestep but also over larger distances and on the long-term when using IVS. Furthermore, the comparisons of PET indicate that a precise simulation of secondary radiation is very important to understand and prevent localized negative effects of e.g., multiple shortwave reflections. These highly detailed results could be accomplished for a large, high-rise model area featuring yet rather low IVS resolutions. To gain an even higher accuracy in modeling results, the model could be simulated with an even higher IVS resolution and an even more accurate digitization of building surfaces and objects. However, the large demand in RAM limits the application potential for simulating larger model areas. In summary, the advantages provided by this new radiation scheme should though overturn this shortcoming. Future urban planning scenarios, architectural material questions, or heat mitigation measure studies using the microclimate model ENVI-met should thus be allowed to obtain more plausible and accurate results with the trade-off of a higher RAM demand.

2.5 References

Acero, J.A., Arrizabalaga, J., 2018. Evaluating the Performance of ENVI-Met Model in Diurnal Cycles for Different Meteorological Conditions. Theoretical and Applied Climatology 131, 455–469. https://doi.org/10.1007/s00704-016-1971-y

Acero, J.A., Herranz-Pascual, K., 2015. A comparison of thermal comfort conditions in four urban spaces by means of measurements and modelling techniques. Building and Environment 93, 245–257. https://doi.org/10.1016/j.buildenv.2015.06.028

Aguerre, J.P., Fernández, E., Besuievsky, G., Beckers, B., 2017. Computing urban radiation: A sparse matrix approach. Graphical Models 91, 1–11. https://doi.org/10.1016/j.gmod.2017.05.002

Arnfield, A.J., 1990. Street design and urban canyon solar access. Energy and Buildings 14, 117–131.

Arnfield, A.J., 1982. An Approach to the Estimation of the Surface Radiative Properties and Radiation Budgets of Cities. Physical Geography 3, 97–122. https://doi.org/10.1080/02723646.1982.10642221

Ayoub, M., 2020. A review on light transport algorithms and simulation tools to model daylighting inside buildings. Solar Energy 198, 623–642. https://doi.org/10.1016/j.solener.2020.02.018

Brown, M.J., Grimmond, S., Ratti, C., 2001. Comparison of Methodologies for Computing Sky View Factor in Urban Environments (No. LA-UR-01-4107). Los Alamos National Lab. (LANL), Los Alamos, NM (United States).

Bruse, M., 2004. ENVI-Met 3.0: Updated Model Overview. University of Bochum. Retrieved from: www.envi-met.com.

Bruse, M., Fleer, H., 1998. Simulating Surface Plant Air Interactions inside Urban Environments with a Three Dimensional Numerical Model. Environmental Modelling & Software 13, 373–384. https://doi.org/10.1016/S1364-8152(98)00042-5

Chapman, L., Thornes, J.E., 2004. Real-Time Sky-View Factor Calculation and Approximation. Journal of Atmospheric and Oceanic Technology 21, 730–741. https://doi.org/10.1175/1520-0426(2004)021<0730:RSFCAA>2.0.CO;2

Chelle, M., Andrieu, B., 1998. The nested radiosity model for the distribution of light within plant canopies. Ecological Modelling 111, 75–91. https://doi.org/10.1016/S0304-3800(98)00100-8

Chen, L., Ng, E., 2013. Simulation of the effect of downtown greenery on thermal comfort in subtropical climate using PET index: a case study in Hong Kong. Architectural Science Review 56, 297–305. https://doi.org/10.1080/00038628.2012.684871

Cohen, M.F., Chen, S.E., Wallace, J.R., Greenberg, D.P., 1988. A progressive refinement approach to fast radiosity image generation, in: Proceedings of the 15th Annual Conference on Computer Graphics and Interactive Techniques, SIGGRAPH '88. Association for Computing Machinery, New York, NY, USA, pp. 75–84. https://doi.org/10.1145/54852.378487

Cook, R.L., Torrance, K.E., 1981. A reflectance model for computer graphics. ACM Siggraph Computer Graphics 15, 307–316.

Crank, P.J., Sailor, D.J., Ban-Weiss, G., Taleghani, M., 2018. Evaluating the ENVI-met microscale model for suitability in analysis of targeted urban heat mitigation strategies. Urban Climate 26, 188–197. https://doi.org/10.1016/j.uclim.2018.09.002

Deru, M., Field, K., Studer, D., Benne, K., Griffith, B., Torcellini, B., Halverson, M., Winiarski, D., Liu, B., Rosenberg, M., Huang, J., Yazdanian, M., Crawley, D., 2010. U.S. Department of Energy Commercial Reference Building Models of the National Building Stock.

Fiala, P., Kadlecová, E., 2010. Progressive Methods in the Numerical Modeling by the Finite Elements 6.

Forouzandeh, A., 2021. Prediction of surface temperature of building surrounding envelopes using holistic microclimate ENVI-met model. Sustainable Cities and Society 70, 102878. https://doi.org/10.1016/j.scs.2021.102878

Glassner, A.S., 1989. An Introduction to Ray Tracing. Morgan Kaufmann.

Gómez, F., Cueva, A.P., Valcuende, M., Matzarakis, A., 2013. Research on ecological design to enhance comfort in open spaces of a city (Valencia, Spain). Utility of the physiological equivalent temperature (PET). Ecological Engineering 57, 27–39. https://doi.org/10.1016/j.ecoleng.2013.04.034

Gortler, S.J., Schröder, P., Cohen, M.F., Hanrahan, P., 1993. Wavelet radiosity, in: Proceedings of the 20th Annual Conference on Computer Graphics and Interactive Techniques - SIGGRAPH '93. Presented at the the 20th annual conference, ACM Press, Not Known, pp. 221–230. https://doi.org/10.1145/166117.166146

Hämmerle, M., Gál, T., Unger, J., Matzarakis, A., 2011. Comparison of models calculating the sky view factor used for urban climate investigations. Theor Appl Climatol 105, 521–527. https://doi.org/10.1007/s00704-011-0402-3

He, X., Miao, S., Shen, S., Li, J., Zhang, B., Zhang, Z., Chen, X., 2015. Influence of sky view factor on outdoor thermal environment and physiological equivalent temperature. Int J Biometeorol 59, 285–297. https://doi.org/10.1007/s00484-014-0841-5

He, Y., Yu, H., Ozaki, A., Dong, N., 2020. Thermal and energy performance of green roof and cool roof: A comparison study in Shanghai area. Journal of Cleaner Production 267, 122205. https://doi.org/10.1016/j.jclepro.2020.122205

Helbig, N., Löwe, H., Lehning, M., 2009. Radiosity Approach for the Shortwave Surface Radiation Balance in Complex Terrain. Journal of the Atmospheric Sciences 66, 2900–2912. https://doi.org/10.1175/2009JAS2940.1

Höppe, P., 1999. The Physiological Equivalent Temperature. A Universal Index for the Biometeorological Assessment of the Thermal Environment. International Journal of Biometeorology 43, 71–75.

Howell, J.R., 1998. The Monte Carlo Method in Radiative Heat Transfer. Journal of Heat Transfer 120, 547–560. https://doi.org/10.1115/1.2824310

Howell, J.R., 1969. Application of Monte Carlo to Heat Transfer Problems, in: Irvine, T.F., Hartnett, J.P. (Eds.), Advances in Heat Transfer. Elsevier, pp. 1–54. https://doi.org/10.1016/S0065-2717(08)70128-X

Hu, W., Qin, K., 2007. Interactive Approximate Rendering of Reflections, Refractions, and Caustics. IEEE Transactions on Visualization and Computer Graphics 13, 46–57. https://doi.org/10.1109/TVCG.2007.14

Huttner, S., 2012. Further development and application of the 3D microclimate simulation ENVI-met (Dissertation). Johannes Gutenberg-University Mainz.

Lee, H., Mayer, H., Chen, L., 2016. Contribution of trees and grasslands to the mitigation of human heat stress in a residential district of Freiburg, Southwest Germany. Landscape and Urban Planning 148, 37–50.

Lee, W.-L., Liou, K.N., Hall, A., 2011. Parameterization of solar fluxes over mountain surfaces for application to climate models. Journal of Geophysical Research: Atmospheres 116. https://doi.org/10.1029/2010JD014722

Mardaljevic, J., 1999. Daylight Simulation: Validation, Sky Models and Daylight Coefficients.

Matzarakis, A., Amelung, B., 2008. Physiological Equivalent Temperature as Indicator for Impacts of Climate Change on Thermal Comfort of Humans, in: Thomson, M.C., Garcia-Herrera, R., Beniston, M. (Eds.), Seasonal Forecasts, Climatic Change and Human Health: Health and Climate, Advances in Global Change Research. Springer Netherlands, Dordrecht, pp. 161–172. https://doi.org/10.1007/978-1-4020-6877-5_10

Matzarakis, A., Mayer, H., Iziomon, M.G., 1999. Applications of a universal thermal index: physiological equivalent temperature. Int J Biometeorol 43, 76–84. https://doi.org/10.1007/s004840050119

Meinzer, H.-P., Meetz, K., Scheppelmann, D., Engelmann, U., Baur, H.J., 1991. The Heidelberg ray tracing model. IEEE Computer Graphics and Applications 11, 34–43.

Middel, A., Lukasczyk, J., Maciejewski, R., Demuzere, M., Roth, M., 2018. Sky View Factor footprints for urban climate modeling. Urban Climate 25, 120–134. https://doi.org/10.1016/j.uclim.2018.05.004

NYC Open Data, D. of I.T.& T. (DoITT), 2019. Building Footprints and Street Trees [WWW Document]. URL data.cityofnewyork.us/Housing-Development/Building-Footprints/

Oke, T.R., 1997. Urban Environments, in: Bailey, W.G., Oke, T.R., Rouse, W.R. (Eds.), The Surface Climates of Canada. Québec: McGill-Queen's University Press, pp. 303–327.

Recker, R.J., George, D.W., Greenberg, D.P., 1990. Acceleration techniques for progressive refinement radiosity, in: Proceedings of the 1990 Symposium on Interactive 3D Graphics, I3D '90. Association for Computing Machinery, New York, NY, USA, pp. 59–66. https://doi.org/10.1145/91385.91419

Rosenfeld, A.H., Akbari, H., Bretz, S., Fishman, B.L., Kurn, D.M., Sailor, D., Taha, H., 1995. Mitigation of urban heat islands: materials, utility programs, updates. Energy and Buildings 22, 255–265. https://doi.org/10.1016/0378-7788(95)00927-P

Roth, M., Lim, V.H., 2017. Evaluation of canopy-layer air and mean radiant temperature simulations by a microclimate model over a tropical residential neighbourhood. Building and Environment 112, 177–189. https://doi.org/10.1016/j.buildenv.2016.11.026

Salata, F., Golasi, I., de Lieto Vollaro, R., de Lieto Vollaro, A., 2016. Urban microclimate and outdoor thermal comfort. A proper procedure to fit ENVI-met simulation outputs to experimental data. Sustainable Cities and Society 26, 318–343. https://doi.org/10.1016/j.scs.2016.07.005

Santamouris, M., 2013. Energy and Climate in the Urban Built Environment. Routledge.

Santamouris, M., Yun, G.Y., 2020. Recent development and research priorities on cool and super cool materials to mitigate urban heat island. Renewable Energy 161, 792–807. https://doi.org/10.1016/j.renene.2020.07.109

Schinasi, L.H., Benmarhnia, T., De Roos, A.J., 2018. Modification of the association between high ambient temperature and health by urban microclimate indicators: A systematic review and meta-analysis. Environmental Research 161, 168–180. https://doi.org/10.1016/j.envres.2017.11.004

Sharmin, T., Steemers, K., Matzarakis, A., 2017. Microclimatic modelling in assessing the impact of urban geometry on urban thermal environment. Sustainable Cities and Society 34, 293–308. https://doi.org/10.1016/j.scs.2017.07.006

Shinzato, P., Simon, H., Duarte, D.H.S., Bruse, M., 2019. Calibration process and parametrization of tropical plants using ENVI-met V4 – Sao Paulo case study. Architectural Science Review 62, 112–125. https://doi.org/10.1080/00038628.2018.1563522

Shirley, P., Morley, R.K., 2008. Realistic Ray Tracing, Second Edition. A K Peters, Ltd.

Simon, H., 2016. Modeling Urban Microclimate: Development, Implementation and Evaluation of New and Improved Calculation Methods for the Urban Microclimate Model ENVI-Met (PhD Thesis). Universitätsbibliothek Mainz, Mainz.

Simon, H., Kissel, L., Bruse, M., 2017. Evaluation of ENVI-met's multiple-node model and estimation of indoor climate, in: Design to Thrive. Presented at the PLEA, Edinburgh, p. 9.

Simon, H., Lindén, J., Hoffmann, D., Braun, P., Bruse, M., Esper, J., 2018. Modeling transpiration and leaf temperature of urban trees – A case study evaluating the microclimate model ENVI-met

against measurement data. Landscape and Urban Planning 174, 33–40. https://doi.org/10.1016/j.landurbplan.2018.03.003
Simon, H., Sinsel, T., Bruse, M., 2020. Introduction of Fractal-Based Tree Digitalization and Accurate In-Canopy Radiation Transfer Modelling to the Microclimate Model ENVI-met. Forests 11, 869. https://doi.org/10.3390/f11080869
Steyn, D.G., 1980. The calculation of view factors from fisheye-lens photographs: Research note. Atmosphere-Ocean 18, 254–258. https://doi.org/10.1080/07055900.1980.9649091
Steyn, D.G., Hay, J.E., Watson, I.D., Johnson, G.T., 1986. The Determination of Sky View-Factors in Urban Environments Using Video Imagery. Journal of Atmospheric and Oceanic Technology 3, 759–764. https://doi.org/10.1175/1520-0426(1986)003<0759:TDOSVF>2.0.CO;2
Tsoka, S., Tsikaloudaki, A., Theodosiou, T., 2018. Analyzing the ENVI-met microclimate model's performance and assessing cool materials and urban vegetation applications–A review. Sustainable Cities and Society 43, 55–76. https://doi.org/10.1016/j.scs.2018.08.009
Wallace, J.R., Elmquist, K.A., Haines, E.A., 1989. A Ray tracing algorithm for progressive radiosity, in: Proceedings of the 16th Annual Conference on Computer Graphics and Interactive Techniques, SIGGRAPH '89. Association for Computing Machinery, New York, NY, USA, pp. 315–324. https://doi.org/10.1145/74333.74366
Wang, Z.-H., 2014. Monte Carlo simulations of radiative heat exchange in a street canyon with trees. Solar Energy 110, 704–713. https://doi.org/10.1016/j.solener.2014.10.012
Wilcox, S., Marion, W., 2008. Users manual for TMY3 data sets.

“ (Simon et al., 2021b).

3 Introduction of fractal-based tree digitalization and accurate in-canopy radiation transfer modeling to the microclimate model ENVI-met

Helge Simon[1], Tim Sinsel[1], Michael Bruse[1]

[1]*Department of Geography, Johannes Gutenberg University Mainz, 55099 Germany*

Summary:

In addition to the advancements in modeling secondary radiative fluxes presented in Section 2, inaccuracies in ENVI-met's radiation modeling are additionally tackled by the development of an Advanced Canopy Radiation Transfer (ACRT) module that accounts for extinction of diffuse as well as scattering of direct shortwave radiation into secondary diffuse radiation within plant canopies. The author could substantially support the implementation of the module that was primarily developed by Helge Simon. Furthermore, a new plant digitization technique developed by Michael Bruse following the Lindenmeyer-system (L-Trees) was presented, which allows complex plant skeleton structures to be defined with a more realistic position, size, and alignment of leaf clusters, thus resulting in a more accurate representation of plants in ENVI-met. Proof-of-concept simulations examined whether the combination of both new features – ACRT and L-trees – refined radiation modeling within and below canopies at street-level and hence yield a higher accuracy of microclimate modeling in general. Aside from developing parts of the ACRT module, the author contributed to this work by preparing and conducting the proof-of-concept simulations as well as writing several sections of the manuscript.

Forests 11(8), August 2020 – published

“

3.1 Introduction

Modern microclimate models like ENVI-met offer a vast range of different surface and wall materials and wall compositions to digitize urban areas. With these, complex urban morphologies and building façades can be replicated very accurately. Accurate replication of plants, especially trees, has been handled rather crudely. However, there is general consensus about the importance of urban vegetation with regard to mitigating the urban heat island (Alavipanah et al., 2015; Fan et al., 2015; Harlan et al., 2006; Lindén, 2011; Middel et al., 2012; Norton et al., 2015). The key positive effects of urban vegetation onto thermal comfort are lowering air and radiative temperature via evaporative cooling and shading (Andersson-Sköld et al., 2015; Bowler et al., 2011; Norton et al., 2015). Furthermore, different species, dimensions and local living conditions strongly determine a plant’s microclimate performance (Andersson-Sköld et al., 2015; Dimoudi and Nikolopoulou, 2003; Honjo and Takakura, 1990; Lee et al., 2016; Oliveira et al., 2011; Phelan et al., 2015; Salata et al., 2015; Savi et al., 2015; Simon et al., 2019). Still trees in microclimate models are only represented by more or less homogeneous clusters of leaf area density (LAD), not accounting for inner canopy diversity or species characteristics nor for local climate stimuli to grow denser leaf clusters in particular directions. While there has been some effort to link clusters of LAD to a tree and thus represent specific trees as objects (Simon, 2016; Simon et al., 2018), individual geometries of specific trees species are – so far – largely neglected.

To allow more detailed modelling of trees, comprehensive information about the structure of the tree (stems, branches, twigs) and the allocation of biomass (leaves, fruits) including the corresponding physiological (thickness, color) and mechanical properties (elasticity, bending properties) are required.

The need of such detailed information contradicts with the few information normally available about a specific tree at a given location. Also, as living organisms, trees of the same species share a large set of common properties such as general crown structure, branching rules and leaf positioning, but can be very different from individual to individual in their final structure.

In order to bridge the gap between the general properties of a plant, which are manageable in a database, and the detailed and specific information of the plant’s three-dimensional structure and physical

properties, numerical algorithms are required that are able to generate realistic plant models from a limited set of algorithmic information. An adaption of one of those numerical algorithms, the fractal-based Lindenmayer-System was introduced into the microclimate model ENVI-met to be able to accurately digitize trees given a manageable set of information about the plant (Lindenmayer, 1968).

Aside from the difficulties in digitizing plant geometries, simulating the radiative processes within plant canopies is quite complex. The radiative processes depend on the quantity and orientation of leaves but also on their physical properties such as reflection, absorption, and transmission. The fact that radiation partially penetrates into and attenuates within plant canopies makes the whole process even more complex.

For direct shortwave radiation, which can be described as a vector quantity, the attenuation can be rather easily described by exponential attenuation equations. The undirected nature of diffuse radiation however increases the difficulty of estimating the reduction of diffuse radiation in porous media such as vegetation. Furthermore, the attenuation of direct shortwave radiation partially leads to scattering and thus produces diffuse radiation within the penetrated media making the estimation of diffuse radiation more complex.

In order to simplify the algorithms for diffuse radiation reduction, climate models generally assume isotropic distribution of diffuse radiation. Using this simplification, the reduction of diffuse shortwave radiation is often calculated using sky view factors (Bruse, 2004).

In previous versions of ENVI-met, the reduction of diffuse shortwave radiation was only handled for interactions with buildings using the local sky view factor (Bruse, 2004). While direct shortwave radiation was attenuated using ray tracing taking into account local Leaf Area Density (LAD), leaf orientation and shortwave transmission, diffuse shortwave radiation was not altered due to vegetation at all.

In order to address this shortcoming, an Advanced Canopy Radiation Transfer (ACRT) Module was implemented following the works of (Pedruzo-Bagazgoitia et al., 2017)). The new module not only estimates the attenuation of diffuse radiation in vegetation canopies but also adds a source function for diffuse radiation due to scattering of direct shortwave radiation within vegetation canopies.

Combining both advancements, the fractal-based tree digitalization using the Lindenmayer-System and the more accurate in-canopy radiation transfer model should lead to much more precise simulation results of not only attenuation of radiation within trees, but also the photosynthesis activity. This in turn leads to better estimations of the latent heat flux, improving the modelling of plant-atmosphere interactions as well as plant vitality parameters, such as the leaf temperatures represented by more realistic values and also more detailed inner canopy patterns.

3.2 Materials and Methods

3.2.1 Algorithmic plant generation

Trees in ENVI-met are generally represented by homogeneous clusters of LAD cells forming a three-dimensional body. Their geometry can be defined by only a few parameters such as general shape (cylindrical, conical, etc.), maximum canopy height and diameter. Variations of LAD within the canopy or typical geometries of specific plant species are negated as of yet resulting in only plausible but not very realistic trees.

Computer based generation and visualization of realistic plants and trees interests a wide range of users and researches from film artists over game designer to botanists. Many different solutions for computer-based plant generation exist differing in their algorithmic approaches used, but partly sharing common concepts. Generally, the methods can be distinguished into Procedural Algorithms and Generative Algorithms.

Procedural Algorithms span a wide range over different numerical methods that describe the architecture of a plant through hierarchical and/or recursive patterns. Depending on the specific algorithm, the structure of a tree emerges through the repetition of a pre-defined construction pattern. The most prominent approach in this category is the so-called Lindenmayer-System ("L-System") (Lindenmayer, 1968; Prusinkiewicz and Lindenmayer, 1990). The basic L-System has been extended over time adding stochastic functions or context-sensitive rules in order to better control the resulting plant.

On the other hand, Generative Algorithms do not start from a pre-defined geometry rule set, but simulate the growth of a tree. This growth simulation can be biologically motivated, e.g. by simulating the competition of buds for light or simultaneously for light and space (Greene, 1989; Longay et al., 2012).

The selection of the best suited approach to construct plants and trees from algorithms in ENVI-met is not an easy choice. On the one hand, the plant structures obtained should be realistic and contain a correct topology in order to calculate tree biomechanics such as wind loads. On the other hand, at least in a first step, a light-weight algorithm is required that allows the representation and simulation of up to a few thousand trees in larger model areas.

Therefore, the classic L-System was chosen as the initial system to create three-dimensional trees in ENVI-met. The main advantage of this basic L-System is the generation of a topological correct tree skeleton in very short time. It also allows fast dynamical adjustments of parts of the skeleton e.g., due to mechanical loads and a re-calculation of the tree skeleton without violating explicitly given growth rules. However, the given implementation leaves spaces for future developments and alternative tree generation algorithms.

L-System has been introduced by Aristid Lindenmayer in the late 1960ies to describe the growth of spatial systems such as cells or plants (Lindenmayer, 1968). Basically, an L-System consist of a string containing different letters and numbers which are used to either execute a specific turtle-based drawing operation in 2D or 3D space or to re-orientate the turtle in space or store and restore its position.

An L-System is a rewriting system that can contain rules for replacing letters with other letters or sequences of letters in each re-writing step. The replaced letters are inserted into the existing L-String and they are also subject to replacement in the next re-writing step hence generating a fractal like sequence.

Figure 3-1 shows the development of an L-System with the following properties:

- Start term (Axiom): **b**
- Replacement Rule 1: **b → a**
- Replacement Rule 2: **a → ab**

Figure 3-1: Classic 5-step development of a simple L-System (Prusinkiewicz and Lindenmayer, 1990).

Figure 3-2 shows a three different tree species generated with the L-System. Using the L-System skeleton, the LAD cluster is then derived, depending on the actual model areal resolution.

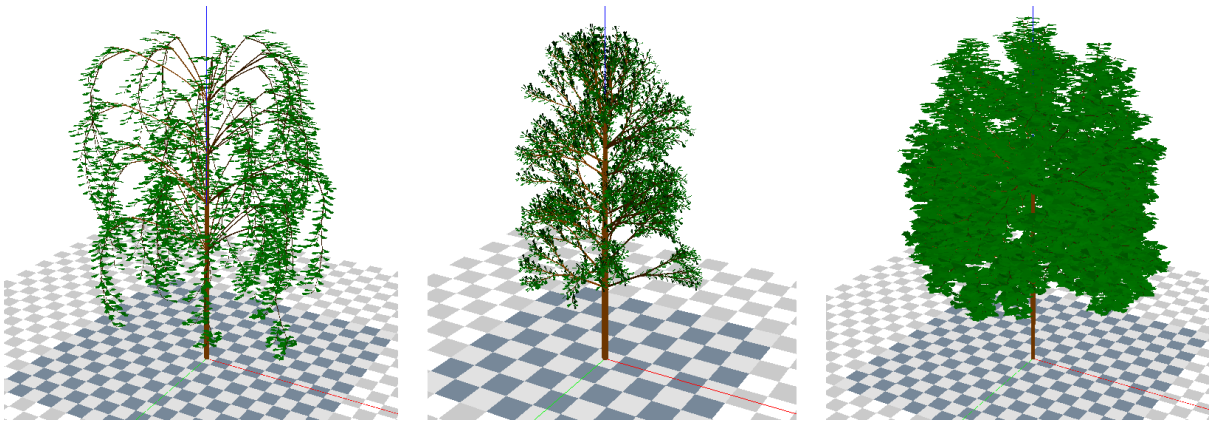

Figure 3-2: Example L-System for Silver Birch (Betula alba) (left), Mountain Ash (Sorbus araucaria) (middle), Field Maple (Acer campestre) (right).

The placement of leaves can be controlled by the user over a wide range of parameters, including leaf size, orientation and positioning. The software allows a wider range of settings to control the leaf placement including the internode length, leaf positioning and phyllotaxis angels. Also, the geometry of the leaf can be set by the user to generate species-depending leaf types. In every stage of the tree generation, the biomechanics of the tree are calculated and considered in the tree skeleton geometry. For each branch segment (typically 0.2 m), the torques generated through the self-loading of the attached child segments are set in correlation to the tree's basic mechanical properties like Young's modulus to estimate the deformation and rotation of each tree segment. The final tree skeleton is obtained, when all generated torques and the internally stored energy in the tree segment through deformation and rotation are balanced. If the user designs a tree which is biomechanically instable from the beginning, it is rejected by ENVI-met. To use the new Lindenmayer based trees (L-Trees) in ENVI-met, the leaf location rasterized in the usual 1 × 1 × 1 m grid and the associated Leaf Area Density for each grid is calculating by summing up the leaf surface inside the assigned grid box.

3.2.2 Advancements in ENVI-met's canopy radiation model

Extinction of shortwave radiation in ENVI-met is handled using a ray tracing algorithm (M. Bruse, 2004): In the ray trace, each cell shoots a linear ray in a predefined direction and checks for obstructions

along its way through three-dimensional space. The ray tracing is implemented using an iterative approach:

$$\mathrm{p(x,y,z,n+1)} = \mathrm{p(x,y,z,n)} + \lambda \mathrm{v} \qquad \textit{Eq. 3-1}$$

with $p(x, y, z, n)$ as the point of the ray at iteration n and λv as a three-dimensional vector heading towards a certain position described by an azimuthal and elevation angle. λv vector's length is sized depending on a grid cell's resolution and direction angle to ensure that grid cells which lie substantially on the ray's path are actually hit at each iteration.

Depending upon the objects (building, single wall, terrain, vegetation) that lie in the ray's path, a local transmission factor ($f_{Obj}(i, j, k)$) ranging from 0 to 1 is obtained. While the ray continues on its way, a product of all individual local transmission factors iteratively forms the total transmission factor (f_{tot}) of the starting grid cell in the ray's direction:

$$\mathrm{f_{tot}(n+1)} = \mathrm{f_{tot}(n)} * \mathrm{f_{Obj}(i,j,k)} \qquad \textit{Eq. 3-2}$$

Different objects carry different transmission factors ($f_{Obj}(i, j, k)$). For direct shortwave radiation, buildings and ground surfaces carry a transmission factor of 0. For single walls, the material's transmission is taken as the object's transmission factor. To calculate the transmission of direct and diffuse shortwave radiation through vegetation grids, i.e. the attenuation of direct and diffuse shortwave radiation, new approaches following the works of (Pedruzo-Bagazgoitia et al., 2017) have been implemented. The new scheme tries to model the processes of shortwave radiation in canopies using three processes:

1. Primary extinction of direct shortwave radiation
2. Extinction of direct shortwave radiation due to scattering and creation of secondary diffuse shortwave radiation
3. Extinction of diffuse shortwave radiation

3.2.2.1 Primary extinction of direct shortwave radiation

Primary extinction of direct radiation is modelled using an extinction coefficient depending on solar elevation (Goudriaan, 1977; Spitters, 1986):

$$\mathrm{k_{dirbl}} = \frac{0.5}{\sin\beta} \qquad \textit{Eq. 3-3}$$

with β as the solar elevation angle above the horizon. Since the primary extinction of direct radiation only accounts for the pure extinction of direct radiation, leaves are considered visually black – thus neither transmitting nor reflecting, only absorbing direct radiation (Goudriaan, 1977; Spitters, 1986).

The transmission factor for primary extinction of direct radiation is then calculated using a ray tracing for every grid in the direction of the sun's position. When hitting a plant grid cell, the local transmission factor is calculated by:

$$f_{Veg,dir,pri}(i,j,k) = (1 - \rho_{dir}) * (1 - \sigma) * e^{-(k_{dirbl}\, LAIc)} \qquad \textit{Eq. 3-4}$$

with $LAIc$ as the sum of Leaf Area Index (LAI) between the grid cell and the sun's position on the ray's path and ρ_{dir} as a sun elevation dependent reflection coefficient of direct radiation on horizontally distributed leaves. As the actual amount of horizontally orientated leaves is unknown, the model considers a leaf angle distribution of 0.5 – representing an average horizontal orientation of 50 % of the leaves(Goudriaan, 1977; Simon, 2016):

$$\rho = \frac{1 - \sqrt{1 - \sigma}}{1 + \sqrt{1 - \sigma}} \qquad \textit{Eq. 3-5}$$

$$\rho_{dir} = \rho \frac{2}{1 + 1.6 \sin\beta} \qquad \textit{Eq. 3-6}$$

After calculating the local transmission factor, the total transmission factor is updated (see Eq. 3-2) and the ray tracing continued until the termination condition of the ray tracing is reached. The direct shortwave radiation of grid cell i, j, k is then calculated by:

$$Q_{dir}(i,j,k) = Q_{dir,top} * f_{tot,dir,pri} \qquad \textit{Eq. 3-7}$$

with $Q_{dir,top}$ as the incoming direct shortwave radiation at model top and $f_{tot,dir,pri}$ as the total transmission factor handling the extinction of radiation within plant canopies according to Eq. 3-4.

3.2.2.2 Extinction of direct shortwave radiation due to scattering of direct radiation and creation of secondary diffuse radiation

To account for creating secondary diffuse radiation due to scattering of direct radiation, the extinction coefficient k_{dirbl} is altered using an empirical constant σ accounting for scattering of direct shortwave radiation in the vertical direction (Goudriaan, 1977; Spitters, 1986):

$$k_{dir} = k_{dirbl} * \sqrt{1 - \sigma} \qquad \textit{Eq. 3-8}$$

The transmission factor for extinction of direct shortwave radiation due to scattering and by that creating secondary diffuse radiation is calculated using a ray tracing of every grid cell towards the sun's position. Upon hitting a plant grid cell, the transmission is, following the works of Pedruzo-Bagazgoitia et al. (2017), then calculated as follows:

$$f_{Veg,dir+dif,sec}(i,j,k) = (1 - \rho_{dir}) * e^{-(k_{dir}\, LAIc)} \qquad \textit{Eq. 3-9}$$

The resulting transmission factor incorporates the sum of the processes of extinction of direct shortwave radiation and creation of secondary diffuse radiation (Pedruzo-Bagazgoitia et al., 2017). Thus, after the ray tracing is terminated, the net creation of secondary diffuse radiation can be calculated in two steps:

Firstly, the combined extinction of direct shortwave radiation and creation of secondary diffuse radiation is calculated by multiplying the total transmission factor with the incoming direct shortwave radiation at model top:

$$Q_{dir+dif,sec}(i,j,k) = Q_{dir,top} * f_{tot,dir+dif,sec} \qquad \textit{Eq. 3-10}$$

with $f_{tot,dir+dif,sec}$ as the total transmission factor handling the extinction of radiation within plant canopies according to Eq. 3-10.

Secondly, the previously calculated primary extinction of only direct radiation is subtracted from the combination of direct radiation's extinction and secondary diffuse radiation's creation due to scattering. The net creation of secondary diffuse radiation is thus:

$$Q_{dif,sec}(i,j,k) = Q_{dir+dif,sec}(i,j,k) - Q_{dir}(i,j,k) \qquad \textit{Eq. 3-11}$$

3.2.2.3 Extinction of diffuse shortwave radiation

The extinction coefficient of diffuse radiation (k_{dif}), however, is quite similar to the extinction coefficient k_{dir}. Since diffuse radiation is considered isotropic, sun angle dependency is neglected and replaced by a constant factor of 0.8 (Pedruzo-Bagazgoitia et al., 2017):

$$k_{dif} = 0.8 * \sqrt{1 - \sigma} \qquad \textit{Eq. 3-12}$$

While (Pedruzo-Bagazgoitia et al., 2017) suggest to calculate the extinction of diffuse radiation only for a vertical column i.e. a ray trace perpendicular to a horizontal surface, a more realistic approach using a hemispherical ray tracing is applied to account for the isotropic nature of diffuse radiation in the model.

Other than in the ray tracing for the direct radiation (see above), the ray trace for diffuse extinction is not directed towards the sun's position, but in all directions of the upper hemisphere of a cell with angular distances of 5° height and 10° azimuthal angle:

$$\lambda v = \begin{pmatrix} \bar{v} * \cos(h) * \cos(a) \\ \bar{v} * \cos(h) * \sin(a) \\ \bar{v} * \sin(h) \end{pmatrix} \qquad \textit{Eq. 3-13}$$

with λv as a three-dimensional ray tracing vector, $\bar{v}$ as the vector length, a as the azimuthal and h as the height angle of the ray.

For each ray an individual transmission factor is calculated:

$$f_{Veg,dif,pri}(i,j,k) = (1-\rho) * e^{-(k_{dif}\, LAIc)} \qquad \textit{Eq. 3-14}$$

The resulting individual transmission factors for every ray trace are then averaged to gain the overall transmission factor for diffuse radiation.

Since the transmission factor of diffuse shortwave radiation extinction does not depend on the current solar elevation, it can be precalculated during the initialization phase of the model and stored in a three-dimensional array. It only needs updating after user-defined intervals (Figure 3-3) to account for changes in the local LAD of deciduous vegetation i.e., leaf shedding.

The extinction of diffuse shortwave radiation is then calculated by:

$$Q_{dif}(i,j,k) = Q_{dif,top} * f_{tot,dif,pri} \qquad \textit{Eq. 3-15}$$

with $Q_{dif,top}$ as the incoming diffuse shortwave radiation at model top.

The total diffuse radiation in grid cell i,j,k is then calculated as the sum of extinct diffuse shortwave radiation and secondary diffuse radiation created by scattering of direct radiation:

$$Q_{dif,tot}(i,j,k) = Q_{dif}(i,j,k) + Q_{dif,sec}(i,j,k) \qquad \textit{Eq. 3-16}$$

3.2.2.4 Enabling/disabling the advanced canopy transfer module

The advanced canopy radiation transfer module can be enabled in the simulation settings of the SIMX file. By default, the module is switched off. If enabled, the user is able to adjust the interval at which the transmission factor analysis is updated. The update interval accounts for effects of leaf shedding onto the radiation calculation. It only takes effect for longer simulation periods when deciduous plants adapt to the environment by shedding their leaves – its value is given in days.

The controlling tags on the SIMX-File are in section *RadScheme* under *AdvCanopyRadTransfer* and *ViewFacUpdateInterval* (Figure 3-3). Both tags can be edited individually since the update of the View-FacUpdateInterval also controls the update interval of the view factors analysis.

```
<RadScheme>
   <radDetail> low </radDetail>
   <IVSMem> 1 </IVSMem>
   <AdvCanopyRadTransfer> 1 </AdvCanopyRadTransfer>
   <ViewFacUpdateInterval> 2 </ViewFacUpdateInterval>
</RadScheme>
```

Figure 3-3: User-defined update interval for the view and transmission factor analysis in the SIMX-File – value is given as integer in days, here 2.

In case the ACRT module is disabled, the extinction of direct shortwave radiation is carried out like in previous versions of ENVI-met:

$$f_{veg}(i,j,k) = e^{-(\omega*(1-t)*LAD(i,j,k)*|\lambda v|)} \qquad \textit{Eq. 3-17}$$

with ω as the leaf orientation, constant at 0.5, t as the shortwave transmittance of the leaves, $LAD(i,j,k)$ as the local leaf area density and $|\lambda v|$ as the length of the current ray segment. The three-dimensional array containing the secondary diffuse radiation is set to 0 and the function calculating the extinction coefficient of diffuse radiation only returns the local sky view factor. This way, the resulting transmission for direct and diffuse shortwave radiation remain identical to previous versions.

3.2.3 Proof-of-concept simulation

In a small model area featuring a standard solid Parametric-Tree and its L-Tree resemblance, the advancements of the algorithmic plant generation and the advanced canopy radiation transfer module is evaluated (Figure 3-4 and Table 2-1). The trees have been modelled to resemble a Balsam poplar with a height of 25 meters as this species features a very heterogenous LAD distribution.

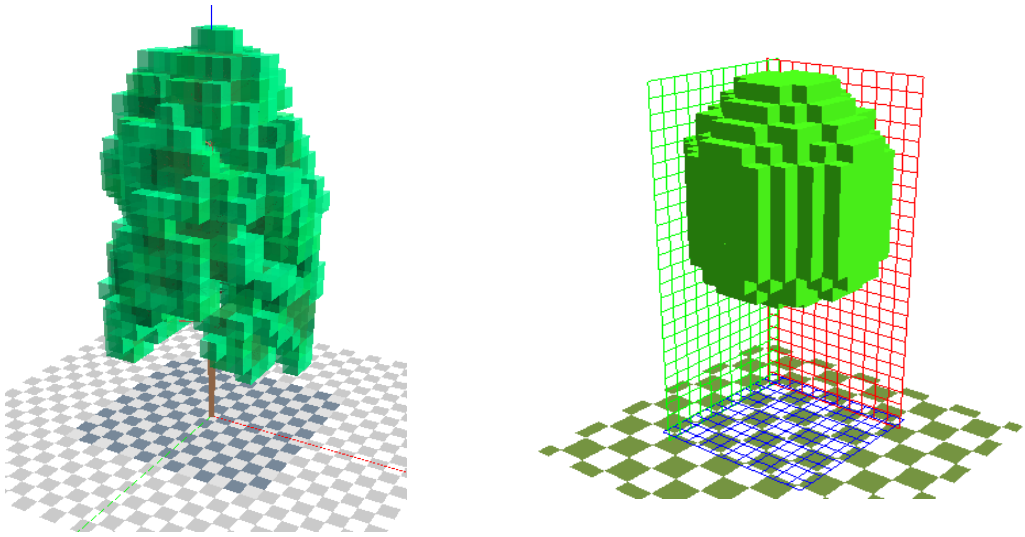

(**a**) (**b**)

Figure 3-4: L-Tree with LAD ranging from 0.025 to 0.825 m2/m3 (a); Parametric-Tree with homogenous LAD of 0.3 (b).

Table 3-1: Parameters of Parametric-Tree and L-Tree.

	Height [m]	**Diameter [m]**	**LAD [m2/m3]**	**Total Leaf Area [m2]**	**Number of LAD cells**
L-Tree	25	11	0.025 – 0.8251	298.36	222
Parametric-Tree	25	11	0.3	460.8	192

[1] LAD varies as it is created based on the leaf setting rule set.

It is to be expected, that the L-Tree, due to its realistic LAD clusters, shows more diverse radiation patterns of direct shortwave radiation. In combination with the advanced canopy radiation transfer module, not only the extinction of diffuse radiation and creation of secondary diffuse radiation should be more realistic, but also the photosynthetic activity and thus leaf temperatures as well as latent heat flux.

The model area consists out of 100 × 70 × 40 grid cells in a resolution of 2 meters × 2 meters × 2 meters and is located in Essen, Germany, thus representing a typical location in Central Europe with Cfb climate in the Köppen-Geiger classification (Figure 3-5).

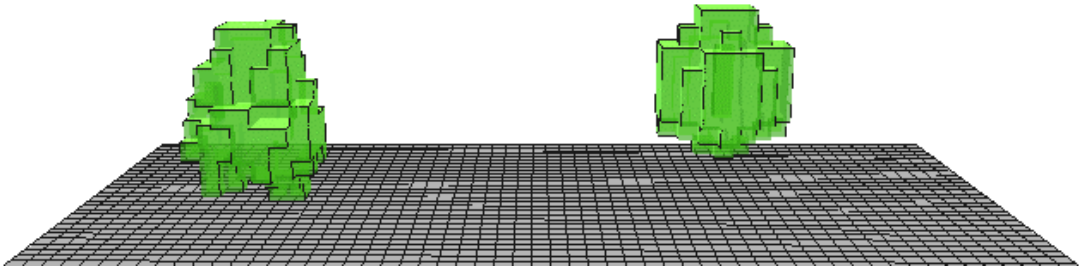

Figure 3-5: Simple model area for the Proof-of-concept simulations. Left: deciduous L-Tree; Right: deciduous Parametric-Tree.

To evaluate the effects of the ACRT module, a second simulation run with the module switched off has been conducted. The simulation has been run for 24 hours starting from June 23rd at 05:00h. The meteorological boundary conditions were set using a simple forcing for a warm summer day with no cloud cover.

The model results are first compared against each other and subsequently against literature values of similar trees. Finally, the impact on thermal comfort underneath the trees is compared between the simulation runs.

3.3 Results and Discussion

To visualize the effects of the advancements of L-Trees and the ACRT module onto the microclimate results, maps showing the absolute values of direct and diffuse radiation as well as difference maps for the two simulation runs have been created. In the difference maps, positive values indicate lower values in the simulation including the ACRT module.

By looking at the differences in direct and diffuse shortwave radiation between the two simulations at noon, the total effect of the L-Trees and the ACRT module can be seen (Figure 3-6). A vertical cut along the centerline of the trees reveals that, for the direct shortwave radiation, the highest reduction occurs at the top of the canopy for both trees. However, the reduction of direct shortwave radiation within the Parametric-Tree canopy is much greater due to its homogenously distributed high LAD. For the L-Tree, the reductions occur more gradually as its LAD is lower on average than the Parametric-Tree's LAD. Both trees show greater extinction of direct shortwave radiation with the ACRT module on. While the inner canopy direct shortwave radiation only drops to a minimum of around 150 W/m^2 for the L-Tree in the ACRT on simulation, the solid structure of LAD in the center of the Parametric-Tree leads to a

massive and rather unrealistic reduction of the direct shortwave radiation: In both simulations, with and without the ACRT module, the direct shortwave radiation completely gets extinct in the inner canopy of the Parametric Tree.

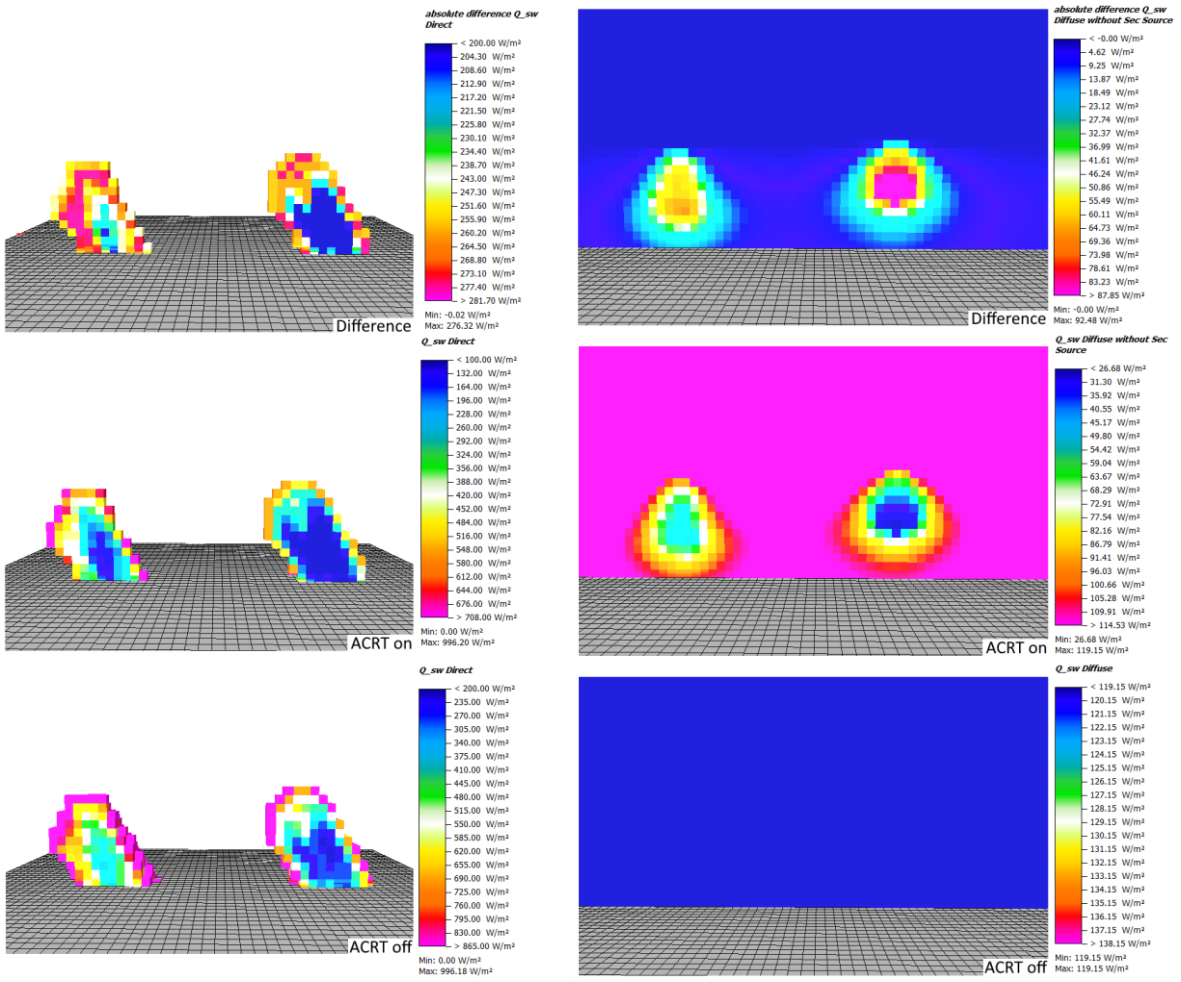

(**a**) (**b**)

*Figure 3-6: Difference and absolute direct (**a**) and diffuse shortwave radiation (**b**) at noon (sun position: 164.4° azimuthal and 58.3° height angle, view direction west), with and without ACRT module for L-Tree (left) and Parametric-Tree (right).*

The comparison of diffuse radiation at noon in Figure 3-6 shows that with the ACRT module, no diffuse shortwave radiation is attenuated in the tree canopies. The result of the ACRT simulation clearly shows the isotropic character of diffuse radiation as the distribution of diffuse radiation is independent on the sun's position. Similarly, to the extinction of direct shortwave radiation, the attenuation of diffuse radiation is greater in the Parametric Tree (down to around 26 W/m^2) compared to the L-Tree (50 W/m^2) (Figure 3-6).

Since diffuse radiation is also created by scattering of direct shortwave radiation when ACRT on, the results for diffuse radiation in Figure 3-7 do not show the total inner canopy diffuse radiation. The amount of diffuse radiation created by scattering of direct radiation (secondary source of diffuse radiation) can be seen in Figure 3-7a. Similar to the direct radiation, more diffuse radiation is created at the outer canopy. In a comparison between both trees, more secondary diffuse radiation is found within the L-Tree's canopy, as direct radiation penetrates deeper inside the L-Tree resulting in more available direct shortwave radiation to be scattered (see above).

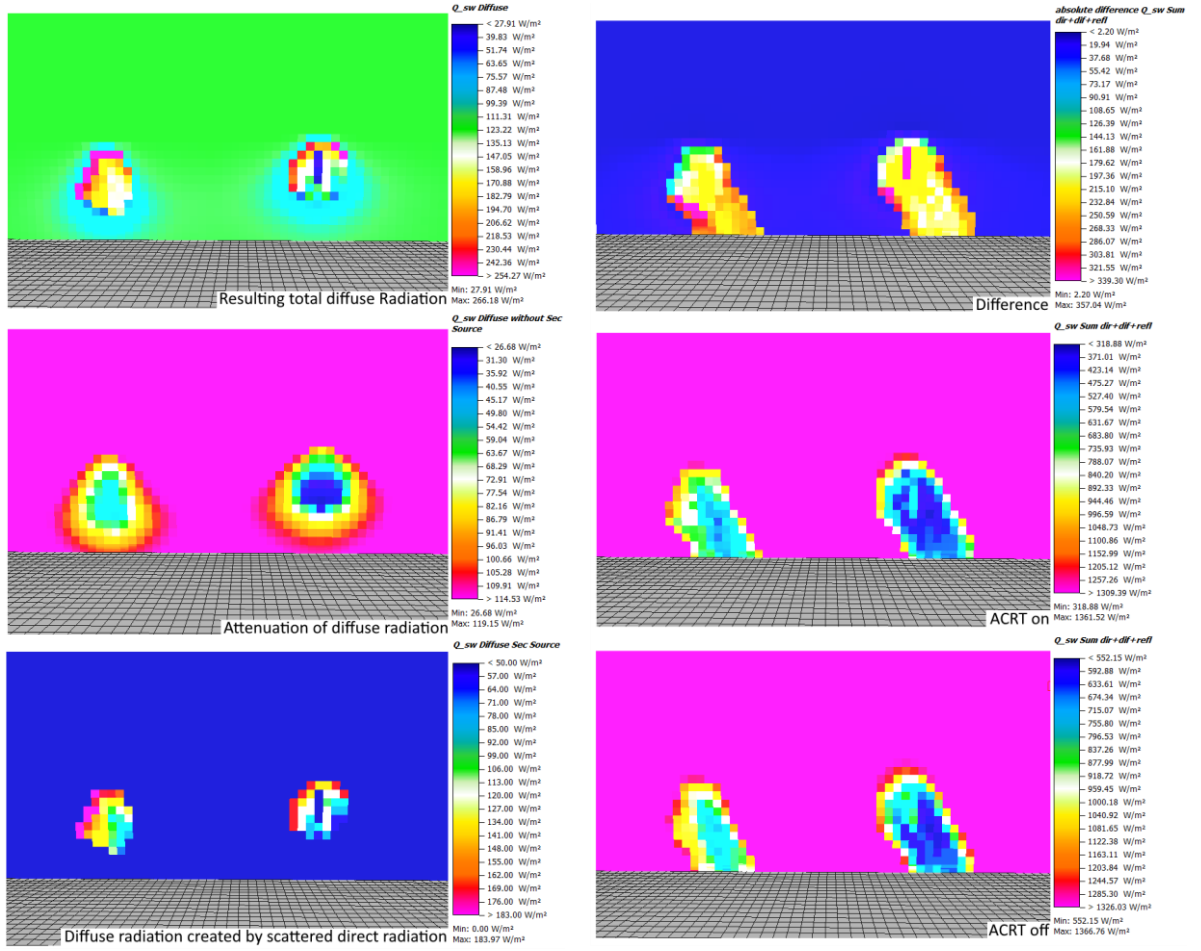

*Figure 3-7: Model output at noon time (sun position: 164.4° azimuthal and 58.3° height angle, view direction: west) for the L-Tree (left) and Parametric-Tree (right): Diffuse shortwave radiation patterns with the ACRT module (**a**); Sum of all shortwave radiation fluxes (direct, diffuse and reflected shortwave radiation) with and without the ACRT module (**b**).*

Looking at the sum of all shortwave fluxes (direct, diffuse and reflected radiation), the increased extinction of direct radiation – and in case the ACRT module is on also the extinction of diffuse shortwave

and the lower creation of secondary diffuse radiation – in the Parametric-Tree leads to significantly lower total shortwave radiation values compared to the L-Tree (around 200 W/m^2 difference). The effect of ACRT accounts for an additional 200 W/m^2 difference between both trees, resulting in inner canopy values for the L-Tree of around 550 W/m^2 with the ACRT module and 750 W/m^2 without the ACRT module. For the Parametric-Tree, the difference is very similar, with 330 W/m^2 with the ACRT module and 550 W/m^2 without the ACRT module.

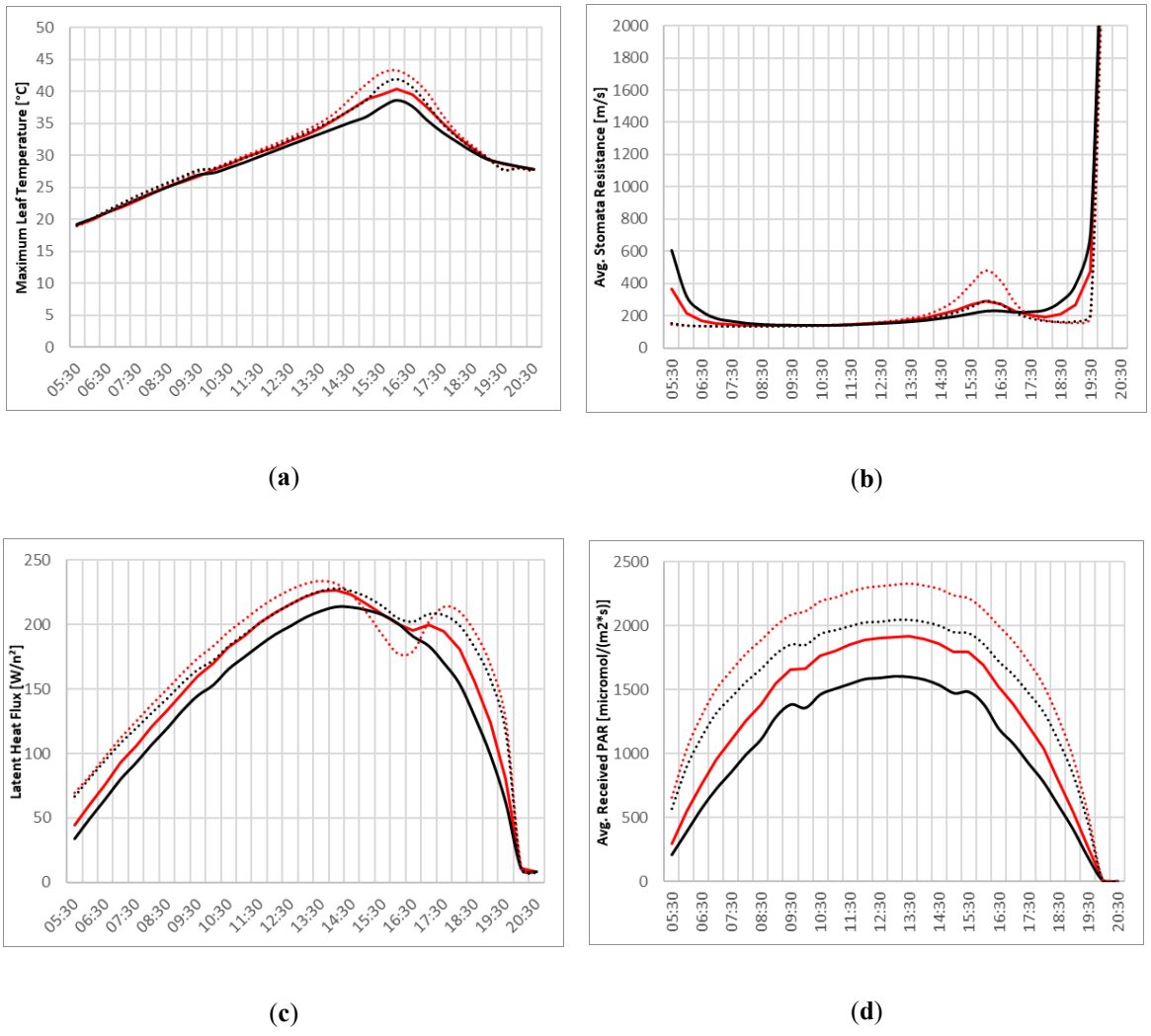

*Figure 3-8: Graphs of various tree parameters: Maximum Leaf Temperature (**a**), Average Stomata Resistance (**b**), Latent Heat Flux (**c**); Average Received Photosynthetic Radiation (**d**). Red lines indicate L-Trees, black lines Parametric-Trees, dashed lines ACRT module off, solid lines ACRT on.*

Because different inner canopy radiation patterns lead to alterations in plant physiology of the trees, several indicators for the tree's behavior have been analyzed for the photosynthetic active hours, i.e., day light hours of the simulation (Figure 3-8).

The diurnal cycles of maximum leaf temperature, average stomata resistance, latent heat flux and average received photosynthetic active radiation (PAR) show large differences of the two trees and with and without the ACRT module.

Maximum leaf temperatures show rather similar values until the afternoon, after which the trees in the simulation without ACRT experience significantly higher maximum leaf temperatures (> 40 °C) indicating thermal stress. This can also be seen in the sudden spike in average stomata resistance of the trees in the ACRT off simulations. The increased stomata resistance leads to lower vapor fluxes which in turn reduces latent heat flux and increases leaf temperatures. Also notable is the less sudden drop of the stomata resistance in the morning and the sudden drop of the stomata resistance in the evening for the ACRT on simulations. This is caused by the introduction of attenuation of diffuse radiation, which leads to a more gradual progression in the morning and evening hours.

The curve of average received PAR corroborates the inner canopy radiation analyses at noon above, with highest values for the L-Tree in the ACRT off simulation and lowest values for the Parametric-Tree in the ACRT on simulation.

In order to entangle the contributions of the advancements of the L-Tree and the ACRT module, Root Mean Square Errors (RSME) between different combinations of Parametric-Tree, L-Tree and ACRT on and ACRT off simulations have been calculated for maximum leaf temperature, average stomata resistance, latent heat flux and average received photosynthetic active radiation (Figure 3-9).

The comparison of the Root Mean Square Errors shows the same general tendencies for all parameters. The biggest differences occur between the L-Tree without the ACRT module and the Parametric-Tree with the ACRT module. This indicates that the advancements of the ACRT module and the L-Tree complement each other, as their combination leads to the highest values of RMSE. Looking at the isolated effects of the L-Tree and the ACRT advancements, it seems, that the ACRT module (comparison between Parametric-Tree with ACRT and Parametric-Tree without ACRT) has a slightly greater effect for all parameters than the equivalent isolated L-Tree advancements (comparison between L-Tree without ACRT and Parametric-Tree without ACRT). The largest effect when only enabling one advancement can be seen in the combination of Parametric-Tree and ACRT on/off. This indicates, that by only

enabling the ACRT module, the parameters of maximum leaf temperature, average stomata resistance, latent heat flux and average received photosynthetic active radiation match the supposedly most realistic simulation featuring an L-Tree with the ACRT module rather closely already. This suggests that the ACRT module has a greater impact onto the plant specific parameters, while the L-Tree implementation alone also constitutes further advancements, their isolated effects seem to have a lesser extend onto the parameters shown.

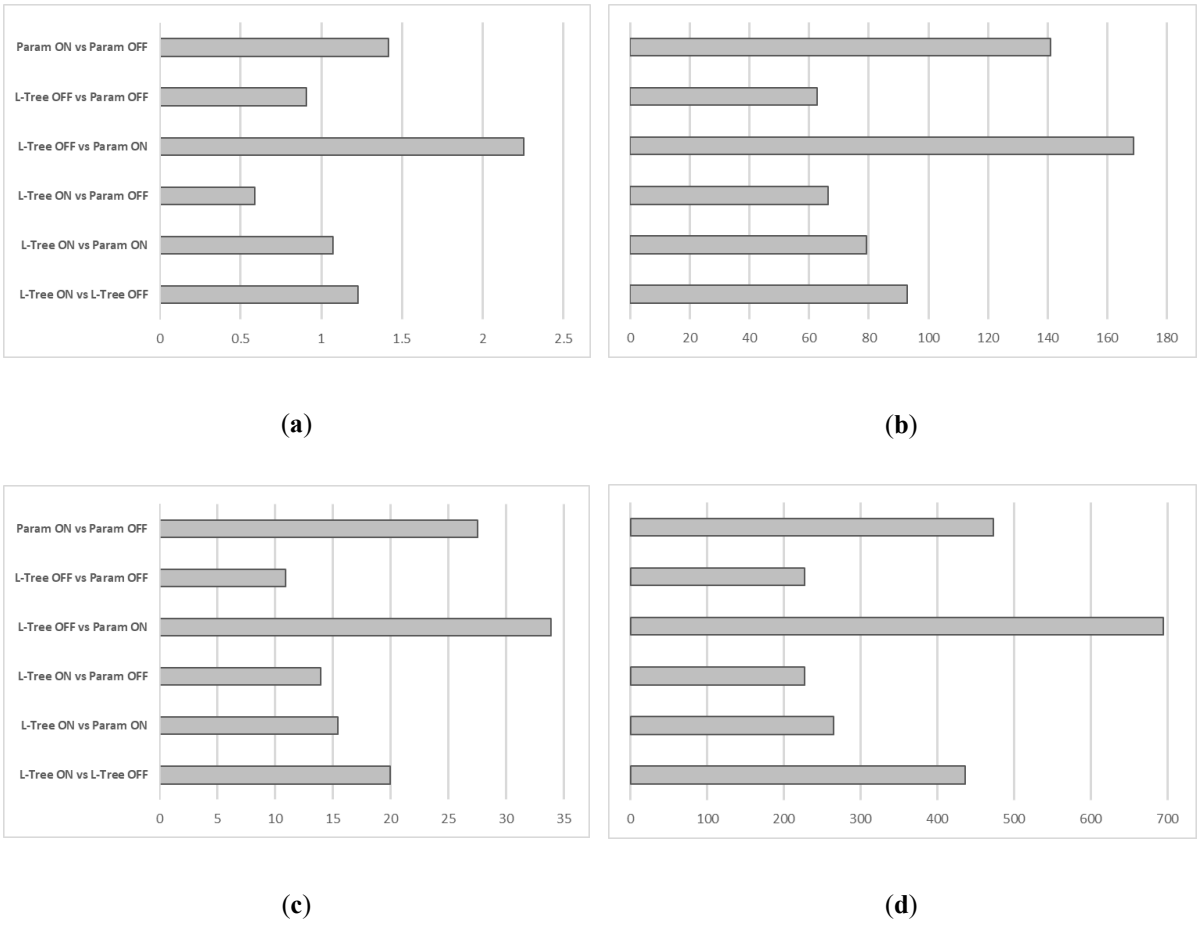

*Figure 3-9: Root Mean Square Error between different combinations of Parametric-Tree, L-Tree and ACRT on and ACRT off: Maximum Leaf Temperature (**a**), Average Stomata Resistance (**b**), Latent Heat Flux (**c**) and Average Received Photosynthetic Radiation (**d**).*

The vertical distribution of shortwave radiation within canopy of all combinations shows a steep decline with decreasing height, most pronounced in ACRT on simulations (Figure 3-10). While the Parametric-Tree with its homogenous LAD structure shows an almost steady decline in the ACRT on simulations, the L-Tree's shortwave radiation reduction varies in its strength. Values at ground level for the ACRT on simulation are however similar with around 40 %. In contrast, both trees show a less pronounced decline of shortwave radiation in the ACRT off simulation, mainly because diffuse radiation is not

attenuated without the ACRT module. The resulting ground level shortwave radiation for the ACRT off simulation lies around 60 % for both trees.

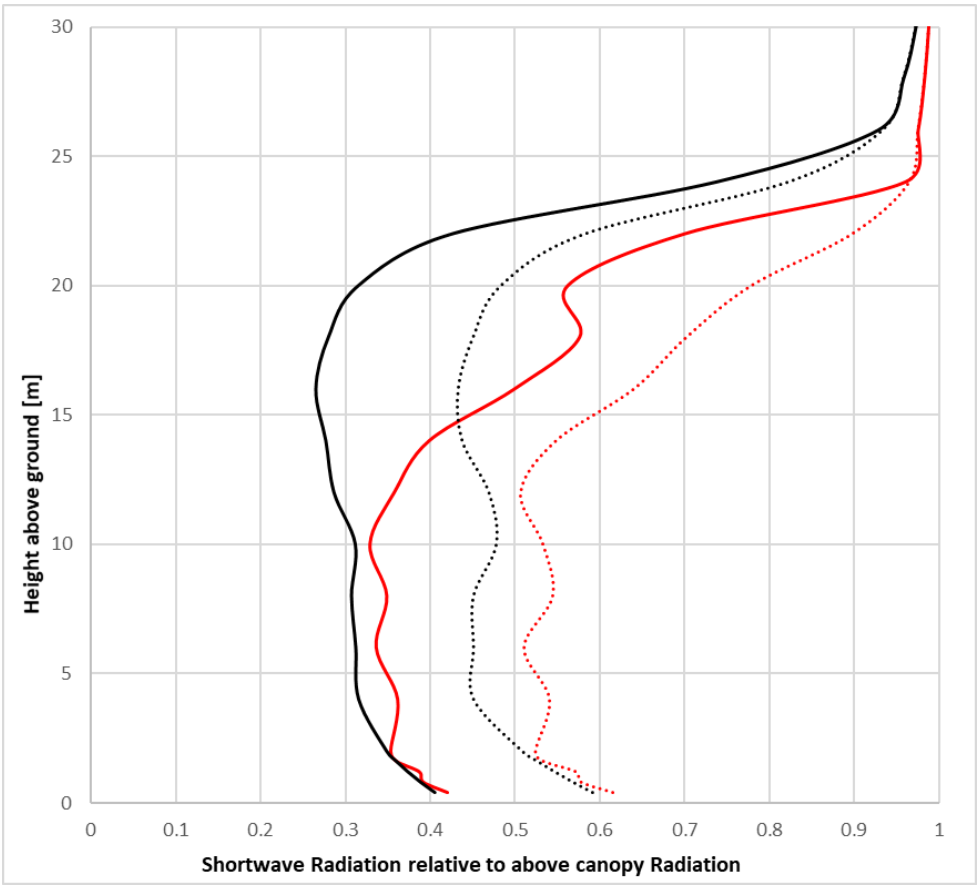

Figure 3-10: Vertical distribution of shortwave radiation through tree centerline at noon; red lines L-Trees, black lines Parametric-Trees, dashed lines ACRT module off, solid lines ACRT on.

Comparing these results with literature values for similar trees (regarding height and LAD), such as Balsam poplar in Mixlight where the authors compared predicted inner canopy radiation transmittance against measured values, shows that the simulation of the L-Tree with ACRT module matches the measured and modelled values of Mixlight quite closely (Stadt and Lieffers, 2000). Other literature values of e.g. Thakur & Kaur (2001) or Bartelink (1998) come to slightly lower ground level values of around 10 to 20 %, however featuring denser trees. Further direct comparison with literature values is constrained, as most studies are carried out on trees in forest stands instead of isolated locations (Brunner, 1998; Cescatti, 1997).

To examine the effect of both advancements onto the thermal comfort, the Physiological Equivalent Temperature (PET) underneath both trees has been calculated in a height of 1.4 meters (Figure 3-11).

The results show generally lower PET values in the ACRT including simulations of around 2 to 3.37 K for both trees. While the PET pattern underneath the parametric tree shows a more homogenous reduction of PET, the PET underneath the L-Tree is heterogeneously distributed as the non-uniform LAD clusters of the L-Tree cause different levels of shading and thus mean radiant temperature.

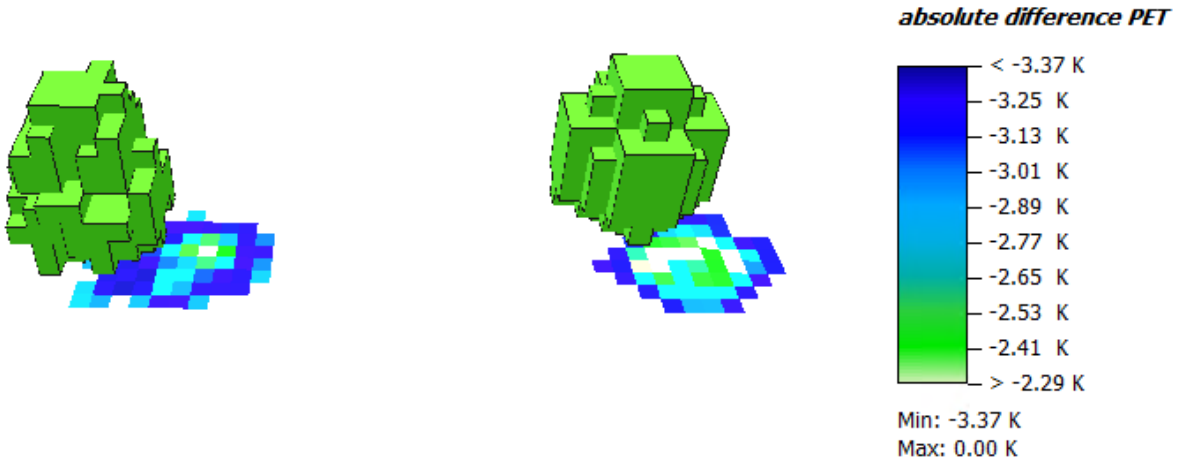

Figure 3-11: Absolute difference in Physiological Equivalent Temperature (PET) at 1.4 meters height level at noon below L-Tree (left) and Parametric Trees (right) between ACRT on and ACRT off simulations. Negative values indicate lower PET values in the ACRT on simulation.

3.4 Conclusions

This contribution presents a combined effort to improve the modelling of the microclimate effect of trees on the one hand and plant vitality parameters on the other. By developing a sophisticated plant digitalization method enabling the much more realistic description of plants, the for microclimate important position and alignment of leaf clusters can be deduced. Further advancements of the inner canopy radiation scheme enabling the attenuation of diffuse radiation and the creation of secondary diffuse radiation by scattering of direct radiation, lead to much more diverse radiation patterns inside and around the plant. In two proof-of-concept simulations, the effects of the advancements were examined regarding the radiative scheme as well as different plant physiological and microclimatic parameters. The results showed significant differences between the tree types as well as the radiative transfers. It can be expected that, with the new advancements, modelling of microclimate effects of trees and plant vitality is considerably improved. Samples from literature values seem to corroborate this finding. However, since no empirical tests have been undertaken yet, the strength of the new approaches needs to be evaluated in

real case scenarios. Due to parallelization, the simulation time is not significantly affected by including L-Trees or the ACRT module and can thus be used in larger, more complex model areas as well.

Results of the thermal comfort beneath the trees showed significant differences in PET as the shading and thus the mean radiant temperature is greatly affected by the new radiation scheme as well as the non-uniform LAD distribution of the L-Trees. This indicates that the use of both advancements will yield a better understanding of not only the plant physiological parameters, but also the effects of trees onto the local microclimate. Future developments of both modules should address the translation of the branching system into the radiative simulation to account for effects like absorption of shortwave radiation by the branches as well. Furthermore, the inclusion of branches should make plant biomechanical simulations possible predicting the probability of branch failure due to wind gusts.

3.5 References

Alavipanah, S., Wegmann, M., Qureshi, S., Weng, Q., Koellner, T., 2015. The Role of Vegetation in Mitigating Urban Land Surface Temperatures: A Case Study of Munich, Germany during the Warm Season. Sustainability 7, 4689–4706.

Andersson-Sköld, Y., Thorsson, S., Rayner, D., Lindberg, F., Janhäll, S., Jonsson, A., Mobacke, U., Bergman, R., Granberg, M., 2015. An integrated method for assessing climate-related risks and adaptation alternatives in urban areas. Climate Risk Management 7, 31–50.

Bartelink, H.H., 1998. Radiation interception by forest trees: a simulation study on effects of stand density and foliage clustering on absorption and transmission. Ecological Modelling 105, 213–225. https://doi.org/10.1016/S0304-3800(97)00165-8

Bowler, D.E., Buyung-Ali, L., Knight, T.M., Pullin, A.S., 2011. Urban greening to cool towns and cities: A systematic review of the empirical evidence. Landscape and Urban Planning 97, 147–155.

Brunner, A., 1998. A light model for spatially explicit forest stand models. Forest Ecology and Management 107, 19–46. https://doi.org/10.1016/S0378-1127(97)00325-3

Bruse, M., 2004. ENVI-met documentation http://www.envi-met.com/documents/Envimet30.PDF. 16.04.2015.

Cescatti, A., 1997. Modelling the radiative transfer in discontinuous canopies of asymmetric crowns. I. Model structure and algorithms. Ecological Modelling 101, 263–274. https://doi.org/10.1016/S0304-3800(97)00050-1

Dimoudi, A., Nikolopoulou, M., 2003. Vegetation in the urban environment: microclimatic analysis and benefits. Energy and Buildings 35, 69–76.

Fan, C., Myint, S.W., Zheng, B., 2015. Measuring the spatial arrangement of urban vegetation and its impacts on seasonal surface temperatures. Progress in Physical Geography 39, 199–219.

Goudriaan, J., 1977. Crop micrometeorology: a simulation study. Cen- ter for Agricultural Publishing and Documentation, Pudoc.

Greene, N., 1989. Voxel space automata: modeling with stochastic growth processes in voxel space, in: Proceedings of the 16th Annual Conference on Computer Graphics and Interactive Techniques, SIGGRAPH '89. Association for Computing Machinery, New York, NY, USA, pp. 175–184. https://doi.org/10.1145/74333.74351

Harlan, S.L., Brazel, A.J., Prashad, L., Stefanov, W.L., Larsen, L., 2006. Neighborhood microclimates and vulnerability to heat stress. Social Science & Medicine 63, 2847–2863.

Honjo, T., Takakura, T., 1990. Simulation of thermal effects of urban green areas on their surrounding areas. Energy and Buildings 15, 443–446.

Lee, H., Mayer, H., Chen, L., 2016. Contribution of trees and grasslands to the mitigation of human heat stress in a residential district of Freiburg, Southwest Germany. Landscape and Urban Planning 148, 37–50.

Lindén, J., 2011. Nocturnal Cool Island in the Sahelian city of Ouagadougou, Burkina Faso. International Journal of Climatology 31, 605–620.

Lindenmayer, A., 1968. Mathematical models for cellular interactions in development II. Simple and branching filaments with two-sided inputs. Journal of Theoretical Biology 18, 300–315. https://doi.org/10.1016/0022-5193(68)90080-5

Longay, S., Runions, A., Boudon, F., Prusinkiewicz, P., 2012. TreeSketch: Interactive Procedural Modeling of Trees on a Tablet 14.

Middel, A., Brazel, A.J., Gober, P., Myint, S.W., Chang, H., Duh, J.-D., 2012. Land cover, climate, and the summer surface energy balance in Phoenix, AZ, and Portland, OR. International Journal of Climatology 32, 2020–2032.

Norton, B.A., Coutts, A.M., Livesley, S.J., Harris, R.J., Hunter, A.M., Williams, N.S.G., 2015. Planning for cooler cities: A framework to prioritise green infrastructure to mitigate high temperatures in urban landscapes. Landscape and Urban Plannin 134, 127–138.

Oliveira, S., Andrade, H., Vaz, T., 2011. The cooling effect of green spaces as a contribution to the mitigation of urban heat: A case study in Lisbon. Building and Environment 46, 2186–2194.

Pedruzo-Bagazgoitia, X., Ouwersloot, H.G., Sikma, M., van Heerwaarden, C.C., Jacobs, C.M.J., Vilà-Guerau de Arellano, J., 2017. Direct and Diffuse Radiation in the Shallow Cumulus–Vegetation System: Enhanced and Decreased Evapotranspiration Regimes. J. Hydrometeor. 18, 1731–1748. https://doi.org/10.1175/JHM-D-16-0279.1

Phelan, P.E., Kaloush, K., Miner, M., Golden, J., Phelan, B., Silva III, H., Taylor, R.A., 2015. Urban Heat Island: Mechanisms, Implications, and Possible Remedies. Annual Review of Environment and Resources 40, 285–307.

Prusinkiewicz, P., Lindenmayer, A., 1990. The Algorithmic Beauty of Plants, The Virtual Laboratory. Springer-Verlag, New York. https://doi.org/10.1007/978-1-4613-8476-2

Salata, F., Golasi, I., de Lieto Vollaro, A., de Lieto Vollaro, R., 2015. How high albedo and traditional buildings' materials and vegetation affect the quality of urban microclimate. A case study. Energy and Buildings 99, 32–49.

Savi, T.S., Bertuzzi, S., Branca, M., Tretiach, M., Nardini, A., 2015. Drought-induced xylem cavitation and hydraulic deterioration: risk factors for urban trees under climate change? New Phytologist 205, 1106–1116.

Simon, H., 2016. Modeling urban microclimate. Development, implementation and evaluation of new and improved calculation methods for the urban microclimate model ENVI-met (Dissertation). Johannes Gutenberg-University Mainz.

Simon, H., Fallmann, J., Kropp, T., Tost, H., Bruse, M., 2019. Urban Trees and Their Impact on Local Ozone Concentration—A Microclimate Modeling Study. Atmosphere 10, 154. https://doi.org/10.3390/atmos10030154

Simon, H., Lindén, J., Hoffmann, D., Braun, P., Bruse, M., Esper, J., 2018. Modeling transpiration and leaf temperature of urban trees – A case study evaluating the microclimate model ENVI-met against measurement data. Landscape and Urban Planning 174, 33–40. https://doi.org/10.1016/j.landurbplan.2018.03.003

Spitters, C.J.T., 1986. Separating the diffuse and direct component of global radiation and its implications for modeling canopy photosynthesis Part II. Calculation of canopy photosynthesis. Agricultural and Forest Meteorology 38, 231–242. https://doi.org/10.1016/0168-1923(86)90061-4

Stadt, K.J., Lieffers, V.J., 2000. MIXLIGHT: a flexible light transmission model for mixed-species forest stands. Agricultural and Forest Meteorology 102, 235–252. https://doi.org/10.1016/S0168-1923(00)00128-3

Thakur, P.S., Kaur, H., 2001. Variation in photosynthesis, transpiration, water use efficiency, light transmission and leaf area index in multipurpose agroforestry tree species. Indian J. Plant Physiol. 6, 249–253.

“ (Simon et al., 2020).

4 Evaluating the thermal-radiative performance of ENVI-met model for green infrastructure typologies: Experience from a subtropical climate

Wanlu Ouyang[1], Tim Sinsel[2], Helge Simon[2], Tobi Eniolu Morakinyo[3], Huimin Liu[4], Edward Ng[1,5,6]

[1]*School of Architecture, The Chinese University of Hong Kong, New Territories, Hong Kong, China*
[2]*Department of Geography, Johannes Gutenberg University Mainz, 55099 Mainz, Germany*
[3]*School of Geography, University College Dublin, Dublin 4, Ireland*
[4]*Institute of Space and Earth Information Science, The Chinese University of Hong Kong, New Territories, Hong Kong, China*
[5]*Institute of Future Cities, The Chinese University of Hong Kong, New Territories, Hong Kong, China*
[6]*Institute of Environment, Energy and Sustainability, The Chinese University of Hong Kong, New Territories, Hong Kong, China*

Summary:

The advancements demonstrated in the previous sections improved ENVI-met's radiation modeling in general and thus positively affected MRT modeling. However, the following detailed evaluation study led by Wanlu Ouyang – comparing measurements of air temperature, relative humidity, as well as six-directional radiation fluxes and the resulting calculated MRT with ENVI-met modeling results in Hong Kong – found that there are still rather large inaccuracies in MRT modeling. The study examined modeled and measured data for six locations that featured three different types of green infrastructure, i.e., a green roof, a green façade, and a tree as well as their three bare counterparts as measurement sites. Furthermore, the demand of both using localized materials and accurate meteorological boundary conditions for the simulations was analyzed by comparing results of several varying simulation configurations to the measurement data. The evaluation study hence provides evaluation results and inaccuracy reports for the developers on the one hand and guidance for the user application of ENVI-met on the other hand. The author contributed to this work by preparing and conducting the microclimate simulations as well as adding ENVI-met modeling expertise and insights during conceptualization and proofreading of the manuscript.

Building and Environment 207, January 2022 – published

“

4.1 Introduction

4.1.1 Background

Due to rapid urbanization processes, global climate change, and intensified heat waves, climate knowledge has been gaining increasing attentions in both academic fields (Mills, 2014) and urban planning and design practices (Eliasson, 2000). In this respect, numerical simulation tools are powerful means for researchers and urban planners to understand the urban climate mechanisms and assess the climate adaptation strategies. Thus, numerical simulation has gained increasingly popularity over the past two decades (Arnfield, 2003). This popularity is justified by the high capacity of modeling to involve the nonlinearity and complexity of urban climate processes (Jamei et al., 2019), and is also supported by the development in both hardware (i.e., increasing computational power of computers) and software (i.e., emerging models or tools) (Mirzaei and Haghighat, 2010). Moreover, numerical modeling can assist the climate-sensitive urban planning, as it can assess the effectiveness of mitigation strategies based on “what-if” scenarios, especially during the planning stages.

In urban climate fields, numerical simulation tools can be classified into two types according to their mechanisms: energy balance model (EBM) based on the energy balance budget, and computational fluid dynamics (CFD) based on the equations of fluid dynamics and conservation of mass, momentum, energy. EBM is mainly for large-scale studies (i.e., city scale), as it approximates the complex buildings with limited grids and applies homogeneous geometry for the whole city (Mirzaei and Haghighat, 2010). Due to absences of air velocity, EBM cannot reproduce the interactions between air velocity and temperature fields, and hence is not suitable for microclimate studies (Mirzaei and Haghighat, 2010). On the contrary, CFD provides detailed and accurate information in the relevant thermal, velocity, radiation fields, and thus is a powerful tool at microclimate scales for buildings’ energy consumption and outdoor thermal comfort (Jamei et al., 2019). Among all of the CFD based models, ENVI-met is one of the most widely used tools in multiple climate backgrounds and for different urban forms with diversified characteristics in buildings and greenery (Tsoka et al., 2018).

4.1.2 ENVI-met model and applications

ENVI-met is designed to simulate the complex atmosphere-vegetation-surface interactions. Specifically, it is a grid-based model with fine resolution (0.5-10m) and uses standard κ-ε turbulence model and Reynolds Averaged Navier-Stokes (RANS) equations (Huttner, 2012). There are several sub-models in ENVI-met: 1) 1D (one-dimensional) boundary model to initialize the simulation and establish the boundary conditions of the 3D model; 2) 3D atmospheric model to simulate all the processes of temperature, humidity, turbulence, radiation fluxes, and pollutants; 3) soil model to calculate the temperature and humidity fluxes in the soil layers; 4) vegetation model to simulate the transpiration rates, leaf temperature of the plants, as well as the heat and vapor interactions between vegetation and atmosphere (Huttner, 2012; Tsoka et al., 2018). Compared with previous versions, the recent version of ENVI-met (V4) has been updated greatly (Simon, 2016). Firstly, a 3D vegetation module has been added for mimicking complex vegetation geometries. Secondly, a "full forcing" scheme has been added to allow the half-hourly measured values as the inputs, i.e., air temperature, relative humidity, cloud cover/ solar radiations, and wind conditions. Thirdly, multiple façade layers have been added to the building module, up to three different materials can be applied with different physical parameters, including reflectivity, absorption, and specific heat capacity. Lastly, ENVI-met version 4.4 has implemented a roof and façade greening module. Hence, these updates of ENVI-met are expected to generate more reliable simulation results (Lee et al., 2016).

ENVI-met has been widely applied to investigate the impacts of urban greening on urban microclimate (Tsoka et al., 2018). Specifically, three green infrastructure (GI) typologies, i.e., ground trees, green walls, and green roofs, are often investigated individually and collectively. For instance, regarding ground trees, ENVI-met was used to investigate the impacts of coverage ratio amount (Ng et al., 2012; Ouyang et al., 2020), tree species (Morakinyo et al., 2017b, 2018, 2020), and planting location (Tan et al., 2017, 2016) on the magnitude of the thermal benefits. In terms of vertical greenery, the model was applied to explore the impacts of green façade ratio (Morakinyo et al., 2019), implementation orientation (Acero et al., 2019; Morakinyo et al., 2019), and planting height (Acero et al., 2019) on cooling effect. For green roof, ENVI-met can examine the effects of roof coverage ratio (Jin et al., 2018; Morakinyo et al., 2017a; Zhang et al., 2019), green roof types and plant characteristics (Berardi, 2016; Morakinyo et

al., 2017a), and planting arrangement (Jin et al., 2018; Zhang et al., 2019) on cooling provision. Overall, the thermal performance was mainly quantified by air temperature, relative humidity, surface temperature, etc., while the radiative performance commonly considered mean radiant temperature, longwave and shortwave radiations, etc. All these parameters are essential for both buildings' energy consumption and outdoor thermal comfort.

4.1.3 Model evaluation and ENVI-met performance

Performance evaluation is an essential step to ensure the reliability of a model, and minimize the probability of making wrong decisions based on the simulation results or gaining an adverse insight in the targeted situations (Matott et al., 2009). Model performance can be distinguished into scientific and operational aspects. The scientific performance is related with the model components, while the operational performance links to the particular applications (Fox, 1981). In our study, the operational performance was evaluated, which refers to comparing the simulation results with the observed data in a given application context (Fox, 1981).

Previous studies have examined the performance of ENVI-met in different perspectives (Tsoka et al., 2018). For instance, the model was evaluated for different seasons (Crank et al., 2020; Roth and Lim, 2017), different meteorological conditions (Acero and Arrizabalaga, 2018), urban spaces (Acero and Herranz-Pascual, 2015), ground surfaces (Yang et al., 2013), tree typologies (Shinzato et al., 2019), tree species (Liu et al., 2018), and applicability in diverse urban forms (Crank et al., 2020), near a tree (Jamei et al., 2019), near façade greening (Jänicke et al., 2015), or for specific microclimate variables (i.e., mean radiant temperature) (Crank et al., 2020; Gál and Kántor, 2020). Based on their evaluation results, as summarized in Appendix Table 4-4, ENVI-met provides relatively accurate estimations of air temperature (AT) and mean radiant temperature (MRT), especially during diurnal periods in summertime. For instance, for AT, two common evaluation metrics performed reasonably, with R^2 ranging from 0.73 ~ 0.99 and root mean squared error (RMSE) ranging from 0.69 ~ 3.97 K; for MRT, R^2 ranged from 0.54 ~ 0.95, and RMSE ranged from 6.44 ~ 16.10 K. Although the evidence came from different climate backgrounds and various built environment, they proved the reliability of ENVI for microclimate analysis and applications.

However, current literatures have evaluated the performance of ENVI-met mainly about the estimations of AT and MRT (Tsoka et al., 2018), yet other microclimate parameters haven been largely overlooked for the performance of ENVI-met (Yang et al., 2013). Based on the limited evidence available, ENVI-met tends to overestimate radiation in the morning and afternoon but underestimates it during noon (Gál and Kántor, 2020; Liu et al., 2018). Accordingly, MRT was also over- and under-estimated (Acero and Arrizabalaga, 2018). To address the limitation regarding the radiation estimations, the Indexed View Sphere (IVS) scheme was introduced in the version 4.4 (Gál and Kántor, 2020). Moreover, in order to tackle the limitations of static solar radiation and wind characteristics (Acero and Arrizabalaga, 2018; Acero and Herranz-Pascual, 2015), recent versions of ENVI-met introduced the full forcing scheme to improve the boundary conditions by involving more meteorological variables, such as half-hourly solar radiation or cloud amount, wind speed and directions (ENVI-met, 2018).

4.1.4 Research objectives

Four research gaps have been mainly identified so far. First, although some studies validated ENVI-met before parametric studies (Abdi et al., 2020; Peng et al., 2020a; Shi et al., 2020), there is scarcely a systematic evaluation study for the recent updates of ENVI-met, i.e., IVS scheme for multiple interactions between surfaces, new full forcing scheme for detailed meteorological boundary conditions, new Advanced Canopy Radiation Transfer (ACRT) module for complex radiation interactions within vegetation canopies (Simon et al., 2018b), and new features in façade and rooftop greening (ENVI-met, 2019). Second, three GI typologies have been examined individually in ENVI-met (Jänicke et al., 2015; Jin et al., 2018; Shinzato et al., 2019), yet it is pending to be explored how ENVI-met performs when including them simultaneously within one homogeneous site. Third, mobile measurement is one of the widely used method to collect microclimate parameters (Middel and Krayenhoff, 2019; Ouyang et al., 2021; Ziter et al., 2019). It is worth examining whether the data from mobile measurement can be applied for ENVI-met model validation. Four, several metrics have been utilized for model evaluation previously, but their sensitivities are scarcely compared.

Therefore, this study aims to systematically evaluate the thermal-radiative performance of ENVI-met model (the latest version V4.4.6) for three GI typologies within a homogeneous site in a subtropical climate city, Hong Kong. Four specific objectives were addressed: 1) to examine the influence of the

inputs and settings on the reliability of ENVI-met; 2) to measure the estimation accuracy of thermal-radiative variables for three GI typologies; 3) to investigate whether the output intervals affect the evaluation results; 4) to explore the sensitivity of different metrics towards the model evaluation results. To achieve these objectives, firstly, a field measurement was taken in six points, three near GI typologies (i.e., green roof, green wall, and ground tree) and three at corresponding reference sites. Secondly, sensitivity analyses were conducted for the model inputs and settings, including four aspects: new radiation scheme (IVS), meteorological boundary conditions, materials parameters, and output intervals. Thirdly, based on the optimal model in the sensitivity analyses, the reliability of ENVI-met was evaluated for six measurement points, nine microclimate variables, and three output intervals by four quantitative evaluation metrics. Finally, the strengths and limitations of ENVI-met were discussed for its applications in the subtropical climate context. This study helps model users including researchers, practitioners (e.g., urban planners and designers), and policy makers extend the understanding in the capabilities and limitations of ENVI-met model, thereby assist developing and implementing climate-sensitive planning strategies.

4.2 Methodology

4.2.1 Study area and measurement site

This study was conducted in Hong Kong (HK), located in the eastern Pearl River Delta by the South China Sea (22.3193° N, 114.1694° E). With a typical humid subtropical climate (Köppen *Cfa*), HK experiences a hot and humid summer with a daily temperature of 28.5 °C and a relative humidity of 80% on average (Development Bureau and Planning Department Hong Kong, 2016). To curb the menace of urban overheat, several urban greening policies have been implemented from building to city scales, e.g., Green master plan (GMP) was developed to provide an overall greening framework for specific areas (Hong Kong Civil Engineering and Development Department, 2004), Practice Note APP-152 was proposed to ensure enough greening coverage ratio for new building developments (Hong Kong Buildings Department, 2016).

The field measurement site was in the Electronic and Mechanical Services Department (EMSD) headquarters located in Kowloon peninsula (see Figure 4-1). This site serves as a successful case for greening implementation in HK, as three GI typologies, namely green roof, green wall, and ground tree, are

incorporated in proximity within the EMSD courtyard. Three measurement points were besides each GI typology, while three reference locations were within 5m distance from corresponding GI point, so that the surrounding environment between paired locations was similar with minimal biases. It is noteworthy that the site provides a homogeneous urban environment with restricted vehicular and pedestrian traffic, thus the impacts of anthropogenic heat are limited for both measurements and modelling.

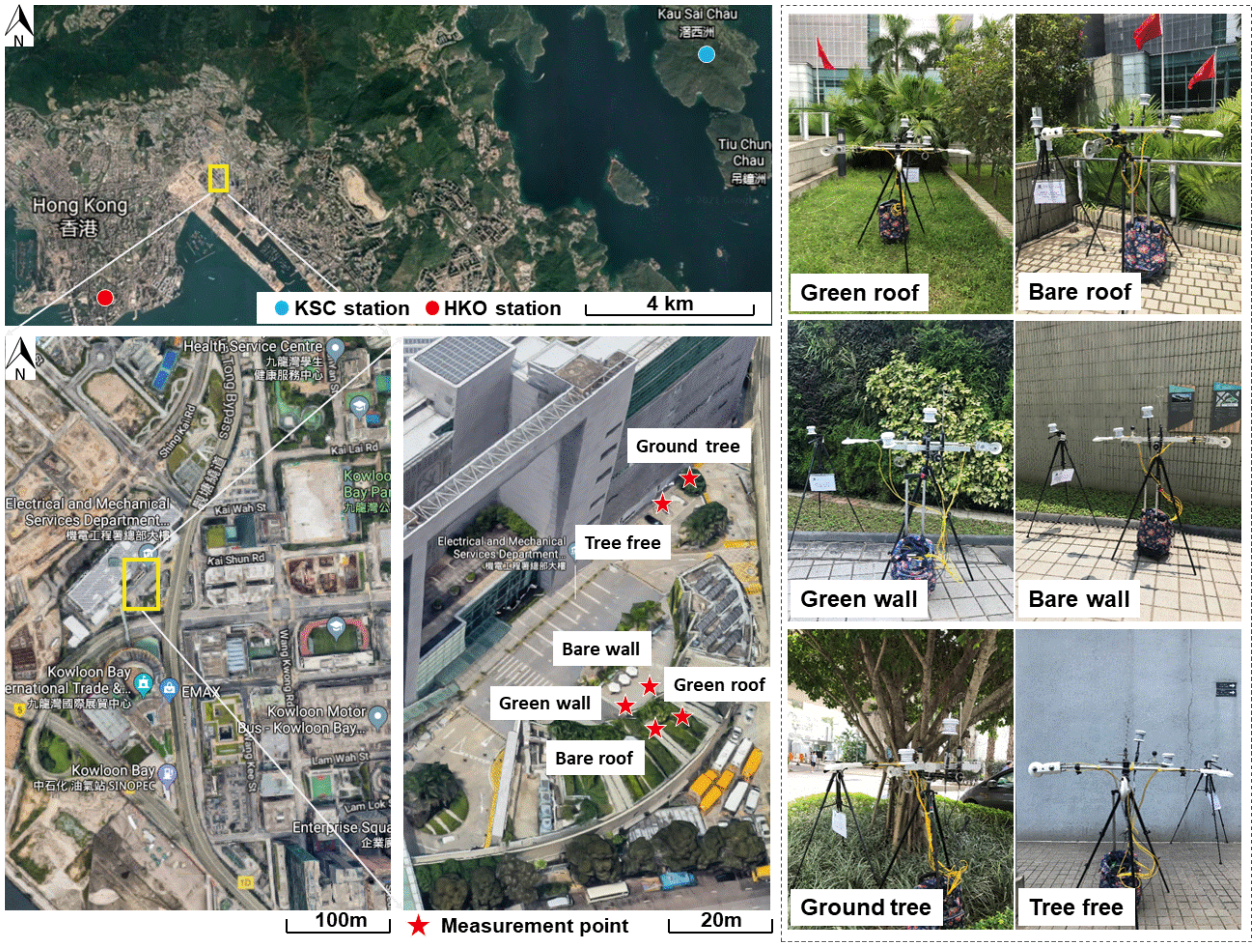

Figure 4-1: Study area and measurement sites (Adapted from Ouyang et al., 2021).

4.2.2 Field measurement and data processing

Thermal-radiative variables were collected near three GI typologies spots and three reference spots (shown in Figure 4-1) between 09:30 ~ 17:25 hr (LST) on four typical summer days: 07th, 09th, 11th, and 12th September in 2019. Both stationary monitoring and mobile measurements approaches were applied for data collection. To measure thermal variables, i.e., air temperature and relative humidity, a HOBO U12-012 logger was set at each of the six measurement points for the stationary monitoring. To measure radiative variables, i.e., six-directional shortwave and longwave radiation, three "four-in-one" radiometers (CNR4) were installed on a balanced tripod stand for the mobile measurement. The instruments

were moved from one point to another in cycle within one hour. Each hour cycle started at green roof and ended at tree-free point, and altogether eight cycles were realized on each measurement day. For each point, at least 2min was ensured for the equipment stabilization, afterwards 5min observations were made before shifting to the next point. The details of the mobile approach, measurement instruments, measurement process, and results were reported in our earlier study (Ouyang et al., 2021).

Subsequently, the collected thermal-radiative data was extracted and averaged based on three time-scales: 10min, 30min, and 1h, which was in accordance with one of the objectives of this study - to test the sensitivity of ENVI-met towards different outputs intervals, so that the feasibility of mobile measurement for ENVI-met validation can be investigated. Mean radiant temperature was calculated based on the radiative elements in six directions with Eq. 3-1:

$$MRT = \sqrt[\frac{1}{4}]{\sum_{i=1}^{6} W_i(a_k K_i + a_l L_i)/a_l\sigma} - 273.15 \qquad \textit{Eq. 4-1}$$

where W_i represents a weighting factor summing up to 1 (equals 0.06 for up/down direction, 0.22 for four lateral directions); K_i and L_i indicate six-directional shortwave and longwave radiation flux densities, respectively; a_k and a_l are the absorption coefficients of the clothed human body (suggested 0.7 and 0.97 respectively); σ represents the Stefan–Boltzmann constant (equals $5.67 * 10^{-8}\ W/m^2\,K^4$).

4.2.3 ENVI-met model configuration

This study evaluated the latest version of ENVI-met (V4.4.6). The actual environment of EMSD, the measurement site, was defined in the area input model. The simulation domain consisted of 250 × 225 × 46 grids with horizontal resolution (Δx and Δy) of 2 m, which is a good tradeoff between the simulation efficiency (simulation time) and the simulation accuracy (Salata et al., 2016). The vertical grids were in varying vertical resolution (Δz) with 0.2 m resolution below 1m height, 1m resolution between 1 m and 10 m, and 30 % telescoping above 55m. To minimize the boundary effects and increase the numerical stability, 10 empty cells were added for each lateral boundary. The building heights ranged from 3 m to 180 m in the domain, and the building with green wall and green roof was 7 m high. The model domain was rotated 45º in the clockwise direction. The actual and modelled built environment were shown in Figure 4-2.

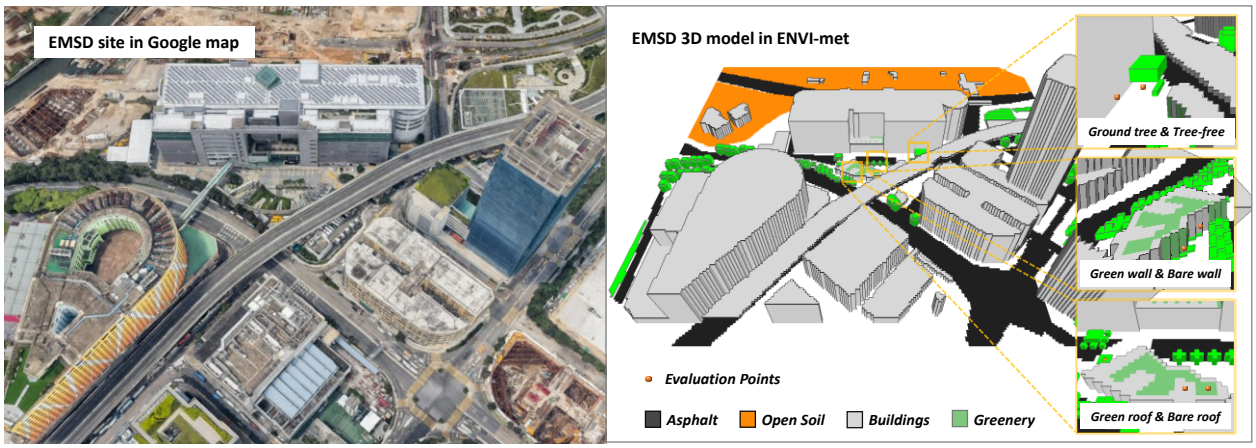

Figure 4-2: The real (left) and modelled (right) built environment of measurement site.

Given that ENVI-met was developed in Germany, the default input parameters for the thermal-radiative properties of construction materials and the features of plants may not be adaptable for other cities (Roth and Lim, 2017). To test the adaptability of the model's default database, sensitivity tests were conducted for both default and localized values. For localized properties, the values were adapted from both existing database, (i.e., default characteristics for building envelope published by Hong Kong Green Building Council (Burton, 2002)) and the values applied in previous local studies (Acero and Arrizabalaga, 2018; Jamei et al., 2019; Kotthaus et al., 2014; Yang et al., 2013). Considering that the material properties in the real site are complex, this study applied representative values for the typical condition in reality. We assumed the ground is built with concrete, the roof is constructed with asphalt and concrete tiles, and the building wall is constructed with heavy concrete and cement; the material properties are the average of the component materials accordingly (Yang et al., 2020). In addition, the green roof and green wall were mimicked by 1D plant (grass) in the new green façade and roof module, while the ground tree was modelled in the 'ALBERO' module. The default and localized values of constructions and plants were listed in the Table 4-1.

Table 4-1: Default and localized characteristics of the construction and plant.

Construction & Plant	Input Parameter [Unit]	Settings	
		Default	**Localized**
Ground pavement	Albedo	0.4	0.15
	Emissivity	0.9	0.9
Building roof	Thickness [m]	0.3	0.3
	Albedo	0.5	0.2
	Emissivity	0.9	0.7
	Thermal conductivity [W/(m.K)]	1.6	1.13
	Specific heat [J/(kg.K)]	850	1060
	Density [kg/m^3]	2220	2225
Building wall	Thickness [m]	0.3	0.3
	Albedo	0.5	0.2
	Emissivity	0.9	0.9
	Thermal conductivity [W/(m.K)]	1.6	1.44
	Specific heat [J/(kg.K)]	850	840
	Density [kg/m^3]	2220	2130
Green roof	Plant height [m]	0.25	0.25
	Leaf area index (LAI) [m^2/m^2]	1.5	2.5
	Plant albedo	0.2	0.2
Green wall	Plant height [m]	0.25	0.25
	Leaf area index (LAI) [m^2/m^2]	1.5	2.5
	Plant albedo	0.2	0.2
Ground tree	Plant height [m]	15	8
	Plant width [m]	11	11
	Leaf area index (LAI) [m^2/m^2]	4.2	4
	Plant albedo	0.18	0.28
	Foliage transmittance	0.3	0.1

To initialize the model, either simple or full forcing scheme can be adopted for boundary meteorological conditions. The simple forcing only requires basic information, while the full forcing scheme needs half-hourly inputs, i.e., solar radiation (solar forcing) or cloud amount (cloud forcing). Current study applied and compared three forcing schemes, including simple, and two full (cloud, and solar) forcing schemes, whose inputs requirements were listed in Table 4-2. The meteorological data was obtained from Hong Kong Observatory (HKO) and Kau Sai Chau (KSC) weather stations (locations were shown in Figure 4-1). Air temperature, relative humidity, wind speed and direction, soil temperature, cloud amount were obtained from HKO, and downward direct and diffuse shortwave radiation were acquired from KSC (Hong Kong Observatory, 2019). As cloud forcing requires the cloud cover conditions in low, medium

and high levels, and HKO only provides the total cloud amount, we set all cloud cover at the medium level. When radiation forcing requires downward longwave radiation that is not measured and provided by Hong Kong Observatory authority, we used the estimation values by ENVI-met based on the Eq. 3-2 (Huttner, 2012; Simon, 2016). We modified the apparent overestimations based on the measurement value on rooftops, as previous study indicated using calculated downward longwave radiation will increase prediction uncertainty (Weihs et al., 2012).

$$Q_{lw}^{\downarrow} = \sum_{n=1}^{N} \sigma T^4(n)[\epsilon_n(m + \Delta m) - \epsilon_n(m)] \qquad \textit{Eq. 4-2}$$

where ϵ_n is the atmosphere emissivity; m is the amount of the water vapor between the lower boundary of layer n and the height z; $(m + \Delta m)$ is the amount of the water vapor of the upper boundary of the layer n and the height z; T is the atmosphere temperature; σ is the Stefan–Boltzmann constant ($= 5.67 * 10^{-8}\ W/m^2\,K^4$).

Table 4-2: Meteorological conditions of three forcing schemes.

Meteorological parameters	**Input value**		
	Simple forcing	**Full forcing**	
		Cloud forcing	**Radiation forcing**
Air temperature (°C)	Daily max and min values	Daily half-hourly profile	Daily half-hourly profile
Relative humidity (%)	Daily max and min values	Daily half-hourly profile	Daily half-hourly profile
Wind speed (m/s)	Daily prevailing wind speed	Daily half-hourly profile	Daily half-hourly profile
Wind direction (°)	Daily prevailing wind direction	Daily half-hourly profile	Daily half-hourly profile
Solar factor/ Cloud/ Radiation	Solar factor adjustments (0.9, 0.8, 0.5)	Daily half-hourly profile (Medium clouds)	Daily half-hourly profile (Direct, diffuse radiations)
Soil initial temperature (°C)	Daily average value in different depth (upper, middle, deep and bedrock layers)	Daily average value in different depth (upper, middle, deep and bedrock layers)	Daily average value in different depth (upper, middle, deep and bedrock layers)
Soil humidity (%)	50, 55, 60, 60 (upper, middle, deep and bedrock layers)	50, 55, 60, 60 (upper, middle, deep and bedrock layers)	50, 55, 60, 60 (upper, middle, deep and bedrock layers)

All simulations were initialized at 06:00hr (UTC = +8), and ran for 13h. Simulation results during 9:30 ~ 17:30hr were used for analysis. The minimal output interval was set as 10min, to be consistent with the mobile measurement interval.

Figure 4-3 showed the framework of this study: first, sensitivity analyses were conducted for the recent model updates; second, the optimal model in the sensitivity analyses was used for model evaluation regarding different GI typologies, output intervals, and thermal-radiative variables. The detailed experimental settings were illustrated in the following two sections.

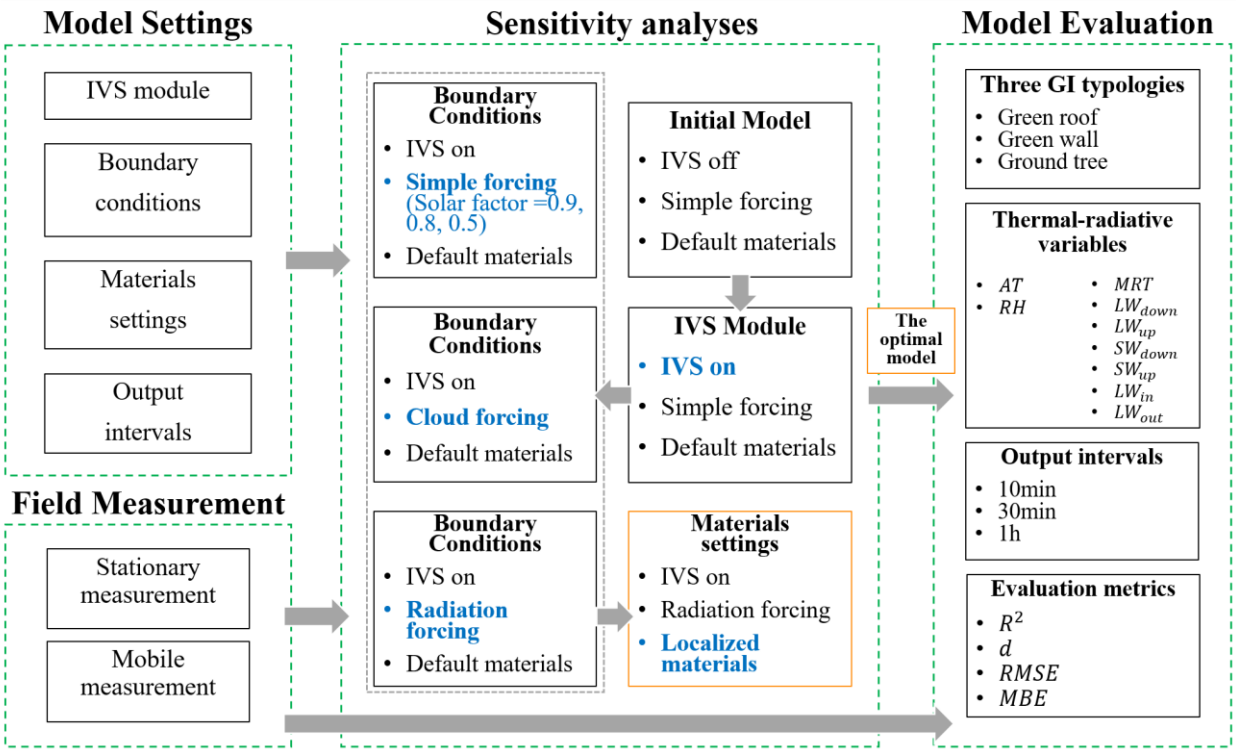

Figure 4-3: Framework illustration of this study.

4.2.4 Sensitivity analyses

To understand the effect of the input variations on the outputs of the model (Saltelli et al., 2004), sensitivity analyses were conducted. Specifically, four aspects were investigated for their impacts on the thermal-radiative outputs of ENVI-met:

1) The new radiation module Index View Sphere (IVS): IVS is a new advanced radiation transfer scheme, which allows a more detailed calculation of secondary radiative transfer. However, it costs higher RAM for computer equipment at exchange for higher accuracy. The sensitivity test aims to show whether the expected accuracy improvement is worth taking higher computer memory with IVS on;

2) Meteorological boundary conditions: the simple forcing and two full forcing (forced cloud and forced radiation) schemes were used and compared to evaluate the impacts of boundary condition settings;

3) Material characteristics of construction and plants: the default and localized settings were both applied to find out the necessity of customizing surface and plant properties for the local case;

4) The output intervals: three output timescales were used and compared in this study (i.e., 10min, 30min, and 1h) to examine the reasonability of applying mobile measurement data to validate ENVI-met model.

To examine the above four aspects, an initial model was started with the default materials, IVS off, and simple forcing. The following models were built with one aspect changed in each run, while other aspects kept constant. The explicit steps and settings are shown in Table 4-3, where words in blue represent the changing setting.

Table 4-3: Model settings and changes for each step.

No	Model Name	Settings			
		IVS Module	**Meteorological Conditions**	**Materials**	**Output intervals**
1	Initial Model	Off	Simple Forcing Solar Factor = 1	Default materials	10min, 30min, 1h
2	IVS on	On	Simple Forcing Solar Factor = 1	Default materials	10min, 30min, 1h
3	SolarFactor0.9	On	Simple Forcing Solar Factor = 0.9	Default materials	10min, 30min, 1h
4	SolarFactor0.8	On	Simple Forcing Solar Factor = 0.8	Default materials	10min, 30min, 1h
5	SolarFactor0.5	On	Simple Forcing Solar Factor = 0.5	Default materials	10min, 30min, 1h
6	CloudForcing	On	Full Forcing (Cloud inputs)	Default materials	10min, 30min, 1h
7	RadiationForcing	On	Full Forcing (Radiation inputs)	Default materials	10min, 30min, 1h
8	LocalizedMaterials	On	Full Forcing	Localized materials	10min, 30min, 1h

*Words in blue indicate the change step by step

4.2.5 Evaluated parameters and statistical metrics

After the sensitivity tests, the optimal model was used for the evaluation analysis. Both thermal and radiative outputs of ENVI-met simulations were evaluated. Thermal parameters included air

temperature (AT) and relative humidity (RH), while radiative parameters considered mean radiant temperature (MRT), downward and upward radiant fluxes, i.e., the downward shortwave and longwave fluxes (SW_{down} and LW_{down}), the upward shortwave and longwave fluxes (SW_{up} and LW_{up}), and wall-outgoing (LW_{out}) and wall-incoming (LW_{in}) longwave fluxes (mainly for green wall and bare wall points). Please see the illustration in Figure 4-4.

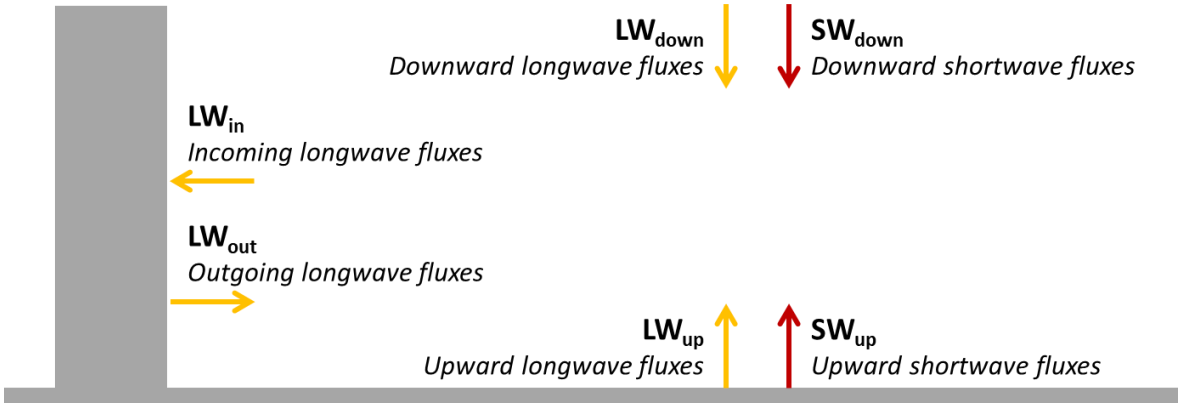

Figure 4-4: Radiation fluxes direction illustration.

Four statistical metrics were primarily adopted in this study for model evaluation: the coefficient of determination (R^2), the index of agreement (d), the root mean square error (RMSE) and its two elements (the systematic root mean square error (RMSEs), the unsystematic root mean square error (RMSEu)), and the mean bias error (MBE) (Moriasi et al., 2007). These four metrics were selected based on the recommendations of Willmott (Willmott, 1982, 1981), i.e., R^2 is an intuitive quantification to describe the model performance, d is complementary for R^2 to assess whether a model's predictions are error free; RMSE measures the average magnitude of the errors (non-negative).

In details, R^2 describes a goodness-of-fit measure for the variances between simulated and measured data, ranging from 0 to 1. d is a dimensionless index to indicate the ratio between the mean square error and the potential error, also ranging from 0 to 1 (Willmott, 1982). RMSE estimates the average magnitude of the errors, consisted of systematic and unsystematic errors: $RMSEs$ and $RMSEu$ (Willmott, 1982). $RMSEs$ quantifies the systematic errors that occur consistently, while $RMSEu$ describes the unsystematic errors that combined small effects into a constant (Yang et al., 2013). MBE measures the average differences between the observations and estimations, which indicates whether the model overestimates (positive values) or underestimates (negative values) the observations (Tsoka et al., 2018).

Overall, higher reliability and accuracy of a model are associated with the conditions of: R^2 and d tending to be 1, RMSE and $RMSEs$ closer to 0, $RMSEu$ nearer to RMSE, and MBE nearer to 0. In addition, to compare the overall performance of different variables, RMSE and MBE of different variables were normalized to be NRMSE and NMBE by using the range of measured data as the denominator (Simon et al., 2018b), so that the different variables with different units can be compared directly. These metrics were calculated through Eq. 3-3 - Eq. 3-7 (Stunder and Sethuraman, 1986; Willmott, 1982).

$$d = 1 - \left[\sum_{i=1}^{N}(S_i - M_i)^2 / \sum_{i=1}^{N}(|S_i'| + |M_i'|)^2\right] \quad \textit{Eq. 4-3}$$

$$RMSE = \left[{RMSE_S}^2 + {RMSE_u}^2\right]^{1/2} = [N^{-1}\sum_i^n (S_i - M_i)^2]^{\frac{1}{2}}$$

$$\text{Where: } RMSEs = \left[N^{-1}\sum_i^n (\widehat{S_i} - M_i)^2\right]^{1/2} \quad \textit{Eq. 4-4}$$

$$RMSEu = \left[N^{-1}\sum_i^n (S_i - \widehat{S_i})^2\right]^{1/2}$$

$$MBE = N^{-1}\sum_{i}^{n}(S_i - M_i) \quad \textit{Eq. 4-5}$$

$$NRMSE = RMSE/(M_{max} - M_{min}) \quad \textit{Eq. 4-6}$$

$$NMBE = MBE/(M_{max} - M_{min}) \quad \textit{Eq. 4-7}$$

where $S_i' = S_i - \bar{M}$, $M_i' = M_i - \bar{M}$, and $\hat{S}_i = a + b * M_i$; S_i is the simulation value by ENVI-met; M_i represents the measurement value; N denotes number of the data; $\bar{M}$ represents the mean of the measurement value; M_{max} is the maximum of the measurement value; M_{min} describes the minimum of the measurement value.

4.3 Results

The simulation results of the 11th Sep, 2019 was briefly reported for two reasons: the weather on this day is a typical summer day in HK with partially cloudy weather conditions (Tan et al., 2017); and the model performance on this day was better compared with other three measurement days.

4.3.1 Sensitivity analysis results

4.3.1.1 By different settings

In this section, eight models with different settings (see Table 4-3 for details) were investigated. With updating settings for each model, the impact of the settings can be evaluated. To cross-compare the

average performance for all microclimate variables and locations, four dimensionless metrics were used, including R^2, d, NRMSE, and NMBE.

As shown in Figure 4-5**,** the model performance was improved as the model settings got updated from the first to the final one (Localized materials), irrespective of output intervals and evaluation metrics. Specifically, the simple forcing with the adjusted solar factors (1, 0.9, 0.5) showed trivial differences based on R^2 and d. However, lower solar factors lead to smaller prediction errors and bias (NRMSE and NMBE). We also found that the cloud forcing model improved prediction accuracy based on R^2, yet deteriorated for other metrics – d, NRMSE, and NMBE. Despite above non-identical evidence, the most efficient settings to improve the model performance were by radiation forcing and localizing materials.

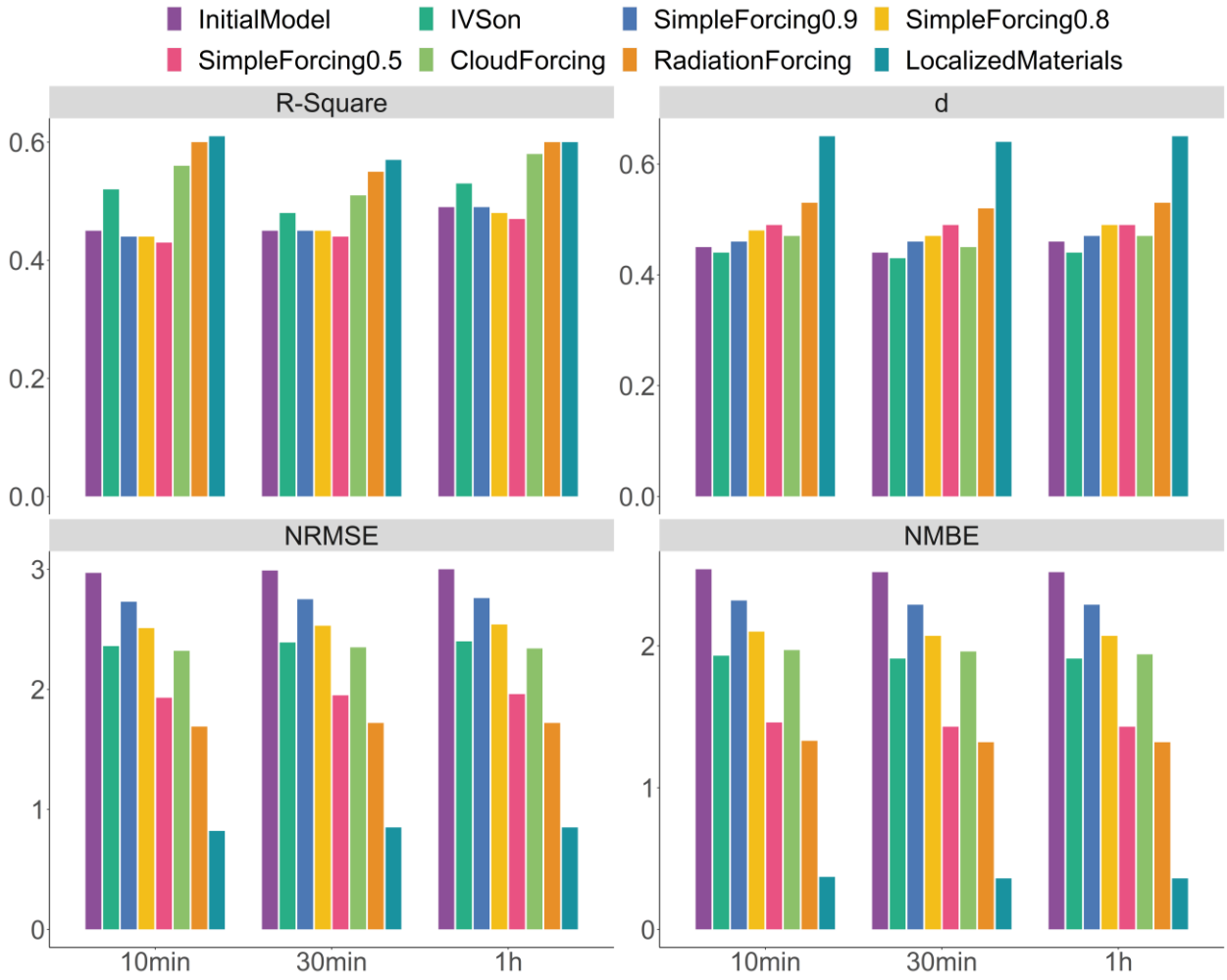

Figure 4-5: Overall model performance by eight settings.

4.3.1.2 By different variables

Figure 4-7 revealed the impacts of model settings on different thermal-radiative variables. SW_{down} was not included here, as it showed high deviation in RMSE and thus covered detailed differences of remaining variables.

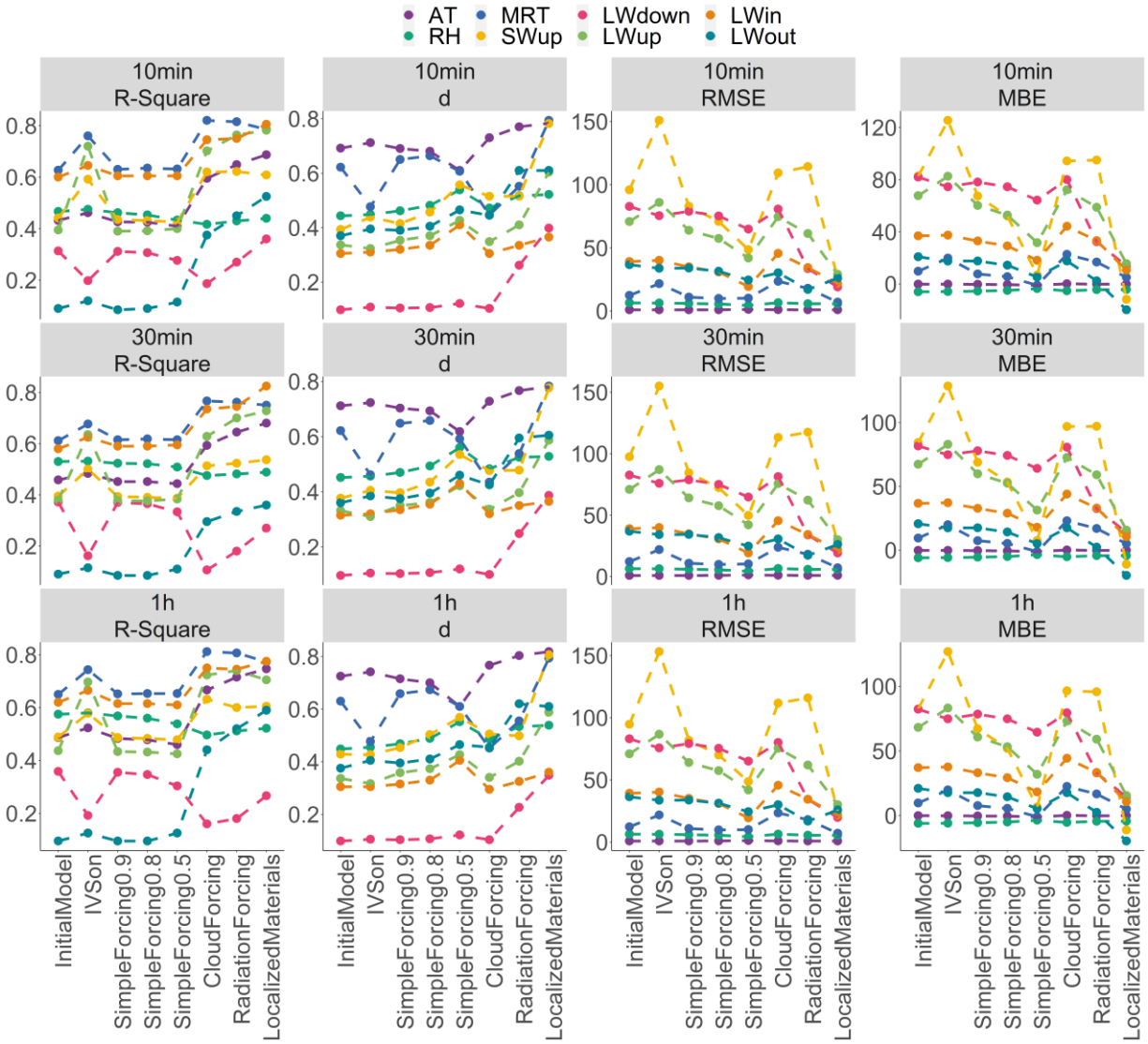

Figure 4-6: Overall model performance by eight variables (unit of RMSE and MBE: °C for AT, MRT; % for RH, W/m^2 for radiation fluxes).

Generally, the prediction accuracy was improved for most of the variables from the initial to the final model. However, the prediction accuracy differed among the variables (shown in Figure 4-6). For instance, variables with the best and stable estimation differ according to four evaluation metrics: MRT based on R^2, AT based on d and RMSE, and AT and RH based on MBE. Across different settings, R^2 of AT was observed to improve from 0.4 to 0.6; SW_{up} estimation was observed to be less accurate with IVS on and full forcing, showing the relatively higher RMSE and MBE; SW_{down} fluctuated minorly

based on R^2 and d, but improved highly based on RMSE and MBE. Output interval rarely impact the patterns, except with MBE where 30 min interval had a lower MBE value than that of 10min and 1h.

4.3.1.3 By different points

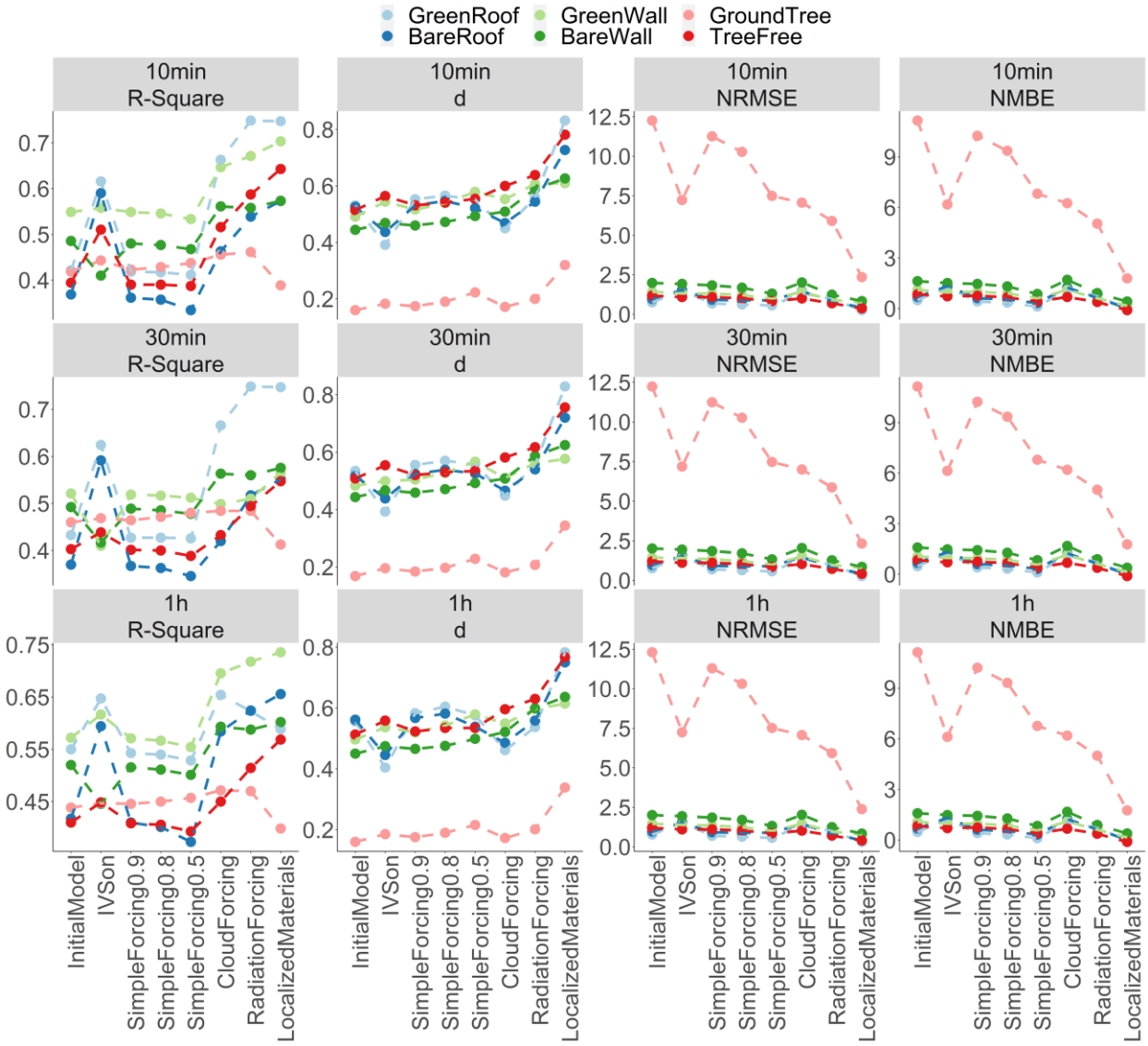

Figure 4-7: Overall model performance by six points.

This section uncovered the impacts of model settings on different locations: green roof (GR), bare roof (BR), green wall (GW), bare wall (BW), ground tree (GT), tree free (TF). Similar with Section 4.3.1.1, four dimensionless metrics were used including R^2, d, NRMSE and NMBE. Overall, almost all points reached the best performance in the final model (Localized materials), with smaller errors, lower biases, regardless of temporal scales. Besides, the model performance in the six points is sensitive to the evaluation metrics (see Figure 4-7). Specifically, based on R^2, the range was 0.40 ~ 0.75; six sites showed little variation among the three simple forcing models, while the performance improved apparently in

two full forcing models (forced cloud and radiation). Using d, six locations presented similar values except for GT site that showed relatively low values from 0.2 ~ 0.4. In terms of the error-based metrics, NRMSE, and NMBE, all sites almost showed insensitive to the chosen model settings, except at GT point had the improved performance in IVS on, full forcing and localized materials models.

Given the results in this section, the optimal model was the Localized materials, which was henceforth selected to evaluate the thermal-radiative performance of ENVI-met. The next two sections mainly discussed nine thermal-radiative variables given their significances in both outdoor thermal comfort and building energy performance. Model developers and users can further understand the simulation deviations based on the detailed illustrations below.

4.3.2 Evaluation in thermal variables

4.3.2.1 Air temperature

Across three output intervals and six points, the performance of ENVI-met in AT was averagely described by R^2 = 0.70, d = 0.79, RMSE = 0.91 °C, and MBE = −0.15 °C. The output intervals did not impact this observation, with slightly better performance for 1h interval and relatively inferior for 30min (R^2 = 0.75 vs. 0.68, d = 0.82 vs. 0.78, RMSE = 0.83 vs 0.97 °C). AT was slightly underestimated in three output intervals (MBE = −0.16 ~ −0.13 °C).

A point-by-point analysis indicated higher variability (see Figure 4-8). R^2 achieved high as 0.90 at GW and relatively lower at BR and TF (0.55). With d, a range of 0.67 ~ 0.91 was observed, highest at BW and lowest at BR. The least error was found at BW (RMSE = 0.54 °C), while the largest error was observed at BR (RMSE = 1.77 °C). The results also showed that ENVI-met tended to underestimate AT at the two rooftop sites (MBE = −0.39 °C and −1.46 °C for GR and BR) and BW (MBE = −0.17 °C), but overestimated AT near GI at pedestrian level (MBE = 0.34 °C for GW and 0.76 °C for GT). TF site had the least MBE nearest to zero (0.04 °C).

It is important to mention that the interpretations for the above values should consider the accuracy of the measurement equipment (HOBO sensor in this study, ±0.3 °C), as some prediction deviations may arise from the measurement errors. The results indicated that ENVI-met has potential limitations to

estimate AT in higher z-level grids, as the AT predictions at roof sites showed high deviations relative to observations at roof-level.

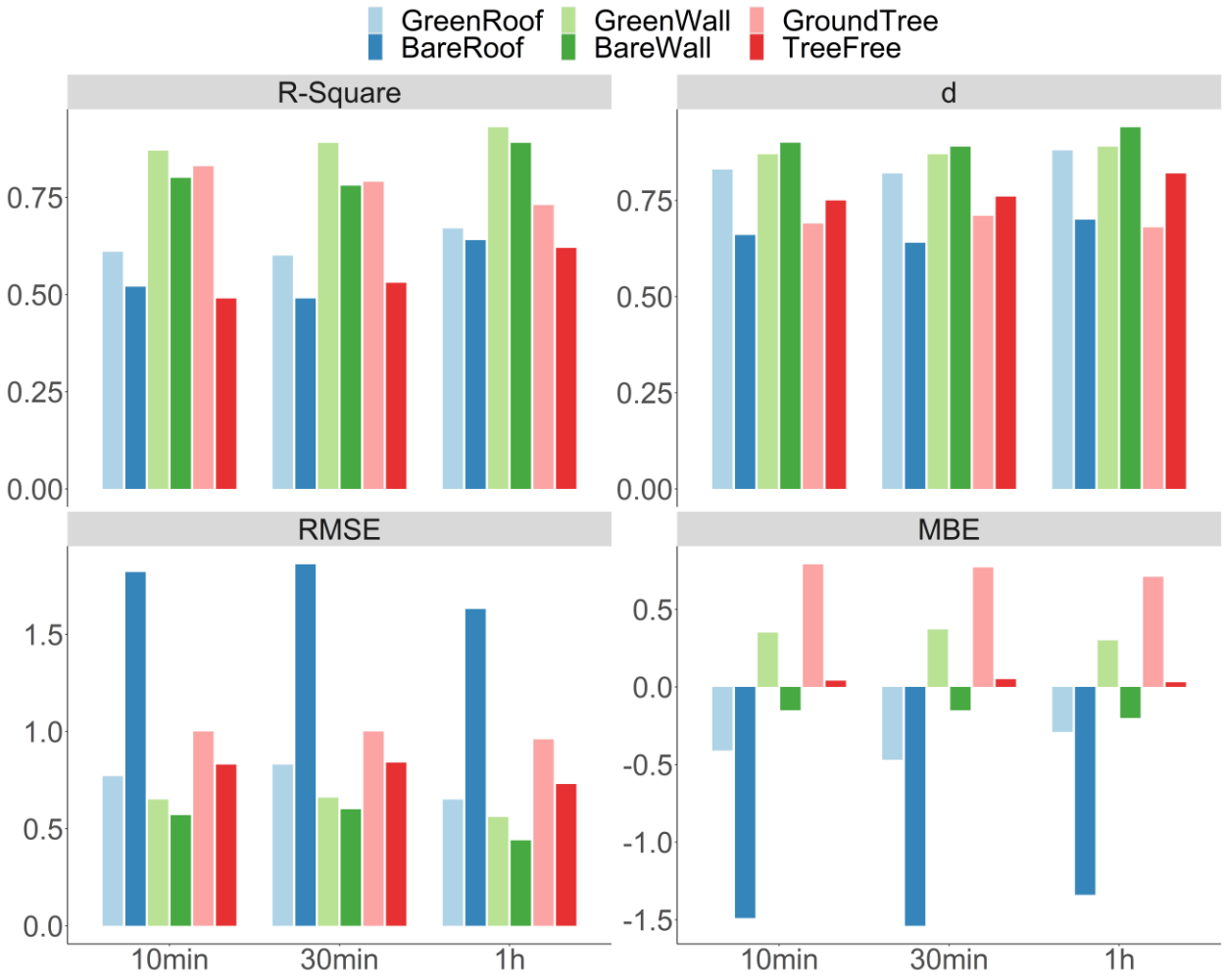

Figure 4-8: Four evaluation metrics in AT (unit of RMSE and MBE: °C).

4.3.2.2 Relative humidity

Irrespective of the output intervals and sites, the overall performance of ENVI-met for RH estimation was averaged R^2 = 0.48, d = 0.53, RMSE = 5.62 %, and MBE = −4.36 %. Three output intervals presented small variations: better performance presented by 1h interval, while the slightly inferior by 10 min (R^2 = 0.52 vs. 0.44, d = 0.54 vs. 0.52, RMSE = 5.45 vs. 5.65 %). ENVI-met underestimated RH at three output intervals (MBE = −4.40 ~ −4.30 %).

For location specific analysis, the model performance shows variability depending on the evaluation metrics (see Figure 4-9). R^2 reached the highest at BW (0.77) and the lowest at TF (0.10). d was high as 0.71 at BR, but low as 0.27 at GT. The estimation error was maximum at GT (RMSE = 8.70 %) and

minimum at BF (RMSE = 3.88 %). ENVI-met underestimated RH in all points, with MBE ranging from -0.91 % ~ -8.12 % (BF ~ GT).

Given the sensor accuracy of HOBO was ±2.5 %, ENVI-met performed well in RH estimation, except near GT. The deviation can be partly attributed to weather condition. We collected data during a typical summer day in HK, with partially cloudy conditions. One study conducted in similar hot-humid sub-tropical climate found that fully cloudy weather lead to distinct discrepancy in water vapor fluxes estimation (Liu et al., 2018).

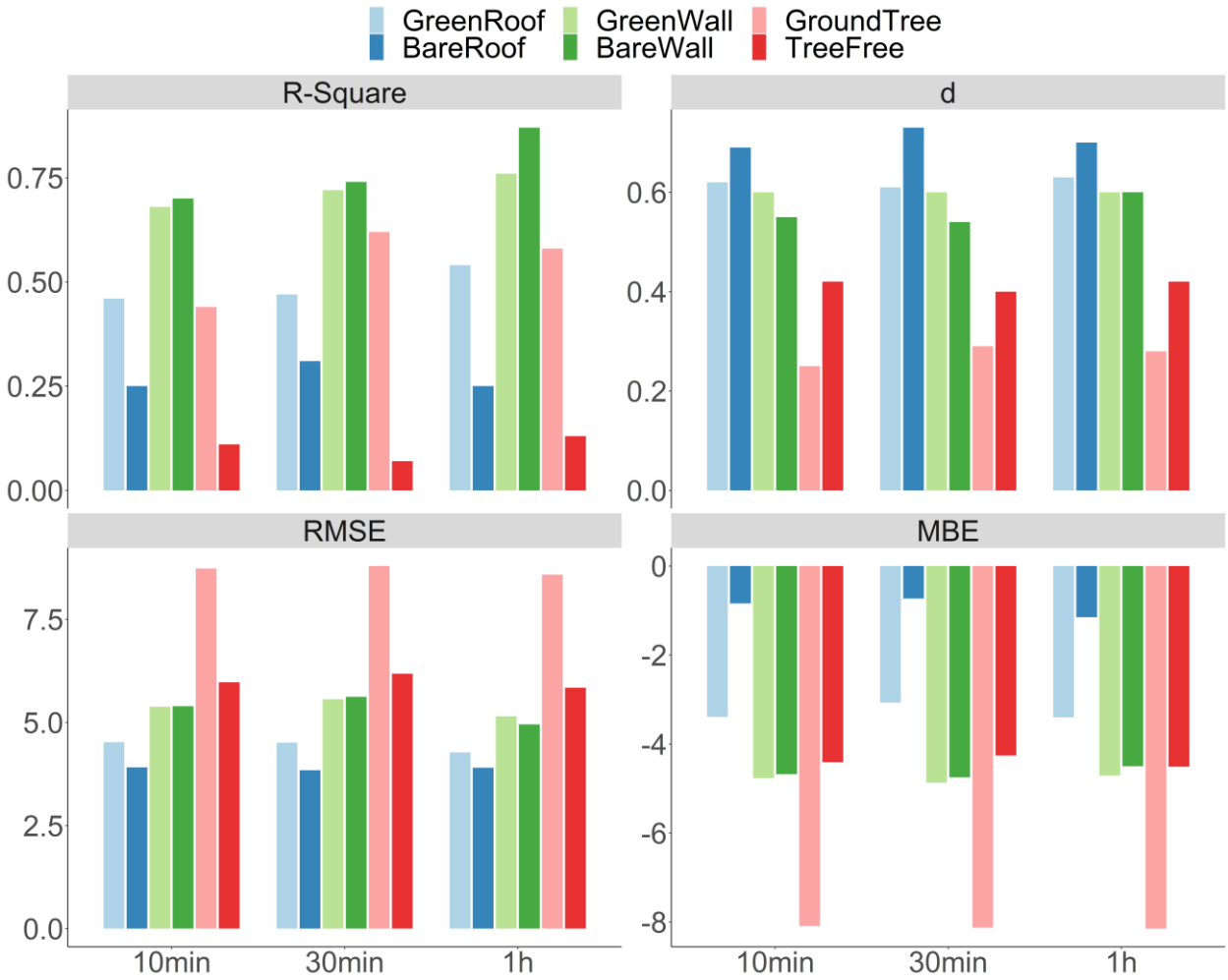

Figure 4-9: Four evaluation metrics in RH (unit of RMSE and MBE: %).

4.3.3 Evaluation in radiative variables

4.3.3.1 Mean radiant temperature

For all output intervals and sites, the average performance in MRT was described by $R^2 = 0.77$, d = 0.79, RMSE = 7.07 °C, and MBE = 4.96 °C. The differences of three output intervals were insignificant. 10min showed the highest d (0.79) and R^2 (0.79), with a relatively low RMSE (6.99 °C); 30min

performed moderately lower d (0.78) and R^2 (0.75), higher RMSE (7.12 °C). MRT was overestimated for three output intervals, with MBE = 4.89 ~ 4.99 °C.

Concerning the location-related differences, inconsistences were observed (see Figure 4-10). R^2 showed that TF had the highest value (0.87) whereas BW presented the lowest value (0.62). Based on d, except for GT with a low value as 0.37, other five sites presented 0.81 or even higher. The smallest error was presented in GT and TF sites (RMSE = 5.79 and 5.57 °C respectively), while largest error was found in GW (RMSE = 8.61 °C). According to MBE values, MRT was overestimated for all six points, ranging 1.28 ~ 7.81 °C (BW ~ GW).

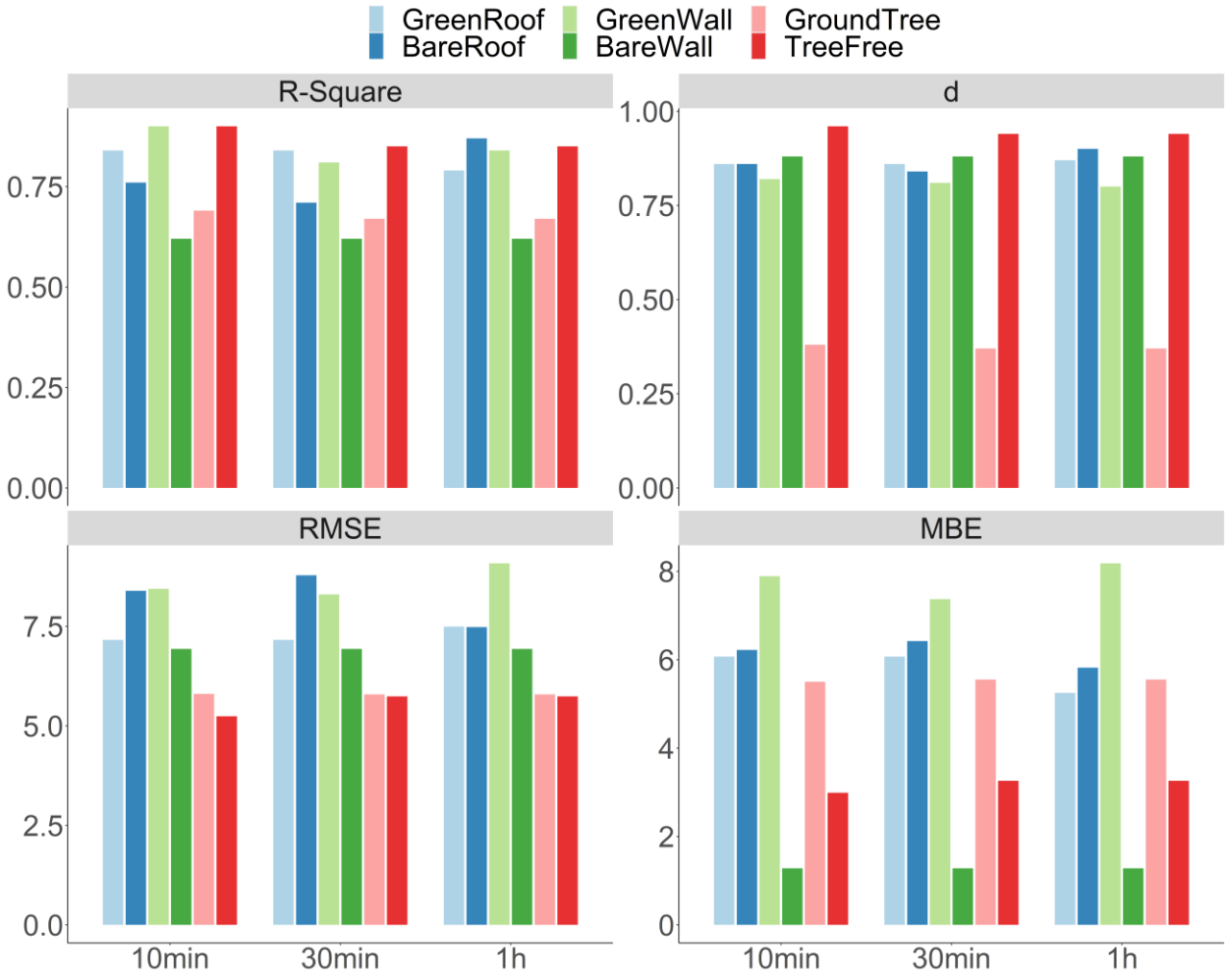

Figure 4-10: Four evaluation metrics in MRT (unit of RMSE and MBE: °C)

Although six-directional method is widely identified as the most accurate approach for MRT measurement (Chen et al., 2014; Krüger et al., 2014), the systematic errors arising from the sensors and the unsystematic errors related with experimental operation should also be considered when interpreting the above results.

4.3.3.2 Down- and upward fluxes

Shortwave fluxes

Downward shortwave radiation

In ENVI-met, downward shortwave radiation (SW_{down}) is the aggregation of diffuse shortwave radiation from sky, reflected shortwave radiation from surrounding environment, and incoming direct shortwave radiation (Huttner, 2012). Generally, the overall performance of SW_{down} was: moderate variance (R^2 = 0.52), decent agreement (d = 0.74), low bias (MBE = −18.96 W/m^2), but large deviation (RMSE = 220.44 W/m^2). Different output intervals showed minor discrepancies, 10min performed better than 30min with R^2 = 0.55 vs. 0.50, d = 0.75 vs. 0.73, and RMSE = 220.44 vs. 212.19 W/m^2. SW_{down} was underestimated marginally (MBE = −29.39 ~ −12.71 W/m^2) for three intervals.

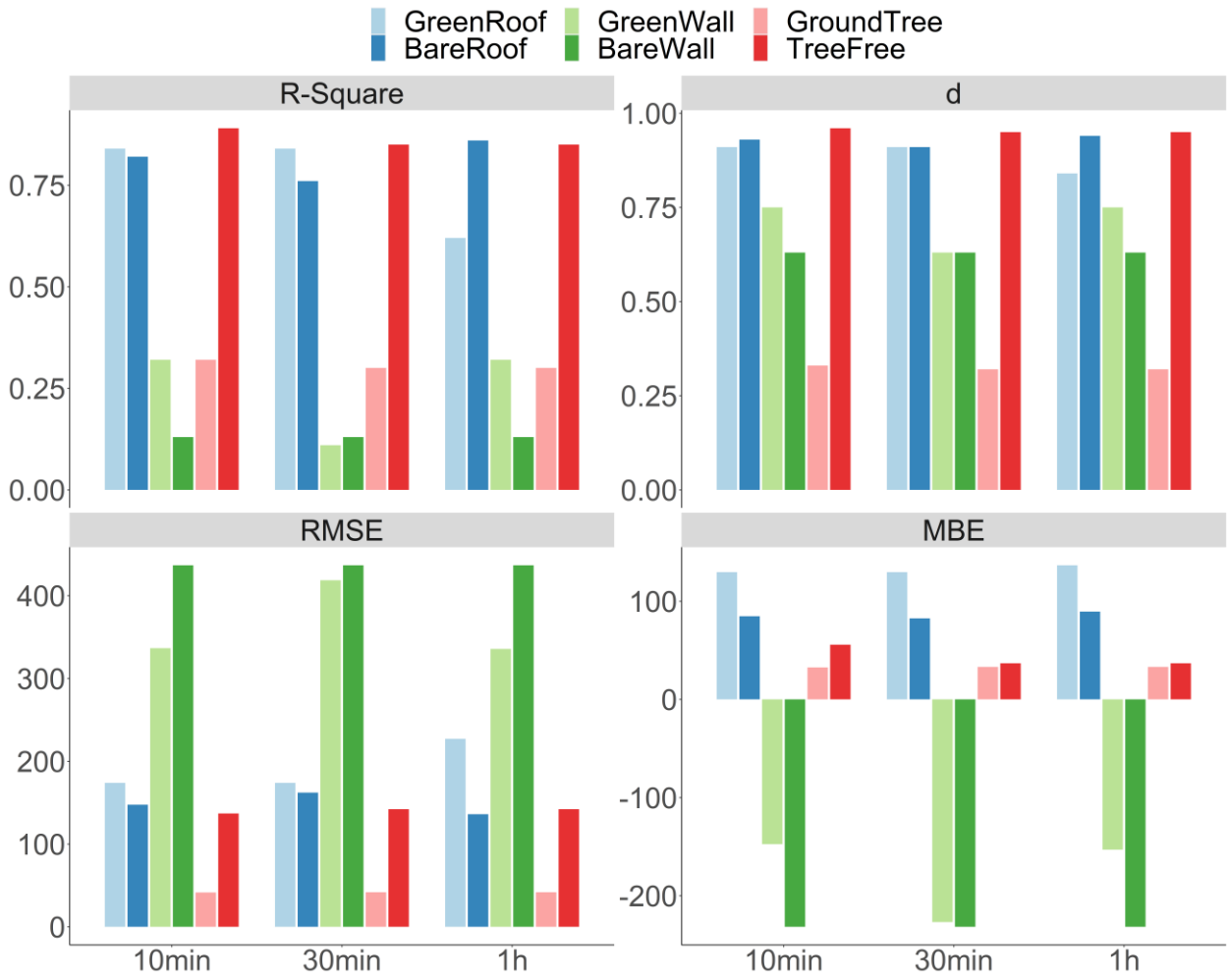

Figure 4-11: Four evaluation metrics in SW_{down} (unit of RMSE and MBE: W/m^2).

The differences among the six sites were rather complex. Quantified by R^2, TF yielded better performance (0.86), whereas BW and GW showed inferior performance (0.13 and 0.25 respectively) (see

Figure 4-11). Higher d was found at BR (0.93) and TF (0.95), while the lowest at GT (0.32). Two wall points presented large errors (RMSE = 363.67 and 436.68 W/m^2 for GW and BW) and underestimated bias (MBE = −175.77 and −231.70 W/m^2). At the other four sites, RMSE ranged 41.73 ~ 191.65 W/m^2 (GT ~ GR). Besides, there was moderately overestimation at the roof sites (MBE = 132.01 and 85.62 W/m^2 for GR and BR) and slight overestimation at GT and TF (MBE = 32.94 and 43.14 W/m^2).

There are several possible reasons to explain the discrepancies of SW_{down} estimation. As this study applied mobile measurement to collect radiative variables, unsystematic errors due to operations should be considered. The shading discrepancy was also reported in a previous study to explain the errors of radiative variables estimation (Gál and Kántor, 2020). Besides, SW_{down} is highly sensitive to building geometry in ENVI-met. This study collected the wall sites data near an arc-shaped wall. Although the model mimicked the reality to the utmost, shading errors may lead to large deviations of SW_{down} estimation. Furthermore, calculating shortwave fluxes requires segregating global solar radiation into direct and diffuse components accurately (Wang and Zacharias, 2015), which also brings some prediction deviations.

Upward shortwave radiation

ENVI-met predicted upward shortwave radiation (SW_{up}) by calculating the fraction of ground reflected shortwave radiation over the overall incoming shortwave radiation (Huttner, 2012). Throughout all output intervals and points, SW_{up} was predicted reasonably with averaged R^2 = 0.58, d = 0.79, RMSE = 26.25 W/m^2, and MBE = −11.37 W/m^2. Minor differences were found among three output intervals, but 1h outperformed in d = 0.81, R^2 = 0.61, and RMSE = 25.31 W/m^2.

Figure 4-12 showed the performances for six locations, with the highest R^2 in GR (0.80), the best d in two roof points (0.91) and TF (0.92). GT showed the lowest error and bias (RMSE = 5.98 W/m^2 and MBE = 4.02 W/m^2), yet the lowest R^2 = 0.05. Furthermore, ENVI-met tended to underestimate SW_{up} in GR (MBE = −11.00 W/m^2), two wall points (−17.31 and −39.33 W/m^2 for GW and BW), and TF (−5.34 W/m^2), but overestimate SW_{up} marginally in GT (4.02 W/m^2). MBE of BR was close to zero (0.75 W/m^2).

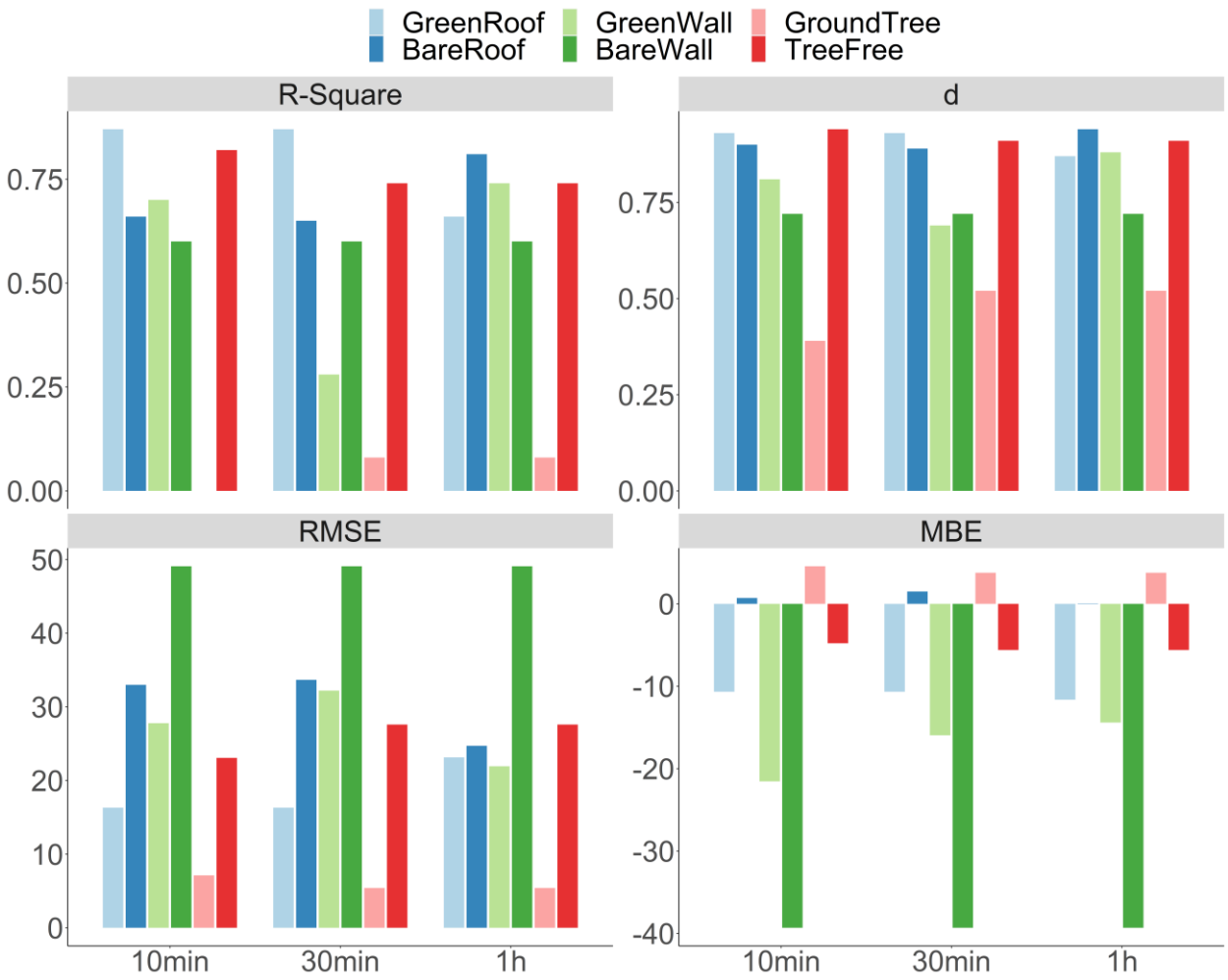

Figure 4-12: Four evaluation metrics in SW_{up} (unit of RMSE and MBE: W/m^2).

With IVS scheme on, ENVI-met no longer estimated SW_{up} based on domain-wide mean albedo like previous versions, which largely improved the estimation performance (Simon et al., 2021). However, the intra-domain prediction deviations for multiple points are worth attention.

Longwave fluxes

Downward longwave radiation

In ENVI-met, downward longwave radiation (LW_{down}) consisted of emitted radiations from the sky, surrounding vegetation and buildings, as well as reflected radiations from buildings. Overall, for all output intervals and points, LW_{down} estimation was measured by relatively low d (= 0.38) and R^2 (= 0.30), low error (RMSE = 19.34 W/m^2) and bias (MBE = 13.89 W/m^2). Trivial variances were found for three output intervals: 10min yielded better performance with higher R^2 (0.36) and d (0.40), lower MBE (13.68 W/m^2), while 1h underperformed with a marginally higher error (RMSE = 19.78 W/m^2) and bias (MBE = 14.27 W/m^2).

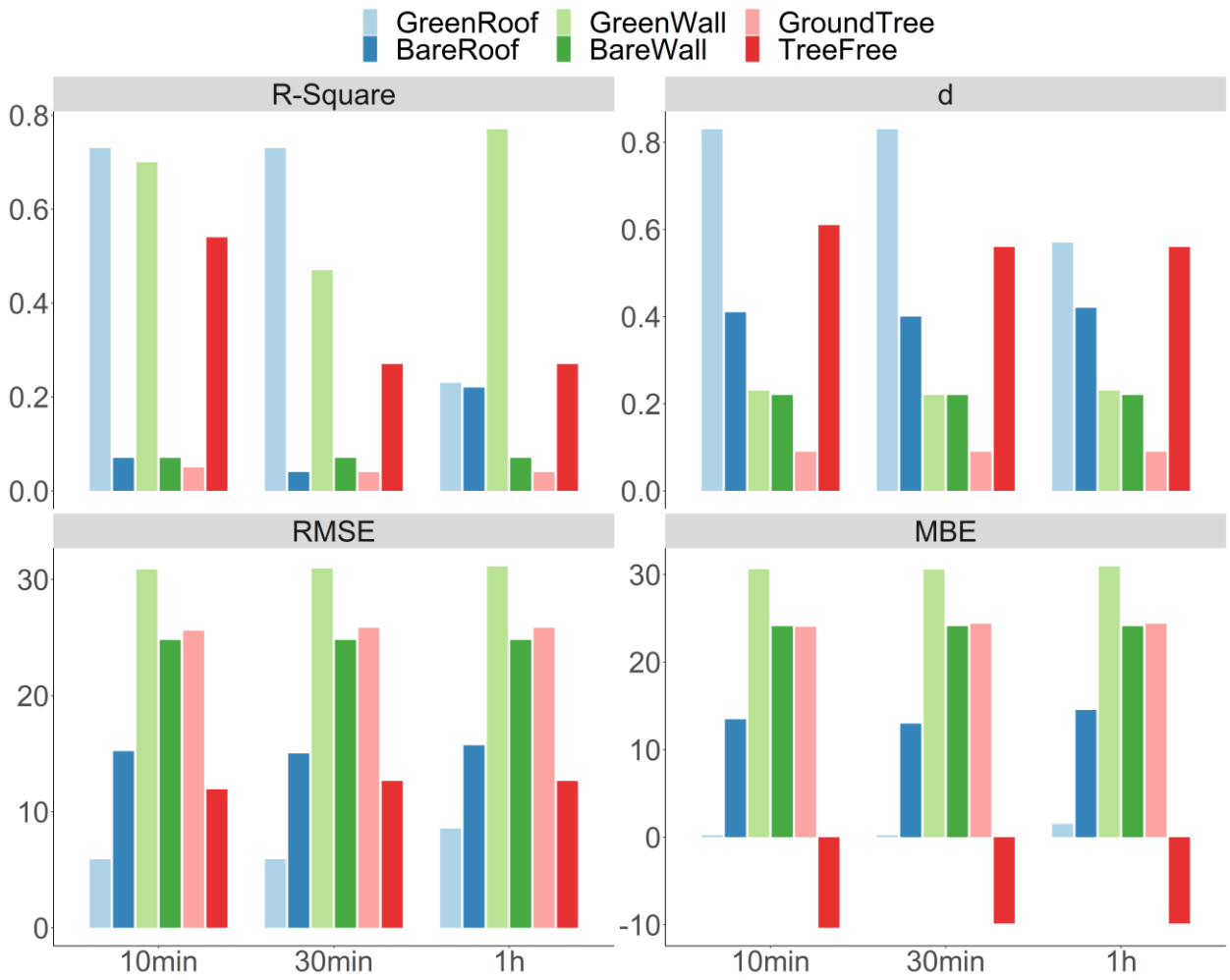

Figure 4-13: Four evaluation metrics in LW_{down} (unit of RMSE and MBE: W/m^2).

About six sites (shown in Figure 4-13), ENVI-met underpredicted LW_{down} for TF site (MBE = −10.03 W/m^2), while overpredicted LW_{down} for the remaining five sites (MBE = 0.64 ~ 30.71 W/m^2). The implications of R^2 and other three metrics were reverse for BR, GW, and TF points. For example, GW showed a reasonable R^2 (0.65), yet relatively low d (0.23); BR had a relatively high d (0.41), but low R^2 (0.11).

The rather poor estimation of LW_{down} in two wall points can also be attributed to the arch-shaped wall described in Section 3.3.2 already. The deviations of LW_{down} in ground tree were partially explained by the shading effects of the canopy and surrounding buildings, estimation errors of leave surface temperature, and imperfect tree shape modelling and LAD values.

Upward longwave radiation

Upward longwave radiation (LW_{up}) was mainly dependent on the ground emitted radiations (Morakinyo et al., 2019). For all output intervals and sites, LW_{up} was reasonably predicted with R^2 = 0.74, d = 0.59,

RMSE = 29.68 W/m^2, and MBE = 15.53 W/m^2. As for output intervals, 10min outperformed with highest R^2 (0.78) and d (0.60), and lowest RMSE (29.07 W/m^2), while 1h showed the lowest MBE (15.45 W/m^2).

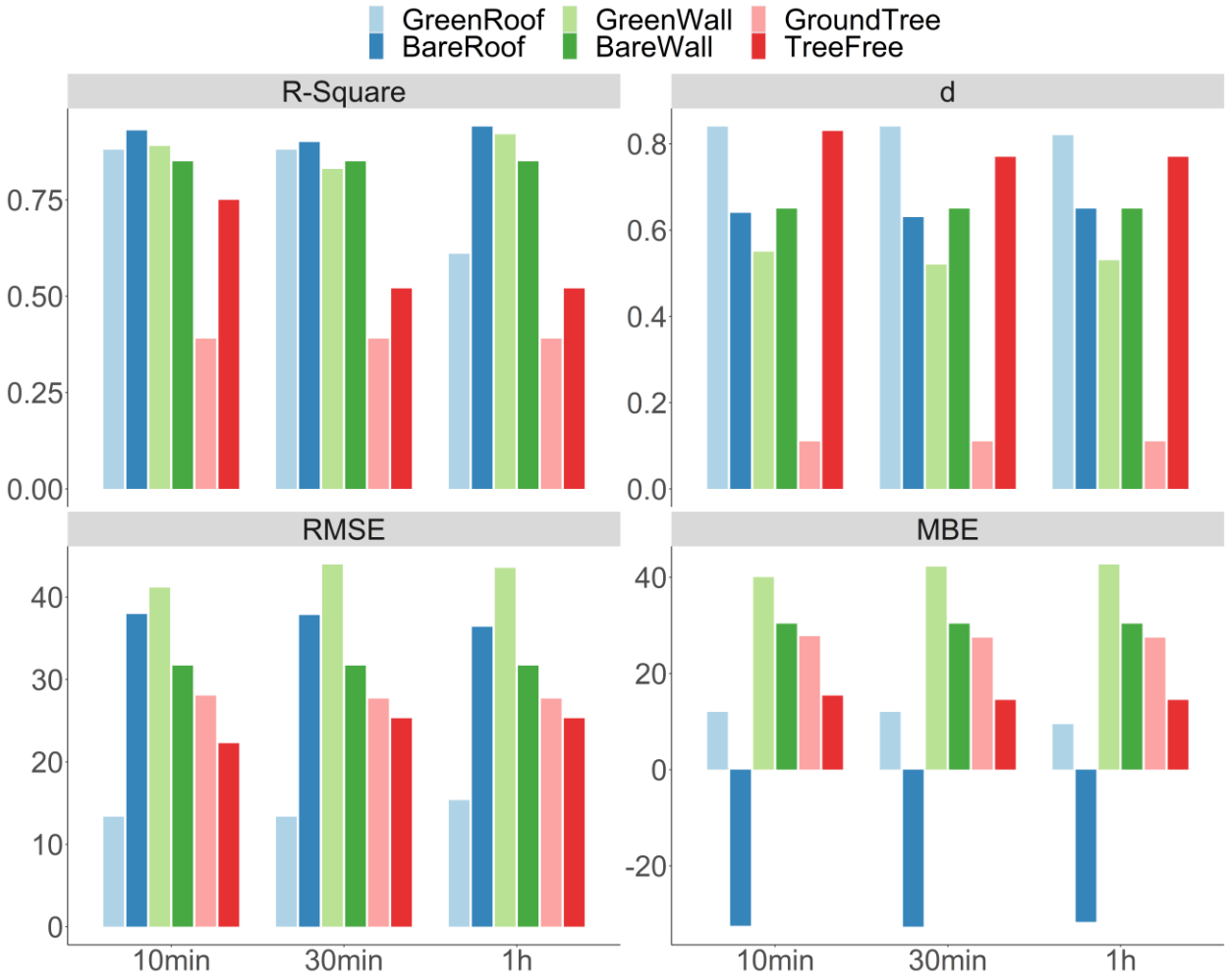

Figure 4-14: Four evaluation metrics in LW_{up} (unit of RMSE and MBE: W/m^2).

Concerning six points, BR presented the highest R^2 (0.92), when GR outperformed with the highest d (0.83), lowest error (RMSE = 14.03 W/m^2) and bias (MBE = 11.15 W/m^2). As depicted in Figure 4-14, GW showed the largest errors (RMSE = 42.87 W/m^2) and highest bias (MBE = 41.62 W/m^2) among the six sites. Besides, GT showed a lowest d (0.11) and R^2 (0.39). ENVI-met underestimated LW_{up} at BR (MBE = −32.27 W/m^2), and overestimated LW_{up} in the remaining sites with MBE = 11.15 ~ 41.62 W/m^2. Three output intervals for six points demonstrated almost consistent performances, except in TF. TF outperformed in 10min with larger R^2 and d, and lower RMSE and MBE.

ENVI-met V4.4.6 estimated the upwelling longwave fluxes based on the seen view facets through IVS scheme, rather than the average surface temperature in the domain in the previous versions (Simon et al., 2021). This apparently improved the LW_{up} radiation estimation, compared with previous study (Gál and Kántor, 2020).

4.3.3.3 Incoming and outgoing longwave fluxes near walls

Incoming longwave fluxes

Incoming longwave radiation (LW_{in}) involves the longwave radiation emitted by atmosphere and vegetation, and reflected by surrounding buildings towards the walls (Huttner, 2012). Summarizing all output intervals and wall points, LW_{in} was estimated with high R^2 (0.80) and moderate d (0.36), low errors (RMSE = 21.74 W/m^2) and bias (MBE = 10.61 W/m^2). Regarding output intervals, little difference was found, especially between 10min and 1h: R^2 = 0.81 vs. 0.78, d = 0.37 vs. 0.36, RMSE = 21.74 vs. 21.71 W/m^2, and MBE = 10.62 vs. 10.69 W/m^2.

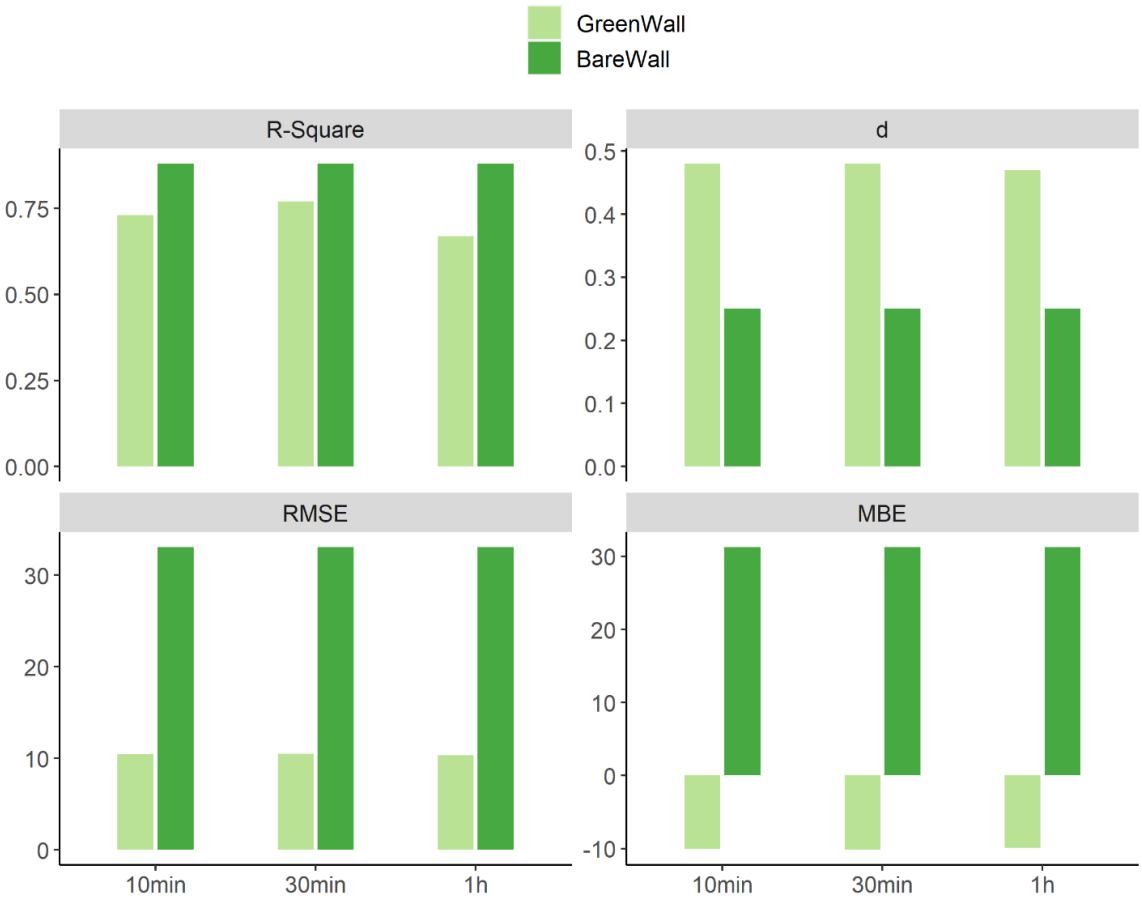

Figure 4-15: Four evaluation metrics in LW_{in} (unit of RMSE and MBE: W/m^2).

For two wall points, R^2 was high (0.72 and 0.88 for GW and BW, respectively) (see Figure 4-15). Irrespective of output intervals, BW presented a higher d than GW (0.48 vs. 0.25), while GW outperformed with a lower RMSE (10.43 vs. 33.05 W/m^2). Moreover, ENVI-met tended to overestimate the LW_{in} near BW (MBE = 31.25 W/m^2) and underestimate LW_{in} the near GW (MBE = $-10.02 W/m^2$).

Outgoing longwave fluxes

Outgoing longwave fluxes (LW_{out}) represent the longwave radiation emitted and reflected by the walls towards the atmosphere. Across all output intervals and wall points, LW_{out} averagely presented low R^2 (0.49), reasonable d (0.61), RMSE (25.96 W/m^2) and MBE (-19.82 W/m^2). The differences among output intervals were insignificant: the same value of d (0.61), RMSE = 25.83 ~ 26.07 W/m^2, MBE = $-19.87 \sim -19.75$ W/m^2, while R^2 showed moderately larger range at 0.36 ~ 0.59.

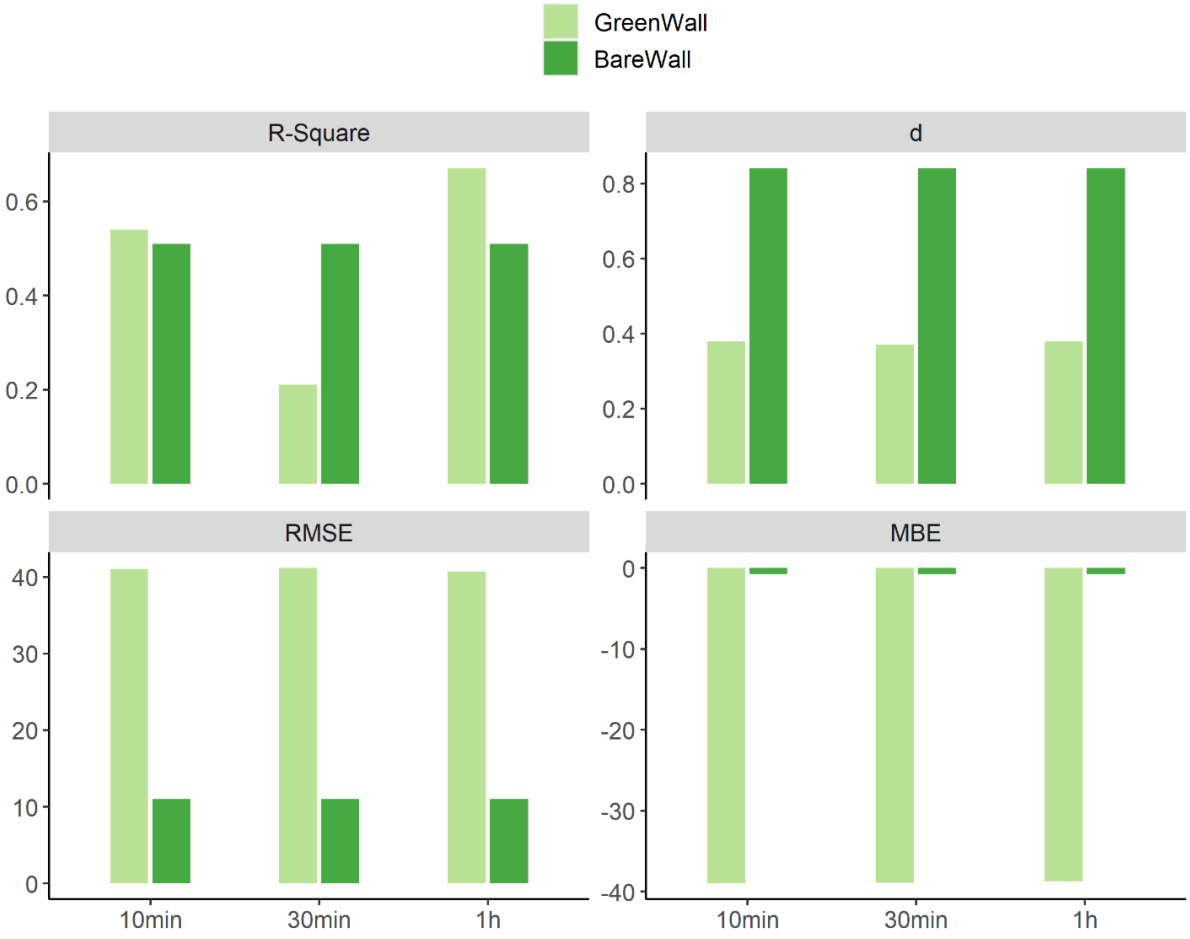

Figure 4-16: Four evaluation metrics in LW_{out} (unit of RMSE and MBE: W/m^2).

Regarding two wall points, similar with LW_{in}, d was lower for GW and higher for BW (0.38 vs. 0.84), which was consistent for three output intervals (see Figure 4-16). BW presented a slightly higher R^2

than GW (0.51 vs. 0.47), yet had a lower RMSE (10.98 vs. 40.94 W/m^2). ENVI-met overestimated LW_{out} for both wall sites, with MBE = −0.74 ~ −38.90 W/m^2 for BW ~ GW.

4.4 Discussion

4.4.1 ENVI-met performance and evaluation metrics

According to previous studies of ENVI-met evaluation, as summarized in Table 4-4, thermal variables were investigated mostly. AT was evaluated in all listed studies and generally performed reasonably with high R^2 and low errors. Humidity was quantified by different variables, i.e., relative humidity, absolute humidity, and specific humidity, which makes inter-comparison an intricate task. Radiative variables, especially longwave and shortwave fluxes in different directions, were less investigated. MRT, as a significant variable for outdoor thermal comfort, showed larger variations than AT and RH. One possible reason is that MRT fluctuates widely towards solar radiation and the surrounding environment, which may not be explicitly mimicked by ENVI-met, especially when a coarse model is compared with a finer reference data (Gál and Kántor, 2020).

This study evaluated and compared the thermal-radiative performance of ENVI-met in six points, including three GI typologies and corresponding reference sites. The results indicated that the prediction capability of ENVI-met varied among different variables and sites. For different variables, ENVI-met performed better in estimating thermal variables with average R^2 (0.70 and 0.48 for AT and RH) and d (0.79 and 0.53 respectively), low errors (RMSE = 0.91 °C and 5.62 % respectively) and bias (MBE = −0.15°C and −4.36 % respectively). The performance of radiative variables was not consistent. As MRT was most accurately estimated (R^2 = 0.77, d = 0.79, RMSE = 7.07 °C, MBE = 4.96 °C), SW_{down} was estimated with the largest deviations with R^2 = 0.52, d = 0.74, RMSE = 220.44 W/m^2, MBE = -18.96 W/m^2. Concerning six sites, ENVI-met responded differently, i.e., ground or roof level, with or without greening, with different GI typologies. Two roof points exerted higher errors than ground sites when estimating AT and MRT (RMSE = 0.75 ~ 1.77°C for AT, 7.27 ~ 8.22°C for MRT, all above the average values). Current literature scarcely provided similar evidence supported by measurement data, a study validated ENVI-met and found slightly lower errors than our study (RMSE = 1.07 ~ 1.21 °C for AT, 4.27 ~ 6.13 % for RH) (Jin et al., 2018), see in Table 4-5. One parametric study without field measurement claimed that ENVI-met should be used with caution for roof-level mitigation strategies (Crank et

al., 2018). The reason lies in the grid-dependence at roof level, so that errors and uncertainties were introduced albeit less than the effects of mitigation strategies. This partly explained the large errors at roof level observed in our study, as in ENVI-met, the grid resolution at roof level cannot be refined into five sub-grids like the lowest cell on ground level. Regarding wall points, compared with a previous study that measured both bare and green walls and then evaluated the simulation results (Jänicke et al., 2015), our study revealed similar error range in MRT (RMSE = 6.93 ~ 8.61 °C vs. 7.98 ~ 8.30 °C for our study and reference study respectively), but smaller deviations in LW_{down} (24.79 ~ 30.98 W/m^2 vs. 115.27 ~ 209.60 W/m^2) and SW_{up} (27.30 ~ 49.08 W/m^2 vs. 61.86 ~ 87.12 W/m^2). These values indicated that the MRT discrepancies in our study mainly came from solar radiation deviations, while the solar radiation errors arose from the complex geometry of walls, as well as the mismatch between coarse model and finer reference data, which has been explained in Section 3.3.1. In terms of ground points with and without trees, our study revealed smaller error ranges than related studies (Crank et al., 2020; Gál and Kántor, 2020; Jamei et al., 2019; Liu et al., 2018; Shinzato et al., 2019). Involving new ACRT module, TF site in our study performed better than similar site in another study in subtropical climate background, with the errors of AT (RMSE = 0.80 vs. 1.13 °C in our study and reference study) and SW_{down} (RMSE = 140.36 vs. 185.52 W/m^2). Moreover, GT site showed much better results. Comparing with studies in subtropical humid climate and arid climate (Crank et al., 2020; Liu et al., 2018), our study showed smaller errors in AT (RMSE = 0.99 °C vs. 3.97 °C for our study and reference study respectively), MRT (RMSE = 5.79 °C vs. 10.97 ~ 18.13 °C), and SW_{down} (RMSE = 41.73 vs. 242.15 W/m^2). This indicates the new Advanced Canopy Radiation Transfer (ACRT) module improves the estimations of microclimate parameters in canopies (Simon et al., 2020).

Concerning evaluation metrics, some studies only used R^2 for model evaluation and validation (Kyriakodis and Santamouris, 2017; Morakinyo et al., 2019, 2017b, 2016; Müller et al., 2014; Tan et al., 2016; Wang et al., 2016; Wang and Zacharias, 2015). Our study revealed variable results by different evaluation metrics, which indicated that single evaluation metric may limit our overall understanding of the model performance. In accordance with the suggestions in previous studies (Liu et al., 2021; Stunder and Sethuraman, 1986; Willmott, 1982), we underscored the necessary to apply multiple metrics for model evaluation and validation in the future.

4.4.2 ENVI-met settings for localized context

To evaluate recent updates of ENVI-met, this study compared the impacts of different model settings on the model performance of ENVI-met, including four aspects: IVS module, meteorological boundary conditions, materials, and output intervals. Our results indicated that the newly implemented IVS scheme yielded higher accuracy and faster speed at the cost of higher requirement in RAM requirement. It significantly decreased the errors of radiation fluxes in $SW_{down,}$ LW_{down}, and LW_{out}, especially for GW and GT sites. Besides, we found that radiation forcing and localized materials settings are essential to improve the overall model performance. Since radiation forcing requires detailed information in direct and diffuse radiations, simple forcing scheme with adjusted solar factors or cloud forcing with cloud amounts (in oktas unit) is usually an alternative in previous studies. However, our study found that solar factor adjustment in simple forcing may improve the performance in some variables, i.e., SW_{up}, SW_{down}, and LW_{in}, but decreased the estimation accuracy in AT. This was also discussed in a previous study that solar factor adjustment has both conceptual and implementation limitations (Gál and Kántor, 2020). Cloud forcing performed better than simple forcing with adjusted solar factors, yet inferior to the radiation forcing. Regarding materials settings, the default parameters in ENVI-met are not necessarily applicable to anywhere considering that building materials and features are diverse in different regions (Roth and Lim, 2017). This study compared the model predictions using the default and localized parameters in materials, and confirmed the necessity to localize the material parameters for buildings, vegetation and soil. In terms of output intervals, little differences existed among three temporal scales, especially between 10min and 1h intervals. This result justified that the mobile measurement could be used for ENVI-met model validation, if the measuring instruments fulfill the requirement of accuracy and prevision, and the measurement scheme is scientifically designed.

It is important to note that different variables and locations/ sites responded differently towards the model settings. Therefore, if any variable or location needs to be targeted or prioritized, the model settings should be tuned based on research objectives. If there are many targeted locations or variables, some compromises may be made in necessary to ensure a balanced performance.

4.4.3 Significance and implications of this study

Model evaluation is an essential process for model developers, users, and policy practitioners to gain awareness in the limitations and uncertainties of a specific model. Based on the evaluation results, the model can be improved, invalid conclusions can be avoided, and effective strategies can be developed (Jakeman et al., 2006). To the best of our knowledge, this study is a first attempt to have a systematic evaluation for the updates in latest version ENVI-met (V4.4.6). Our study also contributes by evaluating the thermal-radiative performance of ENVI-met for three GI typologies simultaneously. Experience of this study is focused on a typical subtropical city; thus, the findings of this study could be transferred to other cities in similar climate background.

For model developers, our study indicated that the latest version of ENVI-met model performed better based on IVS scheme, detailed full forcing scheme, and new ACRT module. Hereafter, potential improvements are expected to provide users flexible selections and detailed instructions in settings. The inputs of cloud forcing need low, medium, and high levels of cloud amounts, when the inputs of radiation forcing need downward direct and diffuse shortwave radiation and downward direct longwave radiation. As weather stations may only provide total cloud amount or global solar radiation (Weihs et al., 2012), introducing a subdivision module for solar radiation and cloud amount would be a convenience for users. Besides, MRT calculation in ENVI-met is different with other models (e.g., RayMan, SOLWEIG) regarding the shape of the standing man (Holmer et al., 2018), therefore it should be helpful for users to select body shape factors based on the research objective. In addition, ENVI-met is deficient in refining mesh for rooftop level, thus leading to larger errors at rooftop than on ground (Crank et al., 2018). In order to further investigate the rooftop mitigation strategies, the introduction of vertical mesh refinement in roof level would be very welcomed.

For urban climate researchers, model evaluation and validation are necessary before further applications (Liu et al., 2021). According to a comprehensive review of ENVI-met validation studies (Tsoka et al., 2018), only 54.74 % (52 out of 92 selected studies) have reported the evaluation and validation results. Even among those validated studies, most of them only assessed AT. Other microclimate variables were lacking validation despite of their importance in outdoor thermal comfort and indoor energy saving studies, i.e., only 30.77 % assessed MRT prediction, 19.23 % validated RH and surface temperature

estimation, and 9.62 % evaluated wind speed performance (Tsoka et al., 2018). Given these case studies are featured with different background climate, building morphology, surface characteristics, etc., the validation and evaluation results are not transferable among sites. Therefore, it is necessary to validate the model for the targeted research objectives. This study also underscores the necessity of localizing settings regarding the surface features and vegetation characteristics.

For urban planners and policy practitioners, our study can provide valuable information in comprehensive evaluation of ENVI-met performance. Better interpretations in the simulation results are based on a full understanding of both strengths and limitations of the model, so that the planning strategies and policies making can be tailored based on scientific evidence.

4.4.4 Limitations and further studies

The following limitations of this study should be noted for a better interpretation. First, this study took stationary measurement to collect thermal variables and mobile measurement to obtain radiative variables. Although the differences between 10min and 1h output intervals were little, future studies could take stationary measurements for radiative variables and compare the results with our study. Second, this study only focused on daytime as the outdoor activities are more intense during diurnal periods. However, considering nighttime UHI phenomenon is even severer, evaluating how ENVI-met model performs in the nocturnal periods is another possible direction. Third, our study was taken in a typical subtropical climate city, whose results may be confined within the cities in similar climate backgrounds. More comprehensive evaluation studies are welcomed in different climate backgrounds. Another important perspective is about the impacts of meteorological conditions on ENVI-met (Acero and Arrizabalaga, 2018). There is also the need to standardize the distance between weather station for acquiring forcing data and study area. Running nested simulations may be a promising alternative when the distance is too far (Simon et al., 2018a). Besides, model inter-comparison with other widely used models, i.e., SOLWEIG, RayMan, also needs follow-up studies (Crank et al., 2020; Gál and Kántor, 2020).

4.5 Conclusion

In the coming decades, sustainable urban planning and design will face more intense challenges in the context of climate change and urban overheat. Numerical modelling is a powerful tool to aid urban

planners and managers in advancing climate mitigation strategies. ENVI-met, as a microclimate CFD-based model, has been widely used to support climate-sensitive planning. One of the main hypotheses of this kind of application is to interpret the simulation results correctly and comprehensively.

This study was motivated to provide a systematic evaluation of the recent updates of ENVI-met. Besides, how is the performance of ENVI-met to simulate three GI typologies simultaneously is another main focus. Sensitivity analyses were conducted for the inputs and settings of ENVI-met, including new radiation calculation IVS scheme (on and off), meteorological conditions (simple, cloud and radiation forcing), construction surface properties and plant parameters (default and localized settings), and output intervals (10min, 30min, 1h). Model evaluation was conducted for three GI typologies, nine thermal-radiative parameters, and three output intervals. The simulation results were compared with the data derived from the field measurement based on four evaluation metrics. According to the results, following aspects can be summarized:

- For ENVI-met model settings, models delivered the best performance with full forcing and localized materials. Therefore, localization is necessary for both meteorological boundary conditions and materials. Radiation forcing should be prioritized, while cloud forcing could be alternative if the radiation inputs cannot be acquired. Simple forcing with adjusted solar factors should be avoided in the applications. Moreover, IVS module can improve the model's reliability in estimating radiative variables with around 15 % faster speed, although it required higher RAM usage.
- For ENVI-met model performance regarding spatial locations, the model can reproduce different thermal-radiative characteristics among the GI typologies simultaneously, while presenting lower errors on ground sites than at rooftop sites.
- For ENVI-met model performance regarding temporal output intervals, the simulation differences were insignificant, which justified using mobile measurement in model validation on the premise that the measurement campaign is carefully designed.
- For ENVI-met model performance regarding variables, AT and MRT were estimated by ENVI-met with satisfied accuracy, while remaining thermal-radiative variables were reasonably

estimated. The prediction of radiative variables was improved by the IVS scheme, and the precision of in-canopy radiation was enhanced by the ACRT module. The accuracy of downward shortwave radiation was highly dependent on the radiative interactions of buildings, plants, and atmosphere, which further affected MRT significantly. Thus, regular-shaped buildings are more recommended for evaluation/ validation-oriented measurement.

- For ENVI-met model performance regarding evaluation metrics, the simulation results were sensitive to the metrics. Multiple metrics are suggested in future studies for model validation.

This study emphasized the significance of ENVI-met model valuation before further applications. Radiation forcing and localized settings are necessary to obtain a reliable model. The results of this study indicate the potential directions for model improvement. Besides, this study also helps model users distinguish both the capabilities and limitations of ENVI-met, so that the model result interpretation can be strengthened and urban planning and design strategies can be advanced based on scientific evidence.

4.6 Acknowledgements

This study is supported by a postgraduate studentship and the "3rd round Vice-Chancellor's Discretionary Fund" from the Chinese University of Hong Kong, and the RGC research grant (No. 14617220) from the Research Grants Council (RGC) of Hong Kong.

4.7 References

Abdi, B., Hami, A., Zarehaghi, D., 2020. Impact of small-scale tree planting patterns on outdoor cooling and thermal comfort. Sustainable Cities and Society 56, 102085. https://doi.org/10.1016/j.scs.2020.102085

Acero, J.A., Arrizabalaga, J., 2018. Evaluating the Performance of ENVI-Met Model in Diurnal Cycles for Different Meteorological Conditions. Theoretical and Applied Climatology 131, 455–469. https://doi.org/10.1007/s00704-016-1971-y

Acero, J.A., Herranz-Pascual, K., 2015. A comparison of thermal comfort conditions in four urban spaces by means of measurements and modelling techniques. Building and Environment 93, 245–257. https://doi.org/10.1016/j.buildenv.2015.06.028

Acero, J.A., Koh, E.J.Y., Li, X., Ruefenacht, L.A., Pignatta, G., Norford, L.K., 2019. Thermal impact of the orientation and height of vertical greenery on pedestrians in a tropical area. Build. Simul. 12, 973–984. https://doi.org/10.1007/s12273-019-0537-1

Arnfield, A.J., 2003. Two Decades of Urban Climate Research: A Review of Turbulence, Exchanges of Energy and Water, and the Urban Heat Island. International Journal of Climatology 23, 1–26.

Berardi, U., 2016. The outdoor microclimate benefits and energy saving resulting from green roofs retrofits. Energy and Buildings 121, 217–229. https://doi.org/10.1016/j.enbuild.2016.03.021

Burton, E., 2002. Measuring Urban Compactness in UK Towns and Cities. Environ Plann B Plann Des 29, 219–250. https://doi.org/10.1068/b2713

Chen, Y.-C., Lin, T.-P., Matzarakis, A., 2014. Comparison of mean radiant temperature from field experiment and modelling: a case study in Freiburg, Germany. Theor Appl Climatol 118, 535–551. https://doi.org/10.1007/s00704-013-1081-z

Crank, P.J., Middel, A., Wagner, M., Hoots, D., Smith, M., Brazel, A., 2020. Validation of seasonal mean radiant temperature simulations in hot arid urban climates. Science of The Total Environment 749, 141392. https://doi.org/10.1016/j.scitotenv.2020.141392

Crank, P.J., Sailor, D.J., Ban-Weiss, G., Taleghani, M., 2018. Evaluating the ENVI-met microscale model for suitability in analysis of targeted urban heat mitigation strategies. Urban Climate 26, 188–197. https://doi.org/10.1016/j.uclim.2018.09.002

Development Bureau and Planning Department Hong Kong, 2016. Hong Kong 2030+: Towards a planning vision and strategy transcending 2030.

Eliasson, I., 2000. The use of climate knowledge in urban planning. Landscape and Urban Planning 48, 31–44. https://doi.org/10.1016/S0169-2046(00)00034-7

ENVI-met, 2019. Features: Green & Blue Technologies [WWW Document]. URL https://www.envi-met.com/features/ (accessed 3.18.20).

ENVI-met, 2018. New Features Winter-Release 2018/2019 [WWW Document]. URL https://www.envi-met.com/wp-content/uploads/2019/07/ENVI-met-new-features-winter-release-2018.pdf (accessed 3.18.20).

Fox, D.G., 1981. Judging Air Quality Model Performance: A Summary of the AMS Workshop on Dispersion Model Performance, Woods Hole, Mass., 8–11 September 1980. Bulletin of the American Meteorological Society 62, 599–609. https://doi.org/10.1175/1520-0477(1981)062<0599:JAQMP>2.0.CO;2

Gál, C.V., Kántor, N., 2020. Modeling mean radiant temperature in outdoor spaces, A comparative numerical simulation and validation study. Urban Climate 32, 100571. https://doi.org/10.1016/j.uclim.2019.100571

Holmer, B., Lindberg, F., Thorsson, S., 2018. Mean radiant temperature and the shape of the standing man. Presented at the ICUC 10, New York.

Hong Kong Buildings Department, 2016. Practice Note for Authorized Persons, Registered Structural Engineers and Registered Geotechnical Engineers APP-152 45.

Hong Kong Civil Engineering and Development Department, 2004. Greening Master Plan.

Hong Kong Observatory, 2019. Summary of Meteorological and Tidal Observations in Hong Kong.

Huttner, S., 2012. Further development and application of the 3D microclimate simulation ENVI-met (Dissertation). Johannes Gutenberg-University Mainz.

Jakeman, A.J., Letcher, R.A., Norton, J.P., 2006. Ten iterative steps in development and evaluation of environmental models. Environmental Modelling & Software 21, 602–614. https://doi.org/10.1016/j.envsoft.2006.01.004

Jamei, E., Seyedmahmoudian, M., Horan, B., Stojcevski, A., 2019. Verification of a bioclimatic modeling system in a growing suburb in Melbourne. Science of The Total Environment 689, 883–898. https://doi.org/10.1016/j.scitotenv.2019.06.399

Jänicke, B., Meier, F., Hoelscher, M.-T., Scherer, D., 2015. Evaluating the Effects of Façade Greening on Human Bioclimate in a Complex Urban Environment. Advances in Meteorology 2015, e747259. https://doi.org/10.1155/2015/747259

Jin, C., Bai, X., Luo, T., Zou, M., 2018. Effects of green roofs' variations on the regional thermal environment using measurements and simulations in Chongqing, China. Urban Forestry & Urban Greening, Wild urban ecosystems: challenges and opportunities for urban development 29, 223–237. https://doi.org/10.1016/j.ufug.2017.12.002

Kotthaus, S., Smith, T.E.L., Wooster, M.J., Grimmond, C.S.B., 2014. Derivation of an urban materials spectral library through emittance and reflectance spectroscopy. ISPRS Journal of Photogrammetry and Remote Sensing 94, 194–212. https://doi.org/10.1016/j.isprsjprs.2014.05.005

Krüger, E.L., Minella, F.O., Matzarakis, A., 2014. Comparison of different methods of estimating the mean radiant temperature in outdoor thermal comfort studies. Int J Biometeorol 58, 1727–1737. https://doi.org/10.1007/s00484-013-0777-1

Kyriakodis, G.-E., Santamouris, M., 2017. Using Reflective Pavements to Mitigate Urban Heat Island in Warm Climates - Results from a Large Scale Urban Mitigation Project. Urban Climate. https://doi.org/10.1016/j.uclim.2017.02.002

Lee, H., Mayer, H., Chen, L., 2016. Contribution of trees and grasslands to the mitigation of human heat stress in a residential district of Freiburg, Southwest Germany. Landscape and Urban Planning 148, 37–50.

Liu, Z., Cheng, W., Jim, C.Y., Morakinyo, T.E., Shi, Y., Ng, E., 2021. Heat mitigation benefits of urban green and blue infrastructures: A systematic review of modeling techniques, validation and scenario simulation in ENVI-met V4. Building and Environment 200, 107939. https://doi.org/10.1016/j.buildenv.2021.107939

Liu, Z., Zheng, S., Zhao, L., 2018. Evaluation of the ENVI-Met Vegetation Model of Four Common Tree Species in a Subtropical Hot-Humid Area. Atmosphere 9, 198. https://doi.org/10.3390/atmos9050198

Matott, L.S., Babendreier, J.E., Purucker, S.T., 2009. Evaluating uncertainty in integrated environmental models: A review of concepts and tools. Water Resources Research 45. https://doi.org/10.1029/2008WR007301

Middel, A., Krayenhoff, E.S., 2019. Micrometeorological determinants of pedestrian thermal exposure during record-breaking heat in Tempe, Arizona: Introducing the MaRTy observational platform. Science of The Total Environment 687, 137–151. https://doi.org/10.1016/j.scitotenv.2019.06.085

Mills, G., 2014. Urban climatology: History, status and prospects. Urban Climate, Measurement and modelling of the urban atmosphere in the present and the past 10, 479–489. https://doi.org/10.1016/j.uclim.2014.06.004

Mirzaei, P.A., Haghighat, F., 2010. Approaches to study Urban Heat Island – Abilities and limitations. Building and Environment 45, 2192–2201. https://doi.org/10.1016/j.buildenv.2010.04.001

Morakinyo, T.E., Dahanayake, K.W.D.Kalani.C., Adegun, O.B., Balogun, A.A., 2016. Modelling the effect of tree-shading on summer indoor and outdoor thermal condition of two similar buildings in a Nigerian university. Energy and Buildings 130, 721–732. https://doi.org/10.1016/j.enbuild.2016.08.087

Morakinyo, T.E., Dahanayake, K.W.D.Kalani.C., Ng, E., Chow, C.L., 2017a. Temperature and cooling demand reduction by green-roof types in different climates and urban densities: A co-simulation parametric study. Energy and Buildings 145, 226–237. https://doi.org/10.1016/j.enbuild.2017.03.066

Morakinyo, T.E., Kong, L., Lau, K.K.-L., Yuan, C., Ng, E., 2017b. A study on the impact of shadow-cast and tree species on in-canyon and neighborhood's thermal comfort. Building and Environment 115, 1–17. https://doi.org/10.1016/j.buildenv.2017.01.005

Morakinyo, T.E., Lai, A., Lau, K.K.-L., Ng, E., 2019. Thermal benefits of vertical greening in a high-density city: Case study of Hong Kong. Urban Forestry & Urban Greening, Green Infrastructures: Nature Based Solutions for sustainable and resilient cities 37, 42–55. https://doi.org/10.1016/j.ufug.2017.11.010

Morakinyo, T.E., Lau, K.K.-L., Ren, C., Ng, E., 2018. Performance of Hong Kong's common trees species for outdoor temperature regulation, thermal comfort and energy saving. Building and Environment 137, 157–170. https://doi.org/10.1016/j.buildenv.2018.04.012

Morakinyo, T.E., Ouyang, W., Lau, K.K.-L., Ren, C., Ng, E., 2020. Right tree, right place (urban canyon): Tree species selection approach for optimum urban heat mitigation - development and evaluation. Science of The Total Environment 719, 137461. https://doi.org/10.1016/j.scitotenv.2020.137461

Moriasi, D.N., Arnold, J.G., Van Liew, M.W., Bingner, R.L., Harmel, R.D., Veith, T.L., 2007. Model evaluation guidelines for systematic quantification of accuracy in watershed simulations. Transactions of the ASABE 50, 885–900.

Müller, N., Kuttler, W., Barlag, A.-B., 2014. Counteracting urban climate change: adaptation measures and their effect on thermal comfort. Theor Appl Climatol 115, 243–257. https://doi.org/10.1007/s00704-013-0890-4

Ng, E., Chen, L., Wang, Y., Yuan, C., 2012. A study on the cooling effects of greening in a high-density city: An experience from Hong Kong. Building and Environment 47, 256–271. https://doi.org/10.1016/j.buildenv.2011.07.014

Ouyang, W., Morakinyo, T.E., Ren, C., Liu, S., Ng, E., 2021. Thermal-irradiant performance of green infrastructure typologies: Field measurement study in a subtropical climate city. Science of The Total Environment 764, 144635. https://doi.org/10.1016/j.scitotenv.2020.144635

Ouyang, W., Morakinyo, T.E., Ren, C., Ng, E., 2020. The cooling efficiency of variable greenery coverage ratios in different urban densities: A study in a subtropical climate. Building and Environment 174, 106772. https://doi.org/10.1016/j.buildenv.2020.106772

Peng, L.L.H., Jiang, Z., Yang, X., He, Y., Xu, T., Chen, S.S., 2020a. Cooling effects of block-scale facade greening and their relationship with urban form. Building and Environment 169, 106552. https://doi.org/10.1016/j.buildenv.2019.106552

Peng, L.L.H., Jiang, Z., Yang, X., Wang, Q., He, Y., Chen, S.S., 2020b. Energy savings of block-scale facade greening for different urban forms. Applied Energy 279, 115844. https://doi.org/10.1016/j.apenergy.2020.115844

Roth, M., Lim, V.H., 2017. Evaluation of canopy-layer air and mean radiant temperature simulations by a microclimate model over a tropical residential neighbourhood. Building and Environment 112, 177–189. https://doi.org/10.1016/j.buildenv.2016.11.026

Salata, F., Golasi, I., de Lieto Vollaro, R., de Lieto Vollaro, A., 2016. Urban microclimate and outdoor thermal comfort. A proper procedure to fit ENVI-met simulation outputs to experimental data. Sustainable Cities and Society 26, 318–343. https://doi.org/10.1016/j.scs.2016.07.005

Saltelli, A., Tarantola, S., Campolongo, F., Ratto, M., 2004. Sensitivity analysis in practice: a guide to assessing scientific models. Wiley Online Library.

Shi, D., Song, J., Huang, J., Zhuang, C., Guo, R., Gao, Y., 2020. Synergistic cooling effects (SCEs) of urban green-blue spaces on local thermal environment: A case study in Chongqing, China. Sustainable Cities and Society 55, 102065. https://doi.org/10.1016/j.scs.2020.102065

Shinzato, P., Simon, H., Duarte, D.H.S., Bruse, M., 2019. Calibration process and parametrization of tropical plants using ENVI-met V4 – Sao Paulo case study. Architectural Science Review 62, 112–125. https://doi.org/10.1080/00038628.2018.1563522

Simon, H., 2016. Modeling Urban Microclimate: Development, Implementation and Evaluation of New and Improved Calculation Methods for the Urban Microclimate Model ENVI-Met (PhD Thesis). Universitätsbibliothek Mainz, Mainz.

Simon, H., Kropp, T., Sohni, F., Bruse, M., 2018a. Downscaling Climate Models: Running Nested Simulations In The Microclimate Model ENVI-Met, in: 34th PLEA Conference 2018: Smart and Healthy within the 2-Degree Limit. Hongkong. In Review Process.

Simon, H., Lindén, J., Hoffmann, D., Braun, P., Bruse, M., Esper, J., 2018b. Modeling transpiration and leaf temperature of urban trees – A case study evaluating the microclimate model ENVI-met against measurement data. Landscape and Urban Planning 174, 33–40. https://doi.org/10.1016/j.landurbplan.2018.03.003

Simon, H., Sinsel, T., Bruse, M., 2021. Advances in Simulating Radiative Transfer in Complex Environments. Applied Sciences 11, 5449. https://doi.org/10.3390/app11125449

Simon, H., Sinsel, T., Bruse, M., 2020. Introduction of Fractal-Based Tree Digitalization and Accurate In-Canopy Radiation Transfer Modelling to the Microclimate Model ENVI-met. Forests 11, 869. https://doi.org/10.3390/f11080869

Stunder, M., Sethuraman, S., 1986. A statistical evaluation and comparison of coastal point source Dispersion Models. Atmospheric Environment (1967) 20, 301–315. https://doi.org/10.1016/0004-6981(86)90032-6

Tan, Z., Lau, K.K.-L., Ng, E., 2017. Planning strategies for roadside tree planting and outdoor comfort enhancement in subtropical high-density urban areas. Building and Environment 120, 93–109. https://doi.org/10.1016/j.buildenv.2017.05.017

Tan, Z., Lau, K.K.-L., Ng, E., 2016. Urban tree design approaches for mitigating daytime urban heat island effects in a high-density urban environment. Energy and Buildings, SI: Countermeasures to Urban Heat Island 114, 265–274. https://doi.org/10.1016/j.enbuild.2015.06.031

Tsoka, S., Tsikaloudaki, A., Theodosiou, T., 2018. Analyzing the ENVI-met microclimate model's performance and assessing cool materials and urban vegetation applications–A review. Sustainable Cities and Society 43, 55–76. https://doi.org/10.1016/j.scs.2018.08.009

Wang, Y., Berardi, U., Akbari, H., 2016. Comparing the effects of urban heat island mitigation strategies for Toronto, Canada. Energy and Buildings, SI: Countermeasures to Urban Heat Island 114, 2–19. https://doi.org/10.1016/j.enbuild.2015.06.046

Wang, Y., Zacharias, J., 2015. Landscape modification for ambient environmental improvement in central business districts – A case from Beijing. Urban Forestry & Urban Greening 14, 8–18. https://doi.org/10.1016/j.ufug.2014.11.005

Weihs, P., Staiger, H., Tinz, B., Batchvarova, E., Rieder, H., Vuilleumier, L., Maturilli, M., Jendritzky, G., 2012. The uncertainty of UTCI due to uncertainties in the determination of radiation fluxes derived from measured and observed meteorological data. Int J Biometeorol 56, 537–555. https://doi.org/10.1007/s00484-011-0416-7

Willmott, C.J., 1982. Some Comments on the Evaluation of Model Performance. Bulletin of the American Meteorological Society 63, 1309–1313. https://doi.org/10.1175/1520-0477(1982)063<1309:SCOTEO>2.0.CO;2

Willmott, C.J., 1981. On the Validation of Models. Physical Geography 2, 184–194. https://doi.org/10.1080/02723646.1981.10642213

Yang, J., Wong, M.S., Ho, H.C., Krayenhoff, E.S., Chan, P.W., Abbas, S., Menenti, M., 2020. A semi-empirical method for estimating complete surface temperature from radiometric surface temperature, a study in Hong Kong city. Remote Sensing of Environment 237, 111540. https://doi.org/10.1016/j.rse.2019.111540

Yang, X., Zhao, L., Bruse, M., Meng, Q., 2013. Evaluation of a Microclimate Model for Predicting the Thermal Behaviour of Different Ground Surfaces. Building and Environment 60, 93–104.

Zhang, G., He, B.-J., Zhu, Z., Dewancker, B.J., 2019. Impact of Morphological Characteristics of Green Roofs on Pedestrian Cooling in Subtropical Climates. International Journal of Environmental Research and Public Health 16, 179. https://doi.org/10.3390/ijerph16020179

Zhang, L., Zhan, Q., Lan, Y., 2018. Effects of the tree distribution and species on outdoor environment conditions in a hot summer and cold winter zone: A case study in Wuhan residential quarters. Building and Environment 130, 27–39. https://doi.org/10.1016/j.buildenv.2017.12.014

Ziter, C.D., Pedersen, E.J., Kucharik, C.J., Turner, M.G., 2019. Scale-dependent interactions between tree canopy cover and impervious surfaces reduce daytime urban heat during summer. PNAS 116, 7575–7580. https://doi.org/10.1073/pnas.1817561116

4.8 Appendix

Table 4-4: Evaluation results of the ENVI-met in previous studies (only evaluation studies were included) SH: specific humidity; Gflux: ground heat fluxes; AH: absolute humidity; SR: solar radiation. Cfb: Marine West Coast Climate; Cfa: Humid subtropical climate; Af: Tropical rainforest climate; Bwh: Subtropical Desert Climate.

Ref	Location Period	Model	Climate	Variable	Evaluation metrics						
					R^2	d	RMSE	RMSEs	RMSEu	MAE	MBE
Acero and Arriza balaga, 2018	Bilbao, Spain 6-8th Aug 2010	V4.0	Cfb	AT (°C)	0.92~0.99	0.83~0.94	1~2.07	0.81~2.05	0.28~0.66	0.83~1.82	(−1.54) ~ (−0.17)
Yang et al., 2013	Guangzhou, China 29th Aug. - 2th Sep, 2010	V4.0	Cfa	AT (°C)	0.94	0.97	1.01	0.62	0.79	-	-
				SH (g/kg)	0.52	0.78	0.84	0.55	0.64	-	-
				Gflux (W/m^2)	0.91	0.97	28.3	6	27.6	-	-
Roth and Lim, 2017	Singapore Oct 2012, Jan, July 2013	V3.1	Af	AT (°C)	0.77~0.98	0.87~0.98	0.52~1.41	0.2~1.37	0.22~0.83	0.40~1.21	(−0.51)~2.2
				MRT (°C)	0.59~0.83 Day 0~0.83 Night	0.77~0.96 Day 0.11~0.86 Night	6.44~14.1 Day 4.29~9.18 Night	1.45~9.56 Day 4.22~9.17 Night	6.24~11.2 Day 0.37~1.06 Night	5.01~12.7 Day 4.22~9.08 Night	(−6.99)~5.7 1 Day (−9.08)~(−4.22) Night
Jänicke et al., 2015	Berlin, Germany 23 July, 2013	V3 V4.0	Cfb	AT (°C)	0.87 V3 0.83~0.98V4	-	1.39 V3 0.96~1.68 V4	-	-	1.13 V3 0.86~1.43 V4	-
				SH (g/kg)	0.1 V3 0.1~0.9 1 V4	-	1.44 V3 0.35~1.54 V4	-	-	1.31 V3 0.25~1.4 V4	-

	MRT (°C)	0.95 V3 0.94~0. 95V4	-	7.98 V3 8.18~8.3 V4	-	-	6.72 V3 6.87~6.9 V4	-	
	SW_{down} (W/m^2)	0.91 V3 0.91V4	-	130.46 V3 124.44~128 .17 V4	-	-	50.33 V3 47.12~49.7 V4	-	
	SW_{up} (W/m^2)	0.6 for both	-	61.86 (V3 84.76~87.1 2(V4	-	-	39.84 V3 60.04~62.0 0 V4	-	
	LW_{down} (W/m^2)	0.01 V3 0.82~0. 86 V4	-	209.6 (V3 115.27~116 .32 (V4	-	-	208.03 V3 115.83~114 .85 V4	-	
	LW_{up} (W/m^2)	0.91 V3 0.92~0. 93 V4	-	35.19 (V3 31.7~33.28 (V4	-	-	30.96 V3 27.19~27.6 2 V4	-	
Crank et al., 2020	Arizona, USA 24 Oct 2014, 18 Feb 2015, 23 Mar 2015, 20June 2015, 21 June 2017	V4.3	Bwh	AT (°C)	0.84~0. 9	0.89~0.96	1.45~2.68	0.92~2.36	1.12~1.27	1.39~2.10	(−1.77) ~0.92
				MRT (°C)	0.537~0 .765	0.73~0.88	11.17~16.1	1.56~11.95	9.93~14.14	9.66~12.82	(−2.41) ~11.96

Jamei et al., 2019	Melbourne, Australia 5-6 Jan, 2015	V3.1	Cfb	AT (°C)	-	-	1.01-3.6	-	-	-	-	
Gál and Kántor, 2020	Szeged, Hungary 7-8 Aug, 2016	V4.4.2	Cfb	MRT (°C)	0.89	0.95	6.92	4.71	5.07	6.26	-	
				SW_{down} (W/m^2)	0.94	0.98	78.86	-	-	-	-	
				SW_{up} (W/m^2)	0.33	0.75	40.8	-	-	-	-	
				LW_{down} (W/m^2)	0.79	0.9	18.11	-	-	-	-	
				LW_{up} (W/m^2)	0.5	0.63	56.65	-	-	-	-	
Shinzato et al., 2019	Sao Paulo, Brazil 2nd 5th April, 2016	V4	Cfa	AT (°C)	-	-	0.69~1.9	-	-	-	0.56~1.7	
Liu et al., 2018	Guangzhou, China 17, 28-30 Apri. 2017 26-29 July 2017	V4.2	Cfa	AT (°C)	-	0.9~0.92 Spring 0.61-0.7 Summer	1.63~1.68 Spring 2.48-3.97 Summer	1.39 Spring 2.33-3.14 Summer	0.84~0.95 Spring 0.85~2.44 Summer	1.36~1.37 Spring 2.33~3.14 Summer	1.36 Spring 2.33~3.14 Summer	
				AH (g/kg)	-	0.95~0.96 Spring 0.68~0.71 Summer	1.34~1.44 Spring 2.4~2.53 Summer	1.15~1.31 Spring 2.09~2.22 Summer	0.6~0.69 Spring 1.19~1.23 Summer	1.11~1.22 Spring 2.11~2.31 Summer	(−1.21) ~ (−1.09) Spring (−2.27)~2.08 Summer	
				SR (W/m2)	-	0.78 Spring 0.87 Summer	255.32 Spring 242.15 Summer	51.7 Spring 15.33 Summer	250.03 Spring 241.65 Summer	44.44 Spring 29.42 Summer	−4.8 Spring 12.26 Summer	

This study*	Hong Kong 11 Sep. 2019	V4.4.6	Cfa	AT (°C)	0.62~0.93	0.68~0.94	0.44-1.63	0.23~1.52	0.28~0.69	0.34~1.38	(−1.34) ~ 0.71
				RH (%)	0.13~0.87	0.28~0.70	3.90~8.58	2.16~8.23	1.41~3.65	3.25~8.15	(−8.15) ~ (−1.15)
				MRT (°C)	0.62~0.87	0.37~0.94	5.74~9.08	3.30~8.18	1.47~6.10	4.34~8.18	1.28~8.18
				SW_{down} (W/m^2)	0.13~0.86	0.32~0.95	41.86~436.68	33.64~313.84	24.92~303.64	33.12~301.56	(−231.70) ~ 136.62
				SW_{up} (W/m^2)	0.08~0.81	0.52~0.94	5.41~49.08	4.26~44.43	3.33~21.09	4.01~39.52	(−39.33) ~ 3.76
				LW_{down} (W/m^2)	0.04~0.77	0.09~0.57	8.55~31.13	7.47~30.97	3.15~8.54	7.00~30.94	(−9.87) ~ 30.94
				LW_{up} (W/m^2)	0.39~0.94	0.11~0.82	15.36~43.54	9.54~43.04	3.60~20.74	12.04~42.64	(−31.67) ~ 42.64
				LW_{in} (W/m^2)	0.67~0.88	0.25~0.47	10.36~33.05	10.25~32.67	1.52~5.02	9.88~31.25	(−9.88) ~ 31.25
				LW_{out} (W/m^2)	0.51~0.67	0.38~0.84	10.98~40.67	3.22~40.65	1.44~10.50	8.51~38.75	(−38.75) ~ (−0.74)

*To be consistent with other studies and ensure the cross-comparison, only the results at 1h output interval was reported in this table.

Table 4-5: Validation results of ENVI-met regarding three GI typologies during summer daytime in subtropical climate background (Köppen: Cfa). Referring to the recent review paper (Liu et al., 2021), only those studies in Cfa climate, summer daytime periods, and have detailed measurement illustration were selected. Besides, the measurement conditions in the selected studies were similar with our study, i.e., green roof and bare roof were measured above roof, ground tree was measured under single tree, tree-free site was measured without tree shading.

GI Typology	Variable	Ref	Evaluation metrics						
			R^2	d	RMSE	RMSEs	RMSEu	MAE	MBE
Green roof	AT (°C)	This study*	0.67	0.88	0.65	0.32	0.57	0.52	-0.29
		Jin et al., 2018	-	-	1.21	-	-	-	-
	RH (%)	This study	0.54	0.63	4.27	3.43	2.55	3.89	-3.40
		Jin et al., 2018	-	-	2.92	-	-	-	-
Bare roof	AT (°C)	This study	0.64	0.70	1.63	1.52	0.59	0.52	-0.29
		Jin et al., 2018	-	-	1.07	-	-	-	-
	RH (%)	This study	0.25	0.70	3.90	2.16	3.25	3.89	-3.40
		Jin et al., 2018	-	-	6.13	-	-	-	-
Green wall	AT (°C)	This study	0.93	0.89	0.56	0.49	0.28	0.52	0.30
		Peng et al., 2020b	0.99	-	0.31	-	-	-	-
	RH (%)	This study	0.76	0.60	5.15	4.79	1.88	4.80	-4.71
		Peng et al., 2020b	0.98	-	4.09	-	-	-	-
	LWout (W/m^2)	This study	0.67	0.38	40.67	40.65	1.44	38.75	-38.75
		Morakinyo et al., 2019	0.66		42.00				
Bare wall	AT (°C)	This study	0.89	0.94	0.44	0.28	0.34	0.34	-0.20
		Peng et al., 2020b	0.99	-	0.35	-	-	-	-
	RH (%)	This study	0.87	0.60	4.95	4.74	1.41	4.68	-4.50
		Peng et al., 2020b	0.97	-	4.22	-	-	-	-
	LWout (W/m^2)	This study	0.51	0.84	10.98	3.22	10.50	8.51	-0.74
		Morakinyo et al., 2019	0.7	-	40.70	-	-	-	-
Ground tree	AT (°C)	This study	0.73	0.68	0.96	0.80	0.53	0.85	0.71
		Zhang et al., 2018	-	0.91	1.46	-	-	0.77	-
		Morakinyo et al., 2018	0.81	-	1.00	-	-	-	-
	MRT (°C)	This study	0.67	0.37	5.79	5.60	1.47	5.55	5.55
		Zhang et al., 2018	-	0.78	5.21	-	-	4.82	-
		Morakinyo et al., 2018	0.74	-	2.20	-	-	-	-
Tree free	AT (°C)	This study	0.62	0.82	0.73	0.23	0.69	0.61	0.03
		Morakinyo et al., 2018	0.79	-	1.40	-	-	-	-
	MRT (°C)	This study	0.85	0.94	5.74	3.32	4.68	4.34	3.26
		Morakinyo et al., 2018	0.69	-	3.90	-	-	-	-

*To be consistent with other studies and ensure the cross-comparison, only the results at 1h output interval was reported in this table.

“ (Ouyang et al., 2022).

5 Implementation and evaluation of mean radiant temperature schemes in the microclimate model ENVI-met

Tim Sinsel[1], Helge Simon[1], Wanlu Ouyang[2], Carolina dos Santos Gusson[3], Paula Shinzato[3], Michael Bruse[1]

[1]*Department of Geography, Johannes Gutenberg University Mainz, 55099 Germany*
[2]*School of Architecture, The Chinese University of Hong Kong, New Territories, Hong Kong, China*
[3]*School of Architecture and Urbanism, University of Sao Paulo, Sao Paulo, Brazil*

Summary:

In order to overcome the MRT modeling inaccuracies reported by the evaluation study in Section 4 and hence improve ENVI-met's thermal comfort analysis, new MRT schemes were implemented into the model that are presented in the following work. A new MRT calculation method based on the common six-directional radiation flux measurement approach as well as three differing projection factors, which are needed to approximate the direct shortwave radiation received by a standing human body's shape, were added to ENVI-met. Subsequent proof-of-concept simulations evaluated the performance of the implementations for eight measurement sites in Sao Paulo and Hong Kong. Measurement data was based on MRT values derived from both grey globe temperatures and six-directional radiation flux measurements. The author developed the concept, implemented the different MRT schemes in ENVI-met, prepared and conducted the proof-of-concept simulations, evaluated the measurement comparisons, created the figures, and wrote the manuscript.

Urban Climate – In Review

5.1 Introduction

Research in urban heat stress is gaining increasing relevance as its main causes, i.e., ongoing urbanization and climate change, will even intensify in upcoming years and decades (Broadbent et al., 2020; Krayenhoff et al., 2018). Mitigation strategies are developed and modeled to reduce its fatal health implications such as cardio-vascular diseases up to an increased mortality (Schinasi et al., 2018; Thorsson et al., 2014). Usually, mitigation strategies such as cool roofs or green and blue infrastructure are evaluated by comparing human thermal comfort (HTC) of a status quo against an optimized scenario using measurements or climate modeling (Bartesaghi Koc et al., 2018; Tsoka et al., 2018). One of the most important aspects in evaluating HTC is the mean radiant temperature (T_{mrt}) that describes the interaction of shortwave and longwave radiation fluxes between a human body and the surrounding environment (Kántor and Unger, 2011). Furthermore, T_{mrt} usually is the key variable in biometeorological indices like Predicted Mean Vote PMV (Fanger, 1972), Physiologically Equivalent Temperature PET (Mayer and Höppe, 1987), or Universal Thermal Climate Index UTCI (Bröde et al., 2012) that play a crucial role in determining HTC (Kumar and Sharma, 2020; Potchter et al., 2018).

There are several modeling software for T_{mrt} estimation, such as ENVI-met, SOLWEIG, or RayMan, but some evaluation studies found large deviations between the predicted T_{mrt} and measured values (Gál and Kántor, 2020; Lam et al., 2021). Deficient estimation of T_{mrt} hinders more accurate HTC analysis, and thus affects climate-sensitive strategies making and implications. Among these criticized models, the holistic microclimate model ENVI-met is the most frequently used tool for HTC studies (Crank et al., 2020; Liu et al., 2021) as it is able to simulate three-dimensional wind fields, turbulence, air temperature and humidity, radiative fluxes as well as vegetation- and building-atmosphere interactions for complex urban environments (Bruse, 1999; Bruse and Fleer, 1998; Huttner, 2012; Liu et al., 2021; Simon, 2016; Tsoka et al., 2018).

Previous studies mainly reported three shortcomings of ENVI-met when modeling T_{mrt} and it related elements. The first aspect was the inaccurate representation of longwave emitted and shortwave reflected radiation from adjacent facades, surfaces, or plants (Acero and Herranz-Pascual, 2015; Crank et al., 2020; Gál and Kántor, 2020; Lam et al., 2021; Sharmin et al., 2017; Tsoka et al., 2018; Wallenberg et al., 2020). These inaccuracies were tackled by the recent development of an advanced Indexed View

Sphere (IVS) radiation scheme (Simon et al., 2021). The second issue was that neither diffuse shortwave radiation was attenuated nor direct shortwave radiation scattered by vegetation (Gál and Kántor, 2020), which has also been addressed by the recent implementation of the Advanced Canopy Radiation Transfer (ACRT) scheme (Simon et al., 2020). While these advancements in ENVI-met's modeling of radiative fluxes are expected to increase the accuracy of T_{mrt} estimation in general, a third perspective accounts for the remaining discrepancies between measured and modelled T_{mrt} values. The resembled shape of the body in ENVI-met, reported by Roth and Lim (2017), Holmer et al. (2018) as well as Gál and Kántor (2020), representing a projection factor that is used to determine the amount of perceived shortwave radiation, does not fit the common standard. Besides that suggestion of using a different projection factor to represent a more adequate human body shape, Holmer et al. (2018) also proposed to use a different, more accurate weighting approach for received radiation fluxes from all directions based on Höppe (1992) that is in varying modifications also used by SOLWEIG (Lindberg et al., 2008) and RayMan (Matzarakis et al., 2010; Naboni et al., 2019). Furthermore, standardizing T_{mrt} calculations between different models as well as measurement approaches represents a major goal in urban climate research (Johansson et al., 2014).

After stating the previous T_{mrt} calculations in ENVI-met (Section 5.2.1), the implementation of the common six-directional T_{mrt} weighting approach as well as three projection factors are presented (Section 5.2.2). Measurements of T_{mrt} based on grey globe temperature and six-directional radiative fluxes, respectively, have been conducted (Section 5.2.3) to validate the differently modeled T_{mrt} values of old and new approaches predicted by ENVI-met in proof-of-concept simulations (Section 5.2.4). The varying model results are compared against measured values (Section 5.3.1, 5.3.2) and finally, statistical analysis is applied to evaluate the advancements made by both the presented T_{mrt} implementations as well as IVS and ACRT schemes that have recently been added to the model (Section 5.3.3, 5.3.4).

5.2 Methodology

Mean radiant temperature T_{mrt} [°C] represents the radiative heat load received by a standing human body as a parametrized temperature-dimension index (Fanger, 1972; Kántor and Unger, 2011; VDI, 2008). From the received radiative fluxes (S_{str}), the emissivity of the human body which is equal to the

absorption coefficient for longwave radiation according to Kirchhoff's law ($\varepsilon_p = 0.97$), and the Stefan-Boltzmann constant ($\sigma = 5.67 \cdot 10^{-8}\ Wm^{-2}K^{-4}$), a temperature can be calculated for the human body (Eq. 5-1).

$$T_{mrt} = \sqrt[4]{S_{str} / (\varepsilon_p \cdot \sigma)} - 273.15 \qquad \textit{Eq. 5-1}$$

The most accurate but also most expensive way of determining the mean radiation flux density S_{str} is the six-directional measurement technique featuring a pyranometer that measures shortwave radiation (K_i) and a pyrgeometer that measures longwave radiation (L_i) (Johansson et al., 2014; Kántor and Unger, 2011; Thorsson et al., 2007) (Eq. 5-2).

$$S_{str} = a_k \cdot \sum_{i=1}^{6} K_i \cdot F_i + \varepsilon_p \cdot \sum_{i=1}^{6} L_i \cdot F_i \qquad \textit{Eq. 5-2}$$

with the absorption coefficient $a_k = 0.7$ for shortwave radiation and the angle view factors F_i according to the six individual parts that are measured: the four cardinal directions North, East, South, and West, as well as the upper and lower hemisphere.

While L_i includes both, atmospheric and environmental longwave radiation fluxes, shortwave radiation is distinguished into diffuse as well as reflected parts (D_i) that are equally summed up for the six directions on the one hand and the direct part I^* on the other hand (Eq. 5-3). As direct solar radiation that is received by a standing man is depending on the sun's height angle, it is separately accounted for with a projection factor f_p representing the surface of a cylindrical body in upright position (Kántor and Unger, 2011). It generally decreases with increasing sun height angle but its exact calculation differs between models (Holmer et al., 2018; Naboni et al., 2019; Park and Tuller, 2011; Roth and Lim, 2017).

$$S_{str} = a_k \cdot I^* \cdot f_p + a_k \cdot \sum_{i=1}^{6} D_i \cdot F_i + \varepsilon_p \cdot \sum_{i=1}^{6} L_i \cdot F_i \qquad \textit{Eq. 5-3}$$

In the following, ENVI-met's previously used T_{mrt} calculation (Section 5.2.1) as well as the new implementations (Section 5.2.2) are explained. Furthermore, the methods used to evaluate these implementations are introduced; i.e., measurement campaigns (Section 5.2.3) and modeling studies of all different T_{mrt} calculation configurations (Section 5.2.4).

5.2.1 Previous calculation of mean radiant temperature in ENVI-met

The previously common T_{mrt} calculation in ENVI-met is based on Eq. 5-4 (Bruse, 1999; Huttner, 2012):

$$T_{mrt} = \left[\frac{1}{\sigma} \cdot \left(L + \frac{a_k}{\varepsilon_p} \cdot \left(I^* \cdot f_{p_{envi}} + D + R\right)\right)\right]^{1/4} \qquad \textit{Eq. 5-4}$$

Incoming longwave (L) as well as diffuse (R) and reflected shortwave radiation (D) are based on both object/sky view factors representing the upper hemisphere and ground surface properties representing the lower hemisphere, thus weighted by 50 % each. The accordingly needed properties for the calculation of emitted longwave and reflected shortwave radiation such as temperature, emissivity, and reflectivity are averaged over the whole model domain. The projection factor ($f_{p_{ENVI}}$) after Underwood and Ward (1966) which is accounting for the surface being exposed to direct sunlight depending on the sun height angle (β) is defined in Eq. 5-5:

$$f_{p_{ENVI}} = 0.42 \cdot \cos(\beta) + 0.043 \cdot \sin(\beta) \qquad \textit{Eq. 5-5}$$

5.2.2 Implementation of new mean radiant temperature calculations in ENVI-met

While the previous implementation in ENVI-met was based on the Averaged View Factor (AVF) radiation scheme and thus relied on sky view factors and averaged values, the IVS radiation scheme now enables grid-cell-based T_{mrt} calculations taking into account the longwave and reflected shortwave radiation that is received by the surrounding environment (Huttner, 2012; Simon et al., 2021). This enables a direct translation of T_{mrt} calculation according to the approach described in Eq. 5-1, Eq. 5-2, and Eq. 5-3. All received longwave and reflected shortwave radiation values are summed up for each grid cell, radiation timestep (typically 10 min update interval), and direction (North, East, West, South, Up, Down). According to Eq. 5-3, S_{str} is then calculated by multiplying the respective longwave (L) and reflected shortwave radiation (R) with the according angle factor per direction ($F_v = 0.06$ for vertical directions Up and Down as well as $F_h = 0.22$ for horizontal directions North, West, South, and East) (Eq. 5-6). Diffuse shortwave radiation (D) is not weighted like R since it is considered isotropic in the model.

$$S_{str} = a_k \cdot \left(I^* \cdot f_p + D + \sum_{v=1}^{2} R_v \cdot F_v + \sum_{h=1}^{4} R_h \cdot F_h \right) + \varepsilon_p \cdot \left(\sum_{v=1}^{2} L_v \cdot F_v + \sum_{h=1}^{4} L_h \cdot F_h \right) \quad \textit{Eq. 5-6}$$

Furthermore, three additional projection factors were added to the model and can now be selected for T_{mrt} modeling (Holmer et al., 2018; Naboni et al., 2019): $f_{p_{SOLW}}$ after Höppe (1992) as used in SOLWEIG (Holmer et al., 2015) (Eq. 5-7), $f_{p_{RayM}}$ after the Guideline for German Engineers (VDI, 2008) as used in RayMan and SURM (Fischereit, 2021; Matzarakis et al., 2010) (Eq. 5-8), and $f_{p_{City}}$ after Underwood and Ward (1966), additionally taking the sun's azimuthal angle α into account, as used in the T_{mrt} model CityComfort+ (Huang et al., 2014) (Eq. 5-9).

$$f_{p_{SOLW}} = 0.28 \cdot \cos(\beta) + 0.06 \cdot \sin(\beta) \quad \textit{Eq. 5-7}$$

$$f_{p_{RayM}} = 0.308 \cdot \cos\left(\beta \cdot (0.998 - \beta^2/50000)\right) \quad \textit{Eq. 5-8}$$

$$f_{p_{City}} = 0.0355 \cdot \sin(\beta) + 2.33 \cdot \cos(\beta) \cdot \sqrt{0.0213 \cdot \cos(\alpha)^2 + 0.0091 \cdot \sin(\alpha)^2} \quad \textit{Eq. 5-9}$$

5.2.3 Evaluation measurements

In order to evaluate the improvements made by the new implementations, measurements are used to validate model results of different configurations (Section 5.2.4). Two differing field campaigns at eight sites were used for the evaluation: two in Sao Paulo and six in Hong Kong.

5.2.3.1 Sao Paulo field campaign

The field campaign featuring two sites in Sao Paulo covered 20 consecutive days from April 5th to April 25th 2016. April was selected as it represents average climatic conditions for the humid and subtropical climate of Sao Paulo being close to the autumnal equinox. Measurements of air temperature, relative humidity, wind speed and direction, global radiation and grey globe temperature were simultaneously taken at two measurement sites, called BelaVista and Paulista in the following (Gusson, 2020; C. dos S. Gusson and Duarte, 2016; Gusson et al., 2020; C. D. S. Gusson and Duarte, 2016; Shinzato et al., 2019) (Appendix A). BelaVista measurement site is located in a courtyard in the East of several 45 m high buildings additionally surrounded by small walls and some trees. Paulista measurement site is located in a courtyard in the West of around 100 m high buildings ontop of a 6 m high roof surrounded by additional low-level roof structures and a tree.

T_{mrt} was determined using measurements of grey globe temperature (T_g) featuring a globe with a diameter $d = 0.17\ m$ and an emissivity $\varepsilon = 0.95$, air velocity (V_a) and air temperature (T_a) following Eq. 5-10 (Gusson et al., 2020; ISO 7726, 1998; Kuehn et al., 1970; Thorsson et al., 2007). The empirically adjusted equation published in Thorsson et al. (2007) was not applied due to the given shortwave radiation range (up to 850 W/m²) that would have been exceeded in the present study due to the subtropical climatic conditions.

$$T_{mrt} = \left[\left(T_g + 273.15\right)^4 + \frac{1.1 \times 10^8 \cdot {V_a}^{0.6}}{\varepsilon \cdot d^{0.4}} \times \left(T_g - T_a\right)\right]^{1/4} - 273.15 \qquad \textit{Eq. 5-10}$$

Gathering T_{mrt} from grey globe temperature is a commonly used technique based on the assumption that globe temperature represents an equilibrium between heat fluxes through radiation and convection (Kuehn et al., 1970; Thorsson et al., 2007). As it hence features a composition of radiant and ambient temperatures, the resulting fluxes will not represent T_{mrt} as accurately as the more expensive six-directional radiation flux approach (Kántor et al., 2015). Furthermore, determination of T_{mrt} by grey globe temperature features a rather slow response to changing radiation conditions, especially for globes with large diameters like the one being used here (Guo et al., 2020; Johansson et al., 2014). Due to these downsides, an additional evaluation study featuring measurements in Hong Kong was conducted.

5.2.3.2 Hong Kong field campaign

The Hong Kong evaluation study features stationary measurements of air temperature, relative humidity, wind speed and direction as well as global radiation, and mobile measurements of six-directional radiation fluxes of 10-minute monitoring at 6 different sites: Green Roof, Bare Roof, Green Wall, Bare Wall, Tree, No Tree (Ouyang et al., 2021). Ouyang et al. (2022) showed that ENVI-met was able to resemble the measured radiative fluxes with good agreement in general, if Full Forcing and localized materials are used for modeling. T_{mrt} was determined based on weighted shortwave and longwave radiation fluxes according to Equations 1 and 2. Monitoring was conducted during daytime (09:30 ~ 17:25 LST) at four typical summer days: 07th, 09th, 11th, and 12th September in 2019. September was selected as it represents average climatic conditions for the humid and subtropical climate of Hong Kong being close to the autumnal equinox. The measurement sites extend around and above an arch-shaped, terraced and greened building of 7 m height next to a large 50 m high building and two highways (Appendix B).

5.2.4 Proof-of-concept simulations

Old and new calculation approaches for T_{mrt} are compared between monitored sites as well as different configurations, each indicating a specific set of simulation parameters called configuration in the following. Simulation configurations were run for the two different T_{mrt} calculation approaches (old two-directional method and common six-directional method) and four varying projection factors ($f_{p_{ENVI}}$ / $f_{p_{SOLW}}$ / $f_{p_{RayM}}$ / $f_{p_{City}}$). These resulting eight configurations all feature the new Indexed View Sphere as well as Advanced Canopy Radiation Transfer scheme (Simon et al., 2021, 2020). In order to additionally evaluate the advancements made by the IVS and ACRT modules and to allow a comparison to previous version of ENVI-met (prior to V4.4.5), three additional configurations were run where these modules were simultaneously or individually disabled (IVS off and ACRT on; IVS on and ACRT off; IVS off and ACRT off). To save computational effort, not every combination of the previous eight configuration sets was simulated with the three additional combinations of IVS and ACRT. Only configurations featuring best- and worst-case settings were additionally run with IVS and ACRT enabled or disabled, respectively. Best-case settings are defined as a simulation configuration featuring the more detailed six-directional T_{mrt} calculation approach and the commonly used projection factor $f_{p_{RayM}}$ as it predicted the most accurate results. Worst-case settings feature the old two-directional T_{mrt} calculation as well as the old ENVI-met projection factor $f_{p_{envi}}$.

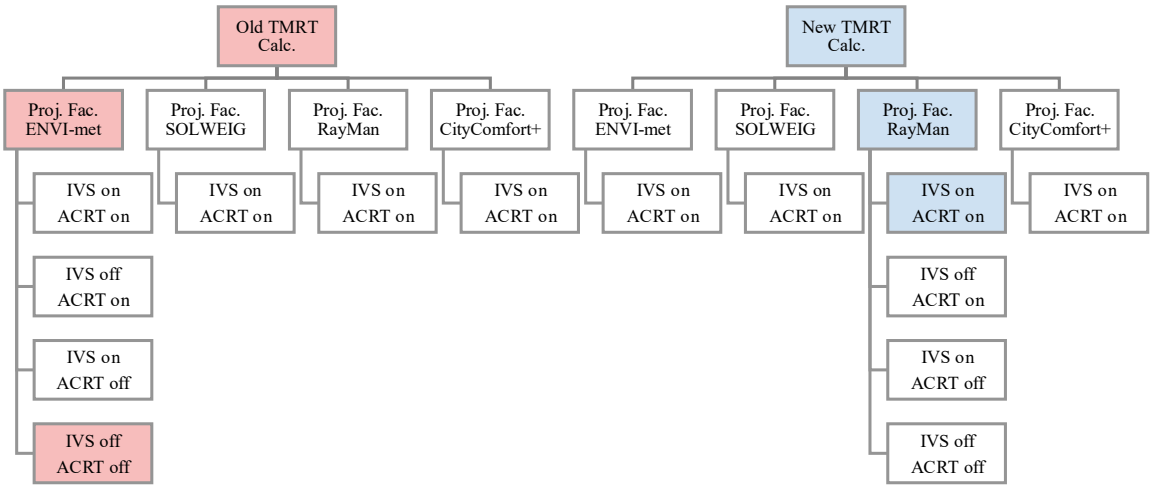

Figure 5-1: Overview on the different simulation configurations simulated per model area featuring worst-case settings marked red and best-case settings marked blue.

The resulting 14 simulation configurations (Figure 5-1) were run for different model areas that featured field campaigns of T_{mrt} measurements described in Section 5.2.3. As the two measurement sites in Sao Paulo are 380 m apart from each other, two separate model areas were created and simulated to allow a higher horizontal resolution of the model domains combined with less computational effort (Appendix A). The measurement sites in Hong Kong are very close to each other and could thus be represented within a single model area (Appendix B). In contrast to a previous ENVI-met validation study featuring the Hong Kong measurement data (Ouyang et al., 2022), its model area was modified by reducing the area extent to be able to use a higher resolution and by refining some model area details.

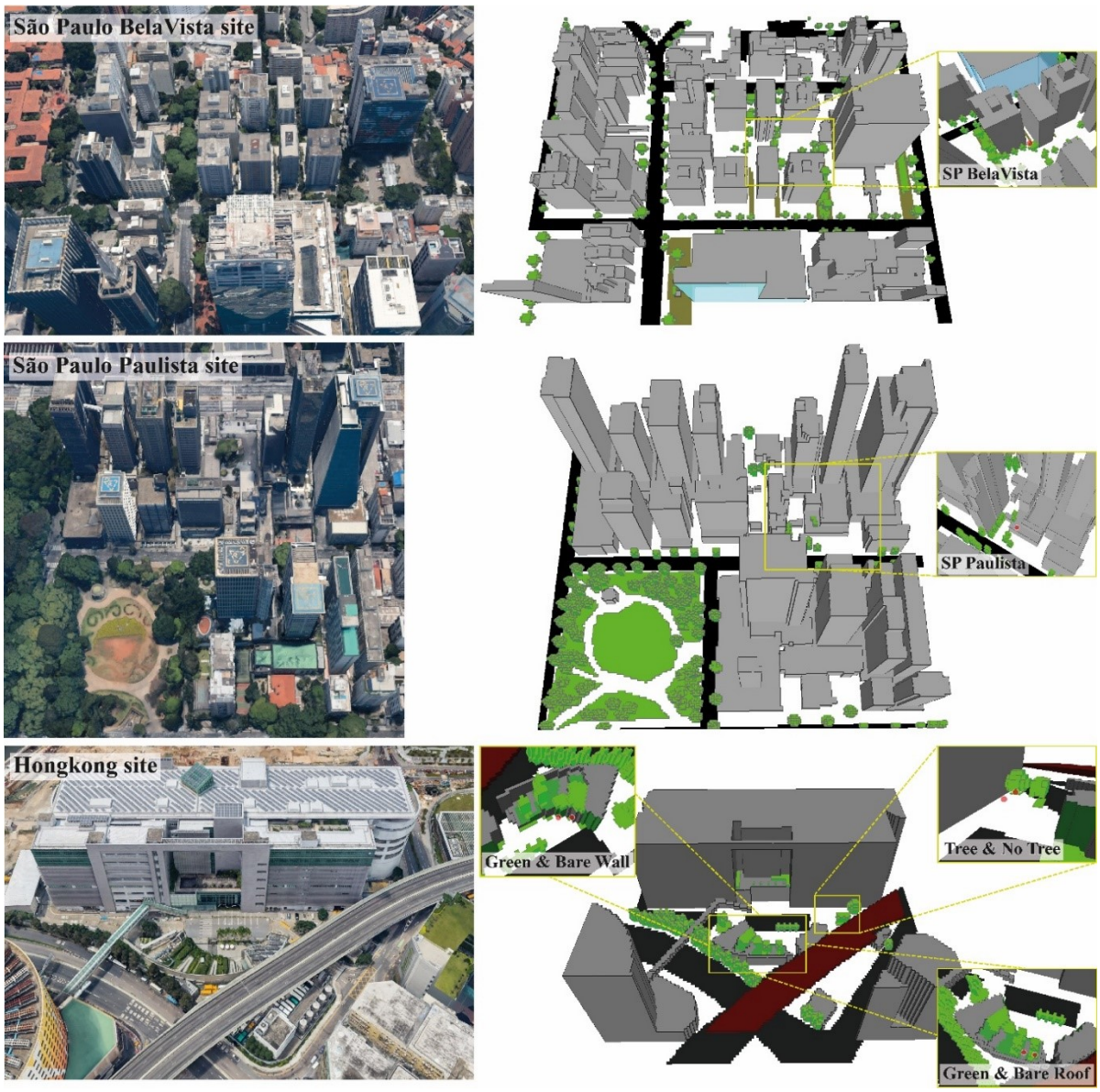

Figure 5-2: Model areas represented in Google Earth and ENVI-met Spaces with measurement sites indicated by red dots.

All three model domains represent rather complex urban environments around the measurement sites featuring all kinds of low- to high-level vegetation, low-rise walls, or curved building structures (Figure 5-2). It is thus necessary to conduct the measurement comparison not only site-specifically but holistically to avoid possible digitization accuracies to be interpreted as general modeling shortcomings. Due to the availability of eight differing measurement sites, a variety of microclimatological conditions is provided that allows a profound analysis on average.

Simulation settings and model area details are demonstrated in Table 5-1. Meteorological boundary conditions were set to Full Forcing mode for all simulations (Appendix C). For Sao Paulo simulations, Full Forcing data regarding air temperature, rel. humidity as well as wind speed and direction is derived from the field campaign measurements that show high agreement with official measurement stations in Sao Paulo, while radiation data originates from microclimatological laboratory measurements at the rooftop of the Institute of Astronomy, Geophysics and Atmospheric Sciences at the University of Sao Paulo (IAGUSP) (Gusson, 2020). Wind speed and direction are held constant at average values during the simulation period in Sao Paulo simulations to dampen large wind direction changes accompanied with the generally low wind speeds. For Hong Kong simulations, Full Forcing data regarding air temperature, rel. humidity as well as wind speed and direction is derived from HKO measurement station, while shortwave radiation data originates from KSC station and longwave radiation is taken from field campaign averages (Ouyang et al., 2022). The simulated periods are selected based on the respective field campaigns to allow a comparison between modeled and measured values. Sao Paulo field campaigns were conducted simultaneously and thus feature the same meteorological boundary conditions for both, BelaVista and Paulista model domains, representing a partly cloudy and a clear-sky day. Hong Kong simulation features a partly cloudy day.

Table 5-1: Parameters of the proof-of-concept simulations.

General Properties	SP BelaVista	SP Paulista	Hong Kong
Start Date and Time (Local)	16.04.2016 04:00	16.04.2016 04:00	11.09.2019 06:00
Duration	48 h	48 h	12 h
Meteorological Boundary Conditions	Full Forcing	Full Forcing	Full Forcing
Location Lat (Lower Left Corner)	23.563° S	23.564° S	22.324° N
Location Lon (Lower Left Corner)	46.654° W	46.658° W	114.204° E
Dimensions	155 × 140 × 35	167 x 167 x 36	152 x 120 x 42
Resolutions (X, Y, Z)	2 × 2 × 2 m	1.5 x 1.5 x 1 m	1.5 x 1.5 x 1.5 m
Lowest Grid Cell Split	Yes	No	Yes
Telescoping: Factor and Starting Height	25% above 40 m	15% above 9 m	30% above 40 m
Height of 3D Model Domain	314 m	335 m	367 m
Model Rotation out of grid north	41°	42°	-45°
Initial Soil Temperature per layer [°C]	26.85, 26.1, 25.43, 24.55	26.85, 26.1, 25.43, 24.55	26.85, 26.1, 25.43, 24.55
Initial Soil Humidity per layer [%]	50, 55, 60, 60	50, 55, 60, 60	50, 55, 60, 60
Output Interval	30 min	30 min	10 min
IVS settings (if enabled):			
Height Angle High Res.	15°	15°	15°
Azimuthal Angle High Res.	15°	15°	15°
Height Angle Low Res.	30°	30°	30°
Azimuthal Angle Low Res.	30°	30°	30°
IVS Res. Height Boundary	10 m	10 m	10 m

Simulation results are analyzed by a statistical comparison against measured field campaign data. Four evaluation metrics are mainly used for the model assessment, including the coefficient of determination (R^2), index of agreement (d), root mean square error (RMSE), and mean bias error (MBE). R^2 and d are used to describe the error variance and agreement. Both are dimensionless and feature a range between 0 and 1 with 0 meaning no agreement between modeled and measured data and 1 representing perfect agreement. RMSE and MBE are selected to demonstrate the error magnitude in K, with MBE additionally being able to show whether the model tends to underestimate (negative values) or overestimate (positive values) measured values (Willmott, 1982). Box plots are used to present the statistical metrics aggregated for the different measurement sites as well as simulations settings. A following regression analysis visually points out the modeling performance depending on the examined sites and parameters.

5.3 Results & Discussion

At first, general results examining the behavior of the different implemented projections factors and diurnal cycles comparing T_{mrt} values of the best- and worst simulations configurations against measurements for eight monitored sites (SP BelaVista, SP Paulista, HK Green Roof, HK Bare Roof, HK

Green Wall, HK Bare Wall, HK Tree, HK No Tree) are presented. Subsequent statistical analysis featuring box plots of R^2, d, RMSE, and MBE as well as linear regression analysis plots for all sites and examined simulation parameters (T_{mrt} calculation method, projection factor, IVS, ACRT) are demonstrated to further investigate the model performance, particularly focusing on the new implementations.

5.3.1 Dependency of projection factors on sun height angle

As projection factors account for the shape of an upright standing human body to estimate the received shortwave radiation, they vary depending on sun height angle: A higher amount of shortwave radiation is received during lower sun height angles since more body surface is exposed to the sun than during noon when only the top of the head and shoulders are hit by direct sunlight. However, $f_{p_{ENVI}}$ features a comparatively wide cylindrical area with high values of around 0.425 at lower sun height angles, while all other projection factors rather estimate values between 0.225 and 0.3 (Figure 5-3). This high projection factor leads to a higher amount of received shortwave radiation during low and medium sun height angles and hence to an overestimation of T_{mrt}. $f_{p_{RayM}}$ is considered to be the most accurate of the four projection factors as it fits a standing body's shape best and is thus neither overestimating received radiation during low sun height angles nor underestimating it during steep sun height angles at noon (Park and Tuller, 2011; VDI, 2008).

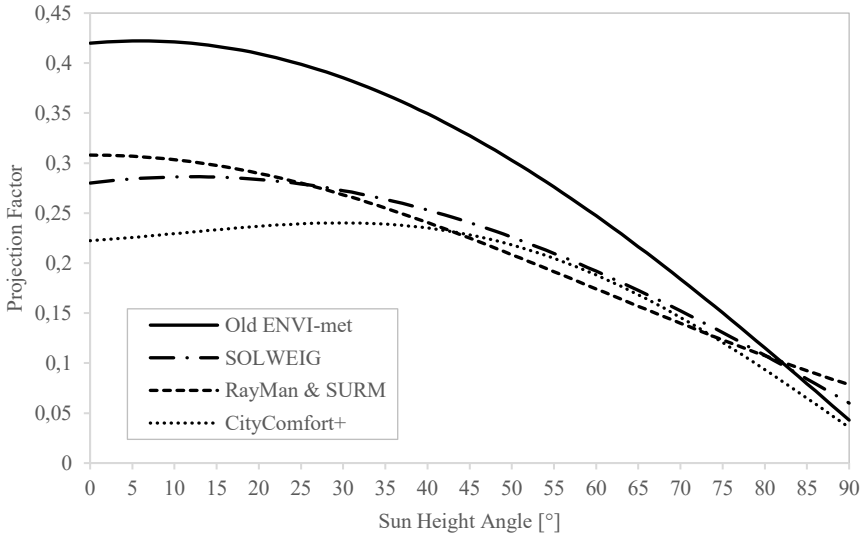

Figure 5-3: Dependency of the implemented projection factors on sun height angle.

5.3.2 Diurnal cycles of modeled and measured T_{mrt} values

When examining the diurnal cycles of T_{mrt} values for each measurement site, it becomes apparent that larger discrepancies are found between measured and worst-case modeled values (Figure 5-4). Previous T_{mrt} modeling in ENVI-met 4.4.5 shows large overestimations during daytime and underestimations during nighttime for all sites. Best-case configuration results featuring the new implementations as well as ENVI-met V5 additions seem to fit measured values better for most monitored sites and particularly follow the evolution of measured T_{mrt} values very well for HK Green Roof, HK Bare Roof, HK Bare Wall, as well as SP BelaVista during daytime (Figure 5-4 a, c, d, f). However, discrepancies between the best-case configurations and measured values are still rather large (5-10 K) for the daytime only simulations at HK Green Wall, HK Bare Wall, HK Tree, and HK No Tree (Figure 5-4 e, g, h) as well as during nighttime in Sao Paulo simulations (Figure 5-4 a, b). The modeled second-day morning spike at SP Paulista is very short term-increase in TMRT and can thus not be found in the slowly-responding grey globe measurements (Figure 5-4 b). Other daytime discrepancies like the long-term overestimation during morning and midday at HK Green Wall (Figure 5-4 e) can be explained by an inaccurate representation of the very complex environment, for example regarding specific shading structures or vegetation extents. The general overestimation of T_{mrt} in HK Tree (Figure 5-4 g) was improved by the new implementations but is still clearly visible, most likely pointing to an inaccurate tree representation regarding Leaf Area Density and size which probably also had an impact on the shading during noon at HK No Tree (Figure 5-4 h) that was not be predicted by modeling.

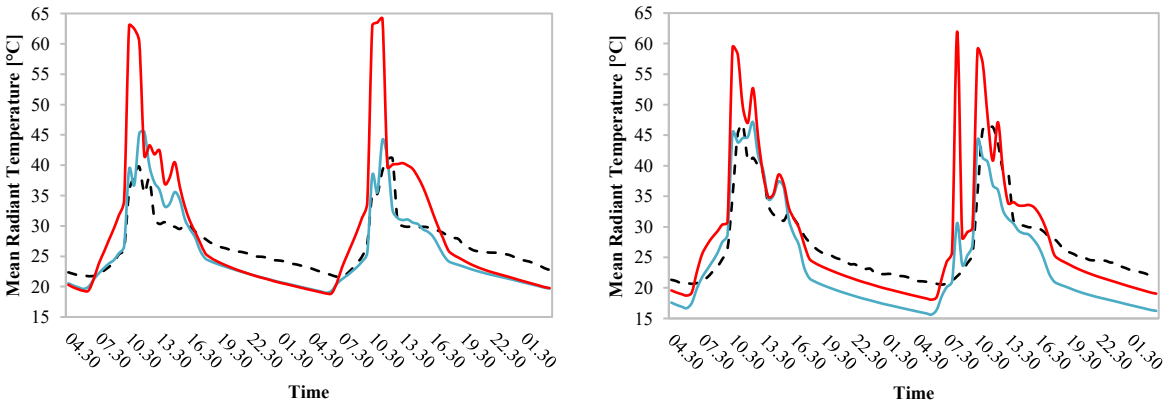

(a) (b)

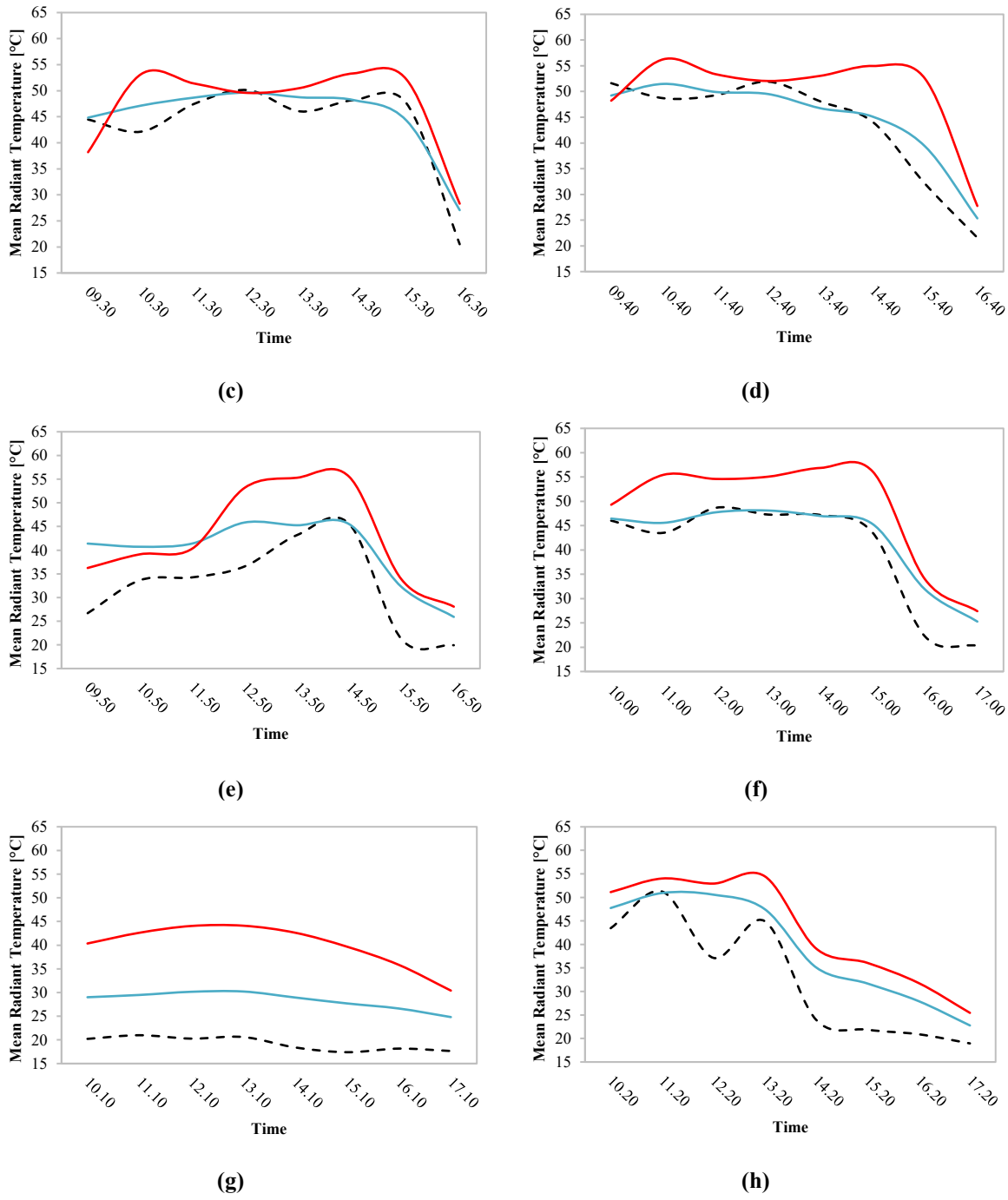

*Figure 5-4: Diurnal cycles of T_{mrt} values featuring measured values (dashed black line), best-case configuration (blue line – New Calc., $f_{p_{RayM}}$, IVS, ACRT) and worst-case configuration (red line – Old Calc., $f_{p_{ENVI}}$, IVS off, ACRT off) for the measurement sites SP BelaVista (**a**), SP Paulista (**b**), HK Green Roof (**c**), HK Bare Roof (**d**), HK Green Wall (**e**), HK Bare Wall (**f**), HK Tree (**g**), HK No Tree (**h**).*

Nighttime T_{mrt} (at SP sites) was derived from grey globe temperature and thus represents an equilibrium state between radiative fluxes and ambient air temperature while ENVI-met's T_{mrt} is based on the radiative fluxes only. During nighttime, when radiative fluxes are only based on longwave radiation and hence feature low values in general, discrepancies between received radiative fluxes from rather cool surfaces and the still rather warm air temperatures are found. These discrepancies are resembled by the

nighttime T_{mrt} between modeled and measured values in SP sites (Figure 5-4 a, b), where grey globe T_{mrt} features only small differences of 0.1 to -1 K compared to air temperature, while ENVI-met predicts 2 to 5 K lower T_{mrt} values. That also applies to previous modeling studies that stated a nighttime underestimation of T_{mrt} when comparing against values from grey globe temperature like in Roth and Lim (2017).

5.3.3 Statistical metrics between measured and modeled T_{mrt} values

In order to analyze the similarities and discrepancies between measured and modeled results more thoroughly, statistical analysis using the parameters R^2, d, RMSE, and MBE is applied (Appendix D). The results consisting out of 14 configurations for each of the eight measurement sites are comprehensively clustered by different measurement sites or simulation settings. In general, high agreement of modeled values with measurements is found with values around 0.75 to 0.85 for R^2 and d (Figure 5-5 a, b). However, prevalent large error magnitudes of around 4 to 9 K and up to 20 K in RMSE reveal distinct discrepancies between measured and modeled values, particularly for the previous calculation approaches (Figure 5-5 c). MBE values of around -2 to 8 K in general state that the model tends to overestimate T_{mrt} (Figure 5-5 d).

The analysis among differing measurement sites shows clear differences. Sao Paulo simulations with measurement sites SP BelaVista and SP Paulista feature good agreements of around 0.75 for R^2 and 0.85 for d as well as moderate error magnitudes in RMSE (~ 4 to 7 K) and a weak negative MBE (~ 0 to -2 K). The small underestimation for Sao Paulo sites is mainly based on their nighttime values that are predicted lower than grey globe T_{mrt} (c.f. Section 5.3.2). Hong Kong measurement sites show very high agreements of 0.8 to 0.95 (R^2) and 0.75 to 0.85 (d) in general with moderate error magnitudes of 7 to 9 K and an overestimation of 4 to 10 K in MBE. However, the observed larger differences in HK Tree are also visible in statistical parameters featuring lower but still moderate agreements of around 0.6 (R^2) and around 0.7 (d) as well as high error magnitudes of up to ~20 K in RMSE and MBE.

Distinct differences on a generally high agreement level are found between the simulation setting clusters featuring mean values of all measurement sites. The old T_{mrt} calculation approach, the old ENVI-met projection factor $f_{p_{ENVI}}$, and IVS off can clearly be identified as worse performer in all statistical

metrics compared to the respective counterpart options. The new six-direction calculation approach, new projection factors, and IVS could improve R^2 and d by around 0.1 to 0.15 as well as RMSE and MBE by around 5 K overall. $f_{p_{RayM}}$ could be identified as best performing projection factor according to lowest error magnitudes in RMSE and MBE, while all three new factors showed equally good agreements in R^2 and d. ACRT featured slightly better agreements than ACRT off but a worse MBE (8 K compared to 2 K). As it creates secondary diffuse radiation due to scattering to accurately feature higher shortwave radiation values below tree canopies, but the model predicted high daily overestimation of T_{mrt} especially for HK Tree, the added shortwave radiation at that point even worsened the error magnitude.

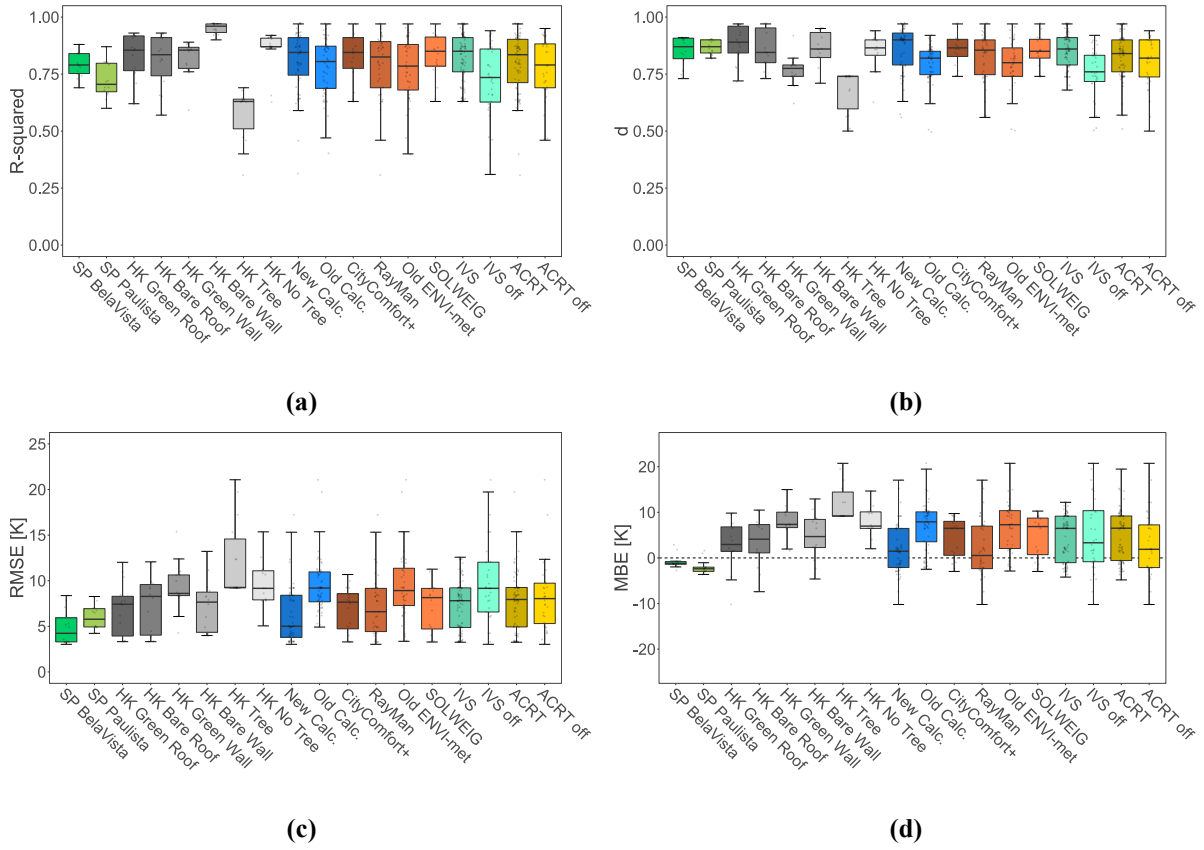

*Figure 5-5: Statistical analysis featuring R^2 (**a**), d (**b**), RMSE (**c**), and MBE (**d**) aggregated by Sao Paulo measurement sites (green) and Hong Kong measurement sites (grey) on the one hand as well as simulation configurations like T_{mrt} calculation methods (blue), projection factors (red), IVS modes (light green), and ACRT modes (yellow) on the other hand.*

Higher agreements and lower error magnitudes for enabled IVS and ACRT configurations in general demonstrated that not only the new implementations of new T_{mrt} calculation approach and different projection factors could improve ENVI-met's modeling but also the previously reported

implementations of Simon et al. (2021) and Simon et al. (2020) yield a higher modeling accuracy and should thus in sum have resolved the previously reported discrepancies (Lam et al., 2021; Tsoka et al., 2018).

5.3.4 Linear regression analysis between measured and modeled T_{mrt} values

To visualize the statistical metrics' findings, linear regression analysis plots featuring scattered points are presented (Figure 5-6). The strong heterogeneity between different measurement sites is displayed in Figure 5-6 a, b where we again find that the model generally overestimated T_{mrt} values. Furthermore, it is corroborated that at HK Tree values were grossly overestimated, while the other HK sites as well as SP sites showed a good agreement but also larger deviations.

The new six-directional T_{mrt} calculation approach features a well improved regression line compared to the old two-directional approach (Figure 5-6 c). Examining the projection factors in Figure 5-6 d, $f_{p_{ENVI}}$ is corroborated to provide the lowest modeling accuracy while $f_{p_{RayM}}$ performs best and there is no difference to be detected among $f_{p_{City}}$ and $f_{p_{SOLW}}$. IVS shows a slightly better regression model than IVS off, while ACRT and ACRT off do not feature any differences (Figure 5-6 e, f).

As the new implementations of both six-directional T_{mrt} calculation approach and frequently used projection factors are now in accordance with state-of-the-art modeling techniques, overestimations of T_{mrt} during daytime are highly probable to be related to ENVI-met's modeled radiation values impairing the T_{mrt} results. These discrepancies were most likely caused by inaccuracies in model areas and databases, i.e. inaccuracies in shape, size, density of vegetation, reflectivity and emissivity of building and soil surface materials, other thermal parameters such as heat conductivity and capacity of walls, forced solar radiation values as well as forced soil temperature and humidity values and initial building temperatures, or the missing representation of windows, other specific building elements such as shading structures as well as parked cars in immediate surrounding of the measurement sites. An example would be an unrealistic high surface reflectivity value that leads to more received shortwave radiation in front of it and thus higher T_{mrt} values during daytime on the one hand. On the other hand, it leads to less energy absorption that is in turn not released by longwave radiation emission hence lowering T_{mrt} values during nighttime. As the general T_{mrt} overestimation error during daytime was found to be massively decreased

for the new six-directional approach to accurately fit the measurements now, the remaining positive deviations at HK Tree and HK No Tree are most likely explained by an inaccurate vegetation representation near these two sites in the HK model area.

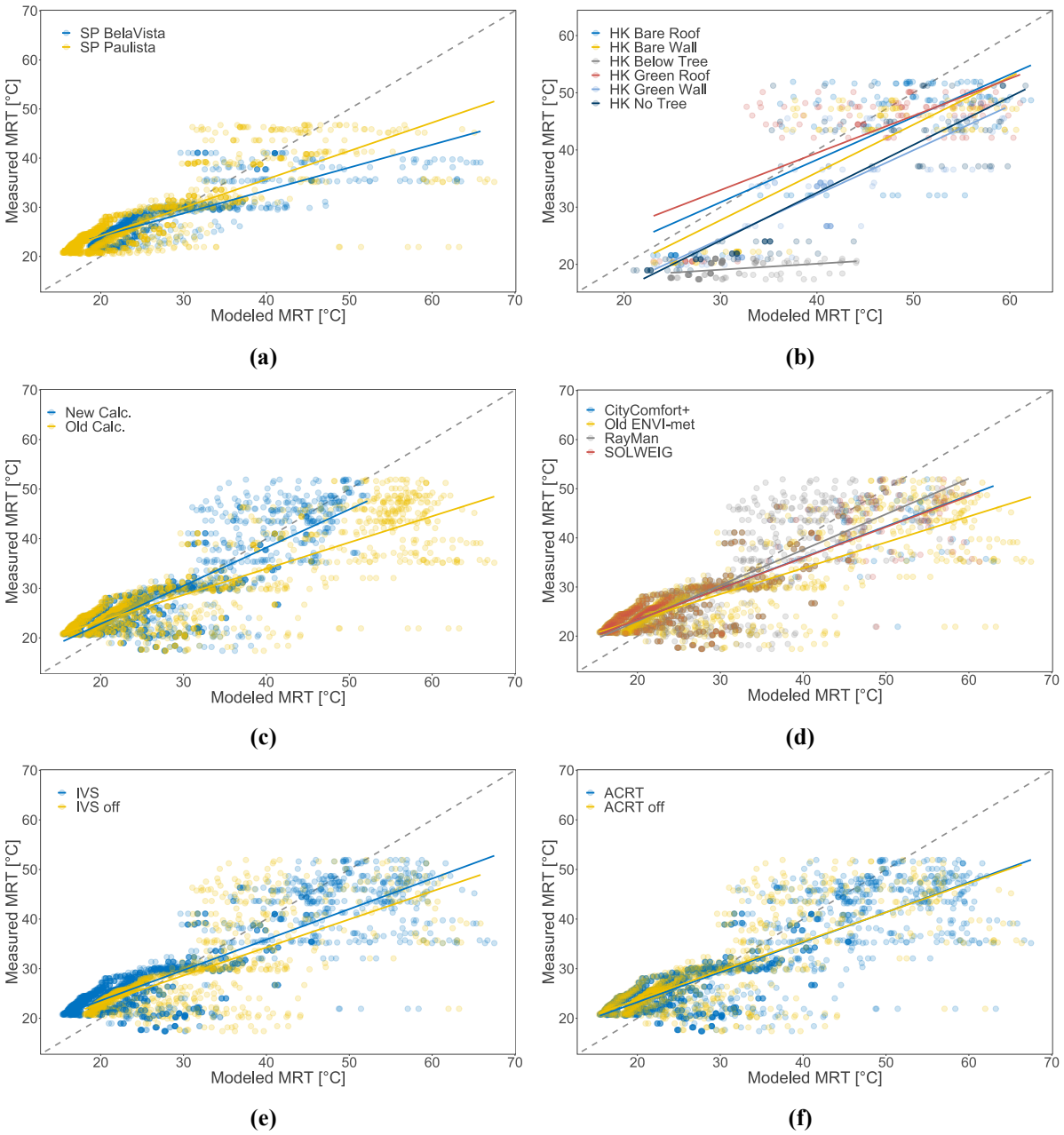

*Figure 5-6: Regression analysis for the different Sao Paulo measurement sites (**a**), Hong Kong measurement sites (**b**), T_{mrt} calculation methods (**c**), projection factors (**d**), IVS modes (**e**), and ACRT modes (**f**), respectively.*

5.4 Conclusion

New implementations in the microclimate model ENVI-met were presented that were found to improve modeling accuracy of T_{mrt} based on evaluation studies. The new six-directional T_{mrt} calculation approach as well as the addition of various established projection factors showed better results in statistical

evaluation for eight different measurement sites of two varying field campaigns in Sao Paulo and Hong Kong. It could thus be demonstrated that the new implementations presented in this manuscript lead to a higher accuracy in microclimate modeling with ENVI-met. Due to the model's widespread application, it can thus be assumed that the quality of numerous upcoming modeling studies, for example evaluating heat mitigation strategies or investigating distinct sustainable urban planning scenarios, will benefit from the presented enhancements. Additionally, recent developments regarding to ENVI-met's radiation scheme called IVS and ACRT module were shown to improve T_{mrt} modeling accuracy in general. While R^2 and d showed high agreements (~0.75 to 0.85) in general, and though RMSE as well as MBE could be improved by around 5 K, still rather large error magnitudes of 4 to 9 K in majority and up to 20 K at a specific site were revealed. These discrepancies are most likely to be explained by simulation input parameters or an inaccurate representation of the very complex sites. However, additional validation studies will be required to further investigate if there might be any systematic errors despite the new implementations. Furthermore, as the proof-of-concept scenarios were limited to very complex urban morphologies in a subtropical climate, evaluation against T_{mrt} values from measurements in different urban environments and climatological conditions needs to be conducted to verify the findings of this study. For instance, prior T_{mrt} modeling studies regarding ENVI-met that pointed out modeling inaccuracies could now be repeated to investigate and validate the proposed advancements.

5.5 Funding

This study is supported by a postgraduate studentship and the "3rd round Vice-Chancellor's Discretionary Fund" from the Chinese University of Hong Kong; the RGC research grant (No. 14617220) from the Research Grants Council (RGC) of Hong Kong; the Coordenação de Aperfeiçoamento de Pessoal de Nível Superior - Brasil (CAPES) - Finance Code 001; FAPESP (Grant #2016/02825-5); and CNPq (Productivity Grant 309669/2015/4).

5.6 References

Acero, J.A., Herranz-Pascual, K., 2015. A comparison of thermal comfort conditions in four urban spaces by means of measurements and modelling techniques. Building and Environment 93, 245–257. https://doi.org/10.1016/j.buildenv.2015.06.028

Bartesaghi Koc, C., Osmond, P., Peters, A., 2018. Evaluating the cooling effects of green infrastructure: A systematic review of methods, indicators and data sources. Solar Energy 166, 486–508. https://doi.org/10.1016/j.solener.2018.03.008

Broadbent, A.M., Krayenhoff, E.S., Georgescu, M., 2020a. The motley drivers of heat and cold exposure in 21st century US cities. PNAS 117, 21108–21117. https://doi.org/10.1073/pnas.2005492117

Bröde, P., Fiala, D., Błażejczyk, K., Holmér, I., Jendritzky, G., Kampmann, B., Tinz, B., Havenith, G., 2012. Deriving the operational procedure for the Universal Thermal Climate Index (UTCI). Int J Biometeorol 56, 481–494. https://doi.org/10.1007/s00484-011-0454-1

Bruse, M., 1999. Die Auswirkungen kleinskaliger Umweltgestaltung auf das Mikroklima. Entwicklung des prognostischen numerischen Modells ENVI-met zur Simulation der Wind-, Temperatur- und Feuchteverteilung in städtischen Strukturen (PhD Thesis). Ruhr-University Bochum, Bochum.

Bruse, M., Fleer, H., 1998. Simulating Surface Plant Air Interactions inside Urban Environments with a Three Dimensional Numerical Model. Environmental Modelling & Software 13, 373–384. https://doi.org/10.1016/S1364-8152(98)00042-5

Crank, P.J., Middel, A., Wagner, M., Hoots, D., Smith, M., Brazel, A., 2020. Validation of seasonal mean radiant temperature simulations in hot arid urban climates. Science of The Total Environment 749, 141392. https://doi.org/10.1016/j.scitotenv.2020.141392

Fanger, P.O., 1972. Thermal comfort: analysis and applications in environmental engineering. McGraw-Hill, New York.

Fischereit, J., 2021. The simple urban radiation model for estimating mean radiant temperature in idealised street canyons. Urban Climate 35, 100694. https://doi.org/10.1016/j.uclim.2020.100694

Gál, C.V., Kántor, N., 2020. Modeling mean radiant temperature in outdoor spaces, A comparative numerical simulation and validation study. Urban Climate 32, 100571. https://doi.org/10.1016/j.uclim.2019.100571

Guo, H., Aviv, D., Loyola, M., Teitelbaum, E., Houchois, N., Meggers, F., 2020. On the understanding of the mean radiant temperature within both the indoor and outdoor environment, a critical review. Renewable and Sustainable Energy Reviews 117, 109207. https://doi.org/10.1016/j.rser.2019.06.014

Gusson, C. dos S., 2020. O impacto da verticalização no microclima urbano e no conforto térmico na escala do pedestre: o papel da geometria e da envoltória dos edifícios (Doutorado em Tecnologia da Arquitetura). Universidade de São Paulo, São Paulo. https://doi.org/10.11606/T.16.2020.tde-29032021-104403

Gusson, C. dos S., Duarte, D.H.S., 2016. Effects of Built Density and Urban Morphology on Urban Microclimate - Calibration of the Model ENVI-met V4 for the Subtropical Sao Paulo, Brazil. Procedia Engineering, Fourth International Conference on Countermeasures to Urban Heat Island, 30-31 May and 1 June 2016 169, 2–10. https://doi.org/10.1016/j.proeng.2016.10.001

Gusson, C.D.S., Duarte, D.H.S., 2016. The effect of density on urban microclimate:, in: Cities, Buildings, People: Towards Regenerative Environments. Presented at the PLEA, Los Angeles, p. 10.

Gusson, C.D.S., Simon, H., Duarte, D.H.S., 2020. Impact of built density and surface materials on urban microclimate for Sao Paulo, Brazil, in: Planning Post Carbon Cities: 35th PLEA Conference on Passive and Low Energy Architecture, A Coruña, 1st-3rd September 2020: Proceedings. Presented at the PLEA, Universidade da Coruña, pp. 818–823.

Holmer, B., Lindberg, F., Rayner, D., Thorsson, S., 2015. How to transform the standing man from a box to a cylinder – a modified methodology to calculate mean radiant temperature in field studies and models. Presented at the ICUC 9, Toulouse, p. 6.

Holmer, B., Lindberg, F., Thorsson, S., 2018. Mean radiant temperature and the shape of the standing man. Presented at the ICUC 10, New York.

Höppe, P., 1992. Ein neues Verfahren zur Bestimmung der mittleren Strahlungstemperatur im Freien. Wetter und Leben 44, 147–151.

Huang, J., Cedeño-Laurent, J.G., Spengler, J.D., 2014. CityComfort+: A simulation-based method for predicting mean radiant temperature in dense urban areas. Building and Environment 80, 84–95. https://doi.org/10.1016/j.buildenv.2014.05.019

Huttner, S., 2012. Further development and application of the 3D microclimate simulation ENVI-met (Dissertation). Johannes Gutenberg-University Mainz.

ISO 7726, 1998. Ergonomics of the thermal environment — Instruments for measuring physical quantities.

Johansson, E., Thorsson, S., Emmanuel, R., Krüger, E., 2014. Instruments and methods in outdoor thermal comfort studies – The need for standardization. Urban Climate, ICUC8: The 8th International Conference on Urban Climate and the 10th Symposium on the Urban Environment 10, 346–366. https://doi.org/10.1016/j.uclim.2013.12.002

Kántor, N., Kovács, A., Lin, T.-P., 2015. Looking for simple correction functions between the mean radiant temperature from the "standard black globe" and the "six-directional" techniques in Taiwan. Theor Appl Climatol 121, 99–111. https://doi.org/10.1007/s00704-014-1211-2

Kántor, N., Unger, J., 2011. The most problematic variable in the course of human-biometeorological comfort assessment — the mean radiant temperature. cent.eur.j.geo. 3, 90–100. https://doi.org/10.2478/s13533-011-0010-x

Krayenhoff, E.S., Moustaoui, M., Broadbent, A.M., Gupta, V., Georgescu, M., 2018. Diurnal interaction between urban expansion, climate change and adaptation in US cities. Nature Clim Change 8, 1097–1103. https://doi.org/10.1038/s41558-018-0320-9

Kuehn, L.A., Stubbs, R.A., Weaver, R.S., 1970. Theory of the globe thermometer. Journal of Applied Physiology 29, 750–757. https://doi.org/10.1152/jappl.1970.29.5.750

Kumar, P., Sharma, A., 2020. Study on importance, procedure, and scope of outdoor thermal comfort –A review. Sustainable Cities and Society 61, 102297. https://doi.org/10.1016/j.scs.2020.102297

Lam, C.K.C., Lee, H., Yang, S.-R., Park, S., 2021. A review on the significance and perspective of the numerical simulations of outdoor thermal environment. Sustainable Cities and Society 71, 102971. https://doi.org/10.1016/j.scs.2021.102971

Lindberg, F., Holmer, B., Thorsson, S., 2008. SOLWEIG 1.0 – Modelling spatial variations of 3D radiant fluxes and mean radiant temperature in complex urban settings. Int J Biometeorol 52, 697–713. https://doi.org/10.1007/s00484-008-0162-7

Liu, Z., Cheng, W., Jim, C.Y., Morakinyo, T.E., Shi, Y., Ng, E., 2021. Heat mitigation benefits of urban green and blue infrastructures: A systematic review of modeling techniques, validation and scenario simulation in ENVI-met V4. Building and Environment 200, 107939. https://doi.org/10.1016/j.buildenv.2021.107939

Matzarakis, A., Rutz, F., Mayer, H., 2010. Modelling radiation fluxes in simple and complex environments: basics of the RayMan model. Int J Biometeorol 54, 131–139. https://doi.org/10.1007/s00484-009-0261-0

Mayer, H., Höppe, P., 1987. Thermal Comfort of Man in Different Urban Environments. Theoretical and Applied Climatology 38, 43–49.

Naboni, E., Meloni, M., Makey, C., Kaempf, J., 2019. The Simulation of Mean Radiant Temperature in Outdoor Conditions: A review of Software Tools Capabilities. Presented at the IBPSA 16, Rome, Italy, pp. 3234–3241. https://doi.org/10.26868/25222708.2019.210301

Ouyang, W., Morakinyo, T.E., Ren, C., Liu, S., Ng, E., 2021. Thermal-irradiant performance of green infrastructure typologies: Field measurement study in a subtropical climate city. Science of The Total Environment 764, 144635. https://doi.org/10.1016/j.scitotenv.2020.144635

Ouyang, W., Sinsel, T., Simon, H., Morakinyo, T.E., Liu, H., Ng, E., 2022. Evaluating the thermal-radiative performance of ENVI-met model for green infrastructure typologies: Experience from a subtropical climate. Building and Environment 207, 108427. https://doi.org/10.1016/j.buildenv.2021.108427

Park, S., Tuller, S.E., 2011. Comparison of human radiation exchange models in outdoor areas. Theor Appl Climatol 105, 357–370. https://doi.org/10.1007/s00704-010-0388-2

Potchter, O., Cohen, P., Lin, T.-P., Matzarakis, A., 2018. Outdoor human thermal perception in various climates: A comprehensive review of approaches, methods and quantification. Science of The Total Environment 631–632, 390–406. https://doi.org/10.1016/j.scitotenv.2018.02.276

Roth, M., Lim, V.H., 2017. Evaluation of canopy-layer air and mean radiant temperature simulations by a microclimate model over a tropical residential neighbourhood. Building and Environment 112, 177–189. https://doi.org/10.1016/j.buildenv.2016.11.026

Schinasi, L.H., Benmarhnia, T., De Roos, A.J., 2018. Modification of the association between high ambient temperature and health by urban microclimate indicators: A systematic review and meta-analysis. Environmental Research 161, 168–180. https://doi.org/10.1016/j.envres.2017.11.004

Sharmin, T., Steemers, K., Matzarakis, A., 2017. Microclimatic modelling in assessing the impact of urban geometry on urban thermal environment. Sustainable Cities and Society 34, 293–308. https://doi.org/10.1016/j.scs.2017.07.006

Shinzato, P., Simon, H., Duarte, D.H.S., Bruse, M., 2019. Calibration process and parametrization of tropical plants using ENVI-met V4 – Sao Paulo case study. Architectural Science Review 62, 112–125. https://doi.org/10.1080/00038628.2018.1563522

Simon, H., 2016. Modeling Urban Microclimate: Development, Implementation and Evaluation of New and Improved Calculation Methods for the Urban Microclimate Model ENVI-Met (PhD Thesis). Universitätsbibliothek Mainz, Mainz.

Simon, H., Sinsel, T., Bruse, M., 2021. Advances in Simulating Radiative Transfer in Complex Environments. Applied Sciences 11, 5449. https://doi.org/10.3390/app11125449

Simon, H., Sinsel, T., Bruse, M., 2020. Introduction of Fractal-Based Tree Digitalization and Accurate In-Canopy Radiation Transfer Modelling to the Microclimate Model ENVI-met. Forests 11, 869. https://doi.org/10.3390/f11080869

Thorsson, S., Lindberg, F., Eliasson, I., Holmer, B., 2007. Different methods for estimating the mean radiant temperature in an outdoor urban setting. Int. J. Climatol. 27, 1983–1993. https://doi.org/10.1002/joc.1537

Thorsson, S., Rocklöv, J., Konarska, J., Lindberg, F., Holmer, B., Dousset, B., Rayner, D., 2014. Mean radiant temperature – A predictor of heat related mortality. Urban Climate, ICUC8: The 8th International Conference on Urban Climate and the 10th Symposium on the Urban Environment 10, 332–345. https://doi.org/10.1016/j.uclim.2014.01.004

Tsoka, S., Tsikaloudaki, A., Theodosiou, T., 2018. Analyzing the ENVI-met microclimate model's performance and assessing cool materials and urban vegetation applications–A review. Sustainable Cities and Society 43, 55–76. https://doi.org/10.1016/j.scs.2018.08.009

Underwood, C.R., Ward, E.J., 1966. The Solar Radiation Area of Man. Ergonomics 9, 155–168. https://doi.org/10.1080/00140136608964361

VDI, 2008. Methods for the human-biometeorological assessment of climate and air hygiene for urban and regional planning. (No. I: Climate), VDI 3787, Sheet 2. Beuth, Berlin.

Wallenberg, N., Lindberg, F., Holmer, B., Thorsson, S., 2020. The influence of anisotropic diffuse shortwave radiation on mean radiant temperature in outdoor urban environments. Urban Climate 31, 100589. https://doi.org/10.1016/j.uclim.2020.100589

Willmott, C.J., 1982. Some Comments on the Evaluation of Model Performance. Bulletin of the American Meteorological Society 63, 1309–1313. https://doi.org/10.1175/1520-0477(1982)063<1309:SCOTEO>2.0.CO;2

5.7 Appendix A – Sao Paulo Field Campaign

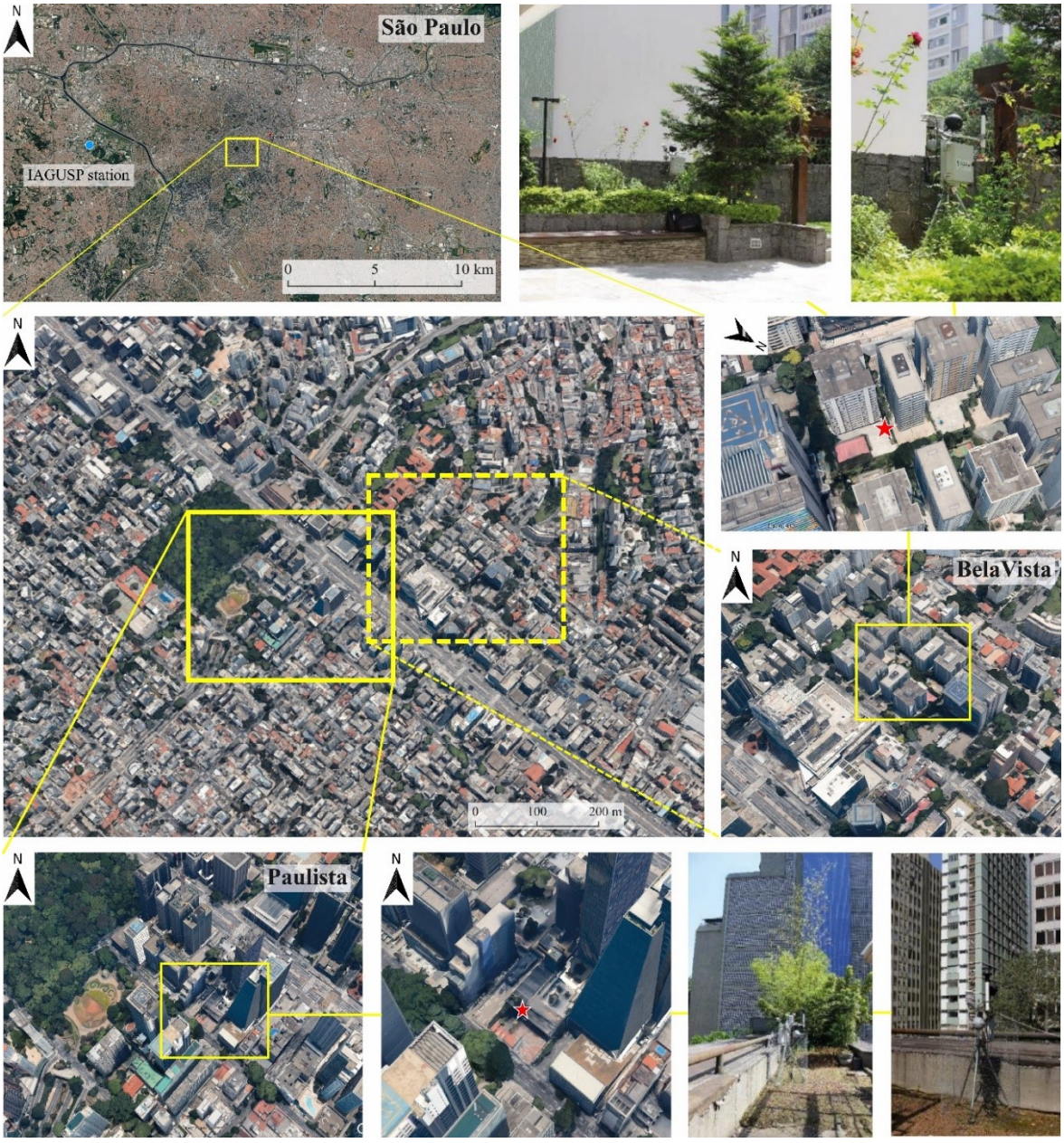

Figure 5-7: Location and representation of measurement sites (red stars) BelaVista and Paulista in Sao Paulo (Gusson, 2020).

Table 5-2: Sensors used for the Sao Paulo field campaigns (Gusson, 2020; Gusson and Duarte, 2016).

Sensor	Variable(s)	Accuracy
Vaisala HMP45C-L12	Air temperature and rel. humidity	± 0.25°C
Gill 2-D Sonic Wind WINDSONIC1-L24	Wind speed and direction	Speed ± 2 % Direction ± 3°
Kipp & Zonen Pyranometer W / Sun Shield CMP3-L12	Global solar radiation	± 5%
Hobo TMCx-HD Grey globe thermometer	Global temperature	± 0.2°C

(diameter = 170 mm)

5.8 Appendix B – Hong Kong Field Campaign

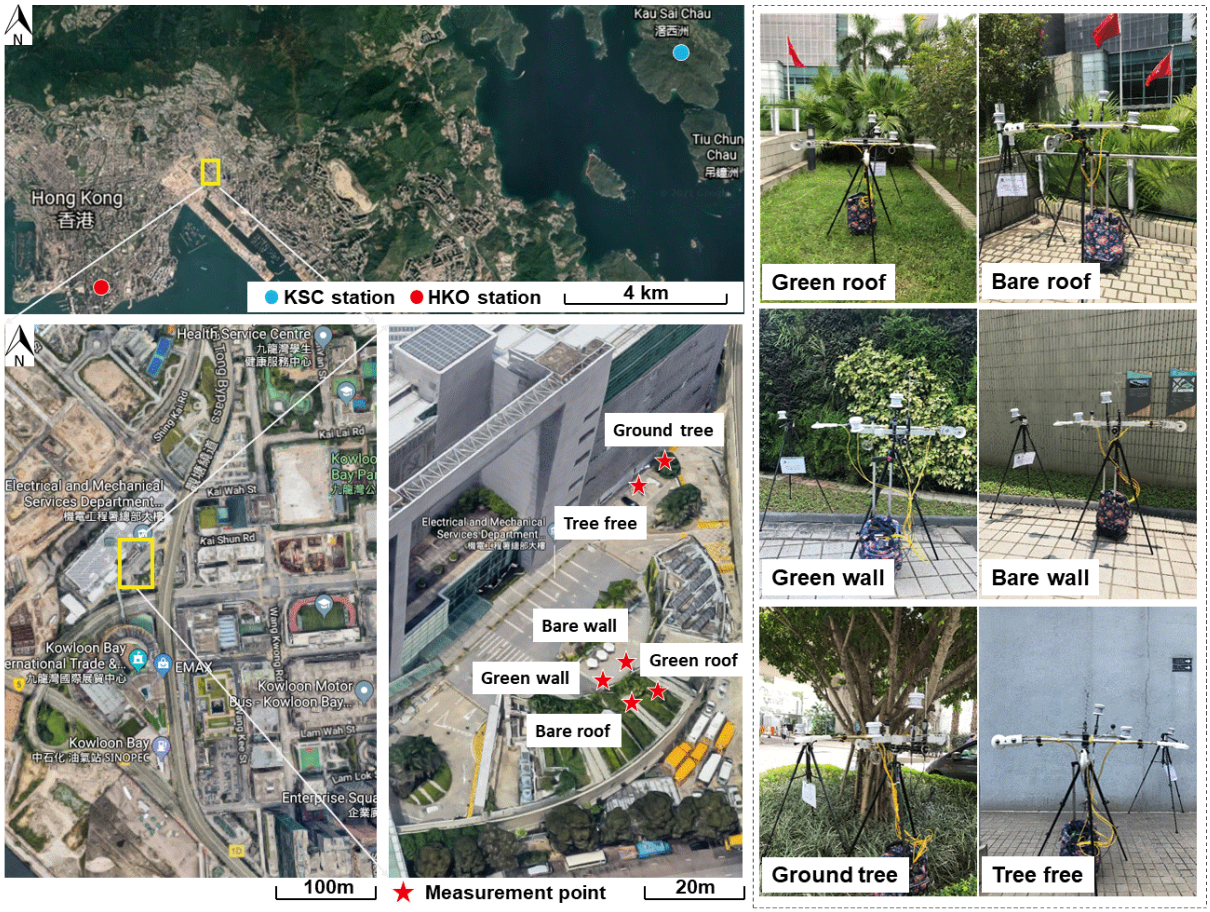

Figure 5-8: Location and representation of measurement sites in Hong Kong (Ouyang et al., 2022).

Table 5-3: Sensors used for the Hong Kong field campaign (Ouyang et al., 2021).

Sensor	Variable(s)	Accuracy
HOBO U12-012	Air temperature	± 0.3° C
	Rel. humidity	± 2.5 %
TESTO 480 Comfort level probe	Wind speed and direction	Speed ± 0.03 ms^{-1} Direction ± 4 %
LI-200SA Pyranometer	Global solar radiation	Typically 80 μA per 1000 Wm^{-2}
TESTO 480 Global thermometer (diameter = 40 mm)	Global temperature	Type K thermocouple, class 1*
TESTO 480 Temperature prove	Air temperature	± 0.2° C
	Rel. humidity	± 1 %
CNR4 Component net radiometers	Shortwave and Longwave radiation	5 to 20 $\mu V/Wm^{-2}$

5.9 Appendix C – Simulation Setup

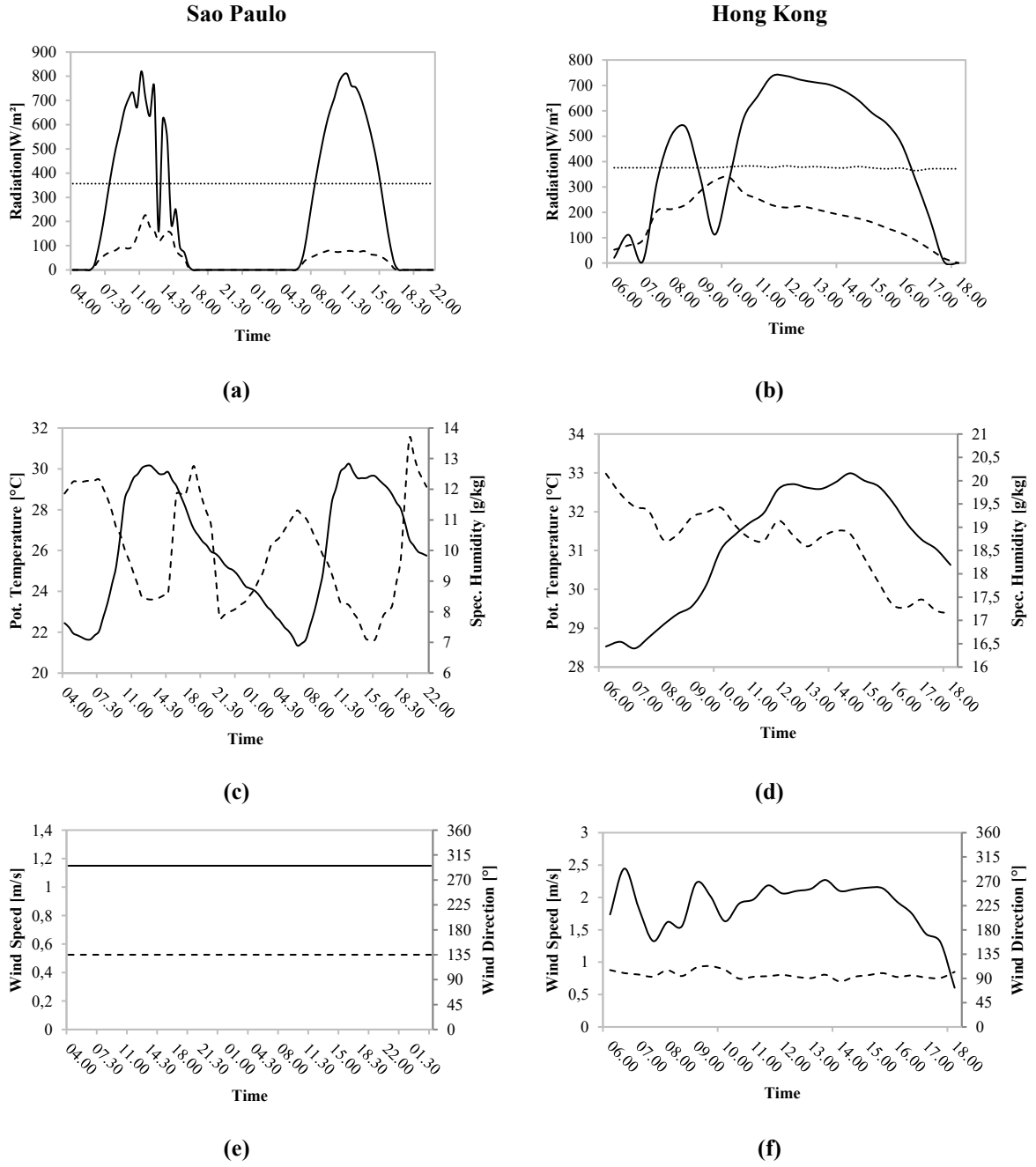

*Figure 5-9: Full forcing boundary conditions for the proof-of-concept simulations depicting direct shortwave (black line), diffuse shortwave (dashed line) and longwave radiation (dotted line) (**a**,**b**), potential air temperature (black line) and specific air humidity (dashed line) (**c**,**d**) as well as wind speed (black line) and wind direction (dashed line) (**e**,**f**).*

5.10 Appendix D – Statistics

Table 5-4: Overview on statistical analysis results.

Measurement Site	Variable	New Calc., CityComfort+, IVS, ACRT	New Calc., old ENVI-met, IVS, ACRT	New Calc., SOLWEIG, IVS, ACRT	New Calc., RayMan, IVS, ACRT Off	New Calc., RayMan, IVS off, ACRT	New Calc., RayMan, IVS off, ACRT off	New Calc., RayMan, IVS, ACRT	Old Calc., CityComfort+, IVS, ACRT	Old Calc., old ENVI-met, IVS, ACRT off	Old Calc., old ENVI-met, IVS off, ACRT	Old Calc., old ENVI-met, IVS off, ACRT off	Old Calc., old ENVI-met, IVS, ACRT	Old Calc., SOLWEIG, IVS, ACRT	Old Calc., RayMan, IVS, ACRT
SP BelaVista	R2	0,84	0,85	0,84	0,88	0,73	0,79	0,84	0,78	0,69	0,75	0,74	0,76	0,79	0,80
	AutoCor	0,92	0,92	0,92	0,94	0,85	0,89	0,92	0,89	0,83	0,87	0,86	0,87	0,89	0,89
	RMSE	3,29	3,36	3,28	3,55	3,31	3,03	3,26	5,31	7,10	8,37	7,84	6,14	5,16	4,92
	MBE	-1,37	-1,30	-1,38	-2,71	-0,76	-1,97	-1,40	-0,97	-1,76	2,87	1,83	-0,72	-1,02	-1,10
	d	0,91	0,91	0,91	0,89	0,90	0,90	0,91	0,84	0,76	0,73	0,75	0,81	0,84	0,85
SP Paulista	R2	0,80	0,79	0,80	0,87	0,66	0,72	0,80	0,67	0,72	0,60	0,68	0,64	0,69	0,69
	AutoCor	0,89	0,89	0,89	0,93	0,81	0,84	0,89	0,82	0,85	0,77	0,82	0,80	0,83	0,83
	RMSE	4,97	5,06	4,94	4,87	4,23	4,26	4,93	7,01	8,27	7,00	6,50	7,82	6,74	6,61
	MBE	-2,96	-2,87	-2,97	-3,62	-1,05	-2,08	-2,99	-2,35	-2,10	1,62	1,03	-2,01	-2,41	-2,49
	d	0,90	0,90	0,90	0,90	0,89	0,88	0,90	0,84	0,82	0,83	0,86	0,82	0,85	0,85
HK Green Roof	R2	0,91	0,93	0,92	0,92	0,62	0,75	0,92	0,85	0,76	0,78	0,71	0,83	0,86	0,87
	AutoCor	0,96	0,97	0,96	0,96	0,79	0,87	0,96	0,92	0,87	0,88	0,84	0,91	0,93	0,93
	RMSE	3,39	3,45	3,35	5,39	7,76	12,02	3,32	7,51	7,34	10,39	6,18	10,95	8,47	7,75
	MBE	1,42	2,13	1,63	-4,20	-4,82	-10,21	1,50	6,50	4,70	9,48	3,77	9,83	7,55	6,91
	d	0,97	0,97	0,97	0,93	0,84	0,72	0,97	0,88	0,90	0,78	0,92	0,78	0,85	0,87
HK Bare Roof	R2	0,93	0,91	0,93	0,91	0,86	0,85	0,93	0,82	0,65	0,66	0,57	0,72	0,81	0,81
	AutoCor	0,97	0,95	0,97	0,95	0,93	0,92	0,97	0,91	0,81	0,81	0,76	0,85	0,90	0,90
	RMSE	3,32	3,88	3,39	4,48	6,60	9,69	3,34	8,09	9,86	12,07	9,25	11,93	9,14	8,47
	MBE	1,08	1,86	1,29	-2,16	-3,64	-7,41	1,17	6,76	7,36	10,49	6,36	10,33	7,85	7,18
	d	0,97	0,96	0,97	0,93	0,84	0,73	0,97	0,86	0,80	0,74	0,80	0,76	0,83	0,85
HK Green Wall	R2	0,76	0,80	0,77	0,89	0,59	0,79	0,77	0,86	0,85	0,88	0,88	0,87	0,86	0,86
	AutoCor	0,87	0,89	0,88	0,94	0,77	0,89	0,88	0,93	0,92	0,94	0,94	0,93	0,93	0,93
	RMSE	8,36	8,51	8,43	4,26	8,71	6,08	8,40	9,96	8,24	15,37	10,64	12,39	11,02	10,62
	MBE	7,04	7,48	7,23	1,95	6,24	1,57	7,16	9,33	6,52	14,98	10,07	11,44	10,27	9,93
	d	0,79	0,79	0,79	0,92	0,74	0,80	0,79	0,76	0,82	0,62	0,74	0,70	0,74	0,75
HK Bare Wall	R2	0,97	0,97	0,97	0,95	0,90	0,93	0,97	0,97	0,92	0,94	0,92	0,95	0,97	0,97
	AutoCor	0,98	0,98	0,99	0,98	0,95	0,97	0,98	0,98	0,96	0,97	0,96	0,98	0,98	0,98
	RMSE	3,99	4,17	4,02	4,88	6,01	8,29	3,99	7,90	7,41	13,22	9,28	11,15	8,90	8,24
	MBE	2,26	2,88	2,45	-2,30	-0,53	-4,62	2,32	7,64	6,49	12,93	8,75	10,64	8,60	7,97
	d	0,95	0,94	0,95	0,91	0,83	0,71	0,95	0,86	0,88	0,71	0,82	0,78	0,84	0,86
HK Tree	R2	0,64	0,64	0,64	0,69	0,31	0,46	0,64	0,63	0,68	0,40	0,47	0,63	0,63	0,63
	AutoCor	0,80	0,80	0,80	0,83	0,55	0,68	0,80	0,79	0,82	0,64	0,68	0,79	0,79	0,79
	RMSE	9,22	9,22	9,22	12,34	15,32	17,23	9,22	9,26	12,35	19,73	21,07	9,26	9,26	9,26

	MBE	9,16	9,16	9,16	12,18	15,20	17,06	9,16	9,20	12,20	19,48	20,75	9,20	9,20	9,20
	d	0,74	0,74	0,74	0,68	0,57	0,56	0,74	0,74	0,68	0,51	0,50	0,74	0,74	0,74
HK No Tree	R2	0,87	0,87	0,87	0,88	0,66	0,63	0,87	0,91	0,92	0,86	0,87	0,92	0,91	0,90
	AutoCor	0,93	0,94	0,93	0,94	0,81	0,80	0,93	0,96	0,96	0,93	0,93	0,96	0,95	0,95
	RMSE	7,80	7,99	7,87	5,05	9,16	9,17	7,82	10,68	8,62	15,36	11,18	12,58	11,27	10,82
	MBE	6,47	6,75	6,53	2,01	4,03	-0,10	6,47	9,73	7,21	14,67	10,32	11,36	10,20	9,79
	d	0,90	0,90	0,90	0,94	0,76	0,63	0,90	0,87	0,91	0,76	0,83	0,84	0,86	0,86

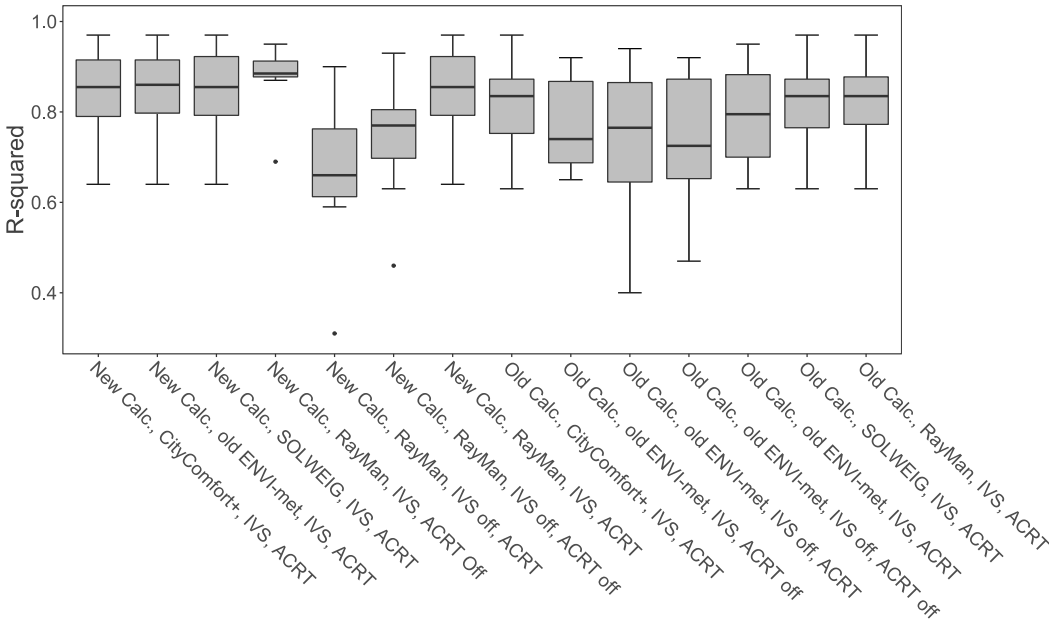

(a)

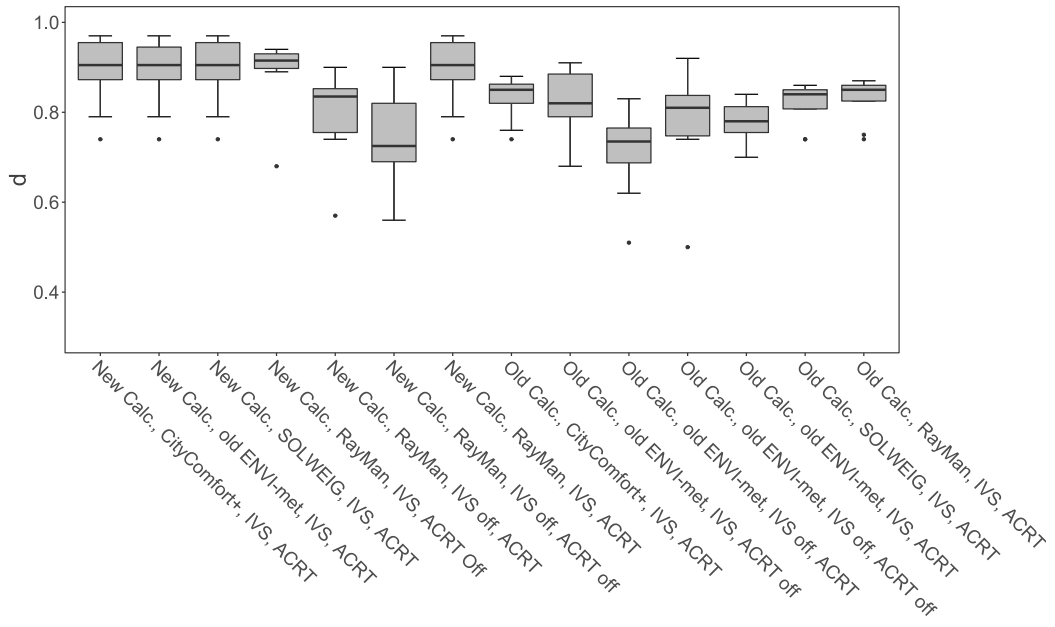

(b)

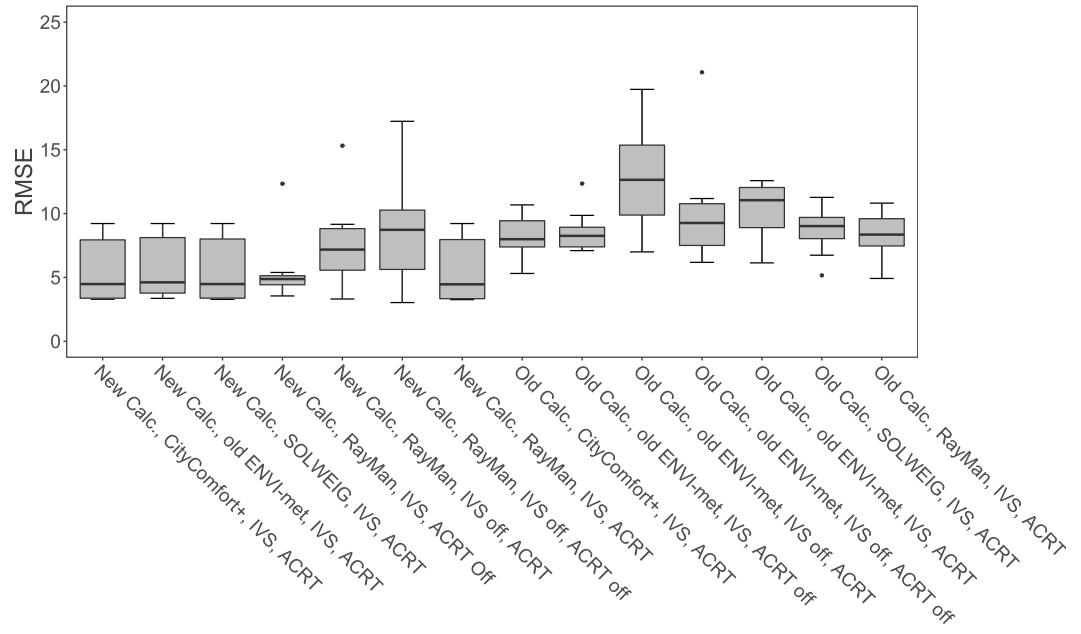

(c)

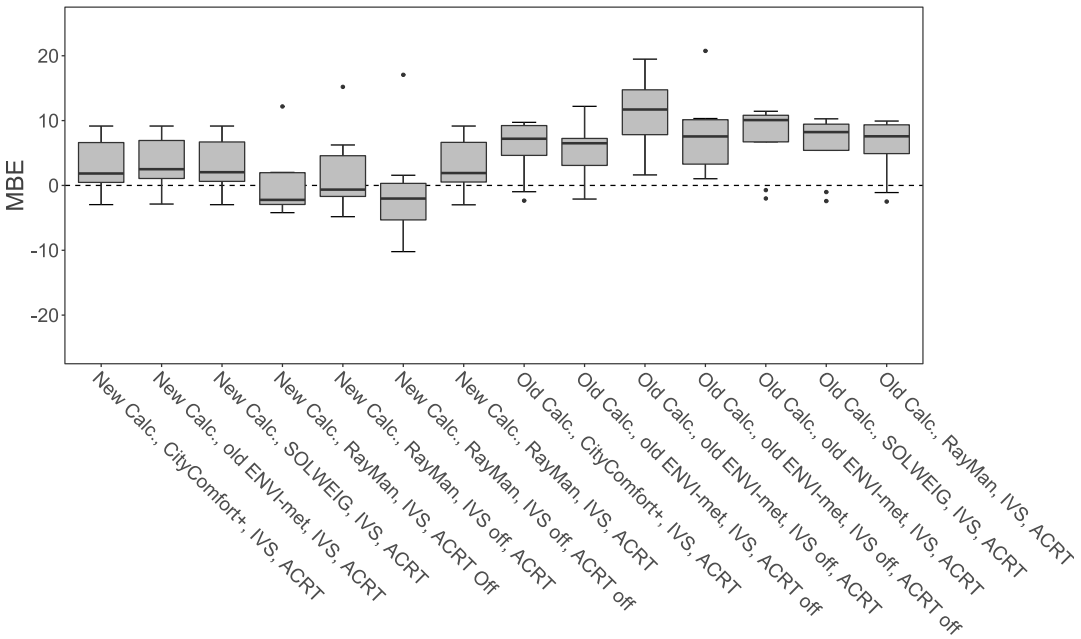

(d)

Figure 5-10: Statistical metrics of all simulated configurations.

6 Implementation of a Lagrangian Stochastic Particle Trajectory Model (LaStTraM) to simulate concentration and flux footprints using the microclimate model ENVI-met

Helge Simon[1], Jannik Heusinger[2], Tim Sinsel[1], Stephan Weber[2], Michael Bruse[1]

[1]*Department of Geography, Johannes Gutenberg University Mainz, 55099 Germany*
[2]*Climatology and Environmental Meteorology, Institute of Geoecology, TU Braunschweig, 38106 Germany*

Summary:

Besides the implementations in and evaluation of ENVI-met regarding radiation and heat stress modeling, the model also features a pollution and chemistry module that is also capable of simulating the effects of water spray. However, its particle distribution modeling is mainly based on local wind flow and, in case of particulate matter, on particle size and density. Thus, in order to validate and refine conducted eddy-covariance measurements that examine the surface-energy exchange of energy and matter, a more detailed analysis of particles' origins is needed. Therefore, the so-called flux footprint or flux source area is analyzed, which represents an estimation of the surface area influencing the signal measured at a detector location. While models were already available for analyzing flux footprints in simplified environments, a new tool called Lagrangian Stochastic Particle Trajectory Model (LaStTraM) has been developed to examine flux footprints for complex environments. Besides the previously presented advancements for the ENVI-met core, LaStTraM enables the ability to analyze flux footprints as a post-processing tool based on stochastics that are applied on ENVI-met's predicted microclimatological conditions for complex urban environments, featuring distinct objects like buildings, trees, meadows, or green roofs. The author supported Helge Simon with the development and coding of LaStTraM, conducted the comparison against other flux footprint models, prepared proof-of-concept simulations, and wrote parts of the manuscript.

Atmosphere 12(8), July 2021 – published

“

6.1 Introduction

The number of study sites for the measurement of the surface-atmosphere exchange of energy and matter such as greenhouse gases (i.e. carbon dioxide, methane, nitrous oxide) has grown substantially during recent years (Baldocchi et al., 2017; Chu et al., 2017; Konopka et al., 2021). Flux data is used to increase process understanding of the terrestrial carbon cycle, to constrain models, and to inform policy makers e.g. in the context of climate change research and for modeling purposes. The state-of-the-art method which is used at measurement sites is the eddy covariance technique. For an accurate interpretation of the flux data, it is necessary to estimate the surface area that influences the signal measured at the detector location, which is the so-called flux footprint or flux source area (Leclerc and Foken, 2014; Schmid, 2002; Vesala et al., 2008). The concentration or flux footprint of a quantity is a function of the characteristics of the earth surface, the state of the atmosphere as well as the height of the detector above ground level. At the surface, the distribution of sources and sinks (homogenous/heterogeneous), the surface roughness length, and the topography are important factors in shaping the footprint’s location and dimensions. Atmospheric stability, wind speed and direction as well as turbulent intensity are atmospheric factors influencing the footprint. For this purpose, several models have been published since the 1990s which can be distinguished into four categories: (1) analytical models (Horst and Weil, 1994; Hsieh et al., 2000; Kljun et al., 2015, 2004; Kormann and Meixner, 2001; Schuepp et al., 1990), (2) Lagrangian stochastic particle dispersion models (LS) (Horst and Weil, 1992; Kljun et al., 2002), (3) large-eddy simulations (LES) (Cai and Leclerc, 2007; Hellsten et al., 2015; Leclerc et al., 1997), and (4) closure models (Kurbanmuradov et al., 2003; Luhar and Rao, 1994; Sogachev et al., 2002).

Most of the available footprint models are valid only in case of a homogeneous source and in flat topography. This includes all models based on analytically derived mathematical expressions to calculate advection and diffusion of the quantity of interest. LES footprint models (Hellsten et al., 2015) and closure models (Sogachev et al., 2002) overcome this limitation, i.e. they are able to simulate fluxes in heterogeneous environments, e.g. high vegetation, forests, and urban areas. One characteristic of the first mentioned type of models is the high computational demand. This means that only computer clusters with hundreds of processors are able to calculate footprints in reasonable time. In contrast,

Reynolds-Averaged Navier-Stokes (RANS) models have lower computational demand and can hence run on personal computers. However, as (Hellsten et al., 2015) state there is no backward-integration approach for any building-resolving LES-LS footprint predictions available yet. Backward-integration approaches represent a backward tracking of particles from target (detector) to source (emission source). Compared to forward tracking from source to target, where a multitude of particles is tracked without ever reaching the detector zone, backward approaches feature a significantly higher computational efficiency as the number of particles eventually reaching the detector zone is already determined at simulation start. That allows to define smaller detector zones to be thus comparable with real measurement devices (Kljun et al., 2002).

In the present study, the microclimate model ENVI-met (Bruse and Fleer, 1998), a RANS model, was coupled to a newly developed Lagrangian model called LaStTraM (Lagrangian Stochastic Trajectory Model) to simulate particle trajectories with a backward-integration approach based on the microclimate's three-dimensional output data in order to close this gap. Since ENVI-met features a sophisticated plant physiology stomata model (A-gs; (Jacobs, 1994)) to simulate transpiration and carbon uptake of plants, the influences of heterogeneous sources and source distributions (e.g. trees, shrubs, grass) on the footprint can be modelled in complex topographies (e.g. within dense and complex urban areas) (Michael Bruse, 2004; Simon et al., 2018). LaStTraM works with all ENVI-met versions including the free LITE version.

To evaluate the capability of the newly developed post-processing Lagrangian model to simulate footprints in a homogeneous scenario, the model results are compared to a well-known Lagrangian model from Kljun et. al. (Kljun et al., 2015, 2004) and an analytic model from Kormann and Meixner (Kormann and Meixner, 2001). Furthermore, the influence of heterogeneous sources in more complex model areas onto the concentration and the flux footprint is discussed.

6.2 Model description

In an offline coupling, all necessary atmospheric parameters for the calculations of LaStTraM are taken from simulation outputs provided by the microclimate model ENVI-met. The model ENVI-met is a prognostic, three-dimensional, high resolution microclimate model. With its physical fundamentals that

are based on the principles of fluid mechanics, thermodynamics, and the laws of atmospheric physics, it is able to calculate three-dimensional wind fields, turbulence, air temperature and humidity, radiative fluxes, and building physics (Bruse, 1999; Simon, 2016).

One of the key features of ENVI-met is the detailed modeling of vegetation. With its high spatial resolution (< 5 meters), ENVI-met allows the simulation of the individual photosynthesis rates, taking into account local solar radiation, air temperature and humidity, wind speed, CO_2 concentration, among other parameters (Michael Bruse, 2004).

The spatial and temporal evolution of the wind field is calculated by applying the non-hydrostatic three-dimensional Navier-Stokes equation. Using the Boussinesq approximation, the density of air can be assumed to be constant (Bruse, 1999; Bruse and Fleer, 1998; Huttner, 2012). Turbulence in ENVI-met is parametrized using a $E - \varepsilon$ 1.5 order closure model. The $E - \varepsilon$ model basically consists of two prognostic equations, one describing the production of turbulent kinetic energy (TKE) and the other its dissipation. In contrast to first order closure models, the $E - \varepsilon$ model allows the simulation of advective processes in horizontally inhomogeneous environments without as much computation time as closure models of higher order (Ali-Toudert, 2005; Bruse, 1999).

The trajectory model horizontally and temporally interpolates all atmospheric parameter outputs from ENVI-met, making it quasi-independent of the ENVI-met model resolution. Both the interpolation as well as the advection of the particles are computed in parallel, making use of all available processor cores. Particles are released simultaneously at the start of a simulation. The interval in which simulation outputs are generated can be set by the user.

To simulate particle trajectories, LaStTraM operates with a backward-integration approach. The particles are "emitted" from the detector and are followed until predefined conditions are met e.g. particles reach coordinates where plants or sources of different compounds, such as CO_2, are located. The particles' starting position can either be set to the center of the detector or can be randomly generated inside the detector's dimensions. The number of particles to be simulated can be set freely by the user. All particles reaching certain areas are individually saved with various information such as their current three-dimensional position as well as their take off and touch down velocities.

6.2.1 Dynamic interpolation of the 3D model domain

To reduce the dependencies of the simulation on the ENVI-met model resolution, all ENVI-met model output variables are dynamically interpolated for every particle and every timestep. The interpolation is carried out using inverse distance weighting (IDW) of all adjacent atmospheric ENVI-met grids to the particle in a 3D Moore neighborhood analysis, i.e. a maximum of 27 neighboring grids are taken into the interpolation (Shepard, 1968):

$$\hat{R}_{int} = \sum_{P_{i-1,j,k}}^{P_{i+1,j,k}} \sum_{P_{i,j-1,k}}^{P_{i,j+1,k}} \sum_{P_{i,j,k-1}}^{P_{i,j,k+1}} w(i,j,k) \cdot R(i,j,k) \qquad \textit{Eq. 6-1}$$

with i,j,k as the ENVI-met grid coordinates of the particle, $\hat{R}_{int}$ as the interpolated value, $R(i,j,k)$ as the ENVI-met model value of the in the grid i,j,k and $w(i,j,k)$ as the weight corresponding to the grid cell i,j,k calculated by:

$$w(i,j,k) = \frac{d(i,j,k)^{-1}}{\sum_{P_{i-1,j,k}}^{P_{i+1,j,k}} \sum_{P_{i,j-1,k}}^{P_{i,j+1,k}} \sum_{P_{i,j,k-1}}^{P_{i,j,k+1}} d(i,j,k)^{-1}} \qquad \textit{Eq. 6-2}$$

with $d(i,j,k)$ as the Euclidean distance calculated using the 3D Pythagorean Theorem between the particles' actual position and the center of all adjacent atmospheric ENVI-met grid cells. Summing up all individual weights, the result must be equal to 1.

In case the particles' vertical position lies below the center of the lowest ENVI-met atmospheric grid cell, the interpolation of the wind vectors u, v, w is carried out using a logarithmic approach:

$$u_{int} = u_{k_0} \cdot \ln\left(\frac{P_z}{z_0}\right) \ln\left(\frac{h_{k_0,c}}{z_0}\right)^{-1}$$

$$v_{int} = v_{k_0} \cdot \ln\left(\frac{P_z}{z_0}\right) \ln\left(\frac{h_{k_0,c}}{z_0}\right)^{-1} \qquad \textit{Eq. 6-3}$$

$$w = w_{k_0} \cdot \ln\left(\frac{P_z}{z_0}\right) \ln\left(\frac{h_{k_0,c}}{z_0}\right)^{-1}$$

with u_{k_0}, v_{k_0}, w_{k_0} as the wind speed at the lowest ENVI-met atmospheric grid cell, z_0 as the roughness length of the surface, and $h_{k_0,c}$ as the height of the center point of the lowest ENVI-met grid cell, *k = 0*.

6.2.2 The Lagrangian Stochastic Model

Based on Weil et al. (2004), the particles advection is calculated by:

$$P_{pos(x,y,z),t+\Delta t} = P_{pos(x,y,z),t} + P_{V,t} \cdot \Delta t \qquad \textit{Eq. 6-4}$$

with $P_{pos(x,y,z),t+\Delta t}$ as the new position of the particle after the time interval, Δt, $P_{pos(x,y,z),t}$ as the original position of the particle, and $P_{V,t}$ as the velocity of the particle. The velocity consists of two parts: A resolved, deterministic part ($P_{v_{res}}$) that is directly simulated based on the interpolated 3D wind vector fields of ENVI-met and a stochastic, random part ($P_{V_{LS}}$):

$$P_V = P_{v_{res}} + P_{V_{LS}} \qquad \textit{Eq. 6-5}$$

The resolved velocity part $P_{v_{res}}$ is calculated by interpolating the ***u, v, w*** wind vectors for every particle position (see Eq. 6-3). The stochastic term of Eq. 6-5, $P_{V_{LS}}$, is derived from the work of Weil et al. (2004), where the considerations of Thomson (1987) are adapted. With these considerations and in accordance to Maronga et al. (2015) and Steinfeld et al. (2008), the difference in the particle's stochastic velocity is calculated by:

$$dP_{V_{LS}} = \frac{3 f_s C_0 \varepsilon}{4} \frac{P_{V_{LS}}}{e_s} dt + \frac{1}{2}\left(e_s^{-1} \frac{de_s}{dt} P_{V_{LS}} + \frac{2}{3} \nabla e_s\right) + (f_s C_0 \varepsilon)^{\frac{1}{2}} d\xi \qquad \textit{Eq. 6-6}$$

with C_0 as a universal constant of the structure function (here set to 3; as in Kljun et al., 2002), ε and e_s as the inverse distance interpolated (see: Eq. 6-1, Eq. 6-2) dissipation and TKE, respectively, $d\xi$ as a random displacement vector whose components are independent from each other and in time (Maronga et al., 2015; Steinfeld et al., 2008; Wilson and Sawford, 1996). The random number is calculated using a normal (Gaussian) distribution where the interval is limited to $\pm 5.0\sigma$. The parameter f_s defines the subgrid-scale TKE fraction of the total TKE (Steinfeld et al., 2008; Weil et al., 2004).

For the conditions at boundary surfaces of buildings and digital elevation models (DEM), the simulation can be operated in two modes: An iterative solution mode, where in case a particle's new position was located inside a surface (buildings, DEM) the advection (Eq. 6-8) would be calculated with new random terms ($(f_s C_0 \varepsilon)^{\frac{1}{2}} d\xi$) until a new position outside a solid structure is found or the maximum of 300 attempts is reached. In case no solution is found, the particle's position will be set to the previous time step. In the second mode, the termination mode, all particles that enter a solid surface (buildings, DEM)

are no longer tracked and removed from the simulation. Regardless of the boundary surfaces mode the model operates with, particles that would enter ground surface will be set to a minimum height of the user's choice (default value 0.0001 m). All particles leaving the lateral or top boundary of the model domain are removed.

While the resolved, deterministic velocity part of particles could be calculated in quite large time steps depending on grid size and velocity (e.g. CFL-Condition), the calculation of particles' Lagrangian stochastic velocity demand much smaller timescales (Weil et al., 2004).

$$dt_{LS} = \frac{4e_s}{3f_s C_0 \varepsilon} \qquad \textit{Eq. 6-7}$$

To ensure small time steps, an upper limit of at least $dt_{LS}/40$ is defined (Maronga et al., 2015).

6.3 Footprint calculation

A variety of information is stored for every particle that reaches its target. This information includes the starting position within the detector, the final position within an emitter, travelled distance, elapsed time, mean velocity, as well as initial and final w wind vector velocity. Since all data is stored for every particle reaching its target, the resulting file might be quite large (e.g., ~5 GB for around 20.000.000 particles reaching a source area).

To determine the relative contribution of a source to a measured concentration or flux at a predefined detector area, calculations can be performed that determine which surfaces / objects in a model area contribute to a measured concentration and flux at a given volume in space using the data information of the particles. The calculations of the concentration footprint C and the flux footprint F are carried out in accordance to Vesala et al. (2008) and (Flesch, 1996):

$$C(x,y,z) = \frac{2}{N}\sum_{i=1}^{n}\frac{1}{w_{Emit,i}}Q(x,y,z) \qquad \textit{Eq. 6-8}$$

$$F(x,y,z) = \frac{2}{N}\sum_{i=1}^{n}\frac{w_{Det,i}}{w_{Emit,i}}Q(x,y,z) \qquad \textit{Eq. 6-9}$$

with x, y, z as the grid coordinates, Q as the source's strength, N as the total number of particles, n as the number of particles reaching the detector zone. $\sum_{i=1}^{n}$ represents the sum of all particles reaching

the target zone, $w_{Det,i}$ the initial w component at a particle's release at starting point within the detector zone and $w_{Emit,i}$ as the w component of wind velocity at touch down at source area (Markkanen et al., 2015; Vesala et al., 2008).

6.3.1 Simulating footprints in homogeneous model area – comparison with other models

In order to evaluate the newly developed model, it is compared against two established and well-known footprint models: the Flux Footprint Predictions model (FFP) by Kljun et al. (2002) and the analytic Kormann-Meixner model (K-M; Kormann and Meixner, 2001). To prove the functionality of the newly developed model LaSTraM, the presented evaluation is held similar to the analysis of these models. It is hence based on two common meteorological cases (stable and unstable) and features the same corresponding detector heights (3 m, 20 m, and 40 m).

The analyzed model area is similar to the one used in (Kljun et al., 2002). It consists of 400 x 400 x 40 grids with a horizontal resolution of 5 m and a vertical resolution of 2 m in a non-equidistant gridding, where the lowest grid cell is split into 5 subcells. The total extent of the area is thus 2000 m x 2000 m x 70 m. The model area features no building structures or other obstacles, the soil was digitized as "loamy soil", and the vegetation was set to grass of 0.2 m height throughout the whole model area, thus creating a homogeneous case.

The ENVI-met simulation was set to start at 6 am on June 23rd, the simulation ran for 24 simulation hours. The meteorological boundary conditions can be seen in Figure 6-1, the boundary conditions for wind speed and direction were constant and set to 2 m s^{-1} in 10 m height and 90° over the whole simulation time. The post processing analysis in LaStTraM was run using the model outputs of the ENVI-met simulations. Each simulation featured 10^8 particles. It took around 5.5 hours to simulate the trajectories of the released 100 million particles in the 2 km x 2 km large area on a personal computer with an Intel Core i7-6700 CPU @ 3.40GHz (Table 6-1).

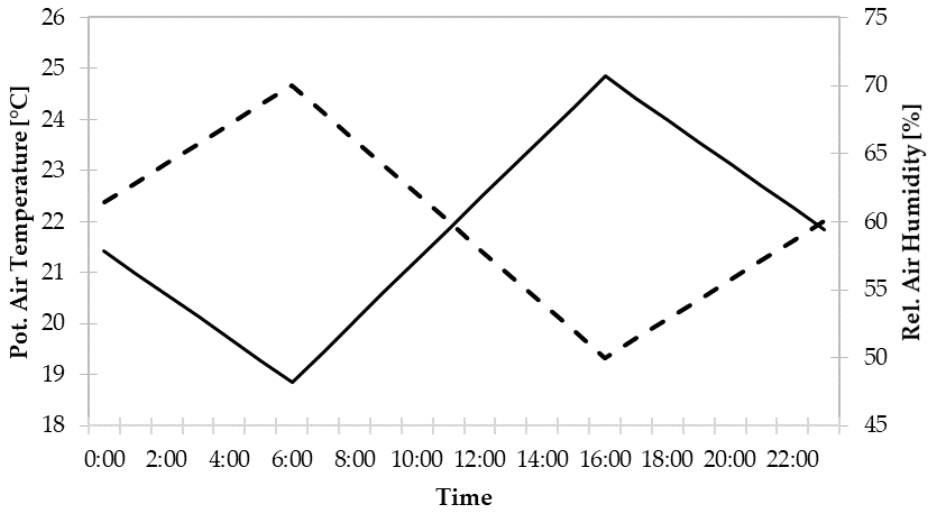

Figure 6-1: Diurnal boundary conditions for potential air temperature (solid line) and relative humidity (dashed line).

Table 6-1: Simulated particles and simulation duration per examined scenario.

Time	Simulated particles	Simulation time
15:00 h (unstable case)	10^8	5 hrs 21 mins
03:00 h (stable case)	10^8	5 hrs 46 mins

The footprint is sensitive to atmospheric stability, surface roughness, measurement height, and wind direction (Kljun et al., 2002; Vesala et al., 2008). Since the atmospheric stability is a prognostic parameter of the microclimate model ENVI-met, the output files have to be analyzed to differentiate between unstable, stable, and neutral conditions. Analysis of the different output files showed an unstable atmosphere at 15:00 h and a stable atmosphere in the early morning hours around 3:00 h (Figure 6-2). In order to compare the LaStTraM results with Kljun et al. (2002) and Kormann and Meixner (2001), the output files of these hours have been used for the further analysis.

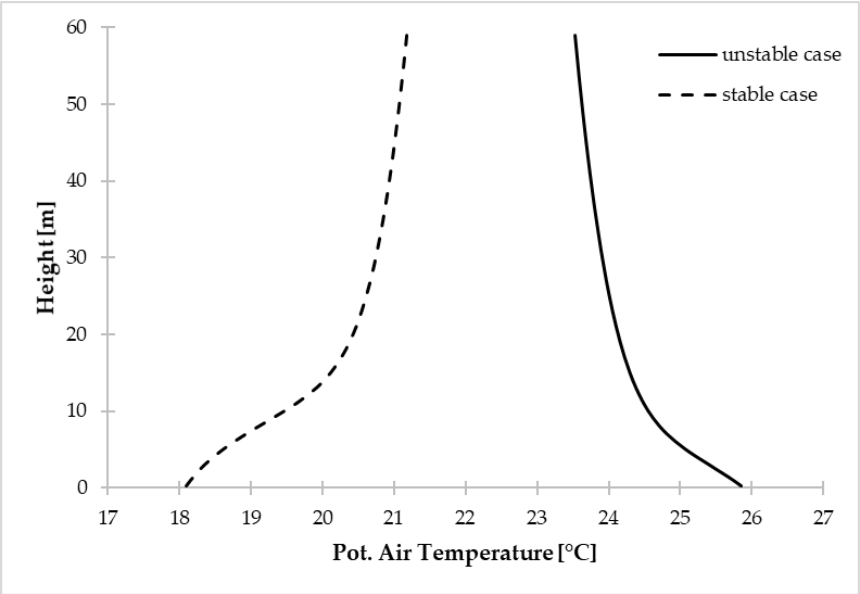

Figure 6-2: Vertical profile of the potential air temperature at 15:00h and 03:00h.

To compare the flux footprint results simulated with LaStTraM against the FFP model and the K-M-model, simulations using combinations of different detector heights (3 m, 20 m and 40 m) and atmospheric stabilities (15:00 h unstable case and 03:00 h stable case) were conducted.

Apart from the friction velocity (u^*), all input parameters for the FFP and K-M model could be directly extracted from the output data of ENVI-met. The friction velocity (u^*) was then calculated by:

$$u^* = \frac{u * \kappa}{\ln\left(\frac{h}{z_0}\right)} \qquad \textit{Eq. 6-10}$$

with u as the wind speed, κ the von Karman constant (here 0.4), h as the height above ground, and z_0 as the roughness length. Table 6-2 shows all input parameters used to run FFP and K-M models.

Table 6-2: Input parameters for running the models FFP and K-M.

Parameter	Detector 3m	Detector 20m	Detector 40m
Vegetation height (z_{veg})	0.2 m	0.2 m	0.2 m
Detector height ($z_{sens40m}$)	3.25 m	20.5 m	40.5 m
Displacement height (d)	2/3 * z_{veg} = 0.134 m		
Measurement height above vegetation (z_{40m})	3.116 m	20.366 m	40.366 m
Mean wind speed at z_m unstable ($umean_{day}$)	1.26 m/s	1.86 m/s	2.00 m/s
Mean wind speed at z_m stable ($umean_{night}$)	1.26 m/s	1.86 m/s	2.02 m/s
Boundary layer height unstable (h_{day})	2500 m		
Boundary layer height stable (h_{night})	800 m		
Obukhov length unstable (ol_{day})	-7.55 m	-7.52 m	-7.51 m
Obukhov length stable (ol_{night})	18.99 m	19.22 m	19.25 m

6.3.2 Simulating footprints in an inhomogeneous model area

By coupling LaStTraM with ENVI-met's three-dimensional model outputs, the model is able to simulate footprints in model areas featuring obstacles such as buildings or vegetation. To evaluate the influence of obstacles on the footprint, a simple inhomogeneous and one complex realistic scenario were analyzed.

In the simple inhomogeneous scenario, a symmetrical obstacle (building) with a height of 20 meters and a tree is added to the homogeneous model area. The detector is then placed in 3 meters above ground at different distances to the obstacle (125 m and 820 m upwind distance from the obstacle) (Figure 6-3).

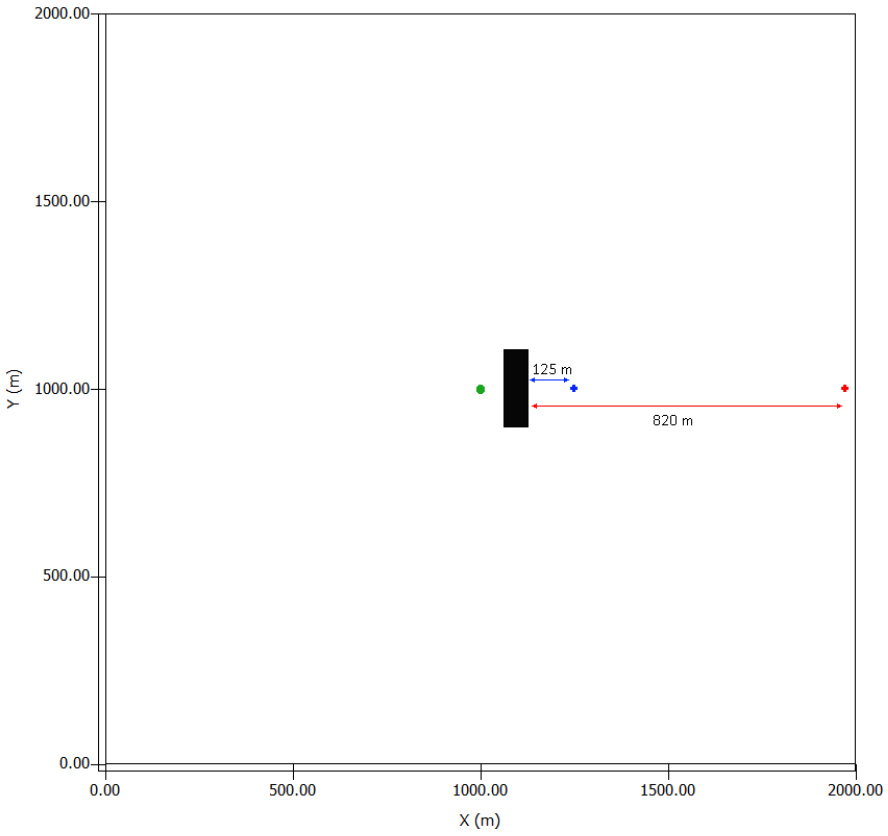

Figure 6-3: Model area for the simple inhomogeneous simulation featuring a building (black) a tree (green) and two detectors (blue and red).

The simple inhomogeneous model run featured identical meteorological boundary conditions as the homogeneous model run. To reduce the computational cost, the model was only run for unstable case at 15:00 h.

6.3.3 Simulating footprints in realistic model area

In a realistic scenario, the performance of LaStTraM is evaluated in an urban model area featuring buildings, different soil, and surface materials, as well as vegetation (Figure 6-4). While this scenario, due to

the lack of empirical data, cannot be seen as prove that the model is operating accurately in a complex environment, the scenario is designed to be a showcase visualizing the capabilities of the model.

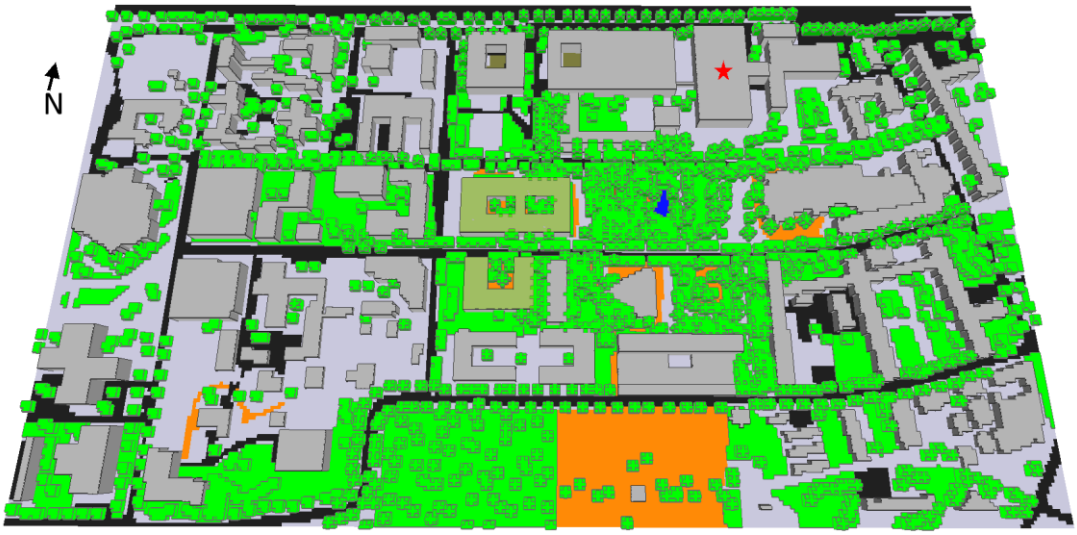

Figure 6-4: Model area for the realistic case simulation. Detector location is indicated by the red star.

The model area is located in Mainz, Germany and extends over 900 meters x 510 meters horizontally and 200 meters vertically in a 3 meters x 3 meters x 2.5 meters resolution. Again, a non-equidistant gridding, where the lowest grid cell is split into 5 subcells is chosen.

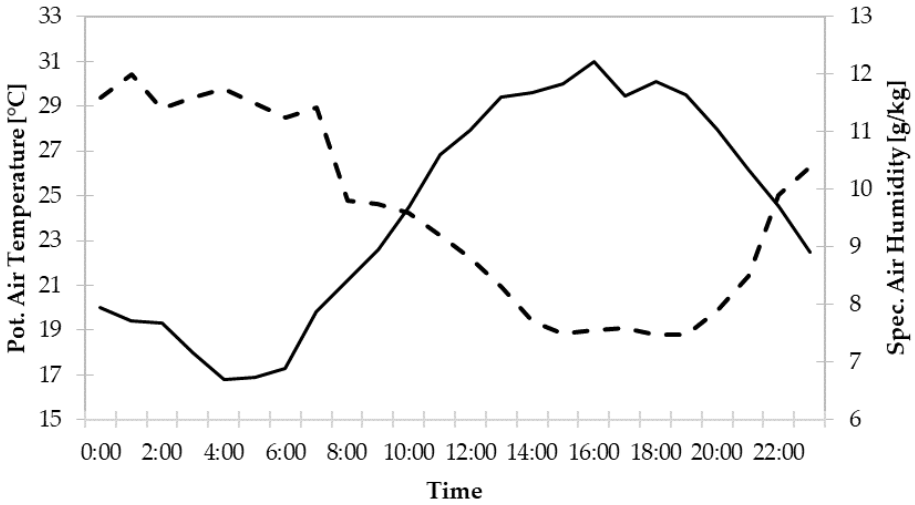

Figure 6-5: Meteorological boundary conditions for the proof-of-concept simulation. Potential air temperature (solid line) and specific air humidity (dashed line).

The meteorological boundary conditions were taken from an Energy Plus Weather File for Frankfurt, Germany. To resemble a hot summer day with clear sky conditions, July 7th was selected as simulation date. The wind speed was set to 1.5 m/s in 10 meters height coming from 230°. The simulation has been

run for 24 hours. Figure 6-5 shows the meteorological conditions for the whole simulation period provided by the EPW-file.

6.4 Results & Discussion

To give an overview on the capabilities of LaStTraM, model results of the homogenous, simple inhomogeneous, and complex model areas are presented. To evaluate the performance of LaStTraM, the results of the homogeneous model area are compared against the FFP model and the K-M-model. Since no other model was available to compare the simple inhomogeneous and complex model area outputs, their results are only visualized, and their plausibility is discussed.

6.4.1 Evaluation of homogeneous model area results

The evaluation of the ENVI-met based footprint simulation LaStTraM with two well-known models, an analytical model and a model that is based on a Lagrangian model (Kljun et al., 2015; Kormann and Meixner, 2001), demonstrates that the modeled footprints are comparable for detector heights of 3 m, 20 m, and 40 m in stable and unstable conditions despite the structural differences of the models (Figure 6-4). In the unstable cases, the maximum footprint contribution (f_{max}) of LaStTraM tends to be higher than the other two models while the length of the footprint (x_{max}) tends to be slightly shorter in LaStTraM. This phenomenon featuring both, an underestimation of f_{max} and an overestimation of the footprint length x_{max} of the FFP and K-M model, was also attested by Heidbach et al. (2017). Similarly, Van de Boer et al. (2013) concluded that the FFP model and two other models rather overestimated the footprint length. Regarding the distance between the detector and f_{max} (x_{max}), LaStTraM shows very similar results compared to the FFP and K-M model with slightly shorter distances in the unstable cases and distances between the FFP and K-M model in the stable cases (Table 6-3).

The footprints generated by LaStTraM show a behavior that is well-known from other models: The footprint length increases with atmospheric stability while f_{max} decreases. Increasing the detectors' height leads to an increase of the footprints' width and x_{max} but decreases f_{max}.

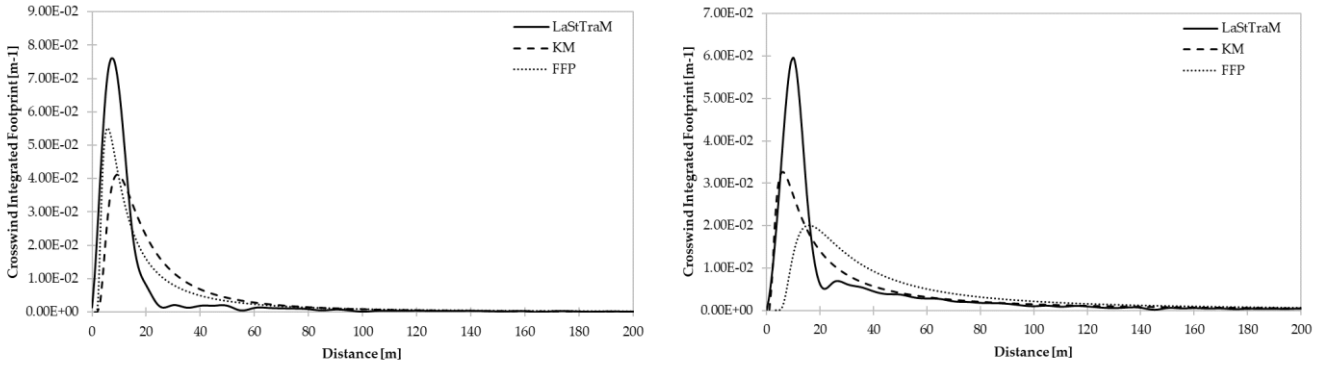

(a)

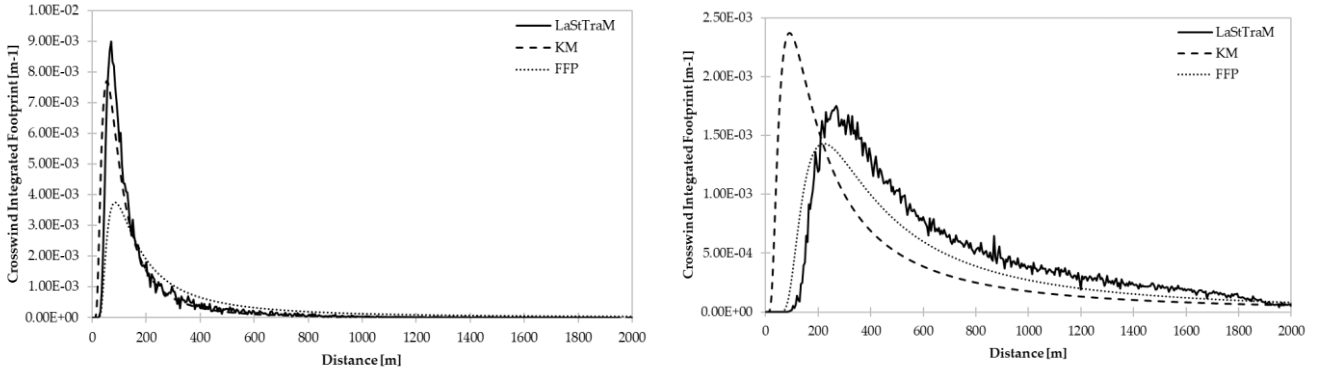

(b)

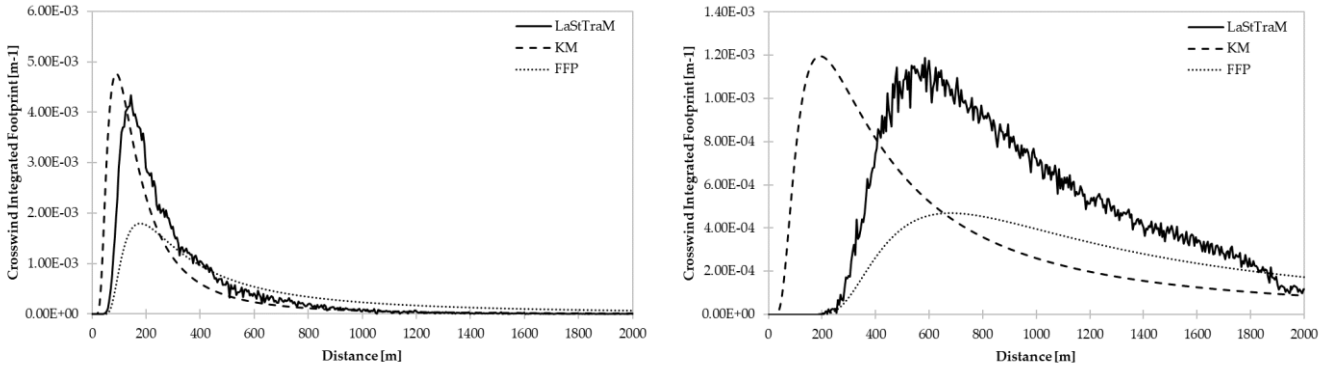

(c)

*Figure 6-6: Comparison of crosswind integrated footprints of LaStTraM, FFP and K-M for different detector heights in an unstable (left column) and stable (right column) case. (**a**) height of detector 3 meters above ground (**b**) height of detector 20 meters above ground (**c**) height of detector 40 meters above ground.*

Looking at the differences in x_{max} between the three models, it becomes clear, that LaStTraM predicts similar results as FFP (Table 6-3). This stands in contrast to f_{max}, where LaStTraM shows more similar values to K-M.

Table 6-3: Crosswind distance between f_{max} and detector (x_{max}).

	Detector 3m			**Detector 20m**			**Detector 40m**		
	LaStTraM	FFP	K-M	LaStTraM	FFP	K-M	LaStTraM	FFP	K-M
Unstable case	7 m	6 m	9 m	69 m	86 m	54 m	148 m	180 m	88 m
Stable case	10 m	16 m	6 m	269 m	226 m	92 m	598 m	690 m	193 m

Aside from the two-dimensional crosswind integrated visualization, LaStTraM saves three-dimensional output files that can be visualized using ENVI-met's visualization tool LEONARDO. Figure 6-7 shows two-dimensional representations of the three-dimensional outputs of the homogeneous model area.

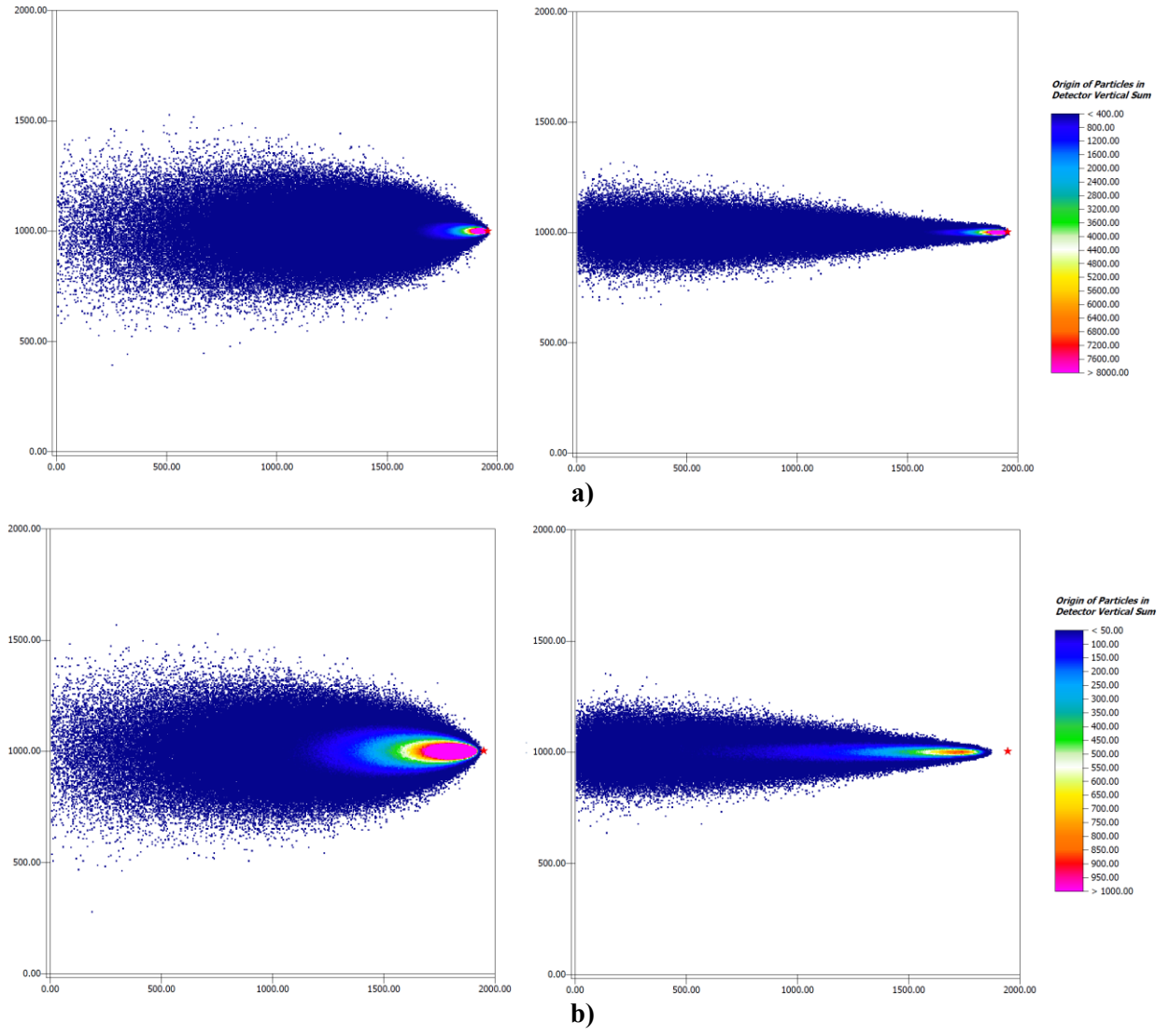

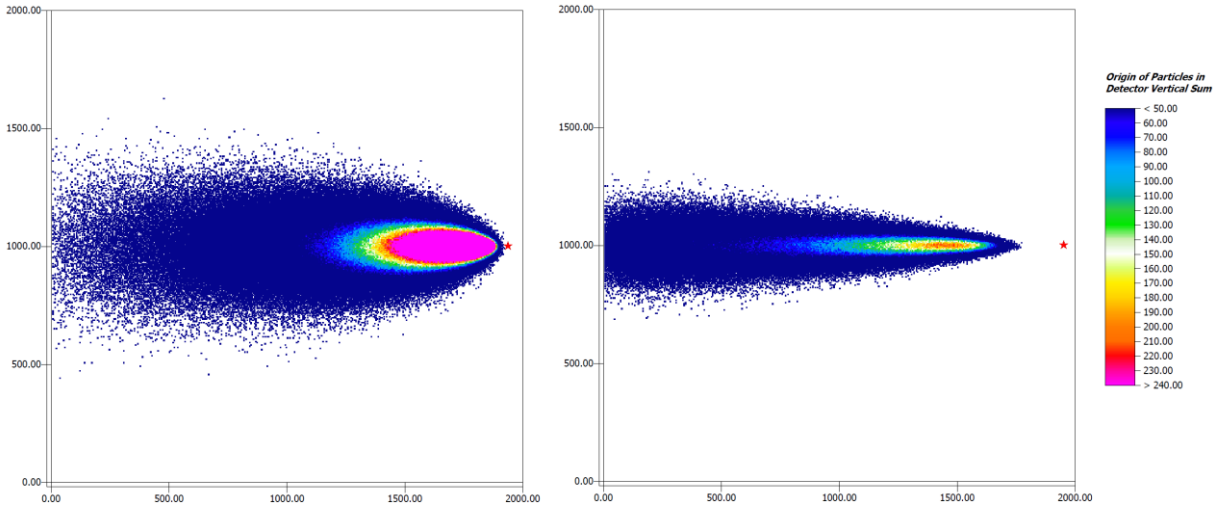

c)

Figure 6-7: Origin of particles modelled for the unstable cases (left) and the stable cases (right) featuring detector heights of 3 meters (a), 20 meters (b) and 40 meters (c) for the homogenous model area. Red star indicates detector position.

The two-dimensional distribution of the footprint shows that the maximum of the three-dimensional footprint is much closer to the detector location in the unstable case than in the stable case (Figure 6-7). Furthermore, the along-wind distance is increased in the unstable case compared to the stable case. In general, the footprint of the unstable case is broader due to more turbulences and thus higher atmospheric mixing during daytime.

The evaluation of the new footprint model in comparison with the established models FFP and K-M shows that LaStTraM is capable of reproducing their results. The calculated footprints resemble the results of both models and even improve the imprecisions mentioned by Heidbach et al. (2017) and Van de Boer et al. (2013), i.e. LaStTraM does most likely not underestimate f_{max} and overestimate the footprint length.

6.4.2 Evaluation of simple inhomogeneous model area results

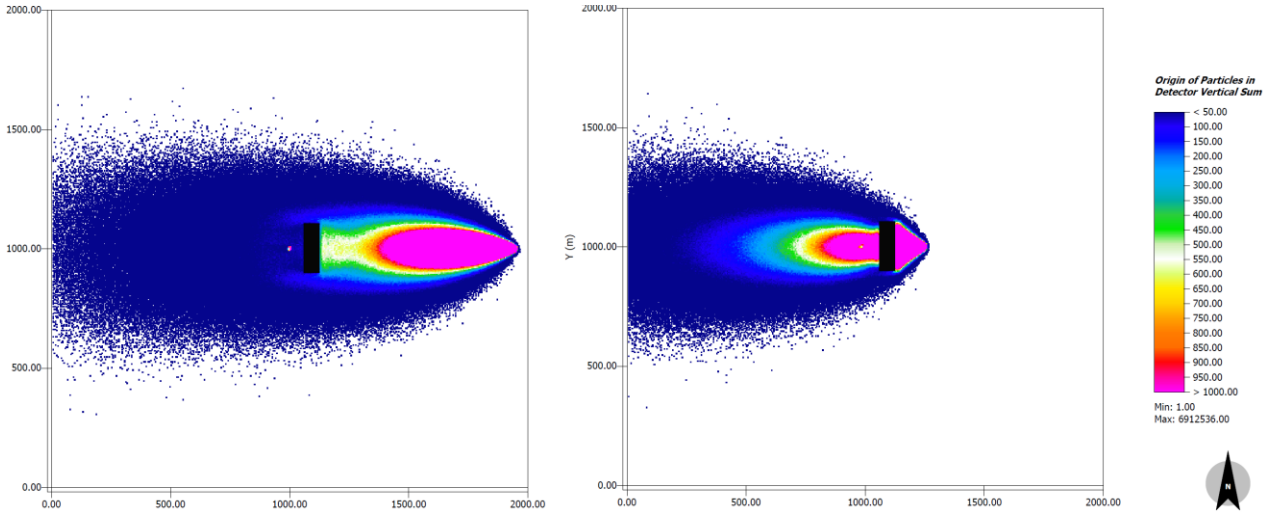

Figure 6-8: Origin of particles modelled for the unstable case featuring a detector height of 3 m with a distance of 820 m (left) and 125 m (right) to building.

The results of the simple inhomogeneous case indicate that the tree contributes significantly different to the footprint compared to the grass vegetation at the same distance to the detector (Figure 6-8). In the simulation where the detector is positioned close to the building, less particles reach the tree compared to grass cells at the same distance. This is caused by the flow induced by the building that leads to a significant updraft downwind of the tree (Figure 6-9). In comparison to the grass at the same location, less particles are thus traced back to the tree from the detector close to the building.

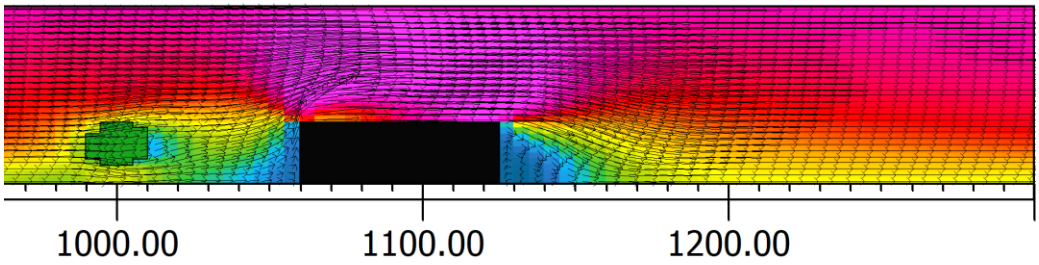

Figure 6-9: Two-dimensional vertical cut visualizing the wind flow in the inhomogeneous model area.

In the simulation, where the detector is placed further downstream of the building the same effect – uplifting of flow and subsequent down-drafting due to the building leads to more particles reaching the tree compared to the grass vegetation below the tree. Furthermore, it can be seen, that despite the simple inhomogeneous model area and the Lagrangian Stochastic approach, where the particles' velocity is calculated including a stochastic, random part ($P_{V\,LS}$ in Eq. 6-7), the vast number of simulated particles (100 million) ensures a high symmetry of the footprint (Figure 6-8Figure 6-6).

Both footprints show greater horizontal extends than in the homogenous results. This is likely caused by the much higher turbulence induced by the complex structures in the model area. Nevertheless, with increasing distance, the number of particles from emitter cells decreases just like in the homogeneous case.

6.4.3 Evaluation of realistic model area results

The results for the realistic model area confirm the general functionality of the model in complex model domains. Despite having no measurement data for this scenario, the distribution of particles shows plausible results: Vegetation closer to the detector are reached by more particles than in further distance and the horizontal extend increases with increased distance from the detector (Figure 6-10). Also, vegetation with greater vertical extent i.e., larger trees are reached more likely by the particles released from the detector. This is especially the case for the trees directly located upwind of the detector as the flow passing through them is lifted and directed upwards towards the detector's location.

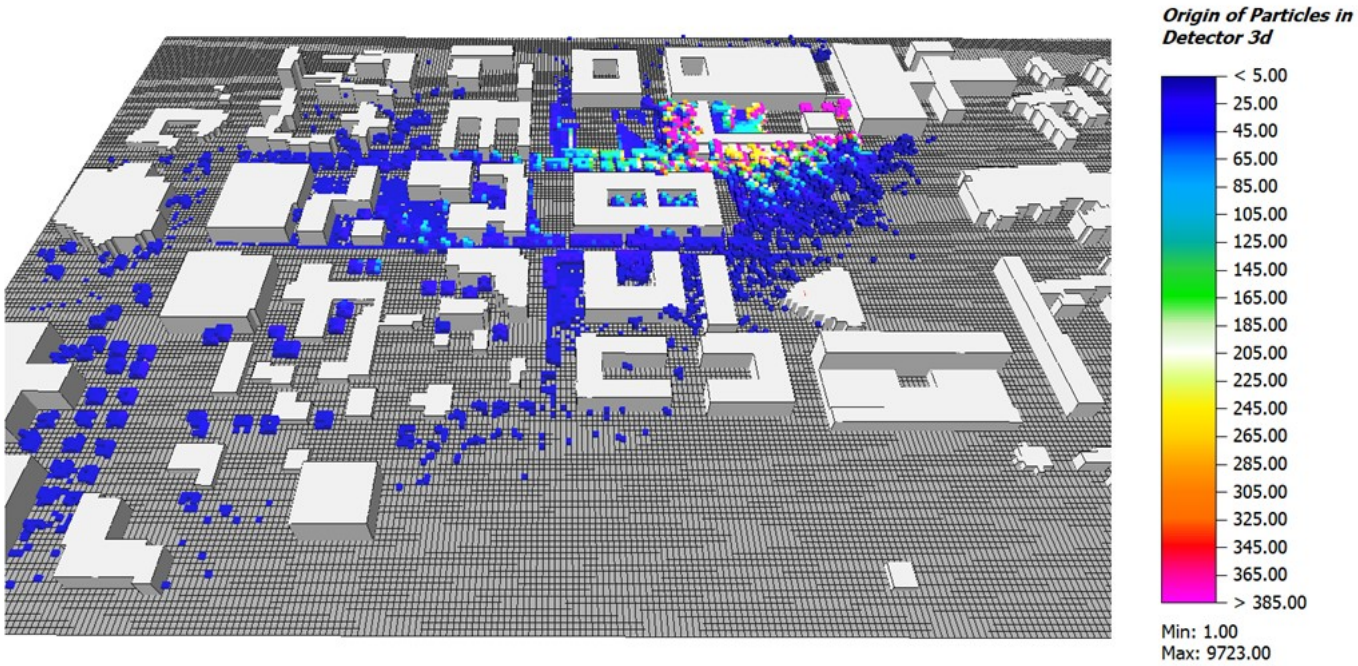

a)

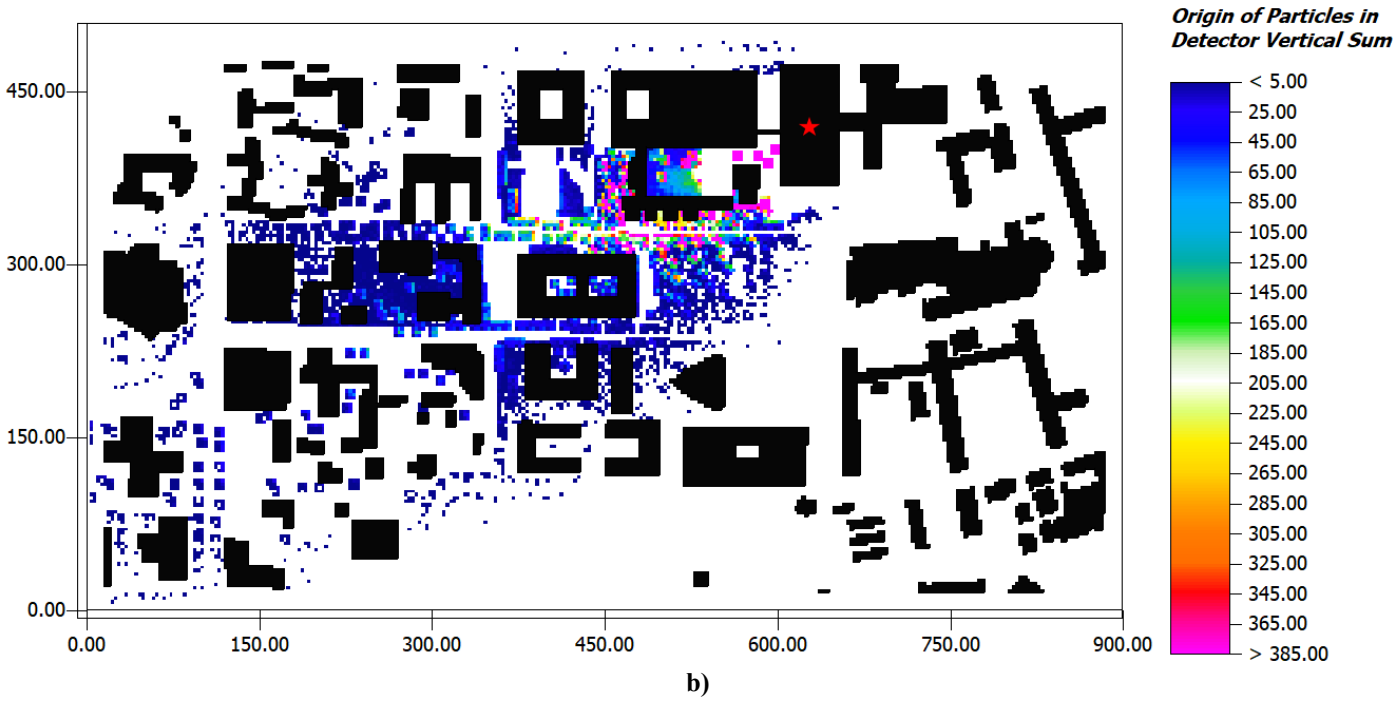

b)

*Figure 6-10: Three-dimensional (**a**) and two-dimensional (**b**) visualization of origin of particles in the complex model area. The red star in (**b**) represents the detector location.*

6.5 Conclusion

Based on the three-dimensional model outputs of the microclimate model ENVI-met, the post-processing tool LaStTraM simulates probability distributions of particles using the Lagrangian Stochastic method. Combining LaStTraM with ENVI-met should allow to simulate flux and concentration footprints in complex urban environments.

A footprint comparison for homogenous model areas between LaStTraM and two established models shows slight deviations for the maximum footprint contribution (f_{max}) and the footprint length (x_{max}). These deviations, however, might be a result of an underestimation of f_{max} and overestimation x_{max} by both the FFP and K-M model as demonstrated by earlier studies (Heidbach et al., 2017; van de Boer et al., 2013). The results of the inhomogeneous model area and the complex model area shows reasonable results where the effects of obstructions alter the particle distribution significantly. While these scenarios provided promising results, a comparison with empirical data would be needed in order to verify the accuracy of the model in complex urban areas.

The great potential of LaStTraM lies in its ensemble with ENVI-met's averaged Navier Stokes model outputs, that should allow the study of footprints in heterogeneous and hilly environments. Our attempt

to simulate a footprint in heterogeneous conditions demonstrated the capabilities of the model, i.e. incorporating three-dimensional emitters as well as the influence of obstacles on particle trajectories.

By incorporating ENVI-met's physiological aspects of vegetation, i.e. the cell based calculation of stomatal conductance and thus transpiration, the simulation of the footprint using LaStTraM can further be improved. Footprints of different compounds can also be studied separately, depending on the variable of interest. For example, the dependency of various compounds on the flux footprint can be studied by defining individual areas/volumes that act as sources of these compounds. All results can then be visualized with the built-in ENVI -met program LEONARDO.

It was demonstrated that 100 million particles within a 2 x 2 km^2 model area can be modelled within a few hours on a PC. The order of magnitude of particle numbers, the model area size as well as the grid resolution are comparable to numbers reported in LES footprint studies before (Hellsten et al., 2015), with the essential difference that the footprint model is run in backwards mode which means that every modelled particle (that hits a source in the model domain) influences the footprint. In contrast to a forward in time trajectory mode, the backwards mode has the advantage that detector does not have to be unrealistically large in order to gather a sufficiently large number of particles, as demonstrated before (Hellsten et al., 2015).

One drawback to eddy covariance users is that the ENVI-met model cannot be run routinely for each 30 min flux averages, which it has in common with all RANS and LES models. A possibility to simulate whole years with the microclimate model ENVI-met could be to split the simulations into partially overlapping timeframes, e.g. 12 simulations, for every month of the year including couple of days of overlap. These could be run on 12 PCs in parallel and the overlapping results could in the end be stitched together to create a year-long simulation (Simon et al., n.d.).

Regardless of the timeframe, LaStTrAM is capable of reproducing typical atmospheric conditions (unstable, stable) that will help to elucidate the origin of measured fluxes in heterogeneous environments. The LaStTraM footprint model is therefore uniquely positioned for eddy covariance studies in complex urban terrains, where the premises of analytic models are generally not met. It also can be used to analyze

flux footprint problems that frequently occur in rural locations when eddy covariance towers are positioned close to forest edges or when other steep changes in roughness occur.

The present work does by far not exploit the whole potential of LaStTraM, as larger and especially more complex areas could be modelled in future studies. Furthermore, it has the potential to model the footprint of reactive gases instead of only inert particles as shown in this study. Vesala et al. (2008) highlight the potential of ensemble-averaged closure models especially for sites with complex topography and canopy heterogeneity. This includes urban sites, which are of increasing interest in surface-atmosphere exchange studies. By combining LaStTraM with ENVI-met, model areas featuring buildings, sources, vegetation, and uneven terrain can be simulated. This makes it a viable tool to calculate and analyze three-dimensional footprints in complex environments.

6.6 References

Ali-Toudert, F., 2005. Dependence of Outdoor Thermal Comfort on Street Design in Hot and Dry Climate (Dissertation). Albert-Ludwigs-Universität Freiburg.

Baldocchi, D., Chu, H., Reichstein, M., 2017. Inter-annual variability of net and gross ecosystem carbon fluxes: A review. Agricultural and Forest Meteorology. https://doi.org/10.1016/j.agrformet.2017.05.015

Bruse, M., 2004. ENVI-Met Implementation of the Jacobs A- Gs Model to Calculate the Stomata Conductance. Bochum.

Bruse, M., 1999. Die Auswirkungen kleinskaliger Umweltgestaltung auf das Mikroklima. Entwicklung des prognostischen numerischen Modells ENVI-met zur Simulation der Wind-, Temperatur- und Feuchteverteilung in städtischen Strukturen (PhD Thesis). Ruhr-University Bochum, Bochum.

Bruse, M., Fleer, H., 1998. Simulating Surface Plant Air Interactions inside Urban Environments with a Three Dimensional Numerical Model. Environmental Modelling & Software 13, 373–384. https://doi.org/10.1016/S1364-8152(98)00042-5

Cai, X., Leclerc, M.Y., 2007. Forward-in-time and Backward-in-time Dispersion in the Convective Boundary Layer: the Concentration Footprint. Boundary-Layer Meteorology 123, 201–218. https://doi.org/10.1007/s10546-006-9141-x

Chu, H., Baldocchi, D.D., John, R., Wolf, S., Reichstein, M., 2017. Fluxes all of the time? A primer on the temporal representativeness of FLUXNET. Journal of Geophysical Research: Biogeosciences 122, 289–307. https://doi.org/10.1002/2016JG003576

Flesch, T.K., 1996. The footprint for flux measurements, from backward Lagrangian stochastic models. Boundary-Layer Meteorology 78, 399–404. https://doi.org/10.1007/978-94-017-0944-6_17

Heidbach, K., Schmid, H.P., Mauder, M., 2017. Experimental evaluation of flux footprint models. Agricultural and Forest Meteorology 246, 142–153. https://doi.org/10.1016/j.agrformet.2017.06.008

Hellsten, A., Luukkonen, S.-M., Steinfeld, G., Kanani-Sühring, F., Markkanen, T., Järvi, L., Lento, J., Vesala, T., Raasch, S., 2015. Footprint Evaluation for Flux and Concentration Measurements for an Urban-Like Canopy with Coupled Lagrangian Stochastic and Large-Eddy Simulation Models. Boundary-Layer Meteorology 157, 191–217. https://doi.org/10.1007/s10546-015-0062-4

Horst, T.W., Weil, J.C., 1994. How Far is Far Enough?: The Fetch Requirements for Micrometeorological Measurement of Surface Fluxes. Journal of Atmospheric and Oceanic Technology 11, 1018–1025. https://doi.org/10.1175/1520-0426(1994)011<1018:HFIFET>2.0.CO;2

Horst, T.W., Weil, J.C., 1992. Footprint estimation for scalar flux measurements in the atmospheric surface layer. Boundary-Layer Meteorology 59, 279–296. https://doi.org/10.1007/BF00119817

Hsieh, C.-I., Katul, G., Chi, T., 2000. An approximate analytical model for footprint estimation of scalar fluxes in thermally stratified atmospheric flows. Advances in Water Resources 23, 765–772. https://doi.org/10.1016/S0309-1708(99)00042-1

Huttner, S., 2012. Further development and application of the 3D microclimate simulation ENVI-met (Dissertation). Johannes Gutenberg-University Mainz.

Jacobs, C.M.J., 1994. Direct impact of atmospheric CO2 enrichment on regional transpiration (Dissertation). Agricultural University Wageningen, Wageningen.

Kljun, N., Calanca, P., Rotach, M.W., Schmid, H.P., 2015. A simple two-dimensional parameterisation for Flux Footprint Prediction (FFP). Geosci. Model Dev. 8, 3695–3713. https://doi.org/10.5194/gmd-8-3695-2015

Kljun, N., Calanca, P., Rotach, M.W., Schmid, H.P., 2004. A Simple Parameterisation for Flux Footprint Predictions. Boundary-Layer Meteorology 112, 503–523. https://doi.org/10.1023/B:BOUN.0000030653.71031.96

Kljun, N., Rotach, M.W., Schmid, H.P., 2002. A three-dimensional backward Lagrangian footprint model for a wide range of boundary-layer stratifications. Boundary-Layer Meteorology 103, 205–226. https://doi.org/10.1023/a:1014556300021

Konopka, J., Heusinger, J., Weber, S., 2021. Extensive Urban Green Roof Shows Consistent Annual Net Uptake of Carbon as Documented by 5 Years of Eddy-Covariance Flux Measurements. J Geophys Res Biogeosci 126. https://doi.org/10.1029/2020JG005879

Kormann, R., Meixner, F.X., 2001. An Analytical Footprint Model For Non-Neutral Stratification. Boundary-Layer Meteorology 99, 207–224. https://doi.org/10.1023/A:1018991015119

Kurbanmuradov, O., Levykin, A., Rannik, U., Sabelfeld, K., Vesala, T., 2003. Stochastic Lagrangian footprint calculations over a surface with an abrupt change of roughness height. Monte Carlo Methods and Applications 9. https://doi.org/10.1515/156939603322663330

Leclerc, M.Y., Shen, S., Lamb, B., 1997. Observations and large-eddy simulation modeling of footprints in the lower convective boundary layer. Journal of Geophysical Research: Atmospheres 102, 9323–9334. https://doi.org/10.1029/96JD03984

Luhar, A.K., Rao, K.S., 1994. Source Footprint Analysis for Scalar Fluxes Measured in Flows over an Inhomogeneous Surface, in: Gryning, S.-E., Millán, M.M. (Eds.), Air Pollution Modeling and Its Application X. Springer US, Boston, MA, pp. 315–323. https://doi.org/10.1007/978-1-4615-1817-4_35

Markkanen, T., Steinfeld, G., Kljun, N., Raasch, S., Foken, T., 2015. Comparison of conventional Lagrangian stochastic footprint models against LES driven footprint estimates. Atmospheric Chemistry and Physics 9, 5575–5586. https://doi.org/10.5194/acp-9-5575-2009

Maronga, B., Gryschka, M., Heinze, R., Hoffmann, F., Kanani-Sühring, F., Keck, M., Ketelsen, K., Letzel, M.O., Sühring, M., Raasch, S., 2015. The Parallelized Large-Eddy Simulation Model (PALM) version 4.0 for atmospheric and oceanic flows: model formulation, recent developments, and future perspectives. Geoscientific Model Development 8, 2515–2551. https://doi.org/10.5194/gmd-8-2515-2015

Schmid, H.P., 2002. Footprint modeling for vegetation atmosphere exchange studies: a review and perspective. Agricultural and Forest Meteorology 113, 159–183. https://doi.org/10.1016/S0168-1923(02)00107-7

Schuepp, P.H., Leclerc, M.Y., MacPherson, J.I., Desjardins, R.L., 1990. Footprint prediction of scalar fluxes from analytical solutions of the diffusion equation. Boundary-Layer Meteorology 50, 355–373. https://doi.org/10.1007/BF00120530

Shepard, D., 1968. A two-dimensional interpolation function for irregularly-spaced data, in: Proceedings of the 1968 23rd ACM National Conference. ACM Press, pp. 517–524. https://doi.org/10.1145/800186.810616

Simon, H., 2016. Modeling Urban Microclimate: Development, Implementation and Evaluation of New and Improved Calculation Methods for the Urban Microclimate Model ENVI-Met (PhD Thesis). Universitätsbibliothek Mainz, Mainz.

Simon, H., Bruse, M., Cramer, L., Sinsel, T., n.d. Improving Building Performance Simulation boundary conditions, in: Proceedings of the 35th International Conference on Passive and Low Energy Architecture. Presented at the Passive and Low Energy Architecture (PLEA 2020), A Coruna, p. 6. https://doi.org/10.17979/spudc.9788497497947

Simon, H., Lindén, J., Hoffmann, D., Braun, P., Bruse, M., Esper, J., 2018. Modeling transpiration and leaf temperature of urban trees – A case study evaluating the microclimate model ENVI-met against measurement data. Landscape and Urban Planning 174, 33–40. https://doi.org/10.1016/j.landurbplan.2018.03.003

Sogachev, A., Menzhulin, G.V., Heimann, M., Lloyd, J., 2002. A simple three-dimensional canopy – planetary boundary layer simulation model for scalar concentrations and fluxes. Tellus B 54, 784–819. https://doi.org/10.1034/j.1600-0889.2002.201353.x

Steinfeld, G., Raasch, S., Markkanen, T., 2008. Footprints in Homogeneously and Heterogeneously Driven Boundary Layers Derived from a Lagrangian Stochastic Particle Model Embedded into Large-Eddy Simulation. Boundary-Layer Meteorology 129, 225–248. https://doi.org/10.1007/s10546-008-9317-7

Thomson, D.J., 1987. Criteria for the selection of stochastic models of particle trajectories in turbulent flows. Journal of Fluid Mechanics 180, 529–556. https://doi.org/10.1017/s0022112087001940

van de Boer, A., Moene, A.F., Schüttemeyer, D., Graf, A., 2013. Sensitivity and uncertainty of analytical footprint models according to a combined natural tracer and ensemble approach. Agricultural and Forest Meteorology 169, 1–11. https://doi.org/10.1016/j.agrformet.2012.09.016

Vesala, T., Kljun, N., Rannik, U., Rinne, J., Sogachev, A., Markkanen, T., Sabelfeld, K., Foken, T., M.Y, L., 2008. Flux and concentration footprint modelling: State of the art. Environmental Pollution 153, 653–666. https://doi.org/10.1016/j.envpol.2007.06.070

Weil, J.C., Sullivan, P.P., Moeng, C.-H., 2004. The Use of Large-Eddy Simulations in Lagrangian Particle Dispersion Models. Journal of the Atmospheric Sciences 61, 2877–2887. https://doi.org/10.1175/jas-3302.1

Wilson, J.D., Sawford, B.L., 1996. Review of Lagrangian stochastic models for trajectories in the turbulent atmosphere. Boundary-Layer Meteorology 78, 191–210. https://doi.org/10.1007/bf00122492

“ (Simon et al., 2021a).

7 PM2.5 exposure differences between children and adults

Lorenz Harr[1], Tim Sinsel[1], Helge Simon[1], Oliver Konter[1], Damian Dreiseitl[1], Philipp Schulz[1], Jan Esper[1,2]

[1]Department of Geography, Johannes Gutenberg University Mainz, 55099 Germany
[2]Global Change Research Institute of the Czech Academy of Sciences (CzechGlobe), Brno, 60300 Czech Republic

Summary:

While the previously presented advancements in modeling could be made as developers of ENVI-met with specific model insights and code accessibility in particular, the author could also contribute to scientific progress by applying the model, e.g., as air quality modeling tool as demonstrated in the following manuscript. Led by Lorenz Harr, air pollution at child and adult height levels was investigated by using low-cost particulate matter measurements on walking routes along kindergartens and schools. The author developed and coded a reanalysis, filtering and extrapolation tool based on an inverse distance weighting algorithm to fit the measured data to an optimal route and to a higher temporal resolution, respectively. To further investigate whether children are exposed to higher air pollution concentrations as they are nearer to the emissions sources of traffic, a simulation study using ENVI-met was conducted featuring specific meteorological conditions of the measurement campaign as well as local traffic emission rates. Besides processing the measurement data, the author contributed to this work by preparing, conducting and evaluating the ENVI-met simulations, and proof-reading the manuscript.

Urban Climate – In Review

7.1 Introduction

Various epidemiological studies provide evidence that air pollution exposure has negative effects on public health causing respiratory and cardiovascular diseases and even increase mortality (Feng et al., 2016; Lelieveld et al., 2019). Fine particles with a size < 2.5 µg/m³ can reach the lungs via the respiratory tract and cause airway inflammation followed by a decrease in lung function and even chronic obstructive pulmonary disease (Gualtieri et al., 2011; Lelieveld et al., 2019; Torres-Ramos et al., 2011).

Children are particularly exposed to ambient particulate matter. They breathe more air per body size and have a greater risk due to their smaller airways than adults (Goldman, 1995; Mazur, 2003). Their respiratory system is not completely developed, which leads to an increased risk of respiratory diseases and exacerbation of asthma (Habre et al., 2014; Nachman and Parker, 2012).

In urban environments, PM2.5 concentration largely stems from locally emitted sources including traffic related particles (exhausts, tyre and break abrasion), house heating, construction sites, soil and biogenic compositions (Azarmi et al., 2016; Karagulian et al., 2019; Kumar et al., 2015). Factors influencing ambient concentrations include the number of emitters as well as mesoscale weather condition. Anticyclonic weather in European autumn and winter is characterized by low wind speeds and little to no precipitation (Czernecki et al., 2017; Graham et al., 2020). Mesoscale high pressure systems lower atmospheric mixing layer heights (MLH) hindering vertical dispersion of air pollutants, which in turn causes an accumulation of locally emitted PM2.5 within the planetary boundary layer (Tang et al., 2016; Wagner and Schäfer, 2017).

Several studies found that pollutant concentration decreases with increasing height above ground (e.g. Goel and Kumar, 2016; Imhof et al., 2005; Kumar et al., 2008; Zauli Sajani et al., 2018; Zhou et al., 2019). However, only a few studies examined vertical differences near the surface in heights < 2m (Garcia-Algar et al., 2015; Goel and Kumar, 2016; Kumar et al., 2017; Sharma and Kumar, 2020). Differences in PM2.5 concentration at this height is arguably most important when it comes to pedestrian exposure. The smaller size of children in comparison to adults means their breath levels are closer to pollutants emitted near ground, making them potentially more vulnerable to emissions by traffic-related exhausts and whirled up fine particles (Kumar et al., 2017; Sharma and Kumar, 2020).

To examine potentially varying exposure differences between adults and children, we measured PM2.5 at two heights, 1.0 m and 1.6 m, in a dense urban environment featuring different traffic intensities. The measurements were conducted using self-designed monitoring systems hosting Alphasense OPC-N3 low-cost sensors (Alphasense, 2018). The sensors are easily portable due to their small size and weight, and perform well under laboratory conditions (Morawska et al., 2018; Sousan et al., 2016), making them suitable for studies about spatial particulate matter exposure (Brattich et al., 2020; Bulot et al., 2019; Jovašević-Stojanović et al., 2019). However, under ambient air conditions in urban areas, the accuracy of measurements is negatively affected by changing particle compositions and even more so by changing relative humidity (Alfano et al., 2020; Brattich et al., 2020; Crilley et al., 2018; Di Antonio et al., 2018). These limitations were addressed by calibrating the sensors and comparing the empirical findings with simulations from a microscale model considering particle advection and dispersion modelling was conducted (Singh et al., 2003).

The main objective of this study is to examine potential differences of PM2.5 exposure between children and adults in an urban area at high spatiotemporal resolution. We (i) compare changes in PM2.5 concentrations related to changing weather conditions, (ii) quantify the absolute and relative exposure differences between children and adults considering the position on the measurement route and absolute PM2.5 concentrations, and (iii) assess findings by comparing measured differences with microclimate simulation outputs.

7.2 Material and methods

7.2.1 Study characteristics

The study was conducted in Mainz-Neustadt, an urban area district of Mainz, the capital of Rhineland-Palatinate in South-West Germany (50.0° N, 8.26° E, Figure 7-1 a). Mainz is an inland city with approximately 220,000 inhabitants, located in a landscape of gently rolling hills along the Rhine River. The climate is temperate with an annual average temperature of 10.7°C and precipitation of 620 mm (Koeppen Cfb). The winters are cool and dry, November to March: mean air temperature is 3.9 °C and mean precipitation 48 mm (Deutscher Wetterdienst, 2021a, 2021b). The urban architecture of this densely populated area consists of compact midrise structures with a grid-based street layout (Stewart

and Oke, 2012). The streets are mostly narrow (10 m wide) and feature low traffic intensity. The city quarter is surrounded by larger multi-lane roads with high traffic volume.

To capture local differences in PM2.5 concentration, a clockwise circular, 5.5 km-long measurement track passes through both, the inner narrower low traffic parts as well as the larger roads of the Neustadt (Figure 7-1 a). The track starts at Mainz Main Station (50.0017° N, 8.2595° E), then runs within the inner part of the district, passing social institutions, i.e., kindergartens, primary and secondary schools as well as nursing and retirement homes. After leaving the center of the quarter, the transect continues along roads with high intensity of traffic, first in southeast, then in southwest direction (Figure 7-1 e) ending at the Main Station.

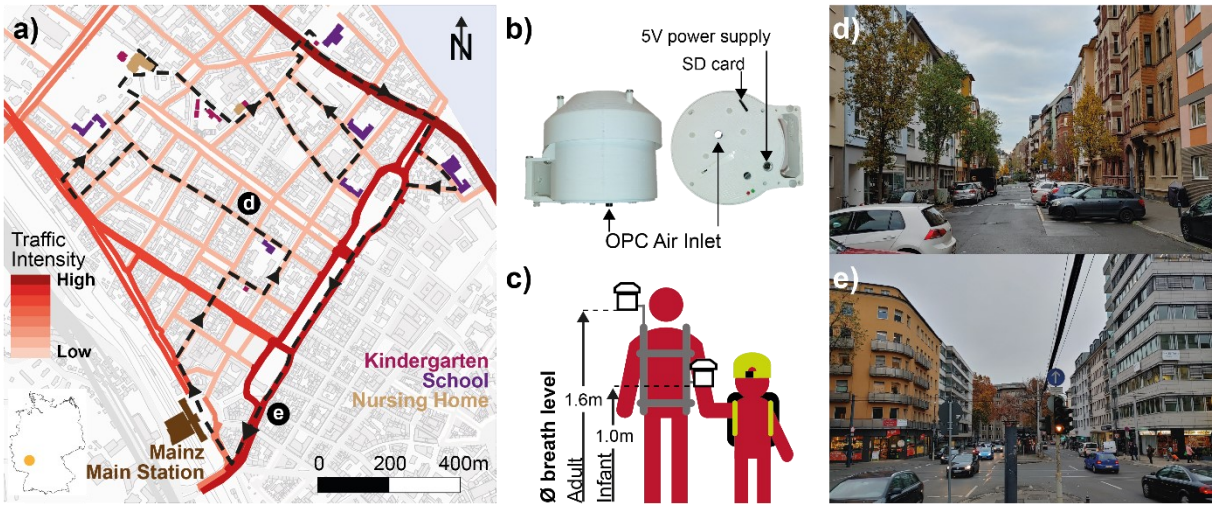

*Figure 7-1: Location of the study district Mainz-Neustadt including the start/end point Mainz main station (brown) of the measurement transect (dashed black line) with nearby social institutions, i.e., kindergartens (pink), primary and secondary schools (purple) and nursing homes (light brown). The streets within the district are colored depending on traffic intensity (**a**). Design of the measurement devices (dimensions: 11.5 cm x 14 cm x 12.5 cm) (**b**). Two devices mounted offset on the front of a wearable rack at breath levels of adults (1.6 m) and children (1.0 m), respectively (**c**). Typical city block street canyons with low (**d**) and high traffic intensity (**e**).*

The measurement campaign took place from 11-20-2019 to 11-27-2019 (Wednesday to Wednesday). The measurement runs were conducted by foot starting at 3:15 pm and ending at ~ 4.30 pm every day covering the time of daily of kindergarten and school endings and start of the rush hour within the study area. For each run, two devices containing a PM sensor (Alphasense, 2018), a GPS module (Simcom, 2021), a ESP32 as microcontroller (Espressif, 2021) and a microSD card for saving the data were used (Figure 7-1 b). The cover of the cases protruded over the side parts were similar to a radiation shield cap to support ventilation of the blown-out PM-sensor air. The devices were mounted at the breath level of

adults (1.6 m, device A) and children (1.0 m, device B). To reduce influences induced by the measuring person, the devices were attached at the front of the body at a distance of 30cm (Figure 7-1 c). Every run was filmed with a camera to facilitate detections of possible local emitters in the postprocessing of the measuring campaign.

7.2.2 Meteorological data

A detailed description of the meteorology during the measurement period is needed as the local weather characteristics affect the type, number, and duration of particulate matter concentrations (Cheng and Li, 2010; Graham et al., 2020; McGregor and Bamzelis, 1995). The central emission network of Rhineland-Palatinate kindly provided 3-min-arithmetic-means of air temperature, relative humidity, precipitation, and atmospheric pressure (Figure 7-9), measured at the station Mainz-Zitadelle (49.9950° N, 8.2739° E) located ~ 1.2 km west of the study area, as well as 3-min-sums of precipitation, wind direction and speed at the station Mainz-Mombach (50.0180° N, 8.2157° E) located ~ 3 km west of the study area (ZIMEN, 2019). Data of the convective inhibition energy (CIN) and mixing-layer height (MLH), indicators for the stability of the air near the ground, were measured with a radiometer located ~ 500 m west of the study area (50.01406°N 8.257°E). These data were provided by the environmental meteorology unit of the environmental state office of Rhineland-Palatinate (Umweltmeteorologie RLP, 2019).

7.2.3 Calibration of PM2.5 sensors

The PM2.5 measurements on both respiratory levels were conducted using an Alphasense OPC-N3 sensor (Alphasense, 2018). The OPC-N3 is a low-cost optical particle counter using the light scattering principle to count particles (Mie, 1908), transfers these into bins according to their estimated size (Bohren and Huffman, 1998) and converts the data into mass concentrations (Walser et al., 2017). During the measurements, no changes to the default settings of the sensor's principles were made.

Both OPC-N3 sensors were manufacture-calibrated following the European Standard EN 481 (Crilley et al., 2018). However, to improve sensor accuracy, a field calibration in an environment comparable to the study area has been conducted (Alfano et al., 2020; Chatzidiakou et al., 2019; Crilley et al., 2020; Gysel et al., 2007; Hagler et al., 2018). This was done from 11-22-2019 to 11-31-2019 at the official measurement station Mainz-Zitadelle (49.9950°N, 8.2739°E) of ZIMEN. Both Alphasense devices were

located side-by-side on the same height measuring PM2.5-concentration at a 1 s interval. The data were then transformed into running 20 s-truncated arithmetic means and humidity-corrected to mitigate the influence of fine particle hygroscopy (Crilley et al., 2018; Petters and Kreidenweis, 2007). The correction is based on the *k*-Köhler-theory considering a particle hygroscopy of $k = 0.33$, density of particles of 1.65 g/cm³ (Crilley et al., 2020), and ambient relative humidity recorded at the official station Mainz-Zitadelle.

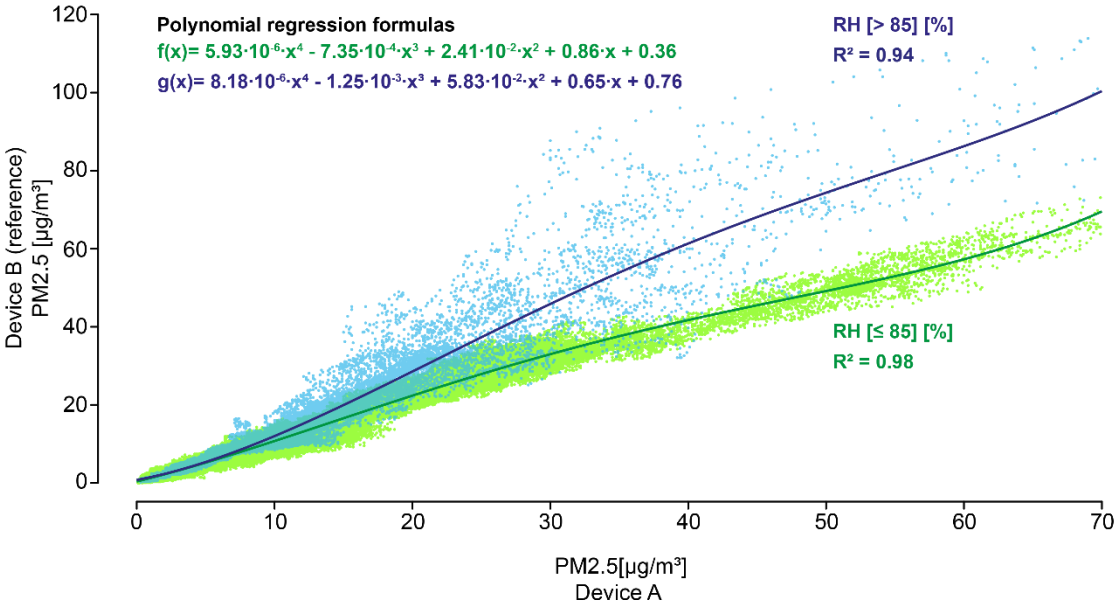

Figure 7-2: Scatter plots and polynomial regression curves of devices A and B for PM2.5 measurements from the adjustment period 12-22-2019 to 12-31-2019. The green data and curve show the measurements for RH ≤ 85% and the blue data for RH > 85% (blue dots and line), as well as the regression equations and coefficients R², respectively.

The scatter plot between PM2.5 data from devices A and B reveal high precision measurements when RH ≤ 85 % as reflected by the explained variance ($R^2 = 0.98$) and data homoscedasticity (Figure 7-2). This allowed a reliable comparison of PM2.5 measurements by transforming the measurements of device A considering the 4th degree polynomial regression model shown as a green curve in Figure 7-2. For the data recorded at RH > 85 %, the PM2.5 correlation and resulting correction are weaker (blue data, Figure 7-2). The scatter plot includes an obvious heteroscedasticity for PM2.5 > 10 µg/m³ largely driven by increased residuals in device A PM2.5-concentrations. This increased variability of OPC-N3 devices is in line with results by Brattich et al., 2020 revealing similar biases for the predecessor device, OPC-N2, and identifying a systematic misclassification of particulate matter sizes during high relative humidity conditions. These results question the reliability of PM2.5 data recorded at RH > 85 %.

Nevertheless, these measurements are fitted with a different model, shown as the blue curve in Figure 7-2, considering the weak reliability for PM2.5 > 10 µg/m³.

7.2.4 Postprocessing analysis

After each measurement run, several postprocessing steps were carried out to support the comparison between heights and among runs. The datasets of devices A and B were adjusted by time (Wickham, 2020), the PM2.5-concentrations, recorded in a 1 s-interval, transformed into a running 20 s-truncated arithmetic mean, and the 10 % highest values removed to mitigate the influence of local short-term emissions (e.g. smokers or street cleaning). Since the duration of the different runs varied slightly and minor inaccuracies affected the recorded GPS data, an additional synchronizing procedure was applied: We calculated a mean standard route considering a concave hull surrounding all runs and retrieving the mean by the skeleton algorithm of the GRASS GIS Processing Toolbox (Fortune, 1987; McCauley et al., 2020). A few remaining inaccuracies were re-digitized manually. The standard route was converted to points with a distance of 20 cm to each other (total n = 27515). Each point was assigned the appropriate PM2.5-concentration, in which all values within a search radius of 15 m are averaged using an inverse distance weighting method (Shepard, 1968). If less than 10 measurements were found, the radius was increased to 50 m.

The PM2.5 data were adjusted using the same humidity correction method as during the calibration (Crilley et al., 2018; Crilley et al., 2020). To compare absolute PM2.5 values, device A data were transformed considering the regression equation from a polynomial fit against the device B data (Figure 7-2).

The adjusted PM2.5 data were analyzed using descriptive statistics, i.e., arithmetic mean, median, standard deviation (SD), and coefficient of variation (CV). Cubic smoothing splines (degrees of freedom = 55, n = 27515) were calculated to reduce the sensitivity of PM2.5 measurements to short-term extreme concentrations. The correlation coefficient R was used to quantify the relation between the measurements of the two heights and respective smoothing splines. To assess differences between 1.0 m and 1.6 m levels, the root-mean-square error (RMSE) was calculated considering daily data, and residuals and relative differences were calculated in cases of pronounced differences in PM2.5-concentrations. Welch's t-test was conducted to assess statistically significant differences in case of unequal variances.

7.2.5 Simulation setup

To examine whether traffic exhausts can be assigned as a cause for varying particulate matter exposures along streets with high traffic intensities, a pollutant dispersion simulation for one exemplary day of the measurement period was conducted. This simulation was performed using the holistic ENVI-met microclimate model, which is able to simulate pollutant concentration distributions for specific meteorological conditions in complex urban environments (Bruse, 1999; Nachman and Parker, 2012; Wania et al., 2012).

The 11-24 was selected as is represents a day of average meteorological conditions and PM2.5 concentrations after a short period of air mass exchange the day before. RH was < 85 % during the time of the run, so the measurements should be reliable (Figure 7-9). The modelled area covers the district of Mainz-Neustadt with a dimension of 280 x 250 x 26 grids at 5 x 5 x 2 m per grid (Table 7-1). The simulation started with full forcing at 11 am using the 30 min mean-meteorological parameters of that day as meteorological boundary conditions (Figure 7-9). Wind speed and direction were set constant to avoid instabilities in the model. Radiation was forced by only cloud coverage as measured values were not available.

Table 7-1: Model parameters of the simulated emissions for 11-24-2019 in ENVI-met.

Start date and time (Local)	11-24-2019 11:00
Duration [h]	10
Wind Speed [m s^{-1}]	1.0
Wind Direction [°]	115
Meteorological Boundary Conditions	Full Forcing
Emission height [m]	0.2
Location Lat (Lower Left Corner)	50.01 °N
Location Lon (Lower Left Corner)	8.25 °E
Dimensions	280 x 250 x 26
Resolutions (X, Y, Z) [m]	5 x 5 x 2
Lowest Grid Cell Splitted	Yes
Telescoping: Factor & Starting Height	30 % above 28 m
Height of 3D Model Domain [m]	221

The applied PM2.5 emissions originating from vehicle exhausts were implemented as source emission profiles at a height of 20 cm in the model. The diurnal profiles of traffic exhaust emissions are based on

the handbook of emission factors for Road Transport (Environmental Protection Agency of Germany (UBA), 2017) and the amounts of emitted PM2.5 in the model area were related to the intensity of traffic per lane (Figure 7-1). Detailed settings about the traffic emission profiles are described in Simon et al. (2019), where model area and traffic intensities were initially used. The relative differences of PM2.5 concentrations were computed between 1.0 m and 1.8 m due to the simulations grid cell resolution of only 0.4 m to compare the model outputs to the measurement data.

7.3 Results

7.3.1 Weather conditions

During the measurement period, the weather situation was dominated by a continental anticyclone centered over Eastern Europe, ~ 2000 km away. On 11-20 and 11-22, Germany was located between a long wave trough in the west and a ridge in the east. This led to weak atmospheric pressure gradients (~Δ 10 hPa around 1003 hPa) and calm weather characterized by low wind speeds (< 0.8 m/s), small daily temperature gradients (max. Δ 5.3 °C, 1.6 °C – 6.9 °C on 11-22) and relative humidity ranging from 72 – 90 %. CIN was subjected to diurnal courses with increasing gradients (Δ 106 J/kg around 89 J/kg to Δ 163 J/kg around 181 J/kg) which led to lower maximum MLH, declining from 386 to 300 m a.g.l., and low stratus conditions in Mainz (Hoffmann, 2019; Figure 7-9). Starting on 11-22 ~ 2:30 pm, the anticyclonic influence was interrupted by weak cyclonal conditions, which led to a dissolution of low stratus in Mainz in the morning of 11-23 (Zeuschner, 2019). Wind speed rose to 1.6 m/s at 11 am, interrupted by an absence of wind at around 2:30 am. The atmospheric pressure gradient decreased slowly reaching a minimum of 982 hPa in the afternoon and TA increased up to 11.7 °C. However, the CIN gradient decreased (Δ83 J/kg 177 J/kg) but remained >100 J/kg indicating that, at the end of 11-23, the ridge of the anticyclone became influential again. Starting on 11-24, the wind speed declined < 0.5 m/s and temperatures and the air pressure increased to maxima of 9.8 °C and 999 hPa, respectively. Moreover, relative humidity rose to a maximum of 92.2 % in the morning of 11-25 and remained > 83.5 % thereafter. On 11-26, the weather changed from an anticyclonic to a calm cyclonic situation characterized by a slowly decreasing air pressure from 999 to 990 hPa, rising temperatures to 11.4 °C, and low wind speeds < 0.5 m/s. However, on 11-27, the last day of the study, wind speed increased again to a

maximum of 1.1 m/s, while temperatures still increased (to 12.3 °C) and precipitation started, summing up to 13.4 mm. The influence of the anticyclone on the weather situation thus retreated.

7.3.2 Recorded PM2.5 concentrations

Figure 7-3 shows the PM2.5-concentrations at the 1.0 and 1.6 m levels for every run of the measurement campaign. The absolute PM2.5 concentrations at both levels differed substantially among runs over the course of the period from 11-20 to 11-27. Mean PM2.5-concentrations at 1.0 m increased from 6.1 µg/m³ on 11-20 to 46.4 µg/m³ on 11-22, then declined massively to 2.7 µg/m³ on 11-23, reached a distinct peak of 67.8 µg/m³ on the next day and then decreased to 2.2 µg/m³ until 11-27 (Table 7-2).

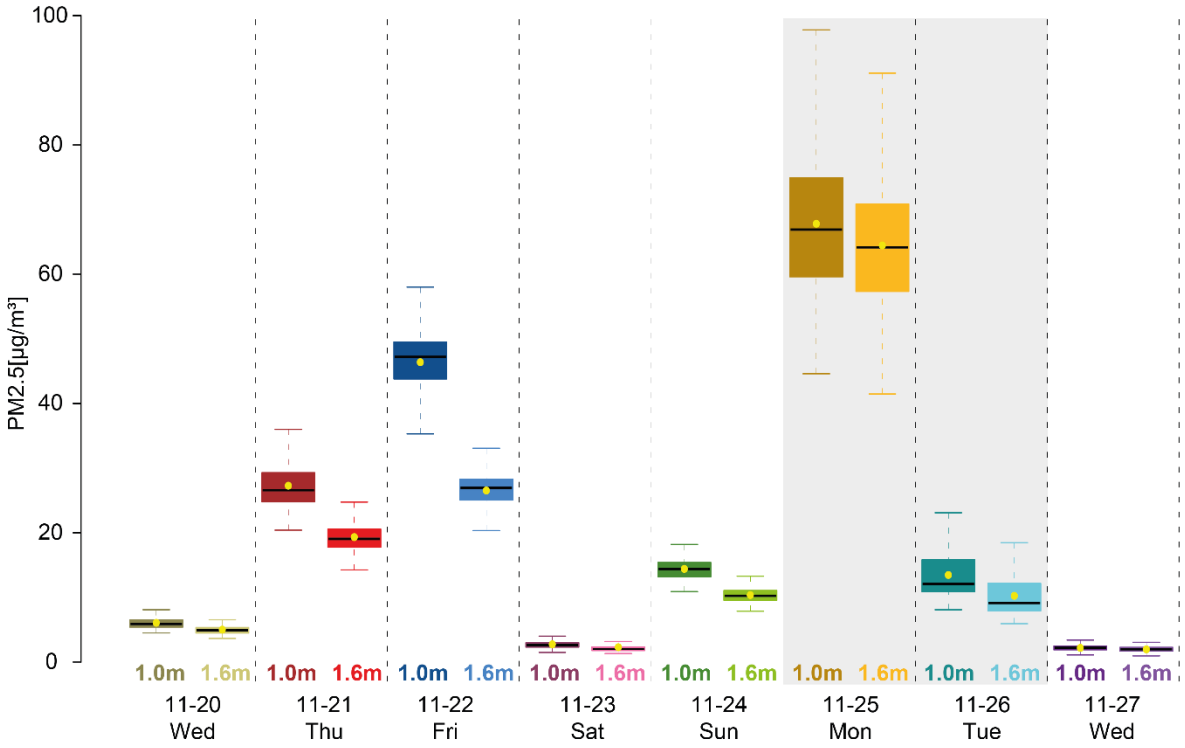

*Figure 7-3: PM2.5-concentrations at the 1.0 and 1.6 m levels for every run from 11-20 to 11-27 visualized as boxplots with whiskers (length 1.5 * interquartile range), median (black bar) and mean (yellow dot). Grey background indicates RH>85% during the run.*

During all days, the PM2.5-concentrations at 1.0 m were higher than on 1.6 m (Table 7-2). On 11-20, 11-21, 11-22 and 11-24 the interquartile ranges (IQR) do not overlap, indicating that at least 75 % of the PM2.5 concentrations measured at 1.6m are lower than at least 75 % of the PM2.5 values at 1.0 m. The temporal distribution along the days (Figure 7-4) shows that on 11-21, 11-22 and 11-24 the concentrations at the children breath level were constantly higher than at adult level (RMSE: 8.2 µg/m³, 20.1

µg/m³, 4.1 µg/m³, respectively). This is also the case for the run on 11-26 (RMSE: 3.4 µg/m³), but the data had to be adjusted using the equation for RH > 85 % (Figure 7-2; Table 7-3).

Table 7-2: PM2.5 characteristics at 1.0 m (grey) and 1.6 m (white) for the 8-day measurement campaign. SD indicates standard deviations, CV coefficient of variation.

date	**11-20**		**11-21**		**11-22**		**11-23**		**11-24**		**11-25**		**11-26**		**11-27**	
Mean PM2.5 [µg/m³]	6.1	5.0	27.3	19.3	46.4	26.5	2.7	2.3	14.4	10.4	67.8	64.4	13.5	10.2	2.2	2.0
Median PM2.5 [µg/m³]	5.9	4.9	26.6	19.1	47.3	26.9	2.6	2.0	14.4	10.3	66.9	64.2	12.1	9.1	2.2	2.0
SD [µg/m³]	1.2	1.1	3.6	2.4	4.7	2.4	0.9	1.4	1.4	1.1	10.6	9.9	3.8	3.3	0.5	0.4
CV	0.19	0.21	0.13	0.12	0.10	0.10	0.33	0.61	0.10	0.10	0.16	0.15	0.28	0.32	0.22	0.20

On 11-20 and 11-23, the 1.0 m PM2.5 concentrations were higher in 97 % and 88 % of all measurement points, independent of the position of the route (RMSE: 1.2 µg/m³, 1.5 µg/m³, respectively). For the remaining six days, the PM2.5 concentrations were significantly higher at 1.0 m than at 1.6 m according to a Welch t-test ($p < 0.01$).

Table 7-3: Meteorological conditions during the measurement campaign from 11-20 to 11-27 including Mean Air temperature (TA) [°C], Mean Relative Humidity (RH) [%], Precipitation Sum [mm], Atmospheric Pressure [hPA], Wind Speed [m/s], Wind Direction [°], Mean Convective Inhibition [J/kg] and Mean Mixing Layer Height [m] (Umweltmeteorologie RLP, 2019; ZIMEN, 2019).

date	**11-20**	**11-21**	**11-22**	**11-23**	**11-24**	**11-25**	**11-26**	**11-27**
TA [°C]	5.0	5.9	6.6	11.5	8.9	6.7	11.1	12.3
RH [%]	77.3	78.1	81	62.5	78	87	86	78
Precipitation [mm]	0	0.1	0	0	0	0	0	4.3
Atmospheric pressure [hPA]	1004	998	996	987	997	999	994	983
Wind direction [°]	116	152	119	90	142	-	-	129
Wind speed[m/s]	0.4	0.1	0.7	0.5	0.1	0	0	0.5
CIN [J/kg]	62	134	113	156	164	149	100	88
MLH [m]	289	239	301	130	116	183	74	54

On 11-25, the PM2.5 concentrations measured by device A were adjusted using the equation for RH > 85 % (Figure 7-2, Table 7-3). Considering the unexplained variance of the adjustment procedure (6 %) as well as the uncertainties for PM2.5 > 10 µg/m³, the recorded differences between children and adult respiratory levels were insignificant on that day. On 11-27, the differences were not distinguishable due to low absolute PM2.5 concentrations including 97 % of measurements < 3 µg/m³ at 1 m, and 99% of

measurements < 3 µg/m³ at 1.6 m, with the absolute differences (~ 0.2 µg/m³) approaching measurement accuracy.

7.3.3 Distribution of PM2.5 along the route

The temporal variability of PM2.5 measurements were low (CV < 0.22) as well as the differences in variability of both heights among the runs (CV difference max. 0.04; Table 7-2). Exceptions are the runs on 11-23 and 11-26: the high CVs (1.0 m: 0.33; 1.6 m: 0.61) on 11-23 were affected by an oncoming person at the beginning of the run, holding a cigarette between 1.0 and 1.6 m, so the devices recorded the short-term pollution shortly one after the other. The higher variabilities on 11-26 (1.0 m: 0.28; 1.6 m: 0.32) could not be attributed to single incidents, explanations could be RH > 85 % as well as weakening of anticyclonic weather.

The distribution of the absolute PM2.5 concentrations indicated common concentration patterns between the two measurement heights ($R_{Run\_all} > 0.8$) (Figure 7-4). This coherence was reduced on days with low PM2.5 concentrations, on 11-23 and 11-27, with $R_{Run} = 0.29$ and $R_{Run} = 0.46$, respectively, when random variability near the measurement accuracy adds uncertainty to the data. However, there is no common temporal pattern among the runs, as some timeseries increase throughout the run (11-21), whereas other decrease (11-22) or show no long-term trend (11-27).

On 11-20 and 11-22, the differences between 1.0 and 1.6 m decline towards the end of the runs, whereas short-term PM2.5 peaks are recorded on 11-20 at ~ 5250 m, 11-23 at ~ 350 m and ~ 5400 – 5500 m, and 11-27 at ~ 4300 m (Figure 7-4). The causes for these peaks differ though, and may include ventilation of a cellar bar (11-20), a smoking person and exceptional high traffic at the main station (11-23), or were simply not detectable (11-27). There are two distinct deviations including mean PM2.5 > 10 µg/m³ detectable in all runs, however. These are located at the ‘Grüne Brücke’, a bridge crossing the ‘Rheinallee’ (Figure 7-4 at 3300 – 3500 m; Figure 7-7, Figure 7-8 dot 3) and the ‘Rheinallee’ close to the crossroad ‘Rheinallee/Kaiserstraße’ (Figure 7-4, Figure 7-6 at 3800 – 4000 m; Figure 7-7, Figure 7-8 dot 4).

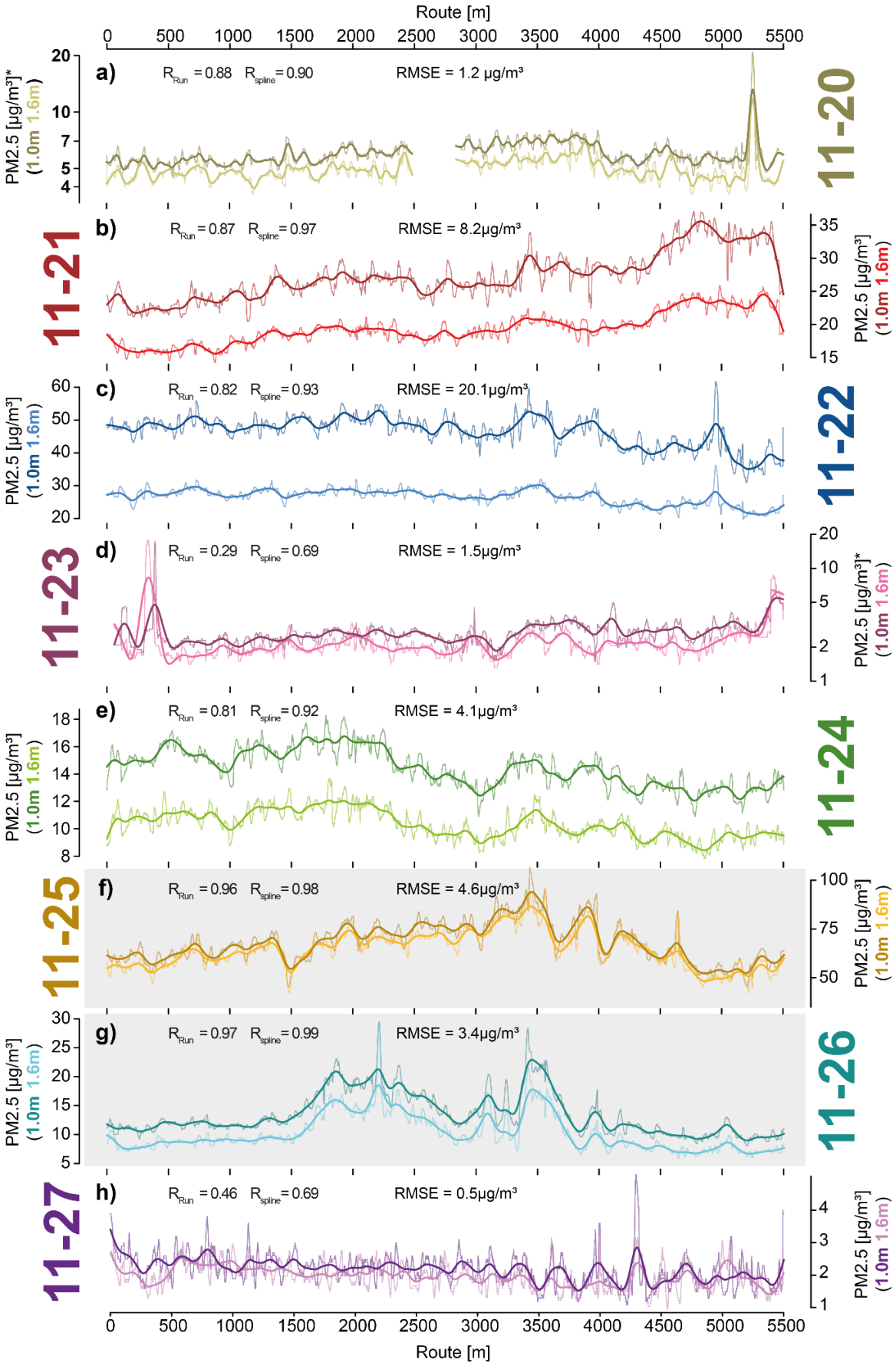

*Figure 7-4: Distribution of 20 s PM2.5 concentrations at 1.0 m (dark curves) and 1.6 m level (bright curves) on days 11-20 (**a**) to 11-27 (**h**) along the route. Bold curves are smoothing splines (df = 55, n = 27515) and grey background indicates runs with RH > 85 %. *Logarithmic y-axis used in panel **a** and **d**.*

The described trends in absolute PM2.5 concentration among the runs change considerably when focusing on the absolute height differences between devices A and B (Figure 7-5). The common PM2.5 patterns of both measurement heights lead to the fact that the differences between top and bottom remain almost the same and thus strong deviations are largely leveled out. Only the mentioned deviations at the 'Grüne Brücke' and 'Rheinallee' were visible on 11-21, 11-22, 11-24 and 11-26.

The PM2.5 residuals persist on most days, except of 11-25 and 11-27 due to indistinguishable differences. However, the residuals differ among the days. The amount and variability of the absolute differences seem to be depended on the level of their absolute value. The higher the particulate matter concentration was, the higher were the residuals and their absolute variability within a run. Only for 11-24 and 11-26 this hypothesis does not apply: The residual IQR of the run at 11-26 (1.0 µg/m³) were slightly larger than the IQR of the run at 11-24 (1.3 µg/m³) although the 11-26 residual mean was smaller (3.2 µg/m³).

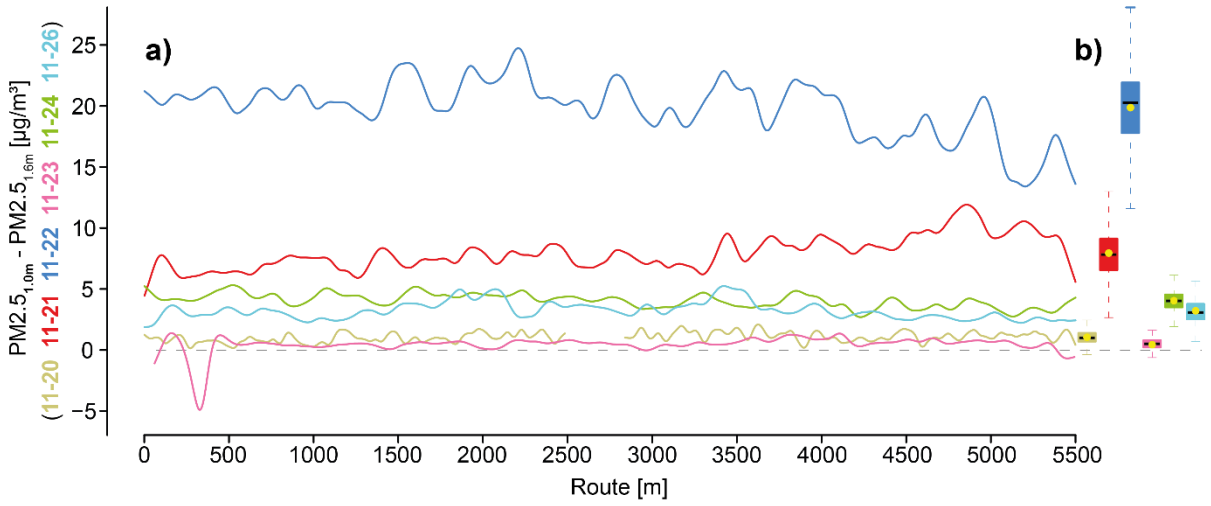

*Figure 7-5: Residuals of PM2.5 concentrations between 1.0 and 1.6m for days of significant PM2.5 height differences shown as smoothed deviations from 20 s PM2.5 concentrations along the route (df = 55, n = 27515) (**a**), and boxplots of the data (**b**).*

To highlight the association between children and adult PM2.5 exposures, splines of the relative differences between 1.0 and 1.6 m were calculated (Figure 7-6). The ratios were largest on 11-22 reaching a maximum value exceeding 188 %, nearly the double exposure for children. Following the residuals (Figure 7-5), relative PM2.5 differences correlate positively on the total amount of the measured PM2.5, as is expressed by the lower ratios on 11-21 (141 %), followed by 11-24 (139 %), 11-26 (133 %) and 11-20 (122 %).

The IQR of the runs range from 11 – 16 %, excluding the run at 11-23, affected by an oncoming smoking person. The relative differences of the run at 11-23 were exceptional, as the values varied massively around the 127 % mean, expressed by an IQR of 29 %. In contrast, the CV was lower, as this metric considers the (high) absolute mean value.

The pronounced extremes of absolute PM2.5 values at the 'Grüne Brücke' at 3300 – 3500 m are also seen in the height differences on 11-21, 11-22, 11-24 and 11-26. Similarly, the high absolute PM2.5 values at the 'Rheinallee' at 3800 – 4000 m also appear on 11-21, 11-22, 11-23, 11-24, 11-26, in the relative difference between devices A and B. Data variability during days with substantial height differences showed no trends. Only on 11-22 the ratios were slightly decreasing along the measurement route.

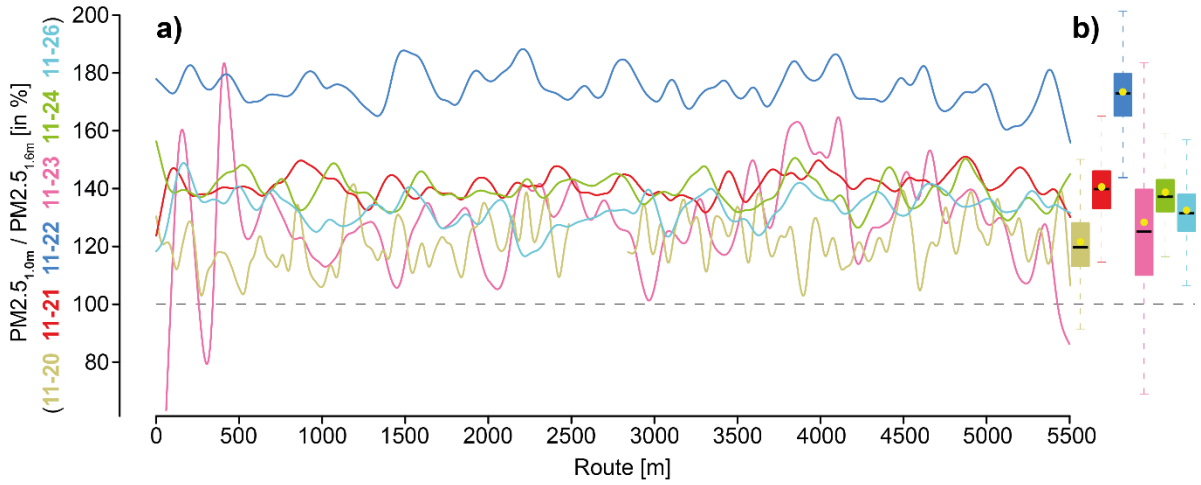

*Figure 7-6: Relative differences of PM2.5 concentrations between 1.0 and 1.6m for days of significant PM2.5 height differences shown as smoothed deviations from 20 s PM2.5 concentrations along the route (df = 55, n = 27515) (**a**), and boxplots of the data (**b**).*

7.3.4 Simulated *versus* measured concentrations

The simulated PM2.5 exposures for the run on 11-24 showed similar results: The relative differences of PM2.5 exposure between 1.0 and 1.8 m were positive across the model area (Figure 7-7, without shading Figure 7-10). Ratios < 100 % could only be found at the borders of the model probably due to boundary modelling artifacts. Relative differences > 110 % were located on the roads with high traffic intensities (Figure 7-1, e.g. Figure 7-7 dot 4) and/or streets with the same direction as the wind (e.g. Figure 7-7, dot 2). Following the measurement route, the simulation underestimated the measured relative differences by ~ 30 % on average (Figure 7-8). Starting with ~ 115 % at Mainz main station, the simulated PM2.5 exposures at 1.0 m were just < 5 % higher than at 1.8 m in the inner part of Mainz-Neustadt and

showed almost no variability in contrast to the measured PM2.5 ratios. Areas close to streets featuring high traffic intensities showed larger relative differences of up to 127 %.

Comparing the relative differences of PM2.5 between the model and measurements along the route (Figure 7-8) confirms that the model predicts both lower values and a lower variability in general. For some locations however, the model simulates similar increases in relative differences when compared to the measurements (Figure 7-8, marked 1 to 6). The relative differences of the simulation increased as the study route passed a street with higher traffic intensity at the western border of the district (Figure 7-8, dot 1).

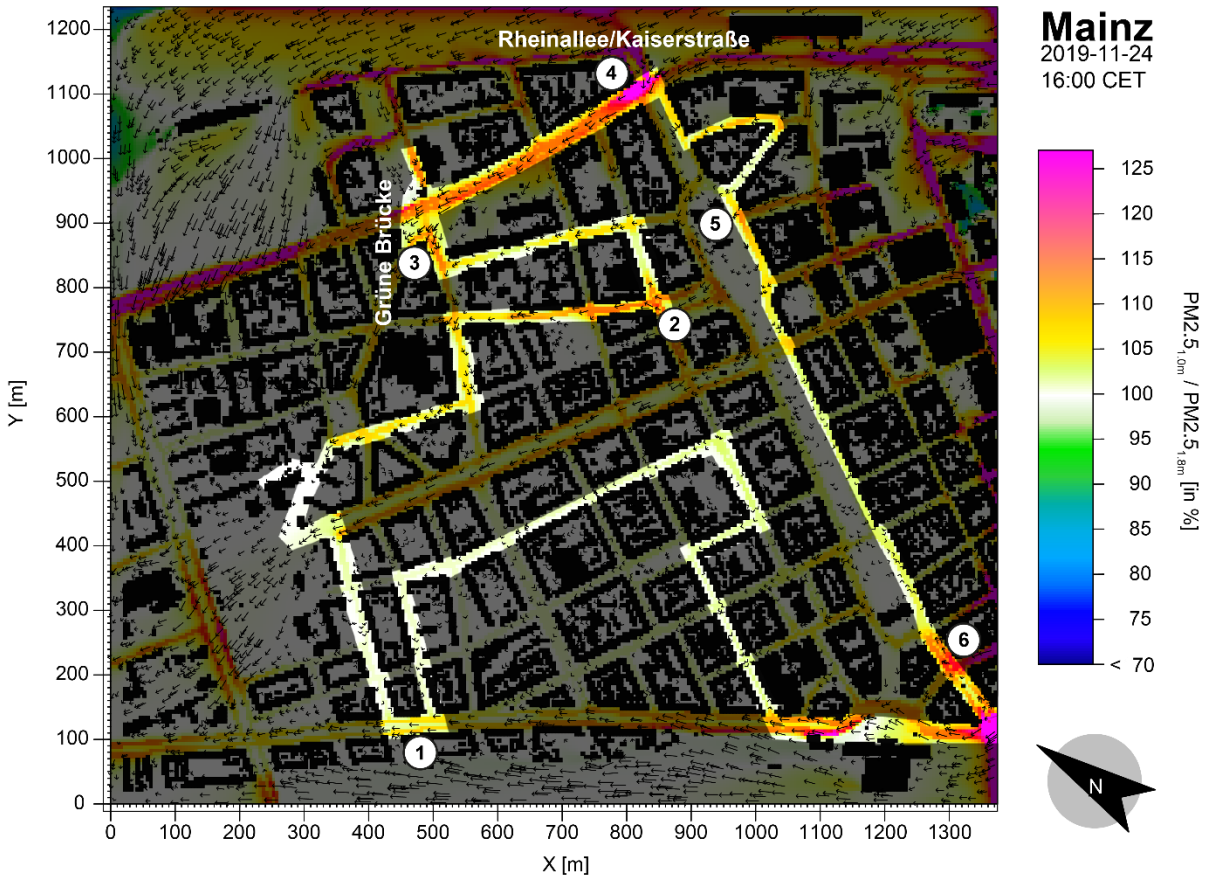

Figure 7-7: Simulated relative differences distribution of PM2.5 concentrations between 1.0 and 1.8m in the study area with the measurement route highlighted. The colors display reduced (blue and green), equal (white) and increased (yellow to red/magenta) PM2.5 exposure at 1.0 m level. The arrows represent horizontal wind speed and direction.

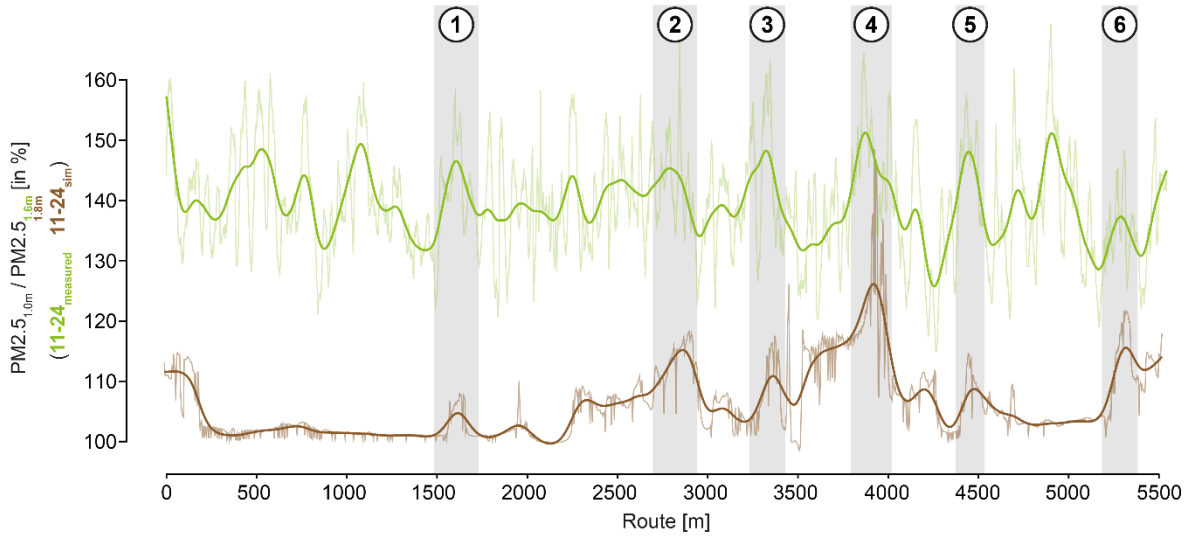

Figure 7-8: Relative PM2.5 exposure differences on 11-24 between 1.0 and 1.6m as measured (green curves) and between 1.0 and 1.8m as simulated (brown curves). Bold curves are smoothing splines (df=55, n=27515).

7.4 Discussion

7.4.1 Influence of weather conditions on PM2.5 exposure

The continental anticyclonic conditions led to a mainly stable and calm weather throughout the study period (Figure 7-10). Several studies (Cheng and Li, 2010; Czernecki et al., 2017; Graham et al., 2020; Hamburger et al., 2011) showed that the longer the stability of anticyclonic weather endured, the higher PM2.5 concentrations increased. Our work corroborates this finding: When the weather situation was stable with low wind speeds < 1 m/s and a lack of precipitation, the PM2.5 values increased from 11-20 and 11-22 (Figure 7-2; Tab .2). From 11-22 to 11-23, the absolute PM2.5 concentrations declined due to a short-term cyclonical influence with wind speeds > 1 m/s. Subsequent to this exchange of air masses, anticyclonic conditions fostered PM2.5 increases on 11-24 and 11-25, until the influence weakened due to an upcoming cyclone with higher wind speed and minor precipitation towards the end of the measurement campaign. However, the concentrations recorded in this study exceeded the European law threshold of 25 µg/m³, as a benchmark for yearly mean PM2.5 exposure (European Parliament and Council (EU), 2008), in only three of eight runs. These effects were observed at both heights, which indicates that the changes in absolute PM2.5 concentrations throughout the week were largely weather driven.

7.4.2 Local emissions and vertical PM2.5 differences

We showed that in six of eight runs, PM2.5 concentrations were significantly higher at the respiratory level of children than of adults. The exposure is at least 41 % higher, and during the calm weather conditions on 11-22, grew up to 89 % (75 % on average), which means that children were exposed up to 24.7 µg/m³ higher PM2.5 concentrations.

Our results are consistent with the findings of studies made by Garcia-Algar et al. (2015), Kumar et al. (2017) and Sharma and Kumar (2020). Garcia-Algar et al. (2015) conducted a study measuring ultrafine particles at the height of strollers (0.55 m) and adults (1.70 m) by foot on three randomly chosen streets with high traffic intensity 20 times on 10 consecutive days in Barcelona, Spain. They showed that the exposure is 10 % higher on stroller level. Kumar et al. (2017) measured PM2.5 exposure to in-pram babies (0.7 m) and the carrying adult (1.4 and 1.6 m) also by foot 32 times on a predefined route (2.1 km) in Guilford, UK during morning (8 to 10 am) and afternoon (3 to 5pm). They found out that in the morning hours, the infants were 5% significantly lower exposed than adults. However, in the afternoon, the concentrations were 10% significantly higher for the children. Sharma and Kumar (2020) reconducted this study in 2018 on a similar but shorter route (2.1 km) in Guildford, UK; showing that the PM2.5 concentrations at 0.7 m were up to 44 % higher in the afternoon.

All of these three studies concluded that traffic-related sources were major factors (Garcia-Algar et al., 2015; Kumar et al., 2017; Sharma and Kumar, 2020). We also assume this due to the prevailing calm weather during our study. McGregor and Bamzelis (1995), for instance, showed that low wind speed, caused by continental anticyclonic conditions, limited air mass exchange in Birmingham, UK and concluded that measured particulate matter had to be emitted locally. The local, ambient PM2.5 in the urban area of Mainz-Neustadt are likely emitted by combustion processes, i.e. traffic and domestic heating, whirled up dust, tyre and break abrasion, as well as floating soil or biogenic compounds and deposited particulate matter (Karagulian et al., 2015). Except domestic heating, all particle sources are close to the surface. In consequence, high traffic volumes are expected cause high particulate matter emissions near the ground. Moreover, the measurement runs (~3:15 pm to ~4:30 pm) took place during the daily afternoon rush hour, a time with higher traffic volume. The rush hour typically starts at ~3 pm with the daily end of education in the kindergartens and all-day schools but also with the end of working days within

the study area. This means that parents are picking up their children, and people are commuting in the beginning rush hour traffic, thereby adding to PM2.5 emissions. The increase of these means of mobility during the afternoon rush hour probably led to higher PM2.5 concentrations near ground and caused larger PM2.5 exposure for children than for adults within the study area.

Additionally, we observed that the absolute and the relative differences in PM2.5 exposure between both levels depended on the total amount of PM2.5. The higher the concentration of particulate matter, the higher the absolute and relative differences (Figure 7-5, Figure 7-6). As stated before, in the case of emissions in calm weather situations with low wind speeds, PM2.5 will remain near the ground. The absolute and relative PM2.5 differences between 1.0 and 1.6 m there increase with increasing PM2.5 concentrations.

The absolute and relative difference between both heights were largely independent of the position on the study route. Even in areas with low traffic, the differences were at the same level than in streets with high traffic intensity. The lack of spatial variability in PM2.5 differences are expressed by high correlations ($R > 0.8$) and similar CV of each run's measurements. Both height levels showed similar courses in PM2.5 concentration, so strong deviation were leveled out after calculating differences.

There are two locations that stood out for relative and absolute PM2.5 concentrations: 'Grüne Brücke' (Figure 7-4 at 3400 – 3500 m; Figure 7-7, Figure 7-8 dot 3) and 'Rheinallee' close to the crossroad 'Rheinallee/Kaiserstraße' (Figure 7-4, Figure 7-6 at 3900 – 4000 m; Figure 7-7, Figure 7-8 dot 4). The 'Grüne Brücke' is a pedestrian bridge with extensive planting crossing the 'Rheinallee', a road with high traffic intensity (Figure 7-1). When the wind arrives from an easterly direction, the bridge and adjacent buildings of the 'Josefstraße' form a barrier for particles perpendicular to the 'Rheinallee' (Table 7-3). On days with high absolute PM2.5 concentrations (11-21, 11-22, 11-24), the traffic-related PM2.5 accumulated and additionally increased the height differences due to a lack of vertical air exchange. These findings corroborate with Gallagher et al. (2015) showing that surrounding buildings are solid barriers for air flow hindering particulate matter to disperse within street canyons. The second site at the 'Rheinallee' is bounded by 5-story-high blocks on two sides in north-south direction, with the northern block tapering down to the intersection 'Rheinallee/Kaiserstraße'. The intersection itself is free of buildings

in the northeast direction. As a result, during easterly winds, traffic-related particles are pushed into the 'Rheinallee' and accumulate behind the crossroad, similar to Grüne Brücke.

Nevertheless, the height differences at both sites were not significantly higher than other extrema during the runs. The relative differences varied more strongly among the days than along the study route. A reason for this is that the absolute and relative differences between 1.0 and 1.6 m levels seem to be dependent of the absolute PM2.5 concentrations controlled by the changing weather conditions throughout the measurement campaign (Figure 7-5).

7.4.3 Influence of traffic-exhaust emissions on PM2.5

The recorded higher PM2.5 exposure of children is supported by the microclimate model simulation. Fed with meteorological parameters from 11-24 as boundary conditions, the model simulated PM2.5 exposure at 4 pm higher at 1.0 than at 1.8m. These differences were also independent of the location on the route (Figure 7-7). The relative differences between children and adult respiratory levels are plausible as PM2.5 was emitted at 0.2 m height in the model. At least six local maxima of simulated relative differences could be allocated to real-world, recorded maxima, even though the horizontal resolution of the model is only 5 x 5 m (Figure 7-7). These sites are located nearby streets with high traffic intensities and where the horizontal dispersion of traffic-related particles is limited by high-rising buildings and narrow streets (Figure 7-7, dots 1-6).

PM2.5 maxima appear related to the low horizontal wind speeds in the simulation combined with the low irradiation due to a closed cloud cover causing lowered thermal convection and, in consequence, low vertical exchange of emitted PM2.5. These findings were limited on traffic-related locations. Within areas of lower traffic occurrences, i.e. the middle of the study area (250 – 1500 m on the route; Figure 7-8), the relative differences show little variability. However, the variance of relative differences was also low at the 'Kaiserstraße' featuring a wide road with fewer obstacles supporting the dispersion of emission, resulting in lower concentrations (4700 – 5250 m on the route). These findings correspond to results of Paas and Schneider (2016) demonstrating that the simulated dispersion of PM10 was also underpredicted throughout the study area. It should be noted though that the simulation represents a snapshot of relative differences for a distinct time. Local variabilities of PM2.5 pollution (e.g. higher number of busses and trucks or a traffic jam at the certain time of measurement) cannot be represented,

so that a reduced variability and fewer maxima were expected. Furthermore, emission sources like tyre and break abrasions as well as whirled up PM2.5, are not simulated, but have a distinct impact on PM2.5 (Karagulian et al., 2019; Sharma and Kumar, 2020). On the other hand, the modelled maxima were more pronounced compared to mean PM2.5 levels, which could be affected by the larger vertical difference of 0.8 m due to the grid cell size. Nevertheless, all relative differences were > 30% lower than the measurements. These underestimated differences could additionally be related to the fact that the model started with a clean atmosphere including no background concentration of particulate matter and only traffic related PM2.5 as an emission source. However, the results of the simulation corroborated that PM2.5 emitted by vehicle exhausts alone are a cause of the measured relative differences in PM2.5 exposure.

7.5 Conclusion

PM2.5 exposure of children and adults was assessed on a route in Mainz-Neustadt from 11-20-to 11-27-2019 during stable weather situations around afternoon rush hours from 3:15 pm to 4:30 pm. Our results show that the absolute PM2.5 exposure at both heights was related to the stability of the weather condition, particularly to wind speeds. We conclude that in six out of eight measurement runs, children were significantly more exposed to PM2.5 than adults, independent of the position along the measurement runs. Relative PM2.5 differences between 1.0 and 1.6 m ranged from 122 % (11-20) to 175 % (11-22) among the runs. The absolute and relative height differences were positively correlated with PM2.5 concentrations. Relative differences also varied more strongly among days than along the study route, whereby the latter showed a tendency towards lower variability with increasing absolute concentrations. Explanatory approaches include accumulation processes of local, near ground emitters causing higher PM2.5 exposure differences between 1.0 and 1.6 m, when the absolute PM2.5 concentrations increase during longer-lasting, calm weather conditions. On the other hand, deviations in absolute PM2.5 was leveled out in differences due to similar progression of the PM2.5 concentrations at both heights. However, two sites with local PM2.5 concentration maxima (‘Grüne Brücke’, ‘Rheinallee’) are still visible in absolute and relative differences.

A simulation of traffic-related PM2.5 exposure within the study area shows similar results, whereby at least six local maxima of simulated relative differences can be attributed to measured maxima. Height

differences in areas with low traffic intensity cannot be displayed by the model, which is why we suggest that other sources including tyre and break abrasion as well as whirled up, play an important role in PM2.5 traffic emission.

We demonstrate that highly time-resolved measurements, and subsequent comparisons, of PM2.5 exposure with low-cost OPC-N3 sensors are appropriate after initial calibration during RH < 85 % conditions. However, since the study includes only eight consecutive measurement runs, further research over a longer period is needed to improve our understanding of PM2.5 exposure differences between children and adults.

7.6 Acknowledgements

We thank the environmental state office of Rhineland-Palatinate, particularly Michael Weißenmayer and Margit von Döhren from Referat 60, Matthias Zimmer and Matthias Voigt from Referat 63, for providing data of the official meteorological measurement stations and the radiometer. The authors thank the municipality of Mainz "Grün und Umweltamt" for providing GIS data for the microclimate simulations. We are also grateful to Klaus E. Rogge for discussions about statistical analysis and to Christian Gnaneswaran for supporting the measurements by foot.

7.7 References

Alfano, B., Barretta, L., Del Giudice, A., Vito, S. de, Di Francia, G., Esposito, E., Formisano, F., Massera, E., Miglietta, M.L., Polichetti, T., 2020. A Review of Low-Cost Particulate Matter Sensors from the Developers' Perspectives. Sensors (Basel, Switzerland) 20 (23). doi:10.3390/s20236819.

Alphasense, 2018. Technical Information Release December 2018: Alphasense Particle Counter OPC-N Range Product Update. http://www.alphasense.com/WEB1213/wp-content/uploads/2019/02/OPC-N3-information-update-Dec-18.pdf. Accessed 1 April 2021.

Azarmi, F., Kumar, P., Marsh, D., Fuller, G., 2016. Assessment of the long-term impacts of PM10 and PM2.5 particles from construction works on surrounding areas. Environmental science. Processes & impacts 18 (2), 208–221. doi:10.1039/c5em00549c.

Bohren, C.F., Huffman, D.R., 1998. Absorption and Scattering of Light by Small Particles. Wiley. doi:10.1002/9783527618156.

Brattich, E., Bracci, A., Zappi, A., Morozzi, P., Di Sabatino, S., Porcù, F., Di Nicola, F., Tositti, L., 2020. How to Get the Best from Low-Cost Particulate Matter Sensors: Guidelines and Practical Recommendations. Sensors (Basel, Switzerland) 20 (11). doi:10.3390/s20113073.

Bruse, M., 1999. Die Auswirkungen kleinskaliger Umweltgestaltung auf das Mikroklima: Entwicklung des prognostischen numerischen Modells ENVI-met zur Simulation der Wind-, Temperatur- und Feuchteverteilung in städtischen Strukturen. Dissertation, Bochum, 217 pp.

Chatzidiakou, L., Krause, A., Popoola, O.A.M., Di Antonio, A., Kellaway, M., Han, Y., Squires, F.A., Wang, T., Zhang, H., Wang, Q., Fan, Y., Chen, S., Hu, M., Quint, J.K., Barratt, B., Kelly, F.J., Zhu, T., Jones, R.L., 2019. Characterising low-cost sensors in highly portable platforms to

quantify personal exposure in diverse environments. Atmospheric measurement techniques 12 (8), 4643–4657. doi:10.5194/amt-12-1-2019.

Cheng, Y.-H., Li, Y.-S., 2010. Influences of Traffic Emissions and Meteorological Conditions on Ambient PM10 and PM2.5 Levels at a Highway Toll Station. Aerosol Air Qual. Res. 10 (5), 456–462. doi:10.4209/aaqr.2010.04.0025.

Crilley, L.R., Shaw, M., Pound, R., Kramer, L.J., Price, R., Young, S., Lewis, A.C., Pope, F.D., 2018. Evaluation of a low-cost optical particle counter (Alphasense OPC-N2) for ambient air monitoring. Atmos. Meas. Tech. 11 (2), 709–720. doi:10.5194/amt-11-709-2018.

Crilley, L.R., Singh, A., Kramer, L.J., Shaw, M.D., Alam, M.S., Apte, J.S., Bloss, W.J., Hildebrandt Ruiz, L., Fu, P., Fu, W., Gani, S., Gatari, M., Ilyinskaya, E., Lewis, A.C., Ng'ang'a, D., Sun, Y., Whitty, R.C.W., Yue, S., Young, S., Pope, F.D., 2020. Effect of aerosol composition on the performance of low-cost optical particle counter correction factors. Atmos. Meas. Tech. 13 (3), 1181–1193. doi:10.5194/amt-13-1181-2020.

Czernecki, B., Półrolniczak, M., Kolendowicz, L., Marosz, M., Kendzierski, S., Pilguj, N., 2017. Influence of the atmospheric conditions on PM10 concentrations in Poznań, Poland. J Atmos Chem 74 (1), 115–139. doi:10.1007/s10874-016-9345-5.

Deutscher Wetterdienst, 2021a. Niederschlag: vieljährige Mittelwerte 1981 - 2010. Deutscher Wetterdienst. https://www.dwd.de/DE/leistungen/klimadatendeutschland/mittelwerte/nieder_8110_fest_html.html?view=nasPublication&nn=16102. Accessed 10 May 2021.

Deutscher Wetterdienst, 2021b. Temperatur: vieljährige Mittelwerte 1981 - 2010. https://www.dwd.de/DE/leistungen/klimadatendeutschland/mittelwerte/temp_8110_fest_html.html%3Fview%3DnasPublication. Accessed 10 May 2021.

Di Antonio, A., Popoola, O.A.M., Ouyang, B., Saffell, J., Jones, R.L., 2018. Developing a Relative Humidity Correction for Low-Cost Sensors Measuring Ambient Particulate Matter. Sensors (Basel, Switzerland) 18 (9). doi:10.3390/s18092790.

Environmental Protection Agency of Germany (UBA), 2017. The Handbook of Emission Factors for Road Transport (HBEFA). https://www2.dmu.dk/AtmosphericEnvironment/Docs/NO2scheme.pdf. Accessed 12.03.21.

Espressif, 2021. ESP32. https://www.espressif.com/en/products/socs/esp32. Accessed 5 February 2021.

European Parliament and Council (EU), 2008. Directive 2008/50/EC of the european Parliament and of the council of 21 May 2008 on ambient air quality and cleaner air for Europe. https://eur-lex.europa.eu/eli/dir/2008/50/oj.

Feng, S., Gao, D., Liao, F., Zhou, F., Wang, X., 2016. The health effects of ambient PM2.5 and potential mechanisms. Ecotoxicology and environmental safety 128, 67–74. doi:10.1016/j.ecoenv.2016.01.030.

Fortune, S., 1987. A sweepline algorithm for Voronoi diagrams. Algorithmica 2 (1-4), 153–174. doi:10.1007/BF01840357.

Gallagher, J., Baldauf, R., Fuller, C.H., Kumar, P., Gill, L.W., McNabola, A., 2015. Passive methods for improving air quality in the built environment: A review of porous and solid barriers. Atmospheric Environment 120, 61–70. doi:10.1016/j.atmosenv.2015.08.075.

Garcia-Algar, O., Canchucaja, L., d'Orazzio, V., Manich, A., Joya, X., Vall, O., 2015. Different exposure of infants and adults to ultrafine particles in the urban area of Barcelona. Environmental monitoring and assessment 187 (1), 4196. doi:10.1007/s10661-014-4196-5.

Goel, A., Kumar, P., 2016. Vertical and horizontal variability in airborne nanoparticles and their exposure around signalised traffic intersections. Environmental pollution (Barking, Essex : 1987) 214, 54–69. doi:10.1016/j.envpol.2016.03.033.

Goldman, L.R., 1995. Children--unique and vulnerable. Environmental risks facing children and recommendations for response. Environmental health perspectives 103 Suppl 6, 13–18. doi:10.1289/ehp.95103s613.

Graham, A.M., Pringle, K.J., Arnold, S.R., Pope, R.J., Vieno, M., Butt, E.W., Conibear, L., Stirling, E.L., McQuaid, J.B., 2020. Impact of weather types on UK ambient particulate matter concentrations. Atmospheric Environment: X 5, 100061. doi:10.1016/j.aeaoa.2019.100061.

Gualtieri, M., Ovrevik, J., Mollerup, S., Asare, N., Longhin, E., Dahlman, H.-J., Camatini, M., Holme, J.A., 2011. Airborne urban particles (Milan winter-PM2.5) cause mitotic arrest and cell death:

Effects on DNA, mitochondria, AhR binding and spindle organization. Mutation research 713 (1-2), 18–31. doi:10.1016/j.mrfmmm.2011.05.011.

Gysel, M., Crosier, J., Topping, D.O., Whitehead, J.D., Bower, K.N., Cubison, M.J., Williams, P.I., Flynn, M.J., McFiggans, G.B., Coe, H., 2007. Closure study between chemical composition and hygroscopic growth of aerosol particles during TORCH2. Atmos. Chem. Phys. 7 (24), 6131–6144. doi:10.5194/acp-7-6131-2007.

Habre, R., Moshier, E., Castro, W., Nath, A., Grunin, A., Rohr, A., Godbold, J., Schachter, N., Kattan, M., Coull, B., Koutrakis, P., 2014. The effects of PM2.5 and its components from indoor and outdoor sources on cough and wheeze symptoms in asthmatic children. Journal of exposure science & environmental epidemiology 24 (4), 380–387. doi:10.1038/jes.2014.21.

Hagler, G.S.W., Williams, R., Papapostolou, V., Polidori, A., 2018. Air Quality Sensors and Data Adjustment Algorithms: When Is It No Longer a Measurement? Environmental science & technology 52 (10), 5530–5531. doi:10.1021/acs.est.8b01826.

Hamburger, T., McMeeking, G., Minikin, A., Birmili, W., Dall'Osto, M., O'Dowd, C., Flentje, H., Henzing, B., Junninen, H., Kristensson, A., Leeuw, G. de, Stohl, A., Burkhart, J.F., Coe, H., Krejci, R., Petzold, A., 2011. Overview of the synoptic and pollution situation over Europe during the EUCAARI-LONGREX field campaign. Atmos. Chem. Phys. 11 (3), 1065–1082. doi:10.5194/acp-11-1065-2011.

Hoffmann, J., 2019. DWD. SXEU31 DWAV 200800. Synoptische Übersicht Kurzfrist. https://www.wetterzentrale.de/article.php?id=70603&lang=1.

Imhof, D., Weingartner, E., Vogt, U., Dreiseidler, A., Rosenbohm, E., Scheer, V., Vogt, R., Nielsen, O.J., Kurtenbach, R., Corsmeier, U., Kohler, M., Baltensperger, U., 2005. Vertical distribution of aerosol particles and NOx close to a motorway. Atmospheric Environment 39 (31), 5710–5721. doi:10.1016/j.atmosenv.2004.07.036.

Karagulian, F., Barbiere, M., Kotsev, A., Spinelle, L., Gerboles, M., Lagler, F., Redon, N., Crunaire, S., Borowiak, A., 2019. Review of the Performance of Low-Cost Sensors for Air Quality Monitoring. Atmosphere 10 (9), 506. doi:10.3390/atmos10090506.

Karagulian, F., Belis, C.A., Dora, C.F.C., Prüss-Ustün, A.M., Bonjour, S., Adair-Rohani, H., Amann, M., 2015. Contributions to cities' ambient particulate matter (PM): A systematic review of local source contributions at global level. Atmospheric Environment 120, 475–483. doi:10.1016/j.atmosenv.2015.08.087.

Kumar, P., Fennell, P., Britter, R., 2008. Measurements of particles in the 5-1000 nm range close to road level in an urban street canyon. Science of The Total Environment 390 (2-3), 437–447. doi:10.1016/j.scitotenv.2007.10.013.

Kumar, P., Khare, M., Harrison, R.M., Bloss, W.J., Lewis, A.C., Coe, H., Morawska, L., 2015. New directions: Air pollution challenges for developing megacities like Delhi. Atmospheric Environment 122, 657–661. doi:10.1016/j.atmosenv.2015.10.032.

Kumar, P., Rivas, I., Sachdeva, L., 2017. Exposure of in-pram babies to airborne particles during morning drop-in and afternoon pick-up of school children. Environmental pollution (Barking, Essex : 1987) 224, 407–420. doi:10.1016/j.envpol.2017.02.021.

Lelieveld, J., Klingmüller, K., Pozzer, A., Pöschl, U., Fnais, M., Daiber, A., Münzel, T., 2019. Cardiovascular disease burden from ambient air pollution in Europe reassessed using novel hazard ratio functions. European heart journal 40 (20), 1590–1596. doi:10.1093/eurheartj/ehz135.

Mazur, L.J., 2003. Pediatric environmental health. Current problems in pediatric and adolescent health care 33 (1), 6–25. doi:10.1067/mps.2003.1.

McCauley, J.D., Aime, A., Blazek, R., Metz, M., 2020. GRASS GIS 7.9.dev Reference Manual: v.voronoi. https://grass.osgeo.org/grass79/manuals/v.voronoi.html.

McGregor, G.R., Bamzelis, D., 1995. Synoptic typing and its application to the investigation of weather air pollution relationships, Birmingham, United Kingdom. Theor Appl Climatol 51 (4), 223–236. doi:10.1007/BF00867281.

Mie, G., 1908. Beiträge zur Optik trüber Medien, speziell kolloidaler Metallösungen. Ann. Phys. 330 (3), 377–445. doi:10.1002/ANDP.19083300302.

Nachman, K.E., Parker, J.D., 2012. Exposures to fine particulate air pollution and respiratory outcomes in adults using two national datasets: a cross-sectional study. Environmental health : a global access science source 11, 25. doi:10.1186/1476-069X-11-25.

Paas, B., Schneider, C., 2016. A comparison of model performance between ENVI-met and Austal2000 for particulate matter. Atmospheric Environment 145, 392–404. doi:10.1016/j.atmosenv.2016.09.031.

Petters, M.D., Kreidenweis, S.M., 2007. A single parameter representation of hygroscopic growth and cloud condensation nucleus activity. Atmos. Chem. Phys. 7 (8), 1961–1971. doi:10.5194/acp-7-1961-2007.

Sharma, A., Kumar, P., 2020. Quantification of air pollution exposure to in-pram babies and mitigation strategies. Environment international 139, 105671. doi:10.1016/j.envint.2020.105671.

Shepard, D., 1968. A two-dimensional interpolation function for irregularly-spaced data, in: Proceedings of the 1968 23rd ACM national conference on -. the 1968 23rd ACM national conference, Not Known. ACM Press, New York, New York, USA, pp. 517–524. doi:10.1145/800186.810616.

Simcom, 2021. Sim28. https://www.simcom.com/product/SIM28.html. Accessed 5 February 2021.

Simon, H., Fallmann, J., Kropp, T., Tost, H., Bruse, M., 2019. Urban Trees and Their Impact on Local Ozone Concentration—A Microclimate Modeling Study. Atmosphere 10 (3), 154. doi:10.3390/atmos10030154.

Singh, R.B., Huber, A.H., Braddock, J.N., 2003. Development of a microscale emission factor model for particulate matter for predicting real-time motor vehicle emissions. Journal of the Air & Waste Management Association (1995) 53 (10), 1204–1217. doi:10.1080/10473289.2003.10466288.

Stewart, I.D., Oke, T.R., 2012. Local Climate Zones for Urban Temperature Studies. Bulletin of the American Meteorological Society 93 (12), 1879–1900. doi:10.1175/BAMS-D-11-00019.1.

Tang, G., Zhang, J., Zhu, X., Song, T., Münkel, C., Hu, B., Schäfer, K., Liu, Z., Zhang, J., Wang, L., Xin, J., Suppan, P., Wang, Y., 2016. Mixing layer height and its implications for air pollution over Beijing, China. Atmos. Chem. Phys. 16 (4), 2459–2475. doi:10.5194/acp-16-2459-2016.

Torres-Ramos, Y.D., Montoya-Estrada, A., Guzman-Grenfell, A.M., Mancilla-Ramirez, J., Cardenas-Gonzalez, B., Blanco-Jimenez, S., Sepulveda-Sanchez, J.D., Ramirez-Venegas, A., Hicks, J.J., 2011. Urban PM2.5 induces ROS generation and RBC damage in COPD patients. Frontiers in bioscience (Elite edition) 3, 808–817. doi:10.2741/e288.

Umweltmeteorologie RLP, 2019. State Office of Rhineland-Palatinate. https://luft.rlp.de/de/umweltmeteorologie/.

Wagner, P., Schäfer, K., 2017. Influence of mixing layer height on air pollutant concentrations in an urban street canyon. Urban Climate 22, 64–79. doi:10.1016/j.uclim.2015.11.001.

Walser, A., Sauer, D., Spanu, A., Gasteiger, J., Weinzierl, B., 2017. On the parametrization of optical particle counter response including instrument-induced broadening of size spectra and a self-consistent evaluation of calibration measurements. Atmos. Meas. Tech. 10 (11), 4341–4361. doi:10.5194/amt-10-4341-2017.

Wania, A., Bruse, M., Blond, N., Weber, C., 2012. Analysing the influence of different street vegetation on traffic-induced particle dispersion using microscale simulations. Journal of environmental management 94 (1), 91–101. doi:10.1016/j.jenvman.2011.06.036.

Wickham, H., 2020. Package 'plyr': Tools for Splitting, Applying and Combining Data; Version 1.8.6. http://had.co.nz/plyr. Accessed 10.02.21.

Zauli Sajani, S., Marchesi, S., Trentini, A., Bacco, D., Zigola, C., Rovelli, S., Ricciardelli, I., Maccone, C., Lauriola, P., Cavallo, D.M., Poluzzi, V., Cattaneo, A., Harrison, R.M., 2018. Vertical variation of PM2.5 mass and chemical composition, particle size distribution, NO2, and BTEX at a high rise building. Environmental pollution (Barking, Essex : 1987) 235, 339–349. doi:10.1016/j.envpol.2017.12.090.

Zeuschner, J., 2019. DWD. SXEU31 DWAV 230800. Synoptische Übersicht Kurzfrist. https://www.wetterzentrale.de/article.php?id=70739&lang=1.

Zhou, S., Wu, L., Guo, J., Chen, W., Wang, X., Zhao, J., Cheng, Y., Huang, Z., Zhang, J., Sun, Y., Fu, P., Jia, S., Chen, Y., Kuang, J., 2019. Vertical distribution of atmospheric particulate matters within urban boundary layer in southern China: size-segregated chemical composition and secondary formation through cloud processing and heterogeneous reactions. doi:10.5194/acp-2019-155.

ZIMEN, 2019. Luft-Überwachung in Rheinland-Pfalz. State Office of Rhineland-Palatinate. https://luft.rlp.de/de/startseite/.

7.8 Appendix

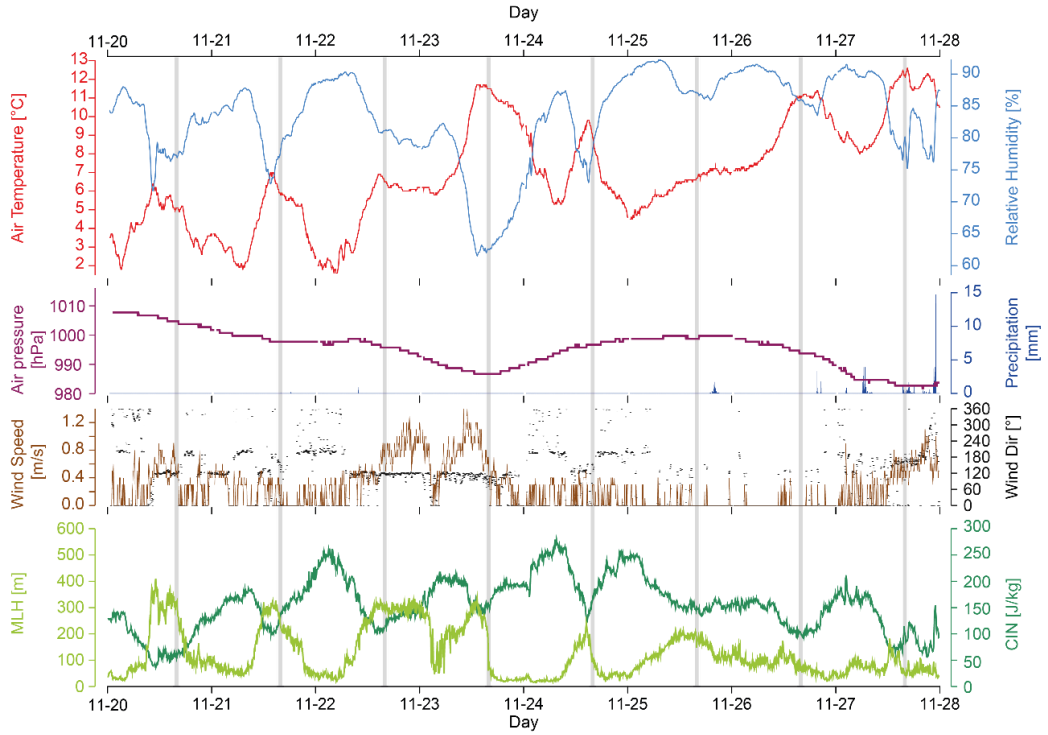

Figure 7-9: Weather conditions during measurement period. Grey bars represent daily measurement periods. Air temperature, relative humidity and air pressure were measured at 2m a.g.l. at the measurement station Mainz-Zitadelle, wind speed and direction 10m a.g.l and precipitation 2m a.g.l. at the measurement station Mainz-Mombach. The mixing layer height (MLH) and the convective inhibition (CIN) were measured with a radiometer at the headquarter of the state office for environment in Mainz.

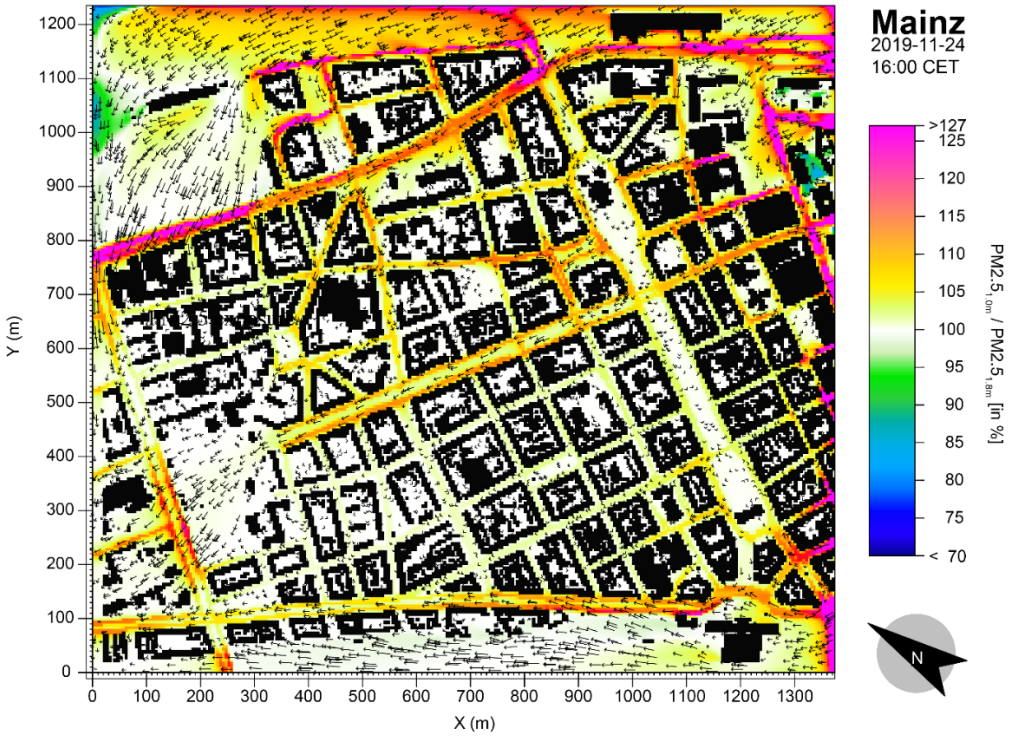

Figure 7-10: Simulated relative differences distribution of PM2.5-concentrations between 1.0m and 1.8m in the study area.

8 Modeling the outdoor cooling impact of highly radiative "super cool" materials applied on roofs

Tim Sinsel[1], Helge Simon[1], Ashley M. Broadbent[2,3], Michael Bruse[1], Jannik Heusinger[4]

[1]*Department of Geography, Johannes Gutenberg University Mainz, 55099 Germany*
[2]*School of Geographical Sciences and Urban Planning, Arizona State University, 85281 Tempe, USA*
[3]*Urban Climate Research Center, Arizona State University, 85281 Tempe, USA*
[4]*Institute of Geoecology, TU Braunschweig, 38106 Germany*

Summary:

Aside from air quality modeling, ENVI-met was applied as research tool for new urban heat mitigation measures regarding passive daytime radiative cooling (PDRC). PDRC gained increasing interest over the last years, as new materials have been developed that combine a very high-albedo (>0.96) and very high emissivity (>0.98), which allows them to stay several degrees Celsius below ambient air temperatures – even during high solar radiation conditions. Due to their high reflectivity and thus negative impact on MRT, these materials are not considered as future street or wall materials but as possible coating for roofs. Previous studies found that they could be able to improve building indoor temperatures and hence lower building energy demands. In order to evaluate their possible outdoor impact on air temperature at pedestrian level when applied on roofs on a larger scale, a sensitivity study using ENVI-met was conducted which is presented in the following. Performances of the new super cool roofs (SCR) were compared against the impacts of both traditional cool and green roofs. The study additionally featured varying building height scenarios of a uniformly built model area to examine a possible dependency of pedestrian-level air temperature cooling on building height. The author prepared, conducted, and evaluated the simulations, and wrote the manuscript.

Urban Climate 38(85), June 2021 – published

“

8.1 Introduction

Most urban agglomerations are experiencing several trends simultaneously (1) growth (densification and sprawl), (2) demographic change to an older and hence more vulnerable population, and (3) greenhouse gas-induced climate warming (Broadbent et al., 2020). These trends can be observed in developed and developing countries and potentially lead, due to the combined effects of increased heat exposure and heightened heat vulnerability, to elevated heat stress in future cities (Schinasi et al., 2018). Urban migration increases the pressure to build high-density housing, which can increase building density and thus the urban heat island (UHI) intensity. These trends reinforce the need for more space-saving heat mitigation measures that harmonize with the built environment. Heat mitigating measures, which have been intensely studied, can be clustered in two groups: (1) measures that concentrate on increasing latent heat fluxes through vegetation, such as parks, street trees and – in order to save valuable space in cities – roof and building façade greening, and (2) measures that focus on modifying the albedo of urban building materials, such as roads, walls, and roofs (Akbari et al., 2016; Aflaki et al., 2017). The general consensus is that vegetation and albedo measures cool the air by up to 2-3 K and 1 K, respectively (Berardi et al., 2020; Yang et al., 2015; Tsoka et al., 2018; Santamouris et al., 2018, 2011; Bowler et al., 2010). Although measures can provide cooling, the warming effects of climate change under a high intensity emissions scenario (RCP 8.5) cannot be offset by intensively applied conventional adaptation measures (i.e., green roofs, cool roofs, street trees) (Krayenhoff et al., 2018). These results emphasize the urgency of reducing global emissions of greenhouse gases as well as searching for alternative and more effective adaptation solutions to cool urban areas.

While previously examined cool materials have reported maximum albedo of 0.85 and an emissivity of 0.9, a new material type was recently reported by independent research groups featuring a very high albedo of > 0.95 and emissivity of > 0.95 (Gentle and Smith, 2015; Mandal et al., 2018; Raman et al., 2014; Zhai et al., 2017). This new material with its high applicability as coating on all kinds of surfaces can potentially be used as a building roof material (Gentle and Smith, 2015) and produced cost-effectively (Zhai et al., 2017). The high reflectivity is typically achieved by a silver layer, while a polymer layer leads to a high longwave emissivity. The thermal characteristics of this new material could

represent a paradigm shift in heat mitigation infrastructure since this material stays cooler than the ambient air temperature under high solar insolation conditions (Mandal et al., 2018). One study reported surface temperatures of this new material being 11 K cooler than a nearby conventional cool roof during daytime (Gentle and Smith, 2015). Due to these superior thermal characteristics, we will hereafter use the term ‘super cool roof’ (SCR) for this new material type being applied on a roof. Recent studies suggest that mass production of this material is practically and economically feasible (Mandal et al., 2018; Zhai et al., 2017). Although ageing and weathering of cool materials is an aspect that can reduce their heat island mitigation effectiveness (Dornelles et al., 2015; Mastrapostoli et al., 2016; Synnefa et al., 2007), this study focuses on their full performance potential when initially applied, i.e. ageing and weathering is not further investigated.

When used as ground or wall material, cool materials with their high reflection of shortwave radiation may lead to heightened mean radiant temperatures at street-level and potential adversely impact human thermal comfort (Falasca et al., 2019; Middel et al., 2020; Schrijvers et al., 2016). This study hence only focuses on the application of (super) cool materials on rooftops, where the high reflection will not substantially affect the thermal comfort of pedestrians. By exploring the potential of this new material type to cool the ambient air temperature in the urban environment when being applied as a roofing solution at scale, we close a research gap not addressed by earlier work that only focused on the implications of super cool materials for building interior cooling (Baniassadi et al., 2018).

Here, we analyzed the cooling impacts of different roof types using idealized neighborhood simulations. Roofing materials are analyzed concerning their cooling impact at pedestrian level. The SCR scenarios are compared with non-reflective roofs (“reference roof”, hereafter RR), conventional high-quality cool roofs (hereafter CR), and green roofs (hereafter GR) to quantify the cooling effectiveness of the new material type. To explore the possible dependencies between cooling strength and building height, all roof type scenarios are simulated for three different building heights of 13 m, 25 m, and 50 m.

8.2 Methodology

To run the simulations with realistic properties for the different roof materials, databases were prepared with precise thermal and radiative parameter values (Section 8.2.1). To analyze and compare the effects

of CR, SCR, and GR on pedestrian-level air temperature depending on building height, a sensitivity study using the microscale model ENVI-met was conducted (Section 8.2.2). To be able to compare modeled values against the measurements of Mandal et al. (2018), the model area location of the sensitivity study was set to New York City (NYC).

8.2.1 Database Preparation

ENVI-met's building properties were adapted for the four different roof types simulated: RR, CR, GR, and SCR. All simulations used the same wall material properties, which were based on the Midrise Apartment Post 1980 Standard for American Housing (Table 8-1; Deru et al., 2010).

Table 8-1: Physical properties of building materials used in the sensitivity study (Deru et al., 2010b; Mandal et al., 2018; Santamouris et al., 2018). These parameters are used for WRF and ENVI-met models.

	Layer	Name	Albedo	Absorptivity	Emissivity	Thickness [m]	Conductivity [W (m K)$^{-1}$]	Density [kg m^{-3}]	Specific Heat (J (kg K)$^{-1}$)
Wall									
	Outside	Concrete	0.2	0.8	0.9	0.2	1.311	2240	836.8
	Middle	Steel frame Insulation	0.2	0.8	0.9	0.08	0.049	265	837
	Inside	1/2IN Gypsum	0.2	0.8	0.9	0.01	0.16	785	830
Roof									
	Outside	RR membrane	0.2	0.8	0.9	0.01	0.16	1121	1460
	Outside	CR membrane	0.85	0.15	0.9	0.02	0.85	1200	1200
	Outside	SCR membrane	0.96	0.04	0.97	0.02	0.85	1200	1200
	Middle	Insulation	0.2	0.8	0.9	0.14	0.049	265	837
	Inside	Metal Decking	0.2	0.8	0.9	0.01	45	7680	418

The physical properties thus represent typical building parameters for housings in NYC to fit the model area location. Roofing materials were also derived from the American Housing database, only the outer layers of the different roof types were altered to resemble RR, CR, or SCR. These alterations include albedo, absorptivity, emissivity, and thickness of the outer layer (as summarized in Table 8-1). CR features the same emissivity as RR (0.9) but a much higher albedo of 0.85, which is a value at the upper

limit of commercially available cool roofs and was used in recent studies as well (Imran et al., 2018). By using the highest possible albedo value being available for cool roofs, it can be examined if they too were a capable of staying below ambient air temperature, as it is claimed for the new SCR material. The SCR material has a very high emissivity of 0.96 and an even higher albedo of 0.97 (Mandal et al., 2018). GR features the same roof material properties as RR but with an additional greening and substrate layer. Here, the default greening of the ENVI-met database with the ID 01NADS is used, featuring a 15 cm thick, irrigated (water coefficient of 0.5) substrate of Sandy Loam and Styrofoam as well as a 30 cm thick simple plant layer with a Leaf Area Index (LAI) of 1.5 m^2/m^2.

8.2.2 Simulation setup

Simulations are performed with the widely used urban microclimate model ENVI-met version 4.4.5 (Bruse, 1999; Huttner, 2012; Simon, 2016). The model calculates three-dimensional wind fields, turbulence, air temperature and humidity, radiative fluxes as well as vegetation- and building-atmosphere interactions (Bruse, 1999; Morakinyo et al., 2017; Nikolova et al., 2011; Simon, 2016). Several studies evaluated ENVI-met as useful and accurate tool for modeling urban environments (Tsoka et al., 2018) featuring an explicit building physics model (Simon, 2016). Building surface temperatures produced by ENVI-met were compared and confirmed by measurements in several studies (Forouzandeh, 2021; Simon et al., 2017; Tsoka et al., 2018; Yang et al., 2013). The review study of Tsoka, Tsikaloudaki, and Theodosiou (2018) reported that all surface temperature evaluation studies showed a high agreement with measurements represented by statistical analysis values between 0.60-0.97 for R^2, 0.20-1.89 for MBE, and 2.1-4.8 °C for RMSE. Based on this high accuracy in urban modeling, ENVI-met was already used several times to examine the effects of cool roof types on the surrounding microclimate (Di Giuseppe et al., 2017; Evola et al., 2017; Huynh and Eckert, 2012; Kolokotroni, 2017; Morakinyo et al., 2017; Ng et al., 2012; Salata et al., 2017; Santamouris et al., 2018; Taleghani et al., 2016, 2014; Tsoka et al., 2018; Wang et al., 2016; Wang and Akbari, 2015).

Table 8-2: Simulation parameters of the sensitivity study in ENVI-met.

Start date and time (Local)	20.07.2018 05:00
Duration [h]	48
Wind Speed [m s^{-1}]	2

Wind Direction [°]	270
Meteorological Boundary Conditions	Full Forcing
Location Lat (Lower Left Corner)	40.72 °N
Location Lon (Lower Left Corner)	-74.02 °E
Dimensions	190 x 190 x 30
Resolutions (X, Y, Z) [m]	4 x 4 x 4
Lowest Grid Cell Splitted	Yes
Telescoping: Factor & Starting Height	20 % above 70 m
Height of 3D Model Domain [m]	249
Building density [%]	33.52

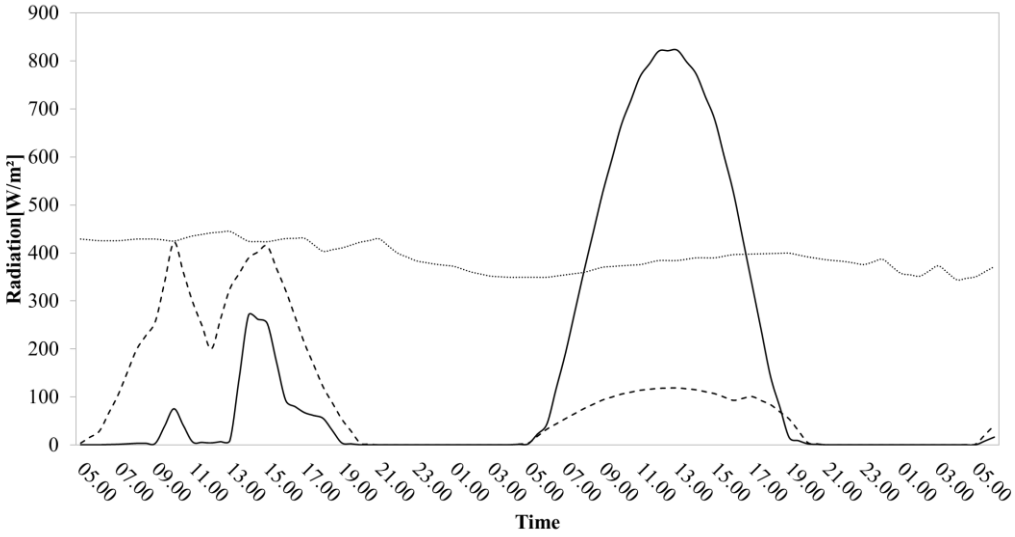

(a)

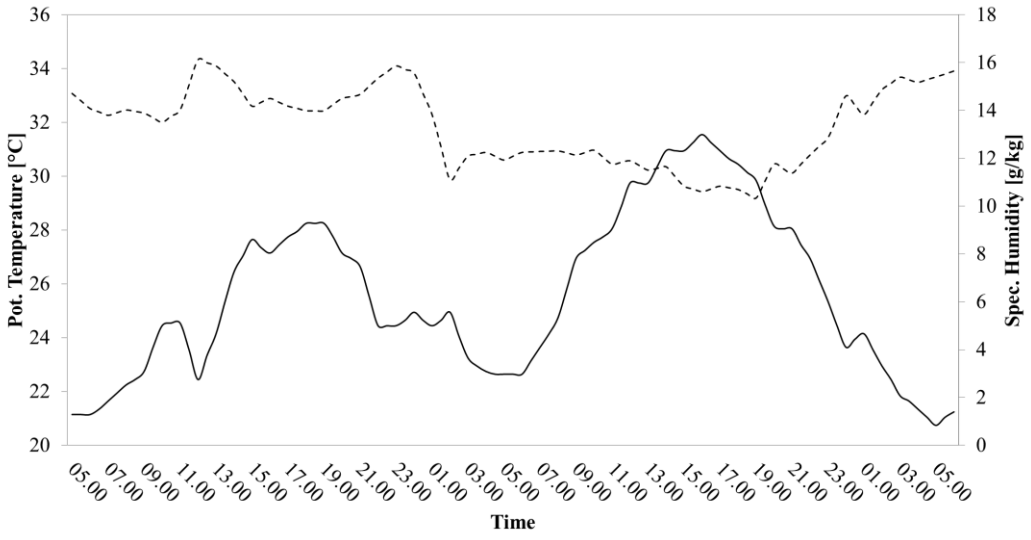

(b)

Figure 8-1: Boundary conditions for the sensitivity study in ENVI-met derived from Energy Plus Weather file for NYC depicting direct shortwave (black line), diffuse shortwave (dashed line) and longwave radiation (dotted line) (a) as well as potential air temperature (black line) and specific air humidity (dashed line) (b).

In order to quantify the effects of RR, CR, SCR, and GR on roof surface temperature and street-level air temperature, we created an idealized domain with a homogenous neighborhood (Figure 8-2). We then simulated the effects of different building heights (13 m, 25 m, 50 m) on air temperature at pedestrian level for the four different roof types. To eliminate all other factors that may influence the microclimate, the same simulation parameters such as time, duration, and meteorological boundary conditions were used in all model runs: a typical hot summer day for NYC starting with sunrise at 05:00. All other simulation parameters were not modified from the default settings of ENVI-met 4.4.5. Meteorological boundary conditions were defined as Full Forcing, meaning that half-hourly intervals of inflow values for wind, temperature, humidity, and radiation can be defined as inflow for the model (Huttner, 2012; Simon, 2016). Full Forcing values were derived from the Energy Plus Weather File for NYC Central Park (Table 8-2 and Figure 8-1) (ASHRAE, 2001). Wind speed and direction were not forced due to very high wind speeds that may have caused strong turbulence in the ENVI-met model. The simulation was set to start on 20th July with a duration of 48 h. The first simulation day served as a spin-up period and the model output of the second day was used for further analysis as it represents a typical hot summer day with clear sky conditions.

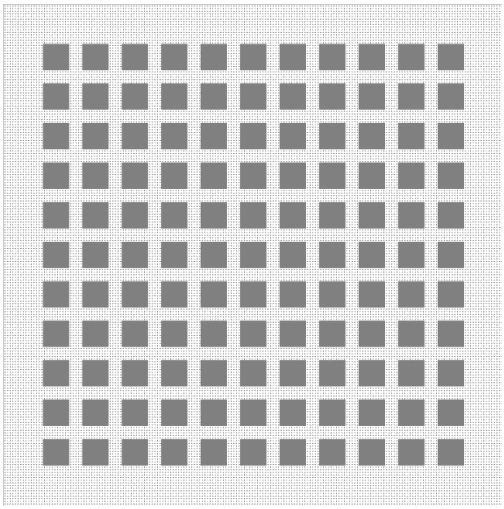

Figure 8-2: Model domain for the sensitivity study in ENVI-met: Grey shapes resemble buildings. The horizontal size of the domain is 760 m by 760 m.

Following Ng et al., 2012, a symmetrical building layout featuring a high building density of 33.52 %, which corresponds to local climate zones open midrise to open highrise depending on the different building heights tested (Table 8-2; Stewart and Oke, 2012). For simplicity, the model domain did not contain any vegetation (besides green roofs in the GR scenario). The buildings are arranged in equidistant spacing of 5 grid cells every 20 meters (Figure 8-2). The soil profile is uniformly defined with the default street of ENVI-met’s database (ID: 0100ST) with an albedo of 0.2. Building parameters are specified in Table 8-1.

8.3 Results & Discussion

In the following section, results of the sensitivity study are presented analyzing the general thermal behavior of CR, SCR, and GR and the differences in cooling performance within the different building height scenarios. At first, roof surface temperatures are compared between different roof types. Conforming to the empirical studies of Gentle and Smith 2015 and Mandal et al. 2018, it is found that the SCR material constantly remains below ambient air temperature (Figure 8-3). Using statistical analysis, the possible driving factors that cause differences in roof surface temperature are explored. Secondly, the cooling effect of pedestrian-level air temperature is examined by analyzing the effect over the diurnal cycle and with spatial distribution maps. In a third step, the relation between building height and air temperature cooling performance at pedestrian level is examined.

8.3.1 Diurnal variation in roof surface temperatures

The surface temperatures of the four different roof types feature distinct thermal behaviors (Figure 8-3). Values were extracted from the same specific roof cell of every scenario. The spin-up day is also included in this part of the analysis to additionally show the different roof types’ behavior under cloudy conditions: The sudden drop in received shortwave radiation during noon of the first simulated day is – in varying strength – also found in all temperature curves. The lowest impact of the drop is observed for SCR temperatures. In general, all roof temperature evolutions follow the pattern of the shortwave radiation with a delay: Notably, the surface temperature maxima of different roof types are shifted to later times of the day. This shift increases as the overall surface temperature of the roof types decreases, i.e., CR reaches its maximum later than RR, and SCR/GR even later than CR.

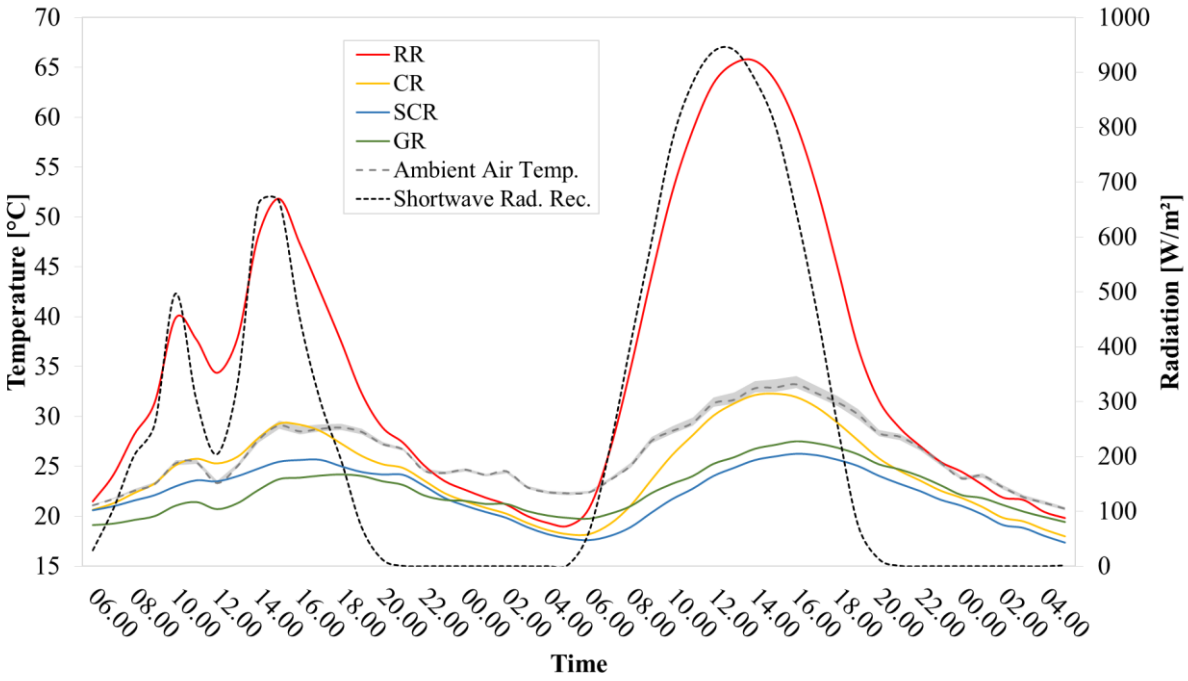

Figure 8-3: Simulated surface temperatures of reference roofs (RR), cool roofs (CR), super cool roofs (SCR) and green roofs (GR) as well as received shortwave radiation and ambient air temperature as average above all different roof types during a 48 h simulation. Grey shadowing around the ambient air temperature curve indicates the minimum and maximum deviation of the ambient air temperature in all roof type scenarios from the average ambient air temperature.

Surface temperatures of SCR and GR remain below the average ambient air temperature at roof level over the whole course of the simulation. The difference between SCR surface temperature and ambient air temperature is more than 6 K during the peak of direct solar radiation (~941 W/m²). Our findings are thus consistent with measurement studies that recorded a temperature drop of around 4-5 K for NYC during slightly weaker solar irradiance of 800-900 W/m² (Mandal et al., 2018; Raman et al., 2014). By contrast, CR matches and RR significantly exceeds ambient air temperatures during the day. Besides the strong performance of SCR, GR features even lower surface temperatures than SCR during the cloudy simulation day and only slightly higher temperatures (approx. 1.3 K) during the clear sky conditions of the second simulated day. These low temperatures in general are not connected to albedo or emissivity of the roof material but are caused by the soil substrate and vegetation. By applying these on the outer surface, these elements shade the RR surface below at all times. Additionally, both substrate and plants, create a latent heat flux by evapotranspiration which cools down their surroundings. This effect is however strongly depending on moisture conditions (Heusinger and Weber, 2017). With the simulated moderate water availability (c.f. Section 8.2.1), the effects are rather comparable with a

situation at the beginning of a heatwave or with an irrigated green roof. In general, green roofs are however not irrigated and thus show weaker performances during longer lasting heat and drought waves (Heusinger et al., 2018; Heusinger and Weber, 2017). The daily minimum and maximum surface temperatures of the four roof types are summarized in Table 8-3.

Table 8-3: Simulated minimum and maximum values of roof surface temperatures and ambient air temperatures averaged above all roofs during the entire model run

	Min. Temperature [°C]	Max. Temperature [°C]
RR	19.05	65.66
CR	18.01	32.27
SCR	17.34	26.26
GR	19.13	27.51
Ambient Air	20.78	33.21

To understand the responses of roof types to meteorological conditions we investigate the correlation between simulated roof surface temperatures and key meteorological variables for the whole 48-hour simulation period. The analysis shows that RR surface temperatures feature a high correlation with incoming shortwave radiation ($R^2 \sim 0.89$) meaning that 89 % of the variation in RR surface temperatures are a direct result of the solar radiation (Table 8-4). Its dependency on ambient air temperature is slightly less significant ($R^2 \sim 0.77$). CR shows the inverse to RR, its surface temperatures largely depend on ambient air temperature ($R^2 \sim 0.86$), while solar radiation plays a less important role ($R^2 \sim 0.57$) in determining surface temperature. The analysis of SCR demonstrates a low dependency of surface temperatures on ambient air temperature ($R^2 \sim 0.69$) and a weak correlation between SCR surface temperature and solar radiation ($R^2 \sim 0.26$). SCR surface temperature therefore seems to be more disconnected from both parameters (at least according to linear correlation). GR has a weak correlation with radiation ($R^2 \sim 0.27$) but features a high dependency on ambient air temperature ($R^2 \sim 0.91$) which can again be explained by the presence of soil substrate and greenery above the roof surface. When examining the dependencies using autocorrelation, which includes a data series shift for temporal lags, we find much higher correlations. Especially, dependencies of CR, SCR, and GR surface temperatures on radiation are increased which matches the observed delay in maxima (Figure 8-3).

Table 8-4: Dependency of ENVI-met's RR, CR, SCR, and GR surface temperatures on radiation and air temperature, respectively calculated by R^2 and by autocorrelation (ACF).

	with Radiation		with Ambient Air Temperature	
	R^2	ACF	R^2	ACF
RR Temperature	0.89	0.94	0.77	0.87
CR Temperature	0.57	0.75	0.86	0.93
SCR Temperature	0.26	0.51	0.69	0.83
GR Temperature	0.27	0.52	0.91	0.96

For RR, CR and SCR, the findings of the regression model analysis clearly point to the albedo and emissivity as being the cause for the different performances: RR has a relatively low albedo and an emissivity of 0.9, meaning its surface temperature is driven by the large changes in solar radiation over the course of the day. Whereas CR, with its significantly higher albedo (0.85) but identical emissivity (0.9) to RR (albedo of 0.2), acts as an intermediate with rather high correlations for both air temperature and solar radiation. For the SCR, having the highest albedo (0.96) and emissivity (0.97), the diurnal cycle of the surface temperature is rather decoupled from the diurnal cycle of shortwave radiation but mirrors the evolution of air temperature throughout the diurnal cycle with a temporal lag.

8.3.2 Cooling effect of roof types on pedestrian-level air temperature

In order to compare the air temperature cooling impact of the different roof types at pedestrian level, air temperatures at 1.5 m height are averaged for all building height scenarios and plotted for the whole diurnal cycle. Values are extracted and compared for the second day to analyze the maximum possible cooling impact during clear sky conditions after the spin-up day. Since the cooling effect increases in downwind direction (Figure 8-5a), analyzed data are taken from the eastern, downwind part of the model domain (indicated by the white box in Figure 8-5a, wind flowing from west to east).

In general, the cooling effect of SCR relative to RR shows a steady rise until it reaches its maximum during midday with air temperature differences up to 0.83 K (Figure 8-4). After midday, these differences decline to 0.2 K during nighttime. The cooling effect during nighttime is explained by the material properties of the roof: SCR's high albedo reduces the amount of energy stored in the roof. In contrast, RR absorbs much more heat during daytime and releases it during nighttime, leading to a cooling effect of SCR even during times of no irradiation. Therefore, the cooling effect of SCR might increase during

longer lasting heat waves but proving that was beyond the scope of this study and will require future research.

CR features the same general cooling effect evolution as SCR, however with a lower maximum cooling impact of 0.7 K during midday and a lower cooling of 0.15 K during nighttime. GR shows a lower cooling impact than SCR and CR during morning hours, and reaches the same peak as CR during midday but features the strongest cooling performance during the evening and nighttime. Due to the evapotranspiration, GR performs differently to CR and SCR. Instead of a high albedo and emissivity, the cooling effect of GR stems from the large latent heat flux and thus comparatively low sensible heat flux depending on the water availability of the substrate. With ceasing solar radiation, the photosynthesis stops which in turn lowers the latent heat flux, as only evaporation of the substrate layer can take place. By that, GR’s cooling effect is also lowered during phases of less or no solar radiation and stabilizes around 0.23 K at nighttime. In general, SCR outperforms both CR and GR during daytime with an additional cooling of up to 0.15 K but is slightly outperformed by GR during nighttime by around 0.05 K.

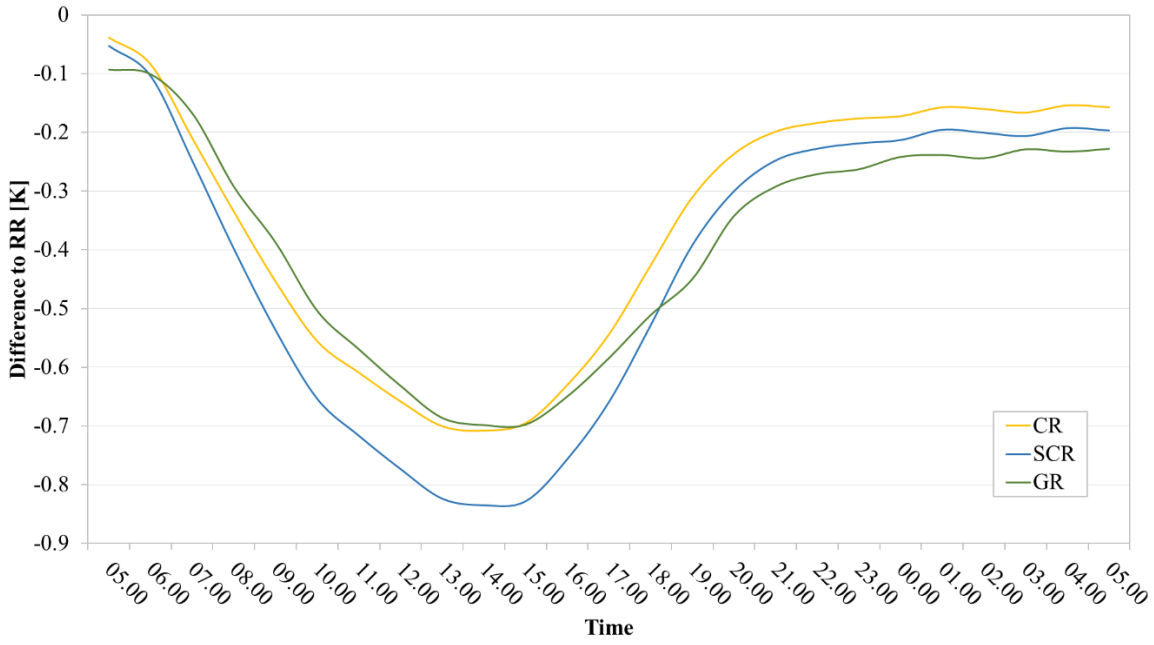

Figure 8-4: Simulated air temperature difference of CR, SCR, and GR compared with RR averaged for all building height scenarios during the diurnal cycle of the second simulated day. Values of 1.2 m height are averaged over free atmosphere cells inside of canyons in the downwind center of the model area indicated by the white box in Figure 8-5.

The spatial distribution of air temperature impacts derived from SCR at the time of maximum cooling (15:00 local time) (c.f. Figure 8-4) shows that the cooling effect quickly converges to a stable value of

around 0.8 K in the downwind center of the model area (Figure 8-5a). This is caused by a wake-interference-flow effect, which describes how cooler air is transported down into the leeward street canyons (Oke, 1987). However, locally, much stronger cooling effects of up to -2.4 K are predicted by the model. These areas are found at the northern and southern boundaries of the built-up area. Right at the edge of these built-up boundaries, positive temperature anomalies up to 1.6 K are predicted. Vertical YZ cuts through the model area at grid cell 154 / 618 m for both RR and SCR in Figure 8-5b provide the explanation for these strong positive and negative temperature anomalies. In RR, both low-albedo street and roof surfaces (albedo 0.2) are heated up by solar radiation causing warmed air to rise due to thermal convection. In the non-built-up area at the northern and southern boundary, wind speeds are stronger than at the model area center as the wind has no obstructions there. Warm air is transported downwind while cooler air from higher levels above the model area center pours in, thereby forming a vortex at both boundaries. In SCR, hot air is only created above low-albedo street surfaces. Cooler air from above the roof surfaces is transported down into the canyons preventing thermal convection and thus the creation of a larger vortex. In contrast to RR, SCR leads to the formation of a smaller vortex at both boundaries moving into the opposite direction. With the hot air rising above the non-built-up streets at the boundaries, cooler air is transported downwards towards the roofs. Due to the counter direction of the vortices in RR and SCR, large temperature deviations can be observed in the comparison plot of Figure 8-5a.

Spatial distribution analysis shows that SCR is capable of reducing pedestrian-level air temperatures over larger areas. However, it also hints to a disadvantage of a large-scale application of SCR as vertical air exchange is minimized which theoretically could lead to health implications in urban areas as they are usually affected by higher levels of air pollution. These implications might be a shortcoming, especially compared to façade and roof greening which has been shown is capable of even reducing air pollution (K. V. Abhijith et al., 2017). We did not directly simulate air pollution particulates or gases, which have complex chemical pathways and dispersion processes, and therefore cannot robustly conclude how large-scale application of cool roofs might impact urban air quality.

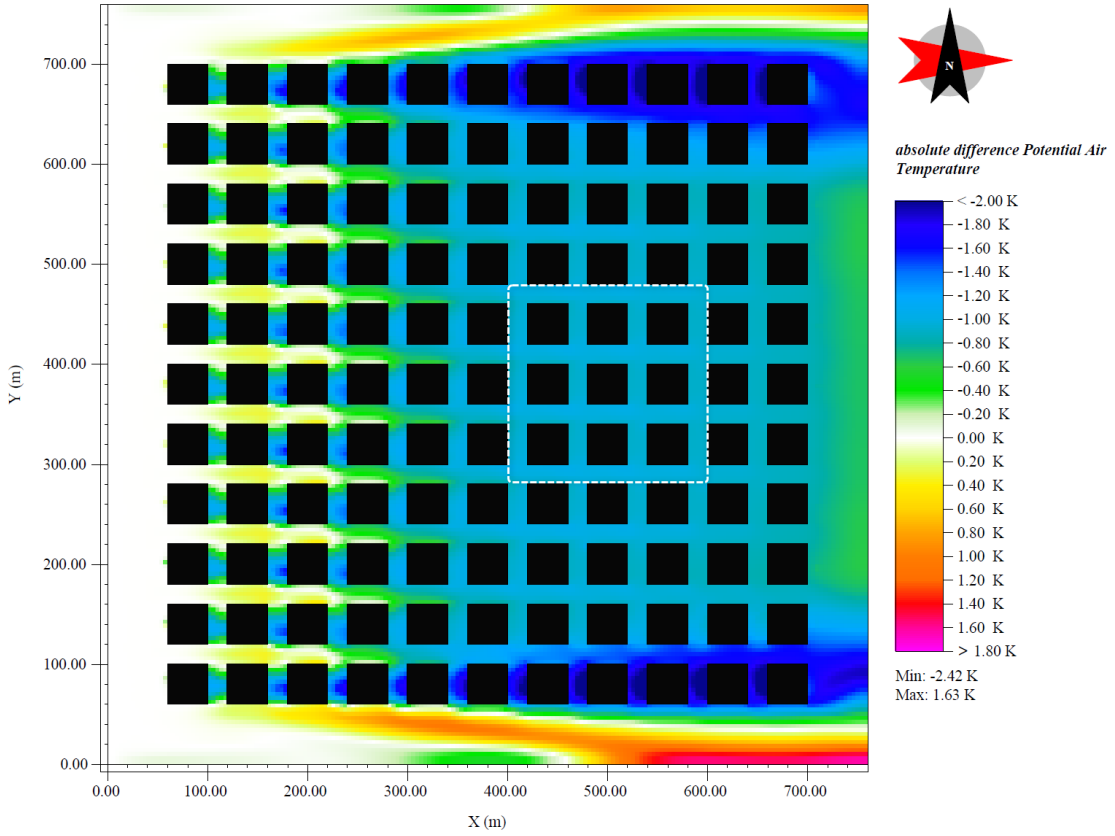

(a)

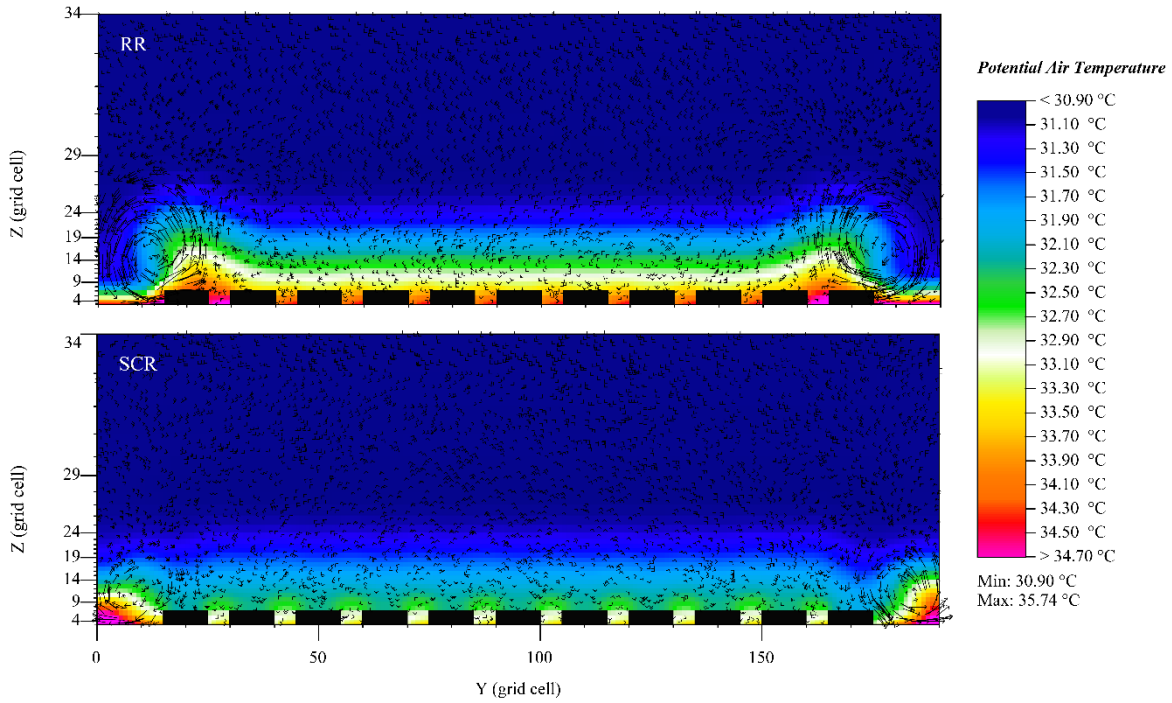

(b)

*Figure 8-5: Simulated air temperature difference between SCR and RR in 13 m building height scenario at time of highest difference (15:00 local time at second simulation day) as horizontal cut in 1.2 m height (c.f. Figure 8-4) (**a**). Simulated air temperature distribution for SCR and RR in the 13 m building height scenario shown as a vertical cut at grid cell 154 / 618 m (**b**). A white, dashed box in (**a**) indicates grid cells that were used for the analysis of air temperature at pedestrian level.*

8.3.3 Dependency of pedestrian-level air temperature cooling impact on building height

Examining the relationship between building height and pedestrian-level air temperature cooling in Figure 8-6a, it can be stated that the cooling performance declines with increasing building height. The cooling performance of SCR at pedestrian level is found to be non-linearly reduced by around 0.003 K per additional meter of building height. This pattern of declining cooling impact with increasing building height is found for all roof types. Cooling strength probably decreases with building height since the cooler air at roof level needs to cover an increased distance until it has an impact at pedestrian level.

Comparing CR, SCR, and GR performances, we again find the largest overall cooling impacts for SCR with a maximum of 0.87 K and an average of 0.32-0.43 K (Figure 8-6a). Maximum temperature reductions of around 0.7 K and averaged cooling effects of 0.25-0.35 K for CR are both in line with previous cool roof study results (Tsoka et al., 2018; Yang et al., 2015). Maximum temperature reductions of around 0.7 K and averaged cooling effects of 0.3-0.4 K for GR are in line with, or slightly higher than, previous cool roof study results (Peng and Jim, 2013; Tsoka et al., 2018).

The polynomial extrapolation of means as well as medians of the pedestrian-level air temperature differences depending on the simulated building heights of 13 m, 25 m, and 50 m indicates that the trend is non-linear (Figure 8-6b). The strength of cooling impact decrease seems to decline with increasing building height for all roof types. All scenarios except the SCR Median extrapolation predict that the cooling impact of both cool and green roofs onto air temperature at pedestrian level vanishes at mean building heights of around 95-110 m. However, further studies with more different building height scenarios will be needed to corroborate these results.

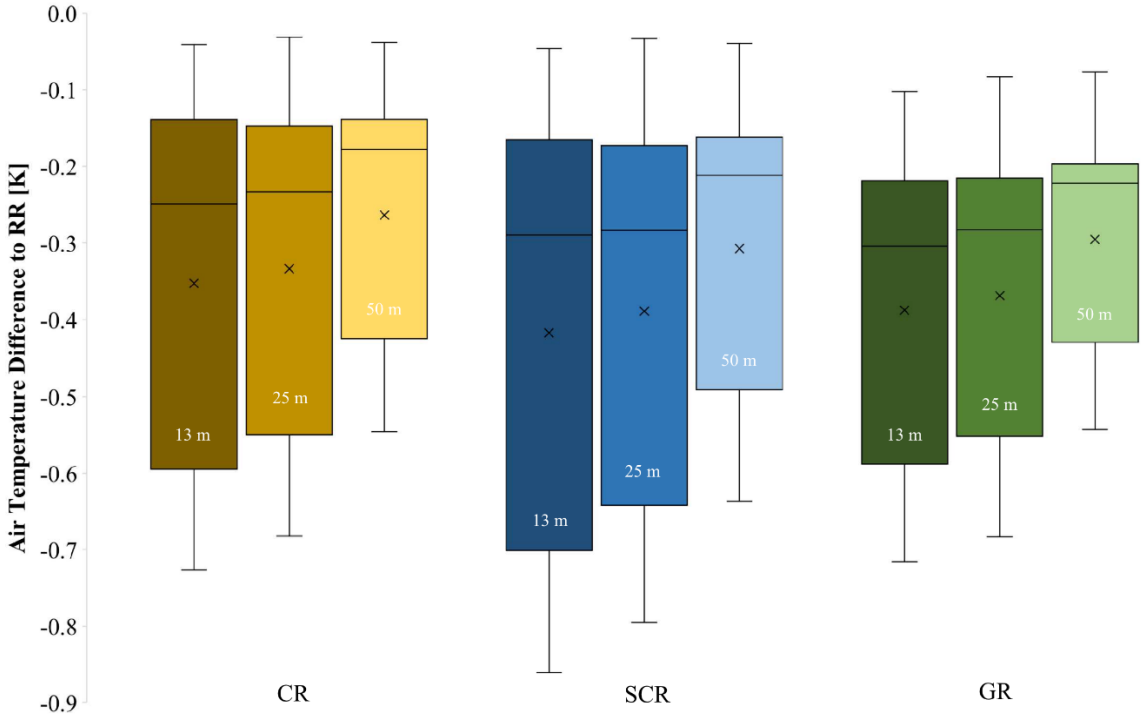

(a)

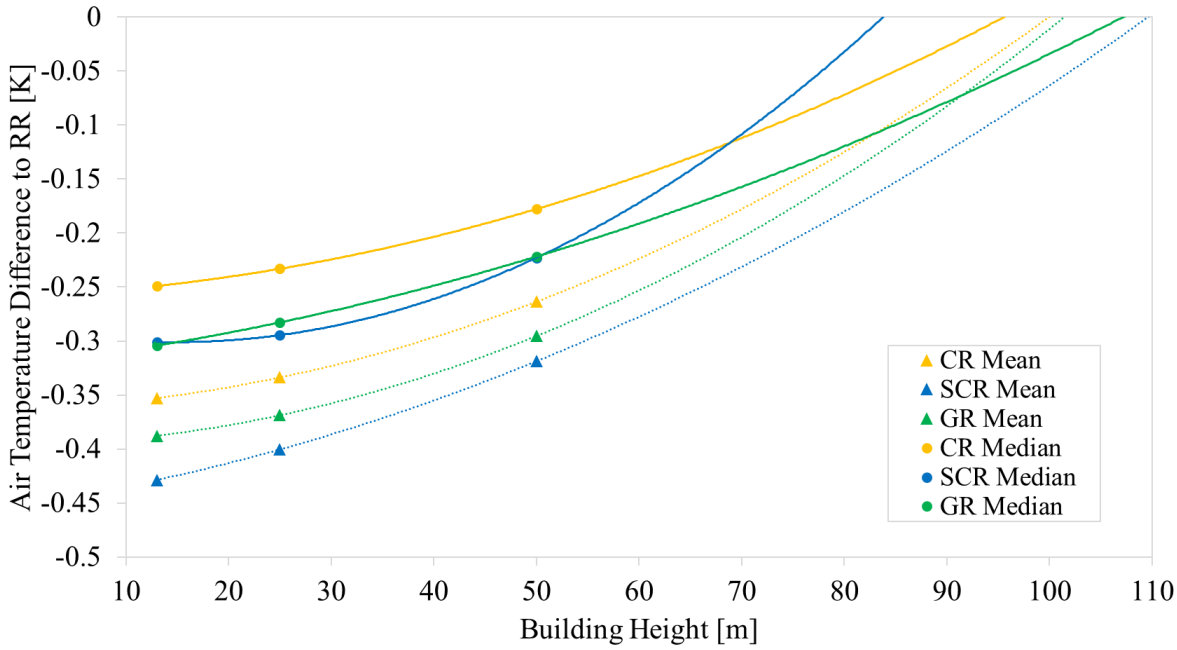

(b)

*Figure 8-6: Simulated pedestrian-level air temperature differences of CR, SCR, and GR to RR depending on building height, where whiskers indicate minimum and maximum values, horizontal line median, cross mean, and boxes second and third quartile (**a**). Mean (dotted lines) and median (solid lines) differences are displayed as polynomial extrapolations for increasing building height in (**b**).*

8.4 Conclusion

Our results demonstrated that, in agreement with the experimental studies, the modeled SCR material remained about 6 K lower than ambient air temperature during times of high solar insolation (Gentle and Smith, 2015; Mandal et al., 2018; Raman et al., 2014). SCR – with an averaged pedestrian-level air temperature cooling of around 0.85 K during midday – performed slightly better than CR and GR by providing an additional pedestrian-level air temperature cooling of 0.1 K to 0.15 K. During nighttime, cooling performance of SCR stabilizes at a low level of around 0.2 K being thus comparable with the cooling impact of CR or GR.

Spatial distribution analysis showed that SCR is capable of reducing pedestrian-level air temperatures over larger areas. However, it also affects the urban wind field if applied on large scale. Cooler air from roof surface level may inhibit vertical air exchange between street and above buildings level that may eventually lead to an accumulation of air pollution in urban street canyons.

Analyzing the effect of building height onto the cooling potential of CR, SCR, and GR on pedestrian-level air temperature showed a clear pattern: The cooling effect decreases with increasing building height. Extrapolations show that the cooling impact declines non-linearly by around 0.003 K per added building height meter and probably ceases at building heights of around 100 m. Observed maximum and average cooling performances of CR and GR matched previous study results.

Overall, the analysis of the UHI mitigation potential of CR, SCR, and GR showed that all three solutions strongly reduce the roof surface temperatures and by that affect the air temperature at pedestrian level during daytime. They are capable of reducing urban heat stress during daytime and also albeit at much smaller degree during nighttime. Not only the effect on the outdoor climate needs to be further examined in meso- and microscale simulations but also the effects onto building energy performance need to be considered. While CR, SCR, and GR might yield beneficial building energy performances and improved outdoor thermal comfort in hot climates, their effect could be unfavorable in moderate climates with cool or cold winters. The potentially negative effects of large-scale SCR applications onto air quality need to be further investigated in air pollution modelling studies. Furthermore, measurement studies need to be conducted to verify all findings of the present study. Additionally, further simulation studies

will be needed to corroborate the cooling impact dependency on building height and to examine the cooling impact of both cool and green roofs in realistic urban environments featuring varying building heights.

8.5 References

Abhijith, K.V., Kumar, P., Gallagher, J., McNabola, A., Baldauf, R., Pilla, F., Broderick, B., Di Sabatino, S., Pulvirenti, B., 2017. Air pollution abatement performances of green infrastructure in open road and built-up street canyon environments – A review. Atmospheric Environment 162, 71–86. https://doi.org/10.1016/j.atmosenv.2017.05.014

Aflaki, A., Mirnezhad, M., Ghaffarianhoseini, Amirhosein, Ghaffarianhoseini, Ali, Omrany, H., Wang, Z.-H., Akbari, H., 2017. Urban heat island mitigation strategies: A state-of-the-art review on Kuala Lumpur, Singapore and Hong Kong. Cities 62, 131–145. https://doi.org/10.1016/j.cities.2016.09.003

Akbari, H., Cartalis, C., Kolokotsa, D., Muscio, A., Pisello, A.L., Rossi, F., Santamouris, M., Synnefa, A., Wong, N.H., Zinzi, M., 2016. Local climate change and urban heat island mitigation techniques – the state of the art. Journal of Civil Engineering and Management 22, 1–16. https://doi.org/10.3846/13923730.2015.1111934

ASHRAE, 2001. International Weather for Energy Calculations (IWEC Weather Files), [Online], Available: https://www.ashrae.org/technical-resources/bookstore/as hrae-international-weather-files-for-energy-calculations-2-0-iwec2.

Baniassadi, A., Sailor, D.J., Crank, P.J., Ban-Weiss, G.A., 2018. Direct and indirect effects of high-albedo roofs on energy consumption and thermal comfort of residential buildings. Energy and Buildings 178, 71–83. https://doi.org/10.1016/j.enbuild.2018.08.048

Berardi, U., Jandaghian, Z., Graham, J., 2020. Effects of greenery enhancements for the resilience to heat waves: A comparison of analysis performed through mesoscale (WRF) and microscale (Envi-met) modeling. Science of The Total Environment 747, 141300. https://doi.org/10.1016/j.scitotenv.2020.141300

Bowler, D.E., Buyung-Ali, L., Knight, T.M., Pullin, A.S., 2010. Urban Greening to Cool Towns and Cities: A Systematic Review of the Empirical Evidence. Landscape and urban planning 97, 147–155.

Broadbent, A.M., Krayenhoff, E.S., Georgescu, M., 2020. The motley drivers of heat and cold exposure in 21st century US cities. PNAS 117, 21108–21117. https://doi.org/10.1073/pnas.2005492117

Bruse, M., 1999. Die Auswirkungen kleinskaliger Umweltgestaltung auf das Mikroklima. Entwicklung des prognostischen numerischen Modells ENVI-met zur Simulation der Wind-, Temperatur- und Feuchteverteilung in städtischen Strukturen (PhD Thesis). Ruhr-University Bochum, Bochum.

Deru, M., Field, K., Studer, D., Benne, K., Griffith, B., Torcellini, B., Halverson, M., Winiarski, D., Liu, B., Rosenberg, M., Huang, J., Yazdanian, M., Crawley, D., 2010. U.S. Department of Energy Commercial Reference Building Models of the National Building Stock.

Di Giuseppe, E., Pergolini, M., Stazi, F., 2017. Numerical assessment of the impact of roof reflectivity and building envelope thermal transmittance on the UHI effect. Energy Procedia, Sustainability in Energy and Buildings 2017: Proceedings of the Ninth KES International Conference, Chania, Greece, 5-7 July 2017 134, 404–413. https://doi.org/10.1016/j.egypro.2017.09.590

Dornelles, K., Caram, R., Sichieri, E., 2015. Natural Weathering of Cool Coatings and its Effect on Solar Reflectance of Roof Surfaces. Energy Procedia, 6th International Building Physics Conference, IBPC 2015 78, 1587–1592. https://doi.org/10.1016/j.egypro.2015.11.216

Evola, G., Gagliano, A., Fichera, A., Marletta, L., Martinico, F., Nocera, F., Pagano, A., 2017. UHI effects and strategies to improve outdoor thermal comfort in dense and old neighbourhoods. Energy Procedia, Sustainability in Energy and Buildings 2017: Proceedings of the Ninth KES International Conference, Chania, Greece, 5-7 July 2017 134, 692–701. https://doi.org/10.1016/j.egypro.2017.09.589

Falasca, S., Ciancio, V., Salata, F., Golasi, I., Rosso, F., Curci, G., 2019. High albedo materials to counteract heat waves in cities: An assessment of meteorology, buildings energy needs and pedestrian thermal comfort. Building and Environment 163, 106242. https://doi.org/10.1016/j.buildenv.2019.106242

Gentle, A.R., Smith, G.B., 2015. A subambient open roof surface under the Mid-Summer sun. Advanced Science 2, 1500119.

Heusinger, J., Sailor, D.J., Weber, S., 2018. Modeling the reduction of urban excess heat by green roofs with respect to different irrigation scenarios. Building and Environment 131, 174–183. https://doi.org/10.1016/j.buildenv.2018.01.003

Heusinger, J., Weber, S., 2017. Surface Energy Balance of an Extensive Green Roof as Quantified by Full Year Eddy-Covariance Measurements. Science of The Total Environment 577, 220–230. https://doi.org/10.1016/j.scitotenv.2016.10.168

Huttner, S., 2012. Further development and application of the 3D microclimate simulation ENVI-met (Dissertation). Johannes Gutenberg-University Mainz.

Huynh, C., Eckert, R., 2012. Reducing Heat and Improving Thermal Comfort through Urban Design – A Case Study in Ho Chi Minh City. IJESD 480–485. https://doi.org/10.7763/IJESD.2012.V3.271

Imran, H.M., Kala, J., Ng, A.W.M., Muthukumaran, S., 2018. Effectiveness of green and cool roofs in mitigating urban heat island effects during a heatwave event in the city of Melbourne in south-east Australia. Journal of Cleaner Production 197, 393–405. https://doi.org/10.1016/j.jclepro.2018.06.179

Kolokotroni, M., 2017. Cool materials in the urban built environment to mitigate heat islands: potential consequences for building ventilation. 38th AIVC International Conference.

Krayenhoff, E.S., Moustaoui, M., Broadbent, A.M., Gupta, V., Georgescu, M., 2018. Diurnal interaction between urban expansion, climate change and adaptation in US cities. Nature Climate Change.

Mandal, J., Fu, Y., Overvig, A.C., Jia, M., Sun, K., Shi, N.N., Zhou, H., Xiao, X., Yu, N., Yang, Y., 2018. Hierarchically porous polymer coatings for highly efficient passive daytime radiative cooling. Science 362, 315–319. https://doi.org/10.1126/science.aat9513

Mastrapostoli, E., Santamouris, M., Kolokotsa, D., Vassilis, P., Venieri, D., Gompakis, K., 2016. On the ageing of cool roofs: Measure of the optical degradation, chemical and biological analysis and assessment of the energy impact. Energy and Buildings, SI: Countermeasures to Urban Heat Island 114, 191–199. https://doi.org/10.1016/j.enbuild.2015.05.030

Middel, A., Turner, V.K., Schneider, F.A., Zhang, Y., Stiller, M., 2020. Solar reflective pavements—A policy panacea to heat mitigation? Environ. Res. Lett. 15, 064016. https://doi.org/10.1088/1748-9326/ab87d4

Morakinyo, T.E., Dahanayake, K.W.D.Kalani.C., Ng, E., Chow, C.L., 2017. Temperature and cooling demand reduction by green-roof types in different climates and urban densities: A co-simulation parametric study. Energy and Buildings 145, 226–237. https://doi.org/10.1016/j.enbuild.2017.03.066

Ng, E., Chen, L., Wang, Y., Yuan, C., 2012. A study on the cooling effects of greening in a high-density city: An experience from Hong Kong. Building and Environment 47, 256–271. https://doi.org/10.1016/j.buildenv.2011.07.014

Nikolova, I., Janssen, S., Vos, P., Vrancken, K., Mishra, V., Berghmans, P., 2011. Dispersion Modelling of Traffic Induced Ultrafine Particles in a Street Canyon in Antwerp, Belgium and Comparison with Observations. Science of The Total Environment 412–413, 336–343. https://doi.org/10.1016/j.scitotenv.2011.09.081

Oke, T.R., 1987. Boundary Layer Climates, 2nd ed. Vancouver.

Peng, L.L.H., Jim, C.Y., 2013. Green-Roof Effects on Neighborhood Microclimate and Human Thermal Sensation. Energies 6, 598–618. https://doi.org/10.3390/en6020598

Raman, A.P., Anoma, M.A., Zhu, L., Rephaeli, E., Fan, S., 2014. Passive radiative cooling below ambient air temperature under direct sunlight. Nature 515, 540.

Salata, F., Golasi, I., Petitti, D., de Lieto Vollaro, E., Coppi, M., de Lieto Vollaro, A., 2017. Relating microclimate, human thermal comfort and health during heat waves: An analysis of heat island mitigation strategies through a case study in an urban outdoor environment. Sustainable Cities and Society 30, 79–96. https://doi.org/10.1016/j.scs.2017.01.006

Santamouris, M., Haddad, S., Saliari, M., Vasilakopoulou, K., Synnefa, A., Paolini, R., Ulpiani, G., Garshasbi, S., Fiorito, F., 2018. On the energy impact of urban heat island in Sydney: Climate and energy potential of mitigation technologies. Energy and Buildings 166, 154–164. https://doi.org/10.1016/j.enbuild.2018.02.007

Santamouris, M., Synnefa, A., Karlessi, T., 2011. Using advanced cool materials in the urban built environment to mitigate heat islands and improve thermal comfort conditions. Solar Energy, Progress in Solar Energy 2 85, 3085–3102. https://doi.org/10.1016/j.solener.2010.12.023

Schinasi, L.H., Benmarhnia, T., De Roos, A.J., 2018. Modification of the association between high ambient temperature and health by urban microclimate indicators: A systematic review and meta-analysis. Environmental Research 161, 168–180. https://doi.org/10.1016/j.envres.2017.11.004

Schrijvers, P.J.C., Jonker, H.J.J., de Roode, S.R., Kenjereš, S., 2016. The effect of using a high-albedo material on the Universal Temperature Climate Index within a street canyon. Urban Climate 17, 284–303. https://doi.org/10.1016/j.uclim.2016.02.005

Simon, H., 2016. Modeling Urban Microclimate: Development, Implementation and Evaluation of New and Improved Calculation Methods for the Urban Microclimate Model ENVI-Met (PhD Thesis). Universitätsbibliothek Mainz, Mainz.

Stewart, I.D., Oke, T.R., 2012. Local Climate Zones for Urban Temperature Studies. Bulletin of the American Meteorological Society 93, 1879–1900.

Synnefa, A., Santamouris, M., Apostolakis, K., 2007. On the development, optical properties and thermal performance of cool colored coatings for the urban environment. Solar Energy 81, 488–497. https://doi.org/10.1016/j.solener.2006.08.005

Taleghani, M., Sailor, D., Ban-Weiss, G.A., 2016. Micrometeorological simulations to predict the impacts of heat mitigation strategies on pedestrian thermal comfort in a Los Angeles neighborhood. Environ. Res. Lett. 11, 024003. https://doi.org/10.1088/1748-9326/11/2/024003

Taleghani, M., Tenpierik, M., van den Dobbelsteen, A., Sailor, D.J., 2014. Heat in courtyards: A validated and calibrated parametric study of heat mitigation strategies for urban courtyards in the Netherlands. Solar Energy 103, 108–124. https://doi.org/10.1016/j.solener.2014.01.033

Tsoka, S., Tsikaloudaki, A., Theodosiou, T., 2018. Analyzing the ENVI-met microclimate model’s performance and assessing cool materials and urban vegetation applications–A review. Sustainable Cities and Society 43, 55–76. https://doi.org/10.1016/j.scs.2018.08.009

Wang, Y., Akbari, H., 2015. Development and application of ‘thermal radiative power’ for urban environmental evaluation. Sustainable Cities and Society 14, 316–322. https://doi.org/10.1016/j.scs.2014.07.003

Wang, Y., Berardi, U., Akbari, H., 2016. Comparing the effects of urban heat island mitigation strategies for Toronto, Canada. Energy and Buildings, SI: Countermeasures to Urban Heat Island 114, 2–19. https://doi.org/10.1016/j.enbuild.2015.06.046

Yang, J., Wang, Z.-H., Kaloush, K.E., 2015. Environmental impacts of reflective materials: Is high albedo a ‘silver bullet’ for mitigating urban heat island? Renewable and Sustainable Energy Reviews 47, 830–843. https://doi.org/10.1016/j.rser.2015.03.092

Zhai, Y., Ma, Y., David, S.N., Zhao, D., Lou, R., Tan, G., Yang, R., Yin, X., 2017. Scalable-manufactured randomized glass-polymer hybrid metamaterial for daytime radiative cooling. Science 355, 1062–1066.

“ (Sinsel et al., 2021a).

9 Modeling impacts of super cool roofs on air temperature at pedestrian level in mesoscale and microscale climate models

Tim Sinsel[1], Helge Simon[1], Ashley M. Broadbent[2,3], Michael Bruse[1], Jannik Heusinger[4]

[1]*Department of Geography, Johannes Gutenberg University Mainz, 55099 Germany*
[2]*School of Geographical Sciences and Urban Planning, Arizona State University, 85281 Tempe, USA*
[3]*Urban Climate Research Center, Arizona State University, 85281 Tempe, USA*
[4]*Institute of Geoecology, TU Braunschweig, 38106 Germany*

Summary:

Following the sensitivity study with uniformly built model areas presented in Section 8, a consecutive study analyzed the SCR effect on pedestrian-level air temperature for realistic scenarios featuring complex urban environments in two contrasting cities: New York City and Phoenix. Simulations were not only conducted with ENVI-met but also with the mesoscale model WRF in order to, in a first step, examine the impact of SCR application over entire metropolitan areas, in a second step, use WRF's model output as realistic meteorological boundary conditions for the ENVI-met simulations, and, in a third step, find similarities and discrepancies between both models. As SCR performances differed between NYC and Phoenix scenarios in the prediction of both models, it was additionally investigated whether the discrepancies were caused by the prevailing building morphologies or climatological conditions. While Ashley M. Broadbent conducted the WRF simulations, the author prepared, conducted, and evaluated the ENVI-met simulations, and wrote the majority of the manuscript.

Urban Climate 40, December 2021 - published

“

9.1 Introduction

Heat stress and its health implications are major topics for society as ongoing urbanization and global warming due to anthropogenic climate change intensifies heat stress globally (Broadbent et al., 2020a; Krayenhoff et al., 2018). Since urban heat stress leads to increased morbidity and mortality rates (Schinasi et al., 2018), mitigation measures have been developed and analyzed in a multitude of studies (Aflaki et al., 2017; Akbari et al., 2016; Aleksandrowicz et al., 2017). Such mitigation measures (e.g., green or blue infrastructure) aim to reduce air temperature by evapotranspiration, by repartitioning sensible heat into latent heat. Additionally, mitigation measures utilize high-albedo materials with the objective of reducing the amount of energy absorbed (and stored) in urban environments by reflecting incoming solar radiation. As street-level space is rare and expensive in cities, roof-based solutions such as cool roofs or green roofs are feasible cooling solutions. However, roof-based solutions have lower effects on air temperature at pedestrian level (up to 1 K, respectively) compared to street trees and ground-based vegetation (up to 2-3 K) (Berardi et al., 2020, 2014; Bowler et al., 2011; Heusinger et al., 2018; Heusinger and Weber, 2015; Liu et al., 2021; Santamouris, 2011; Santamouris et al., 2018; Solcerova et al., 2017; Tsoka et al., 2018; Yang et al., 2018, 2015). New cool materials featuring a very high albedo of >0.95 and an emissivity of >0.95, that were reported to stay below ambient air temperatures during high insulation conditions, provide an opportunity to overcome this limitation (Gentle and Smith, 2015; Mandal et al., 2018; Raman et al., 2014; Santamouris and Yun, 2020; Zhai et al., 2017; Zhao et al., 2019). These new materials, based on their objective usually being referred to as “Passive Daytime Radiative Cooling (PDRC)”, have gained increasing interest and relevance as recent studies suggest that they can be easily applied, cost-effective to produce and are efficiently utilizable as an urban heat stress mitigation measure (Anand et al., 2021; Baniassadi et al., 2019; Chen et al., 2021; Chen and Lu, 2020; Mandal et al., 2020; Santamouris and Yun, 2020; Yang and Zhang, 2020). While ageing and weathering is still a major drawback of these materials (Dornelles et al., 2015; Mastrapostoli et al., 2016; Synnefa et al., 2007), ongoing research is addressing this drawback and new advancements, such as self-cleaning materials, may improve their optical durability (Santamouris and Yun, 2020).

A recent sensitivity study demonstrated that a large-scale application of the newly developed materials on rooftops – hereafter referred to as "super cool roof" (SCR) – could lower pedestrian-level air temperatures by around 0.85 K, providing an additional cooling of 0.15 K compared to irrigated green roofs and traditional high-standard cool roofs (Sinsel et al., 2021). Because urban heat stress is largely depending on mean radiant temperature (MRT) (Kántor and Unger, 2011; Thorsson et al., 2014) and highly-reflective materials near pedestrian-level would negatively affect MRT (Falasca et al., 2019; Middel et al., 2020; Schrijvers et al., 2016), the super cool material's potential was only evaluated for roof application, where it was modeled to cool ambient air temperatures by PDRC and to eventually yield air temperature reductions at pedestrian level. Furthermore, the authors showed that the cooling impact of the three different roof types decreased in a nonlinear fashion with rising building height. The sensitivity study was however limited to the simulation of an idealized urban neighborhood featuring uniform building morphologies and an ensemble of different building height scenarios.

The authors pointed out that their findings have to be validated for realistic urban environments. The present study hence intends to fill this gap by utilizing mesoscale and microscale simulations with the Weather Research and Forecasting (WRF) model and ENVI-met (Bruse and Fleer, 1998; Chen et al., 2011), to robustly quantify the potential range of the urban air temperature cooling achieved from SCR in different settings and over different scales. In contrast to the mentioned sensitivity study, ENVI-met's simulated real case scenarios feature complex building morphologies as well as varying building heights and street widths. The SCR scenarios are compared with low-albedo roofs ("reference roof", hereafter RR) and conventional cool roofs (hereafter CR) to quantify the cooling effectiveness of SCR. To capture effects of different urban morphologies and meteorological conditions onto the performance of SCR, we analyze case study scenarios from two contrasting cities: New York City, NY, and Phoenix, AZ.

9.2 Methodology

In contrast to the hypothetical and simplified building layout of the sensitivity study of Sinsel et al. (2021), case study scenarios are developed to examine the cool roofs' performance in two realistic urban environments featuring different climates and urban morphologies. The case study cities are New York City (NYC) at the humid Northeast coast of the USA mostly featuring mid- to high-rise buildings, and Phoenix (PHX) in the arid and hot Southwest of the USA mostly featuring low-rise buildings. For both

locations, mesoscale WRF simulations (Section 2.1) and microscale ENVI-met simulations (Section 2.2) were run to cross-check and compare the cooling impacts of CR and SCR at different modeling scales. By using this dual-modeling approach, it is possible to analyze the atmospheric effects associated with small-scale (1 x 1 km) and large-scale (100 x 100 km) changes in roof types. Additionally, the mesoscale WRF atmospheric fields could be utilized to accurately force ENVI-met with modeled urbanized meteorological conditions instead of using generic data from measurement stations located at distant urban sites or airports. Finally, the results can be compared to find instructive differences and similarities between WRF and ENVI-met.

Table 9-1: Physical properties of building materials used in the case studies for both models, WRF and ENVI-met. (Deru et al., 2010; Mandal et al., 2018).

	Layer	Name	Albedo	Absorptivity	Emissivity	Thickness [m]	Conductivity [W (m K)$^{-1}$]	Density [kg m^{-3}]	Specific Heat (J (kg K)$^{-1}$)
Wall									
	Outside	Concrete	0.2	0.8	0.9	0.2	1.311	2240	836.8
	Middle	Steel frame Insulation for NYC	0.2	0.8	0.9	0.08	0.049	265	837
	Middle	Steel frame Insulation for PHX	0.2	0.8	0.9	0.02	0.049	265	837
	Inside	1/2IN Gypsum	0.2	0.8	0.9	0.01	0.16	785	830
Roof									
	Outside	RR membrane	0.2	0.8	0.9	0.01	0.16	1121	1460
	Outside	CR membrane	0.85	0.15	0.9	0.02	0.85	1200	1200
	Outside	SCR membrane	0.96	0.04	0.97	0.02	0.85	1200	1200
	Middle	Insulation for NYC	0.2	0.8	0.9	0.14	0.049	265	837
	Middle	Insulation for PHX	0.2	0.8	0.9	0.17	0.049	265	837
	Inside	Metal Decking	0.2	0.8	0.9	0.01	45	7680	418

To run the simulations with realistic properties for reference, cool, and super cool roof materials, databases were prepared with precise thermal and radiative parameter values also utilized in Sinsel et al. (2021) with additional specific wall and roof materials for buildings in the PHX scenarios derived from Deru et al. (2010) (Table 9-1). This database was used to define consistent built environment model

parameters across WRF and ENVI-met. Ageing and weathering of high albedo roofs was not considered, i.e. the albedo was assumed to be constant at a maximum value. Therefore, our results provide an upper estimate of the potential cooling impacts of (super) cool roofs.

9.2.1 WRF case studies

Mesoscale case study simulations were conducted with the Advanced Research (ARW) version of the WRF (version 3.6) regional climate model (Skamarock et al., 2008) which is a widely used urban modeling platform (Bhati and Mohan, 2016; Chen et al., 2014; Fallmann et al., 2013; Giannaros et al., 2018; Jandaghian and Berardi, 2020; Morini et al., 2018; Sharma et al., 2017; Vogel and Afshari, 2020). The model setup has three nested domains for all WRF simulations with horizontal grid spacing of 16, 4, and 1 km. On the vertical grid, 42 levels were defined with the lowest model level at 2 m above street-level. Urban morphological parameters were taken from the National Urban Database Access Portal Tool (Ching et al., 2009) and the National Land Cover Database (NLCD) (Multi-Resolution Land Characteristics Consortium (U.S.), 2020) and thus feature spatially explicit parameters (e.g., building height, street width, and impervious fraction) for each WRF grid cell. The 1 km x 1 km WRF grid cell used for the ENVI-met forcing featured the urban classes “high density residential” (zone 32) for NYC and “low density residential (zone 31)” for PHX, respectively.

Urban areas in WRF are represented with the building environment parameterization scheme (BEP). Radiative and thermal properties of urban materials were harmonized with those used in the ENVI-met model displayed in Table 9-1, i.e., parameters for the 10 BEP wall/roof layers were matched with ENVI-met’s 3 model layers in proportion to their thickness. The Bougeault-Lacarrere boundary layer scheme (Bougeault and Lacarrere, 1989) and MM5 surface layer scheme (Jiménez et al., 2012) were used. For shortwave and longwave radiation physics the Rapid Radiative Transfer Model (RRTM) (Mlawer et al., 1997) and Dudhia Scheme (Dudhia, 1989) were used, respectively. For a full list of WRF physics schemes used here, see Broadbent et al. (2020b). Simulation parameters such as dimensions and simulation date/time are specified in Table 9-2Table 9-2. While these case studies represent fictional scenarios in order to examine the outdoor cooling impact by large-scale applications of cool roof materials, the simulations are nevertheless based on realistic meteorological boundary conditions: The simulation period features several consecutive hot summer days based on data of real heat waves for both case

study cities: Lateral boundary conditions for all WRF simulations were obtained from ERA-Interim reanalysis data (European Centre for Medium-Range Weather Forecasts ECMWF ERA-Interim Project 2009). These case study configurations were validated against measurement data (see Appendix).

Table 9-2: Simulation parameters of WRF case studies.

		NYC	PHX
WRF			
	Start date and time (UTC)	15.07.2008 00:00	30.06.2007 00:00
	Duration (hours)	132	132
	Location Lat (Lower Left Corner)	40.30° N	33.03° N
	Location Lon (Lower Left Corner)	74.60° E	112.53° E
	Domain dimensions	100 x 100	100 x 100
	Resolution (horiz.)	1000 m	1000 m
	Spatial Data Source Resolution	30 arcsec	30 arcsec

9.2.2 ENVI-met case studies

Microscale simulations were conducted with the urban microclimate model ENVI-met version 4.4.6 (Bruse, 1999; Bruse and Fleer, 1998; Huttner, 2012; Simon, 2016). ENVI-met simulates three-dimensional wind fields, turbulence, air temperature and humidity, radiative fluxes as well as vegetation- and building-atmosphere interactions, making it a viable tool for modeling urban heat mitigation strategies at the microscale (Liu et al., 2021; Tsoka et al., 2018). ENVI-met's explicit building physics model, is able to predict building surface temperatures, and it has been successfully validated against measurements multiple times (Forouzandeh, 2021; Simon, 2016; Simon et al., 2017; Tsoka et al., 2018; Yang et al., 2013). ENVI-met is thus considered to be suitable for modeling the effect of cool roofs on the urban environment and has been used in numerous modeling studies on this topic (Di Giuseppe et al., 2017; Evola et al., 2017; Falasca et al., 2019; Huynh and Eckert, 2012; Kolokotroni, 2017; Santamouris et al., 2018; Taleghani et al., 2016; Tsoka et al., 2018; Wang et al., 2016).

In both case study cities, an ENVI-met model domain was set up that approximately matched a single WRF grid cell in horizontal extent (i.e., 1 km x 1 km) and location. ENVI-met simulation parameters and characteristics such as dimensions and resolutions for both case study cities are displayed in Table 9-3.

Table 9-3: Simulation parameters of ENVI-met case studies.

		NYC	PHX
ENVI-met			
	Start date and time (Local)	19.07.2008 05:00	02.07.2007 05:00
	Duration (hours)	42	42
	Meteorological Boundary Conditions	Full Forcing	Full Forcing
	Location Lat (Lower Left Corner)	40.7142° N	33.5466° N
	Location Long (Lower Left Corner)	74.0058° W	112.1428° W
	Dimensions (X, Y, Z)	300 x 300 x 38	300 x 300 x 25
	Resolutions (X, Y, Z) [m]	5 x 5 x 4	5 x 5 x 3
	Lowest Grid Cell Splitted	Yes	Yes
	Telescoping: Factor & Starting Height	25 % above 100 m	20 % above 30 m
	Height of 3D Model Domain [m]	444	290
	Max. Building Height [m]	99	21
	Mean Building Height [m]	27.6	5.9
	Standard Dev. Building Height [m]	17.7	2.9
	Building density [%]	38.9	20.2
	Sky View Factor (most street canyons)	0.4-0.75	0.85-0.95

All ENVI-met simulations were run with the meteorological boundary conditions from the WRF control run (i.e., no cool roofs). Forcing ENVI-met simulations by WRF outputs is common practice as it was previously done by e.g. Berardi et al. (2020), Conry et al. (2014), Lee et al. (2017), and McRae et al. (2020, 2018). This approach helps to harmonize the atmospheric conditions above the urban canyon between WRF and ENVI-met, thereby improving inter-comparability between simulations. ENVI-met's CR and SCR scenarios were not forced by the corresponding WRF scenario outputs but the WRF RR output in order to allow the intercomparison of ENVI-met scenario results where cool roofs were only applied on ENVI-met model area scale of around 1 km x 1 km. That means, accumulated large scale cooling effects of applying cool roofs to the whole metropolitan area as simulated in WRF were not used as input for ENVI-met to avoid a distortion of results and to allow a comparison between ENVI-met and WRF cooling impact predictions.

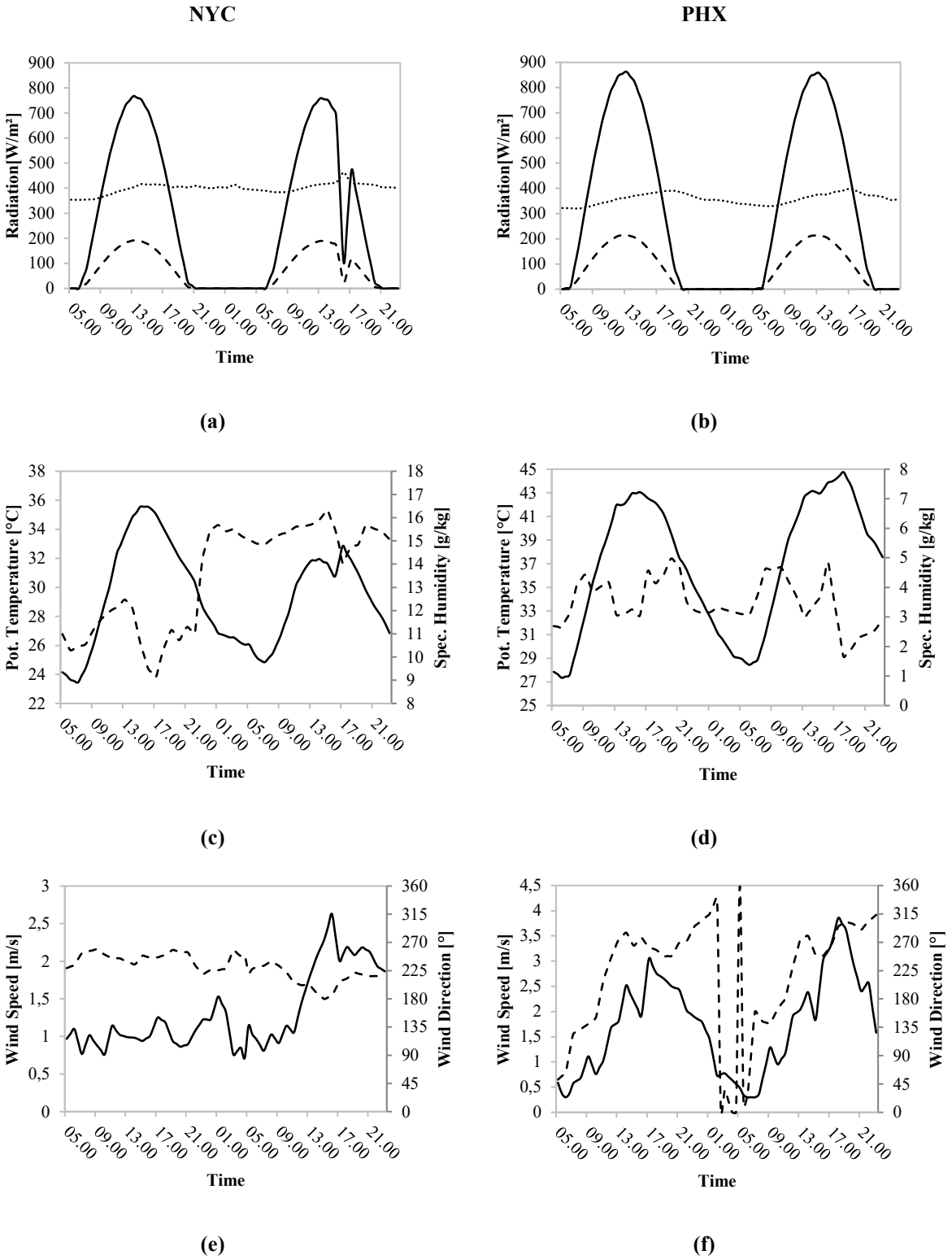

*Figure 9-1: Full forcing boundary conditions for the ENVI-met case studies in NYC and PHX derived from WRF output depicting direct shortwave (black line), diffuse shortwave (dashed line) and longwave radiation (dotted line) (**a**, **b**), potential air temperature (black line) and specific air humidity (dashed line) (**c**, **d**) as well as wind speed (black line) and wind direction (dashed line) (**e**, **f**).*

The meteorological variables used as hourly boundary conditions were air temperature, humidity, wind speed and direction as well as radiation (incoming shortwave direct, diffuse, and longwave) (Full Forcing mode) (Huttner, 2012). Incoming shortwave and longwave radiation and wind direction for the ENVI-met forcing were taken from the corresponding WRF grid cell. The other variables (wind speed, air temperature, relative humidity), which are dependent on wind speed and direction, were calculated as weighted averages from the WRF cells surrounding the ENVI-met domain depending on the prevailing wind direction. In addition to simulating heatwave conditions, the simulation periods were chosen because they featured mostly clear sky conditions. The ENVI-met forcing data (derived form WRF) is shown in Figure 9-1.

The NYC ENVI-met domain is centered at 40.7286° N, -73.9873° E, and features mainly medium-rise buildings that are representative of typical downtown areas in US cities (Table 9-3, Figure 9-2 Figure 9-2a). It is located in the mid-rise Soho district but nevertheless contains also higher buildings of up to 99 m height (Table 9-3, Figure 9-2 c,e). Contrastingly, the PHX ENVI-met domain (centered at 33.5466° N, -112.1428° E) contains an area of low-rise suburban housing that is typical of the US Southwest (Table 9-3, Figure 9-2 b). It features homogenous buildings consisting of one- or two-story family housing and two low-rise suburban centers with larger building complexes such as schools or shopping malls (Figure 9-2 d,f). In contrast to the sensitivity study of Sinsel et al. (2021), where the dependency of the cool roofs' cooling impact on building height is analyzed, the ENVI-met case studies allow to examine the cooling performance under realistic conditions with varying building heights and street widths as well as different climates. In order to examine the reasons for possible differences between NYC and PHX scenarios, additional cross-check simulations were performed in each city using the other city's boundary conditions (i.e., PHX was run with NYC boundary conditions, and vice versa). This cross-check was conducted to study whether differences in the results could be predominantly attributed to climate differences or to differences in building morphologies.

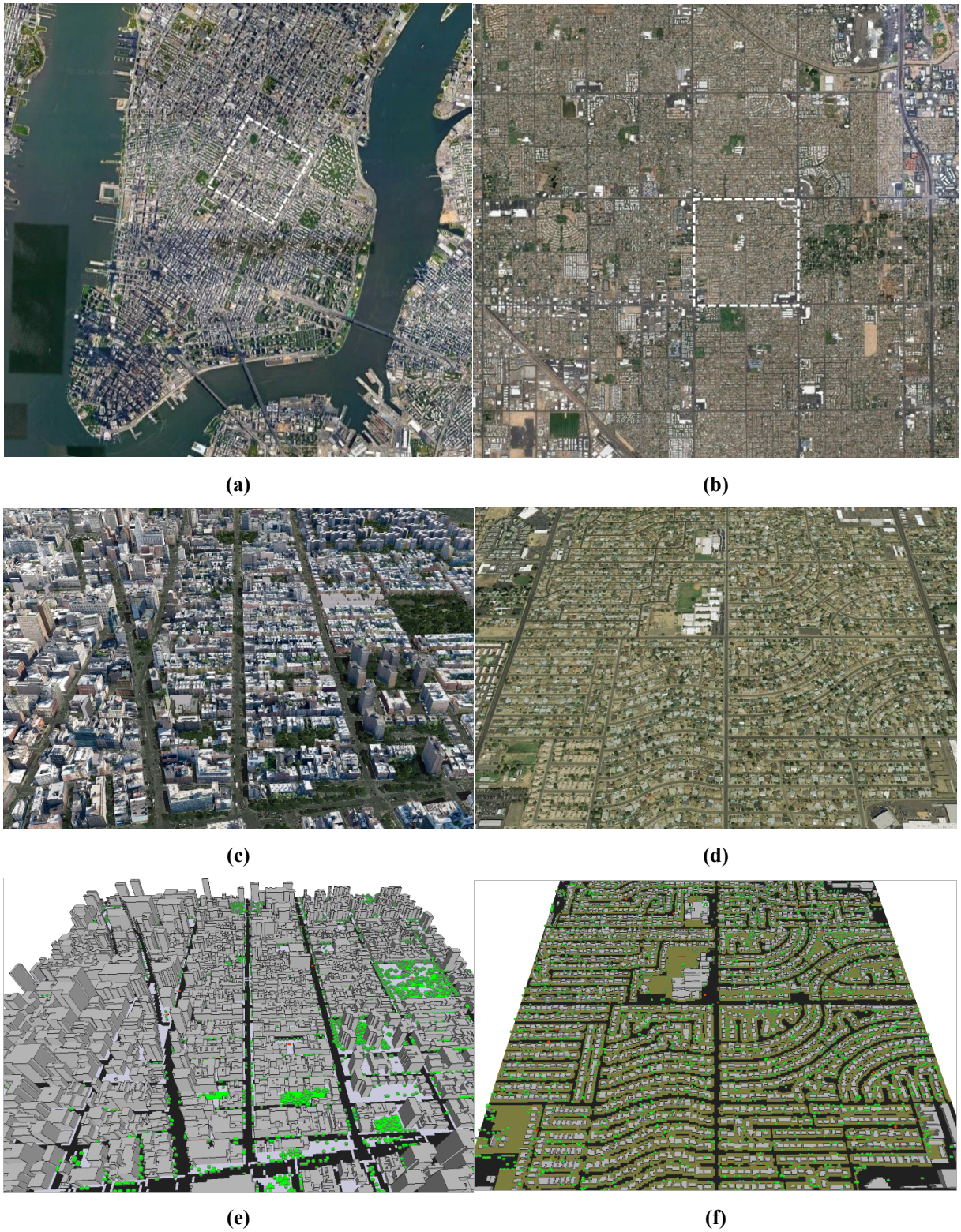

*Figure 9-2: Model area dimensions as topdown view in NYC (**a**) and PHX (**b**) indicated by white boxes in aerial imagery, as 3D view from processed aerial images for NYC (**c**) and PHX (**d**), and as representation in ENVI-met for NYC (**e**) and PHX (**f**) (Google, 2020b, 2020a; NYC Open Data, 2019; Phoenix Open Data, 2019).*

9.3 Results & Discussion

In the following section, results of the case studies are presented. At first, roof surface temperatures are compared between different roof types and between WRF and ENVI-met. Statistical analysis for both

roof surface and air temperatures is presented to further explore similarities and discrepancies between both models. Subsequently, the cooling effect of pedestrian-level air temperature is examined by analyzing the effect with spatial distribution maps and over the diurnal cycle, respectively.

9.3.1 Analysis of modeled roof surface temperatures over the diurnal cycle

When analyzing modeled roof surface temperatures over the diurnal cycle, we find that there are larger discrepancies in their range between NYC and PHX. Due to the location of Phoenix in lower latitudes, the sun height angle is steeper and the same roof area receives a higher amount of radiation than in the higher latitudes of the NYC simulation. The surface temperatures in PHX are thus higher for all roof types in both models compared to the NYC simulation (Figure 9-3). Compared to measured temperature differences between SCR and ambient air temperature in Mandal et al. (2018) featuring ~5 K (NYC) and ~6 K (PHX) during peak solar radiation, we find higher differences of ~8 K (NYC) and 15 K (PHX) in ENVI-met as well as ~5 K (NYC) and 20 K (PHX) in WRF, respectively. However, the measurements were conducted in March, with less steeper sun height angles and at least 13 K lower air temperatures. Furthermore, the review study of Santamouris and Yun (2020) reports that further studies measured differences of up to 17 K which thus likely confirms the validity of the simulations. The prediction of both models that traditional high-end cool roofs as well as SCR stay below ambient air temperature almost during all times is also in agreement with previous studies (Santamouris and Yun, 2020).

Both models predict much higher surface temperatures for RR than for CR and SCR. However, ENVI-met predicts RR surface temperatures of up to 63 °C (NYC) and 71 °C (PHX) at midday, while WRF estimates significantly cooler surfaces temperatures of up to 45 °C (NYC) and 53 °C (PHX) for RR (Figure 9-3). Regarding the CR and SCR temperatures, both models show a much higher agreement. CR and SCR surface temperatures show a small timing offset between ENVI-met and WRF with peak surface temperatures in WRF being slightly later than in ENVI-met. In both scenarios, WRF predicted CR and SCR to keep their higher surface temperatures during evening hours while ENVI-met modeled them to cease more rapidly. Thus, RR, CR, and SCR feature lower surface temperatures in ENVI-met than in WRF when examining times of no irradiation.

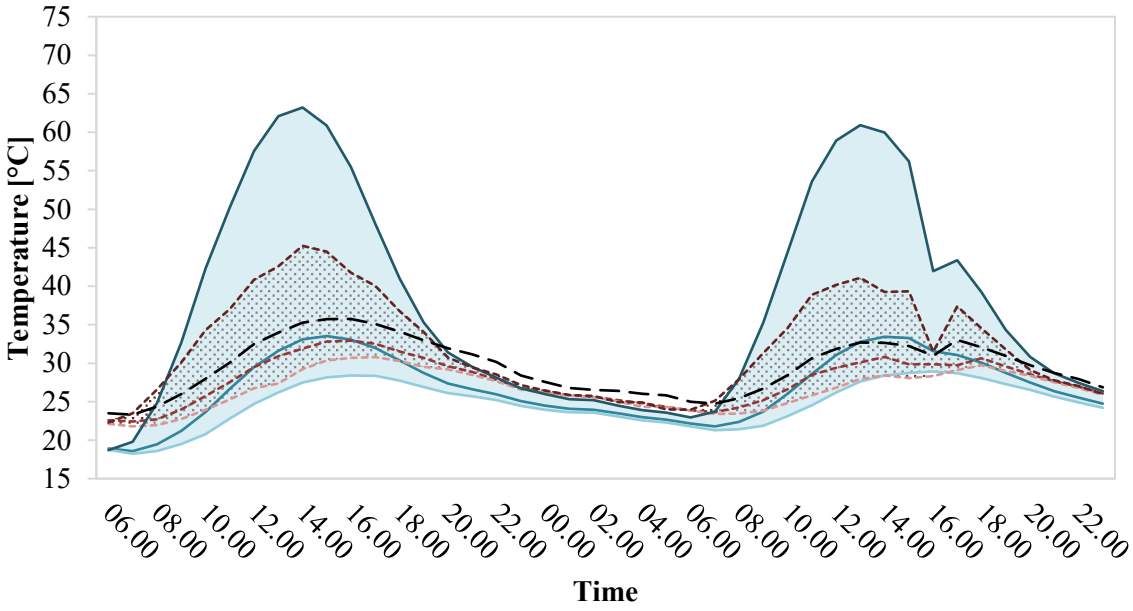

(a)

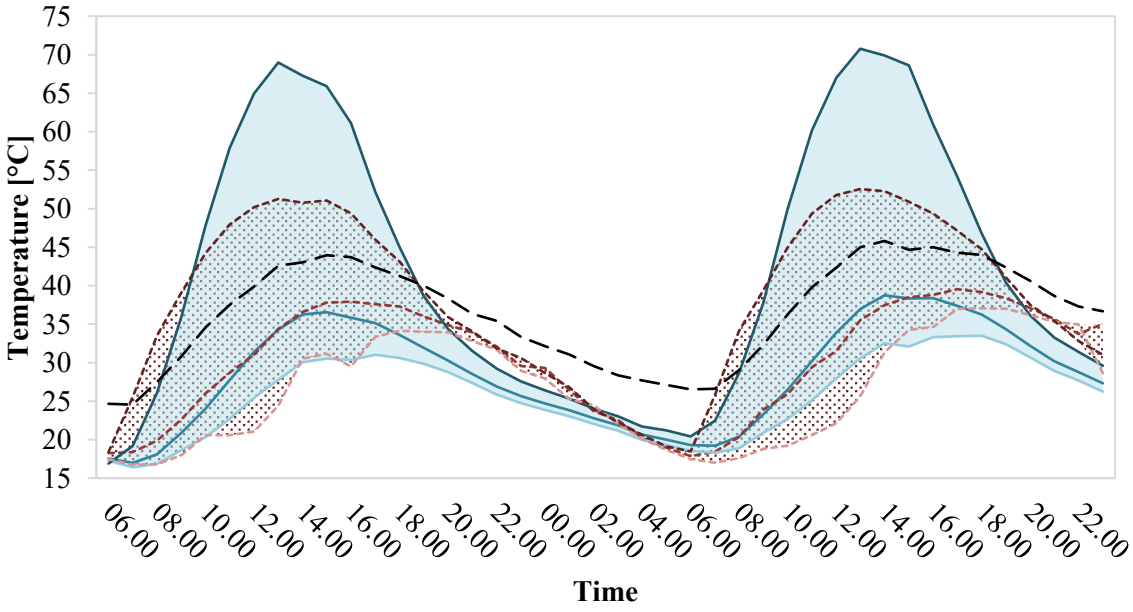

(b)

*Figure 9-3: Comparison of roof surface temperatures from ENVI-met (extracted from one specific roof cell for each scenario) and WRF (extracted from the grid cell corresponding to the ENVI-met domain) for different case study cities NYC (**a**) and PHX (**b**) over the course of the simulation periods. Red (RR), orange (CR), and yellow (SCR) dotted lines indicate WRF results, dark blue (RR), blue (CR) and light blue (SCR) solid lines indicate ENVI-met results, and black dashed line indicates ambient air temperature. Dotted red (WRF) and solid blue (ENVI-met) areas depict the range of possible roof surface temperatures to be predicted between low-albedo (RR) and high-albedo (SCR) roofs for the modeled conditions and locations.*

In general, the range of modeled surface temperatures is significantly larger in ENVI-met compared to WRF. In NYC, ENVI-met predicted lower surface temperatures for SCR than WRF on the one hand and massively higher values for RR (up to 18 K difference) on the other hand. In PHX, ENVI-met results

also feature a larger range in surface temperatures for all times but the morning hours when WRF estimated lower surface temperatures for SCR and higher temperatures for RR than ENVI-met. The drop in direct shortwave radiation during the second modeled day in NYC (c.f. Figure 9-1 a) caused a large reduction in RR surface temperatures of both models, a small impact on CR and SCR roofs in WRF, and almost no impact on CR and SCR in ENVI-met, which was also observed in the sensitivity study of Sinsel et al. (2021).

9.3.2 Model intercomparison of roof surface and air temperatures

Comparing the ENVI-met outputs – averaged over the whole model area – with the corresponding WRF cells, it can be observed that the general shape of the roof and air temperature curves is predicted very similarly by both models which is stated by high R^2 values of around 0.9 (Table 9-4). The RMSE values, however, show some discrepancies between the models of ~0.5 K to 3.5 K for all variables but RR surface temperatures, which showed even larger discrepancies of ~ 9 K.

Table 9-4: Comparison between surface and air temperature values of RR, CR, and SCR between WRF and ENVI-met for NYC and PHX.

NYC	R^2	RMSE [K]
Surface temperature RR WRF vs. ENVI-met	0.95	9.47
Surface temperature CR WRF vs. ENVI-met	0.92	1.87
Surface temperature SCR WRF vs. ENVI-met	0.91	2.15
Air temperature RR WRF vs. ENVI-met	0.99	0.51
Air temperature CR WRF vs. ENVI-met	0.97	0.80
Air temperature SCR WRF vs. ENVI-met	0.98	0.73
PHX		
Surface temperature RR WRF vs. ENVI-met	0.92	8.51
Surface temperature CR WRF vs. ENVI-met	0.89	2.93
Surface temperature SCR WRF vs. ENVI-met	0.80	3.43
Air temperature RR WRF vs. ENVI-met	0.91	2.39
Air temperature CR WRF vs. ENVI-met	0.95	1.95
Air temperature SCR WRF vs. ENVI-met	0.95	2.01

These larger discrepancies especially in surface temperature range may be explained by WRF's simplified building parametrization approach (Chen et al., 2011; Martilli et al., 2002) compared to ENVI-met's explicit building physics model (Simon, 2016). The building surface temperatures produced by ENVI-met were compared and confirmed by measurements in several studies (Simon et al., 2017; Tsoka et al., 2018; Yang et al., 2013). The review study of Tsoka, Tsikaloudaki, and Theodosiou (2018)

reported that all surface temperature evaluation studies showed a high agreement with measurements represented by statistical analysis values between 0.60-0.97 for R^2, 0.20-1.89 for MBE, and 2.1-4.8 °C for RMSE (Tsoka et al., 2018). To our knowledge, an evaluation of roof surface temperatures simulated with the WRF-BEP or WRF-BEP-BEM urban schemes has not been published, yet.

9.3.3 Spatial distribution of (super) cool roofs' cooling effect on pedestrian-level air temperature

To visualize local differences of cooling at pedestrian level, spatial distribution maps for WRF and ENVI-met were generated for 15:00 local time, which is commonly examined for results during daily peak temperatures (Liu et al., 2021). Air temperature reduction by CR/SCR simulated with WRF is especially pronounced in areas of high building density and thus concentrated in Manhattan (around 40.7° N / 73.8° W, Figure 9-4 a,b), where more roof surfaces were replaced by cool materials in the comparison simulations than in the rather sparsely built-up areas in the surrounding. These urban agglomerations in and around Manhattan feature a cooling effect of 0.5 K to 2 K in the CR run and even stronger air temperature reductions of 1 K to 2.75 K in the SCR scenario.

While the general decreases in air temperature at pedestrian level in PHX are similar to the model run in NYC, the differences in performance between CR and SCR are not as pronounced in PHX as they are in NYC (Figure 9-4 c,d). However, strong cooling effects of 1.5 K to 2 K are found for large portions of the Phoenix metropolitan area. Downtown Phoenix features air temperature reductions of up to 3 K. Small positive temperature anomalies (up to 0.75 K) in PHX as well as large positive air temperature anomalies (up to 1.25 K) in NYC can be found in sparsely built-up areas and are probably connected to changes in vertical and horizontal wind patterns due to a different thermal advection that has already been reported in the SCR ENVI-met sensitivity study of Sinsel et al. (2021) and could also be applicable for WRF.

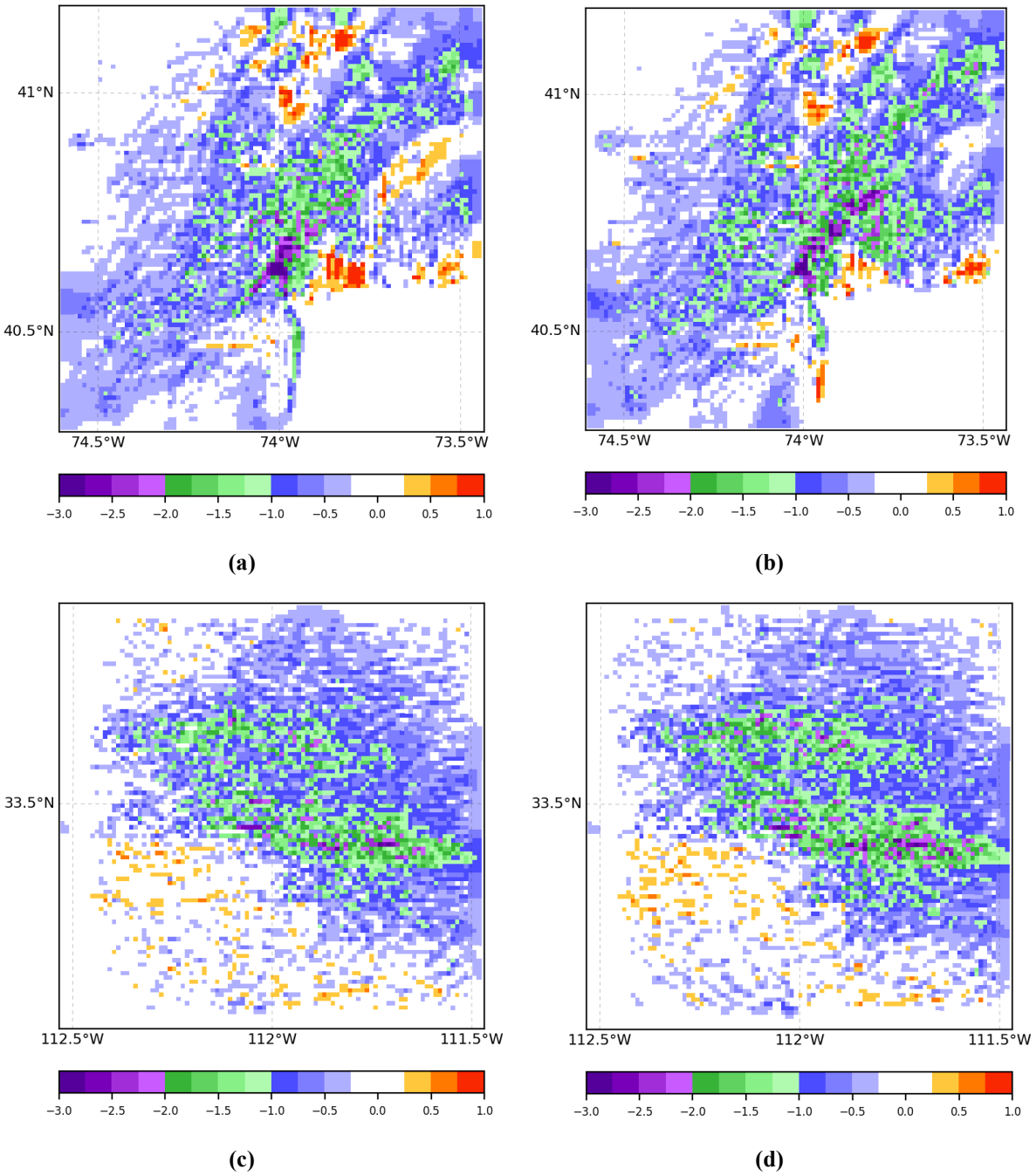

*Figure 9-4: Difference of spatial air temperature distribution of WRF results at pedestrian level between RR and both cool roof scenarios for the case study in NYC at 19.07.2008 15:00: (**a**) comparison between CR and RR, (**b**) comparison between SCR and RR and in PHX at 01.07.2007: (**c**) comparison between CR and RR, (**d**) comparison between SCR and RR.*

Looking at the spatial distribution of air temperature differences at pedestrian level between RR and the two cool roof types at 15:00 in the ENVI-met simulations, quite homogeneous air temperature reductions are predicted for the whole model domain in both cities. In NYC, cooling impact ranges mostly around 0.4 K in both cool roof scenarios and reaches up to 1.4 K and 1.7 K locally in CR and SCR, respectively (Figure 9-5 a,b). These larger deviations are exclusively found near the inflow borders

where the changes in vertical air mixing due to different thermal advection conditions in SCR seem to differ the most compared to RR. For PHX, air temperature reductions at pedestrian level are predicted to be between 0.2 K and 0.9 K in CR and between 0.4 K and 1.1 K in SCR scenario (Figure 9-5 c,d). Highest cooling impacts are – in contrast to NYC – not found at the inflow borders but mainly downwind of the model area where the cooling effect seems to accumulate. Differences between CR and SCR cooling performances are rather small, thus fitting to previous sensitivity study results (Sinsel et al., 2021).

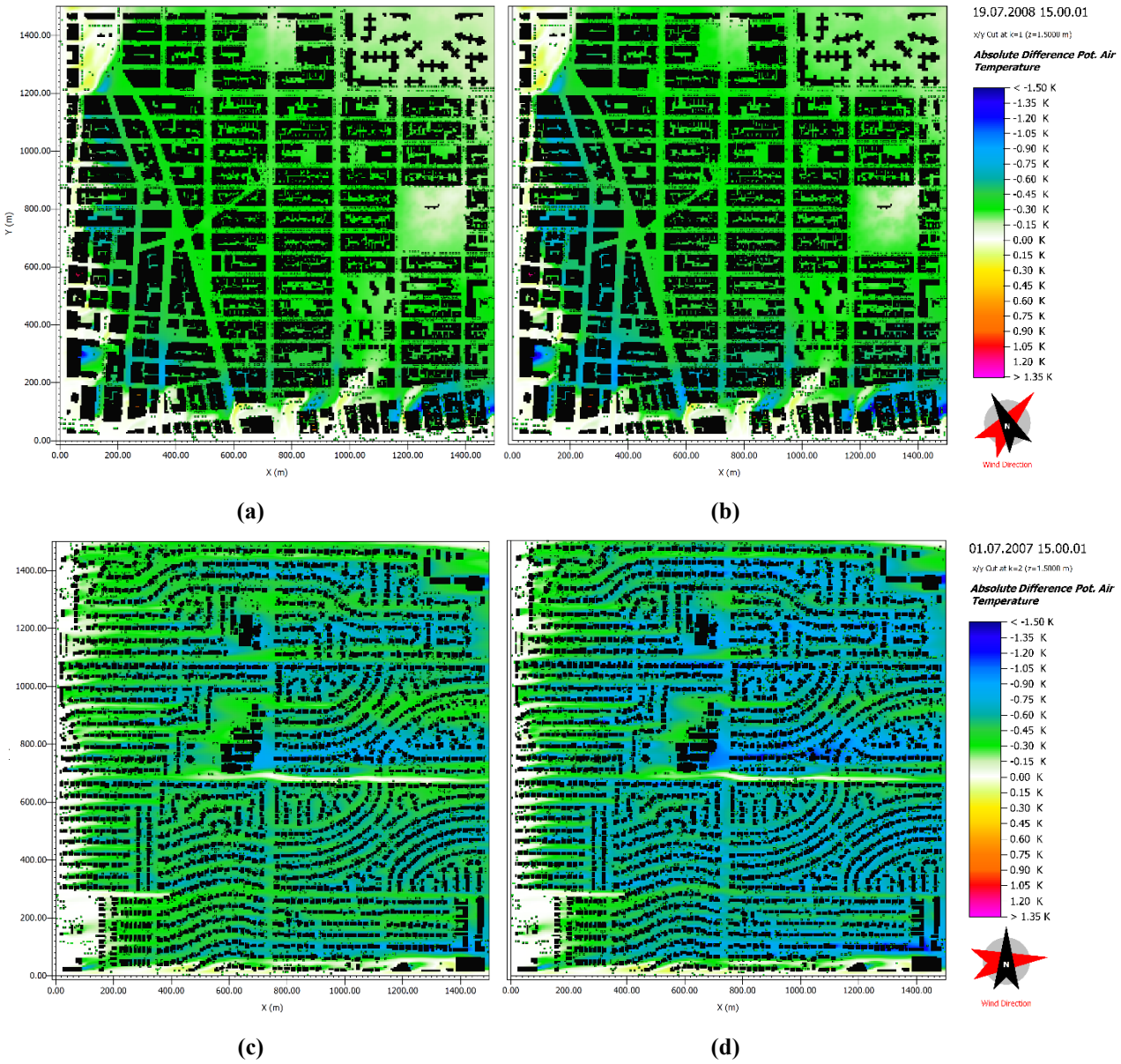

*Figure 9-5: Difference of spatial air temperature distribution of ENVI-met results at pedestrian level between RR and both cool roof scenarios for the case study in NYC at 19.07.2018 15:00: (**a**) comparison between CR and RR, (**b**) comparison between SCR and RR and in PHX at 01.07.2007 15:00: (**c**) comparison between CR and RR, (**d**) comparison between SCR and RR.*

9.3.4 Cooling effect of (super) cool roofs on pedestrian level air temperature over the diurnal cycle

To analyze the cooling effect of cool roofs over the diurnal cycle, the air temperature at pedestrian level was plotted for the case study scenarios of NYC and PHX (Figure 9-6). Values were extracted from the WRF pixel used for ENVI-met's forcing and averaged over the whole model area from ENVI-met's results (without the outer 5 cells at each border due to possible inflow distortion).

In both case studies and both models, air temperatures are significantly lowered during daytimes, however with indistinct peaks at morning, midday, and afternoon hours especially in WRF. The fluctuations in WRF's air temperature differences could be explained by the single grid cell extraction which has to show a much higher variability while being affected by short-term influences than the ENVI-met extraction which is based on an average of all model area grid cells. At nighttime, the air temperature difference slowly ceased to a cooling effect of around 0.1 K in ENVI-met and showed even a warming effect (although short-lived) of up to 0.6 K in WRF.

In ENVI-met, air temperature at pedestrian level is decreased by up to 0.49 K for NYC simulations and by up to 0.94 K for PHX simulations in SCR vs. RR comparisons. On the contrary, WRF simulation results of both case studies showed a much stronger cooling effect of up to 2.51 K for NYC and up to 3.31 K for PHX. Larger cooling effects in WRF simulations are likely explained by the fact that the total area where cool roofs were applied is greater than in the ENVI-met simulations (ENVI-met areas: ~1 km², WRF metropolitan areas: ~30.000 km²). With a larger area of SCR, more roofs in total contribute to a larger, city-wide cooling effect downwind (Broadbent et al., 2020b). The extracted data from the WRF pixel at the ENVI-met model area location is thus influenced by the accumulated cool roof effect of the upwind urban areas. Other explanations could point to differences in the turbulent heat exchange calculation from roof to street-level between both models, especially because ENVI-met predicted significantly higher roof surface temperatures on the one hand and much smaller air temperature reductions at pedestrian level on the other hand. Future work is needed to evaluate the accuracy of the representation of vertical heat exchange in WRF and ENVI-met. A recent systemic review from Krayenhoff et al. (2021) noted that WRF and ENVI-met simulated air temperatures have very different sensitives to roof

albedo changes, suggesting that this discrepancy is caused by differences in the representation of vertical heat exchange.

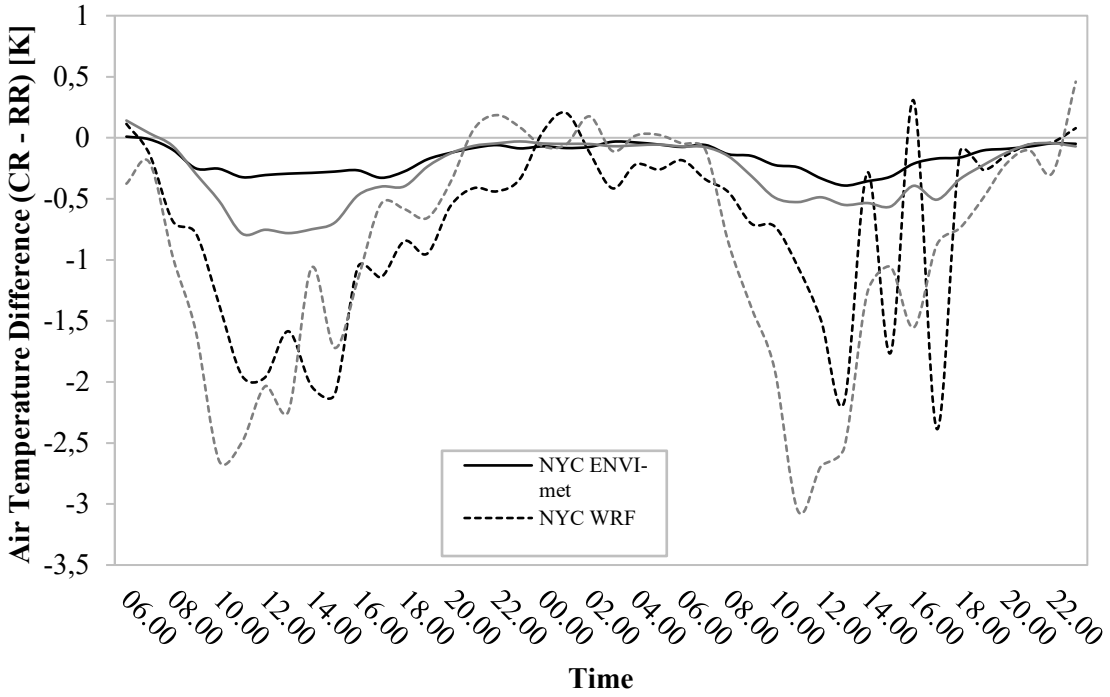

(a)

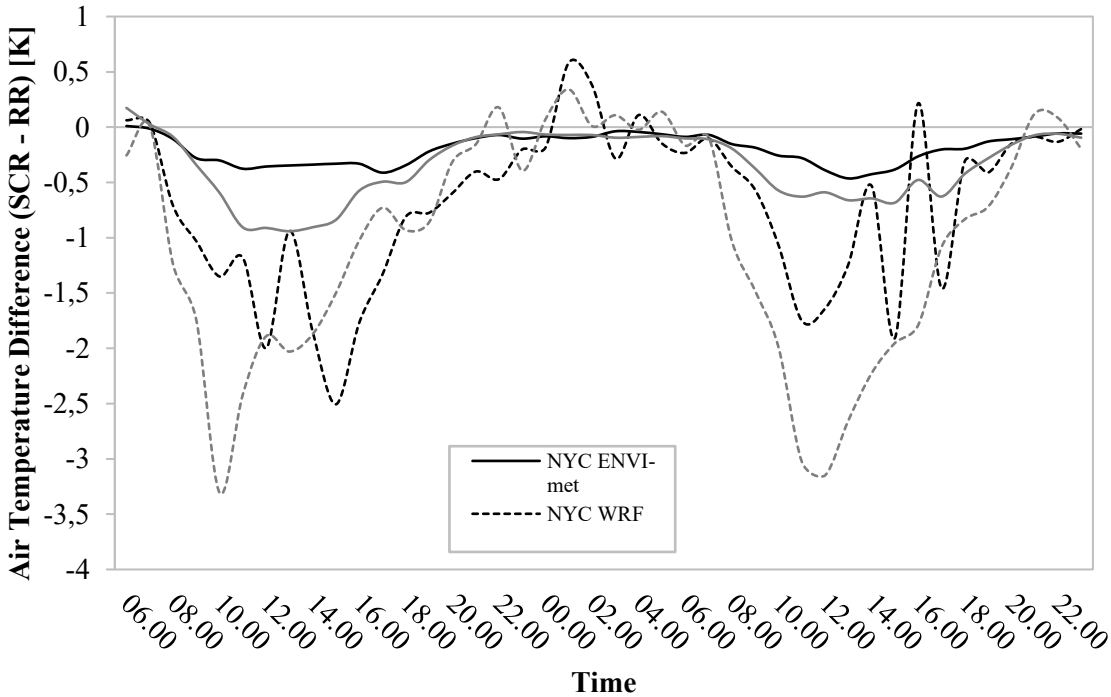

(b)

*Figure 9-6: Difference of WRF's and ENVI-met's air temperatures between CR and RR (**a**) as well as SCR and RR (**b**) at pedestrian level over the course of both simulation periods being extracted from the ENVI-met model area cell for WRF results and averaged over the model area for ENVI-met results, respectively, comparing the different scenarios in NYC and PHX.*

Both models predicted a higher air temperature difference at pedestrian level for PHX where more irradiation and warmer air temperatures are found. Since Sinsel et al. (2021) stated a comparatively low sensitivity of SCR to both radiation ($R^2 \sim 0.26$) and air temperature ($R^2 \sim 0.69$) but an inverse correlation of its cooling impact with increasing building height, the stronger SCR cooling performance in PHX could be assumed to be explained by the low-rise building structure in PHX compared to the medium- to high-rise building structure in NYC. However, a reverse test with ENVI-met simulations featuring the NYC boundary conditions to be run with the PHX model area located in NYC as well as the PHX boundary conditions to be run with the NYC model area located in PHX, could not corroborate this hypothesis. Contrastingly, air temperature reductions by SCR were more or less in the same range as in the simulations featuring the correct model area with realistic building morphologies shown in Figure 9-6. NYC results with low-rise PHX model area showed a slightly higher SCR cooling impact (~0.1 K more reduction), while PHX results with medium- to high-rise NYC model area featured a rather similar or slightly lower SCR cooling impact (~0.1 to ~0.2 K less reduction during daytime) compared to the original scenarios (Figure 9-7).

This cross-check hence points to the conclusion that the meteorological conditions in PHX featuring dry and hot weather as well as steep sun height angles yields better SCR performances in general than the rather warm and humid conditions in NYC. These results are in line with Baniassadi et al. (2019) who conducted an analysis of year-long SCR impacts on building energy performances, which additionally accounts for an increased heating demand for SCR in mild climates with cold winters such as in NYC, while hot climates such as in PHX only benefit from the advantages of SCR. A recent development of a dual-mode device that allows to switch between summer mode (high reflectivity for PDRC) and winter mode (low reflectivity for solar heating) could however overcome this shortcoming (Li et al., 2020). While meteorological conditions were identified as the major driver, the in Sinsel et al. (2021) found discrepancies in cooling impact caused by building height differences between model domains turned out to be a minor factor.

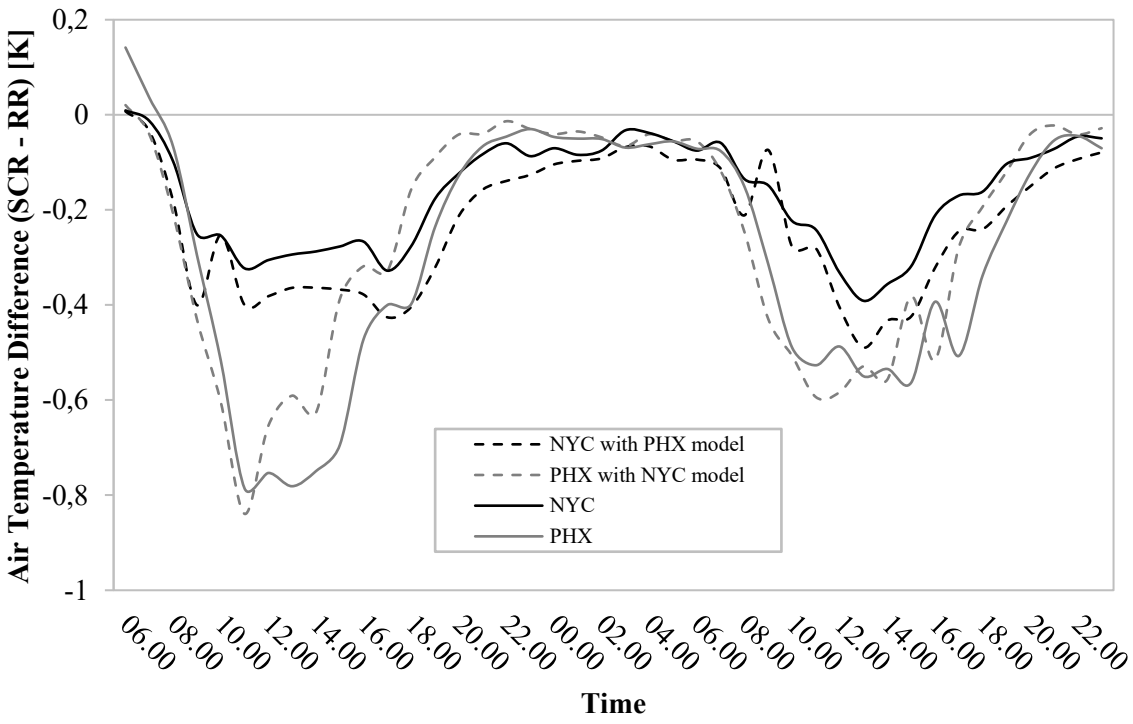

Figure 9-7: Difference of ENVI-met's air temperatures between SCR and RR at pedestrian level over the course of both simulation periods being averaged over the model area. Solid lines feature the original case study results, while dashed lines represent the case study results with exchanged model areas.

9.4 Conclusion

In two realistic case studies, cooling performances of (super) cool roofs were examined in varying meteorological and urban morphological conditions: NYC and PHX. By using mesoscale model WRF and microscale model ENVI-met, the possible cooling impact of widespread CR or SCR application could be evaluated on different scales. Furthermore, both model predictions could be compared against each other showing a high agreement ($R^2 \sim 0.9$, RMSE ~ 2 K) in air temperature and roof surface temperature analysis in general. However, ENVI-met showed a much higher range in modeled roof surface temperatures than WRF. Especially the observed high differences in predicted RR surface temperatures between both models (RMSE ~ 9 K) demonstrate the need for further evaluation of both model physics schemes, e.g., regarding the modeling of vertical heat exchanges. In the future, more studies comparing models at different scales as well as measurement campaigns to evaluate modeling accuracy will be needed.

Modeled CR and SCR surface temperatures as well as their ability to stay below ambient air temperature are in agreement with previous measurement and modeling studies. Spatial distribution maps of air

temperature reductions at pedestrian level showed lower CR/SCR cooling impacts in ENVI-met than in WRF, however with a local cooling up to 1.7 K during midday. The diurnal cycle of air temperature reductions at pedestrian level showed that the maximum cooling effect of SCR was found to be up to 0.49 K (NYC) / 0.94 K (PHX) averaged over the model area in ENVI-met. WRF predicted significantly stronger cooling effects of up to 2.51 K (NYC) / 3.31 K (PHX). Discrepancies between the model results could be explained by the simulation and analysis setup. As expected, PDRC only has a cooling impact during daytime that does not last during nighttime and even turns into a short-lived small warming effect in WRF scenarios.

Differences between SCR cooling performances in NYC and PHX are identified to be primarily related to the climate. Cross-check simulations featuring exchanged model areas excluded the different building morphologies as major driver of the discrepancies. While the prevailing higher building heights of the NYC model area were found to have a small negative effect on SCR cooling performance, which was also stated by a previous sensitivity study, the hot and dry meteorological conditions in PHX were identified as the main cause for the higher impact in pedestrian-level air temperature cooling. Recent building energy performance simulations also suggest that the advantages of SCR application are predominantly related to hot and dry climates, especially when inadvertent negative cooling effects during cold periods with an additional heating demand in winter are considered. However, further studies with differing climatological situations and building morphologies will have to verify these findings to improve guidance for urban planning purposes.

9.5 References

Aflaki, A., Mirnezhad, M., Ghaffarianhoseini, Amirhosein, Ghaffarianhoseini, Ali, Omrany, H., Wang, Z.-H., Akbari, H., 2017. Urban heat island mitigation strategies: A state-of-the-art review on Kuala Lumpur, Singapore and Hong Kong. Cities 62, 131–145. https://doi.org/10.1016/j.cities.2016.09.003

Akbari, H., Cartalis, C., Kolokotsa, D., Muscio, A., Pisello, A.L., Rossi, F., Santamouris, M., Synnefa, A., Wong, N.H., Zinzi, M., 2016. Local climate change and urban heat island mitigation techniques – the state of the art. Journal of Civil Engineering and Management 22, 1–16. https://doi.org/10.3846/13923730.2015.1111934

Aleksandrowicz, O., Vuckovic, M., Kiesel, K., Mahdavi, A., 2017. Current trends in urban heat island mitigation research: Observations based on a comprehensive research repository. Urban Climate 21, 1–26. https://doi.org/10.1016/j.uclim.2017.04.002

Anand, J., Sailor, D.J., Baniassadi, A., 2021. The relative role of solar reflectance and thermal emittance for passive daytime radiative cooling technologies applied to rooftops. Sustainable Cities and Society 65, 102612. https://doi.org/10.1016/j.scs.2020.102612

Baniassadi, A., Sailor, D.J., Ban-Weiss, G.A., 2019. Potential energy and climate benefits of super-cool materials as a rooftop strategy. Urban Climate 29, 100495. https://doi.org/10.1016/j.uclim.2019.100495

Berardi, U., GhaffarianHoseini, AmirHosein, GhaffarianHoseini, Ali, 2014. State-of-the-art analysis of the environmental benefits of green roofs. Applied Energy 115, 411–428. https://doi.org/10.1016/j.apenergy.2013.10.047

Berardi, U., Jandaghian, Z., Graham, J., 2020. Effects of greenery enhancements for the resilience to heat waves: A comparison of analysis performed through mesoscale (WRF) and microscale (Envi-met) modeling. Science of The Total Environment 747, 141300. https://doi.org/10.1016/j.scitotenv.2020.141300

Bhati, S., Mohan, M., 2016. WRF model evaluation for the urban heat island assessment under varying land use/land cover and reference site conditions. Theor Appl Climatol 126, 385–400. https://doi.org/10.1007/s00704-015-1589-5

Bougeault, P., Lacarrere, P., 1989. Parameterization of Orography-Induced Turbulence in a Mesobeta--Scale Model. Monthly Weather Review 117, 1872–1890. https://doi.org/10.1175/1520-0493(1989)117<1872:POOITI>2.0.CO;2

Bowler, D.E., Buyung-Ali, L., Knight, T.M., Pullin, A.S., 2011. Urban greening to cool towns and cities: A systematic review of the empirical evidence. Landscape and Urban Planning 97, 147–155.

Broadbent, A.M., Krayenhoff, E.S., Georgescu, M., 2020a. The motley drivers of heat and cold exposure in 21st century US cities. PNAS 117, 21108–21117. https://doi.org/10.1073/pnas.2005492117

Broadbent, A.M., Krayenhoff, E.S., Georgescu, M., 2020b. Efficacy of cool roofs at reducing pedestrian-level air temperature during projected 21st century heatwaves in Atlanta, Detroit, and Phoenix (USA). Environ. Res. Lett. 15, 084007. https://doi.org/10.1088/1748-9326/ab6a23

Bruse, M., 1999. Die Auswirkungen kleinskaliger Umweltgestaltung auf das Mikroklima. Entwicklung des prognostischen numerischen Modells ENVI-met zur Simulation der Wind-, Temperatur- und Feuchteverteilung in städtischen Strukturen (PhD Thesis). Ruhr-University Bochum, Bochum.

Bruse, M., Fleer, H., 1998. Simulating Surface Plant Air Interactions inside Urban Environments with a Three Dimensional Numerical Model. Environmental Modelling & Software 13, 373–384. https://doi.org/10.1016/S1364-8152(98)00042-5

Chen, F., Kusaka, H., Bornstein, R., Ching, J., Grimmond, C.S.B., Grossman-Clarke, S., Loridan, T., Manning, K.W., Martilli, A., Miao, S., Sailor, D., Salamanca, F.P., Taha, H., Tewari, M., Wang, X., Wyszogrodzki, A.A., Zhang, C., 2011. The Integrated WRF/Urban Modelling System: Development, Evaluation, and Applications to Urban Environmental Problems. International Journal of Climatology 31, 273–288. https://doi.org/10.1002/joc.2158

Chen, F., Yang, X., Zhu, W., 2014. WRF simulations of urban heat island under hot-weather synoptic conditions: The case study of Hangzhou City, China. Atmospheric Research 138, 364–377. https://doi.org/10.1016/j.atmosres.2013.12.005

Chen, J., Lu, L., 2020. Development of radiative cooling and its integration with buildings: A comprehensive review. Solar Energy 212, 125–151. https://doi.org/10.1016/j.solener.2020.10.013

Chen, J., Lu, L., Gong, Q., Wang, B., Jin, S., Wang, M., 2021. Development of a new spectral selectivity-based passive radiative roof cooling model and its application in hot and humid region. Journal of Cleaner Production 307, 127170. https://doi.org/10.1016/j.jclepro.2021.127170

Ching, J., Brown, M., Burian, S., Chen, F., Cionco, R., 2009. National Urban Database and Access Portal Tool, NUDAPT 37.

Conry, P., Fernando, H.J.S., Leo, L.S., Sharma, A., Potosnak, M., Hellmann, J., 2014. Multi-Scale Simulations of Climate-Change Influence on Chicago Heat Island. Presented at the ASME 2014 4th Joint US-European Fluids Engineering Division Summer Meeting collocated with the ASME 2014 12th International Conference on Nanochannels, Microchannels, and Minichannels, American Society of Mechanical Engineers Digital Collection. https://doi.org/10.1115/FEDSM2014-21581

Deru, M., Field, K., Studer, D., Benne, K., Griffith, B., Torcellini, B., Halverson, M., Winiarski, D., Liu, B., Rosenberg, M., Huang, J., Yazdanian, M., Crawley, D., 2010. U.S. Department of Energy Commercial Reference Building Models of the National Building Stock.

Di Giuseppe, E., Pergolini, M., Stazi, F., 2017. Numerical assessment of the impact of roof reflectivity and building envelope thermal transmittance on the UHI effect. Energy Procedia, Sustainability in Energy and Buildings 2017: Proceedings of the Ninth KES International Conference, Chania, Greece, 5-7 July 2017 134, 404–413. https://doi.org/10.1016/j.egypro.2017.09.590

Dornelles, K., Caram, R., Sichieri, E., 2015. Natural Weathering of Cool Coatings and its Effect on Solar Reflectance of Roof Surfaces. Energy Procedia, 6th International Building Physics Conference, IBPC 2015 78, 1587–1592. https://doi.org/10.1016/j.egypro.2015.11.216

Dudhia, J., 1989. Numerical Study of Convection Observed during the Winter Monsoon Experiment Using a Mesoscale Two-Dimensional Model. Journal of the Atmospheric Sciences 46, 3077–3107. https://doi.org/10.1175/1520-0469(1989)046<3077:NSOCOD>2.0.CO;2

Evola, G., Gagliano, A., Fichera, A., Marletta, L., Martinico, F., Nocera, F., Pagano, A., 2017. UHI effects and strategies to improve outdoor thermal comfort in dense and old neighbourhoods. Energy Procedia, Sustainability in Energy and Buildings 2017: Proceedings of the Ninth KES International Conference, Chania, Greece, 5-7 July 2017 134, 692–701. https://doi.org/10.1016/j.egypro.2017.09.589

Falasca, S., Ciancio, V., Salata, F., Golasi, I., Rosso, F., Curci, G., 2019. High albedo materials to counteract heat waves in cities: An assessment of meteorology, buildings energy needs and pedestrian thermal comfort. Building and Environment 163, 106242. https://doi.org/10.1016/j.buildenv.2019.106242

Fallmann, J., Suppan, P., Emeis, S., 2013. Modeling of the Urban Heat Island (UHI) using WRF - Assessment of adaptation and mitigation strategies for the city of Stuttgart. EGU2013-4251.

Forouzandeh, A., 2021. Prediction of surface temperature of building surrounding envelopes using holistic microclimate ENVI-met model. Sustainable Cities and Society 70, 102878. https://doi.org/10.1016/j.scs.2021.102878

Gentle, A.R., Smith, G.B., 2015. A Subambient Open Roof Surface under the Mid-Summer Sun. Advanced Science 2, 1500119. https://doi.org/10.1002/advs.201500119

Giannaros, C., Nenes, A., Giannaros, T.M., Kourtidis, K., Melas, D., 2018. A comprehensive approach for the simulation of the Urban Heat Island effect with the WRF/SLUCM modeling system: The case of Athens (Greece). Atmospheric Research 201, 86–101. https://doi.org/10.1016/j.atmosres.2017.10.015

Google, 2020b. Phoenix [WWW Document]. Google Maps.

Google, 2020a. NYC East Village [WWW Document]. Google Maps.

Heusinger, J., Sailor, D.J., Weber, S., 2018. Modeling the reduction of urban excess heat by green roofs with respect to different irrigation scenarios. Building and Environment 131, 174–183. https://doi.org/10.1016/j.buildenv.2018.01.003

Heusinger, J., Weber, S., 2015. Comparative microclimate and dewfall measurements at an urban green roof versus bitumen roof. Building and Environment 92, 713–723. https://doi.org/10.1016/j.buildenv.2015.06.002

Huttner, S., 2012. Further development and application of the 3D microclimate simulation ENVI-met (Dissertation). Johannes Gutenberg-University Mainz.

Huynh, C., Eckert, R., 2012. Reducing Heat and Improving Thermal Comfort through Urban Design – A Case Study in Ho Chi Minh City. IJESD 480–485. https://doi.org/10.7763/IJESD.2012.V3.271

Jandaghian, Z., Berardi, U., 2020. Comparing urban canopy models for microclimate simulations in Weather Research and Forecasting Models. Sustainable Cities and Society 55, 102025. https://doi.org/10.1016/j.scs.2020.102025

Jiménez, P.A., Dudhia, J., González-Rouco, J.F., Navarro, J., Montávez, J.P., García-Bustamante, E., 2012. A Revised Scheme for the WRF Surface Layer Formulation. Monthly Weather Review 140, 898–918. https://doi.org/10.1175/MWR-D-11-00056.1

Kántor, N., Unger, J., 2011. The most problematic variable in the course of human-biometeorological comfort assessment — the mean radiant temperature. cent.eur.j.geo. 3, 90–100. https://doi.org/10.2478/s13533-011-0010-x

Kolokotroni, M., 2017. Cool materials in the urban built environment to mitigate heat islands: potential consequences for building ventilation. 38th AIVC International Conference.

Krayenhoff, E., Broadbent, A.M., Zhao, L., Georgescu, M., Middel, A., Voogt, J., Martilli, A., Sailor, D., Erell, E., 2021. Cooling hot cities: A systematic and critical review of the numerical modelling literature. Environmental Research Letters (accepted).

Krayenhoff, E.S., Moustaoui, M., Broadbent, A.M., Gupta, V., Georgescu, M., 2018. Diurnal interaction between urban expansion, climate change and adaptation in US cities. Nature Clim Change 8, 1097–1103. https://doi.org/10.1038/s41558-018-0320-9

Lee, T.-J., Yoo, J.-W., Lee, H., Won, H., Lee, S.-H., 2017. Study on the Impacts of Lateral Boundary Conditions and Thermodynamics of Urban Park using Coupling System of WRF / ENVI-met. Journal of Environmental Science International 26, 493–507. https://doi.org/10.5322/JESI.2017.26.4.493

Li, X., Sun, B., Sui, C., Nandi, A., Fang, H., Peng, Y., Tan, G., Hsu, P.-C., 2020. Integration of daytime radiative cooling and solar heating for year-round energy saving in buildings. Nat Commun 11, 6101. https://doi.org/10.1038/s41467-020-19790-x

Liu, Z., Cheng, W., Jim, C.Y., Morakinyo, T.E., Shi, Y., Ng, E., 2021. Heat mitigation benefits of urban green and blue infrastructures: A systematic review of modeling techniques, validation and scenario simulation in ENVI-met V4. Building and Environment 200, 107939. https://doi.org/10.1016/j.buildenv.2021.107939

Mandal, J., Fu, Y., Overvig, A.C., Jia, M., Sun, K., Shi, N.N., Zhou, H., Xiao, X., Yu, N., Yang, Y., 2018. Hierarchically porous polymer coatings for highly efficient passive daytime radiative cooling. Science 362, 315–319. https://doi.org/10.1126/science.aat9513

Mandal, J., Yang, Y., Yu, N., Raman, A.P., 2020. Paints as a Scalable and Effective Radiative Cooling Technology for Buildings. Joule 4, 1350–1356. https://doi.org/10.1016/j.joule.2020.04.010

Martilli, A., Clappier, A., Rotach, M.W., 2002. An Urban Surface Exchange Parameterisation for Mesoscale Models. Boundary-Layer Meteorology 104, 261–304. https://doi.org/10.1023/A:1016099921195

Mastrapostoli, E., Santamouris, M., Kolokotsa, D., Vassilis, P., Venieri, D., Gompakis, K., 2016. On the ageing of cool roofs: Measure of the optical degradation, chemical and biological analysis and assessment of the energy impact. Energy and Buildings, SI: Countermeasures to Urban Heat Island 114, 191–199. https://doi.org/10.1016/j.enbuild.2015.05.030

McRae, I., Freedman, F., Rivera, A., Li, X., Dou, J., Cruz, I., Ren, C., Dronova, I., Fraker, H., Bornstein, R., 2020. Integration of the WUDAPT, WRF, and ENVI-met models to simulate extreme daytime temperature mitigation strategies in San Jose, California. Building and Environment 184, 107180. https://doi.org/10.1016/j.buildenv.2020.107180

McRae, I., Freedman, F., Rivera, A., Li, X., Dou, J.J., Ren, C., Dronova, I., Fraker, H., Bornstein, R., 2018. Bridging WUDAPT, urbanized WRF and ENVI-met research platforms to study the effects of urban morphology and meteorology on building-scale urban design., in: 10th International Conference on Urban Climate/14th Symposium on the Urban Environment. AMS.

Middel, A., Turner, V.K., Schneider, F.A., Zhang, Y., Stiller, M., 2020. Solar reflective pavements—A policy panacea to heat mitigation? Environ. Res. Lett. 15, 064016. https://doi.org/10.1088/1748-9326/ab87d4

Mlawer, E.J., Taubman, S.J., Brown, P.D., Iacono, M.J., Clough, S.A., 1997. Radiative transfer for inhomogeneous atmospheres: RRTM, a validated correlated-k model for the longwave. Journal of Geophysical Research: Atmospheres 102, 16663–16682. https://doi.org/10.1029/97JD00237

Morini, E., Touchaei, A.G., Rossi, F., Cotana, F., Akbari, H., 2018. Evaluation of albedo enhancement to mitigate impacts of urban heat island in Rome (Italy) using WRF meteorological model. Urban Climate 24, 551–566. https://doi.org/10.1016/j.uclim.2017.08.001

Multi-Resolution Land Characteristics Consortium (U.S.), 2020. National Land Cover Dataset (NLCD).

NYC Open Data, D. of I.T.& T. (DoITT), 2019. Building Footprints and Street Trees [WWW Document]. URL data.cityofnewyork.us/Housing-Development/Building-Footprints/

Phoenix Open Data, 2019. Building Footprints [WWW Document]. URL https://www.phoenix-opendata.com/

Raman, A.P., Anoma, M.A., Zhu, L., Rephaeli, E., Fan, S., 2014. Passive radiative cooling below ambient air temperature under direct sunlight. Nature 515, 540–544. https://doi.org/10.1038/nature13883

Santamouris, M., 2011. Using advanced cool materials in the urban built environment to mitigate heat islands and improve thermal comfort conditions. Solar Energy 18.

Santamouris, M., Haddad, S., Saliari, M., Vasilakopoulou, K., Synnefa, A., Paolini, R., Ulpiani, G., Garshasbi, S., Fiorito, F., 2018. On the energy impact of urban heat island in Sydney: Climate and energy potential of mitigation technologies. Energy and Buildings 166, 154–164. https://doi.org/10.1016/j.enbuild.2018.02.007

Santamouris, M., Yun, G.Y., 2020. Recent development and research priorities on cool and super cool materials to mitigate urban heat island. Renewable Energy 161, 792–807. https://doi.org/10.1016/j.renene.2020.07.109

Schinasi, L.H., Benmarhnia, T., De Roos, A.J., 2018. Modification of the association between high ambient temperature and health by urban microclimate indicators: A systematic review and meta-analysis. Environmental Research 161, 168–180. https://doi.org/10.1016/j.envres.2017.11.004

Schrijvers, P.J.C., Jonker, H.J.J., de Roode, S.R., Kenjereš, S., 2016. The effect of using a high-albedo material on the Universal Temperature Climate Index within a street canyon. Urban Climate 17, 284–303. https://doi.org/10.1016/j.uclim.2016.02.005

Sharma, A., Fernando, H.J.S., Hamlet, A.F., Hellmann, J.J., Barlage, M., Chen, F., 2017. Urban meteorological modeling using WRF: a sensitivity study. International Journal of Climatology 37, 1885–1900. https://doi.org/10.1002/joc.4819

Simon, H., 2016. Modeling Urban Microclimate: Development, Implementation and Evaluation of New and Improved Calculation Methods for the Urban Microclimate Model ENVI-Met (PhD Thesis). Universitätsbibliothek Mainz, Mainz.

Simon, H., Kissel, L., Bruse, M., 2017. Evaluation of ENVI-met's multiple-node model and estimation of indoor climate, in: Design to Thrive. Presented at the PLEA, Edinburgh, p. 9.

Sinsel, T., Simon, H., Broadbent, A.M., Bruse, M., Heusinger, J., 2021. Modeling the outdoor cooling impact of highly radiative "super cool" materials applied on roofs. Urban Climate 38, 100898. https://doi.org/10.1016/j.uclim.2021.100898

Skamarock, W., Klemp, J., Dudhia, J., Gill, D., Barker, D., Wang, W., Huang, X.-Y., Duda, M., 2008. A Description of the Advanced Research WRF Version 3. UCAR/NCAR. https://doi.org/10.5065/D68S4MVH

Solcerova, A., van de Ven, F., Wang, M., Rijsdijk, M., van de Giesen, N., 2017. Do green roofs cool the air? Building and Environment 111, 249–255. https://doi.org/10.1016/j.buildenv.2016.10.021

Synnefa, A., Santamouris, M., Apostolakis, K., 2007. On the development, optical properties and thermal performance of cool colored coatings for the urban environment. Solar Energy 81, 488–497. https://doi.org/10.1016/j.solener.2006.08.005

Taleghani, M., Sailor, D., Ban-Weiss, G.A., 2016. Micrometeorological simulations to predict the impacts of heat mitigation strategies on pedestrian thermal comfort in a Los Angeles neighborhood. Environ. Res. Lett. 11, 024003. https://doi.org/10.1088/1748-9326/11/2/024003

Thorsson, S., Rocklöv, J., Konarska, J., Lindberg, F., Holmer, B., Dousset, B., Rayner, D., 2014. Mean radiant temperature – A predictor of heat related mortality. Urban Climate, ICUC8: The 8th International Conference on Urban Climate and the 10th Symposium on the Urban Environment 10, 332–345. https://doi.org/10.1016/j.uclim.2014.01.004

Tsoka, S., Tsikaloudaki, A., Theodosiou, T., 2018. Analyzing the ENVI-met microclimate model's performance and assessing cool materials and urban vegetation applications–A review. Sustainable Cities and Society 43, 55–76. https://doi.org/10.1016/j.scs.2018.08.009

Vogel, J., Afshari, A., 2020. Comparison of Urban Heat Island Intensity Estimation Methods Using Urbanized WRF in Berlin, Germany. Atmosphere 11, 1338. https://doi.org/10.3390/atmos11121338

Wang, Y., Berardi, U., Akbari, H., 2016. Comparing the effects of urban heat island mitigation strategies for Toronto, Canada. Energy and Buildings, SI: Countermeasures to Urban Heat Island 114, 2–19. https://doi.org/10.1016/j.enbuild.2015.06.046

Yang, J., Mohan Kumar, D. llamathy, Pyrgou, A., Chong, A., Santamouris, M., Kolokotsa, D., Lee, S.E., 2018. Green and cool roofs' urban heat island mitigation potential in tropical climate. Solar Energy 173, 597–609. https://doi.org/10.1016/j.solener.2018.08.006

Yang, J., Wang, Z.-H., Kaloush, K.E., 2015. Environmental impacts of reflective materials: Is high albedo a 'silver bullet' for mitigating urban heat island? Renewable and Sustainable Energy Reviews 47, 830–843. https://doi.org/10.1016/j.rser.2015.03.092

Yang, X., Zhao, L., Bruse, M., Meng, Q., 2013. Evaluation of a Microclimate Model for Predicting the Thermal Behaviour of Different Ground Surfaces. Building and Environment 60, 93–104.

Yang, Y., Zhang, Y., 2020. Passive daytime radiative cooling: Principle, application, and economic analysis. MRS Energy & Sustainability 7. https://doi.org/10.1557/mre.2020.18

Zhai, Y., Ma, Y., David, S.N., Zhao, D., Lou, R., Tan, G., Yang, R., Yin, X., 2017. Scalable-manufactured randomized glass-polymer hybrid metamaterial for daytime radiative cooling. Science 355, 1062–1066. https://doi.org/10.1126/science.aai7899

Zhao, D., Aili, A., Zhai, Y., Xu, S., Tan, G., Yin, X., Yang, R., 2019. Radiative sky cooling: Fundamental principles, materials, and applications. Applied Physics Reviews 6, 021306. https://doi.org/10.1063/1.5087281

9.6 Appendix

WRF was evaluated in both New York and Phoenix against 2 m air temperature observations at three locations in both metropolitan areas. The evaluations were completed for the heatwave case study periods. Air temperature data were obtained via the Mesowest website (https://mesowest.utah.edu/), which hosts historical National Weather Service observational data.

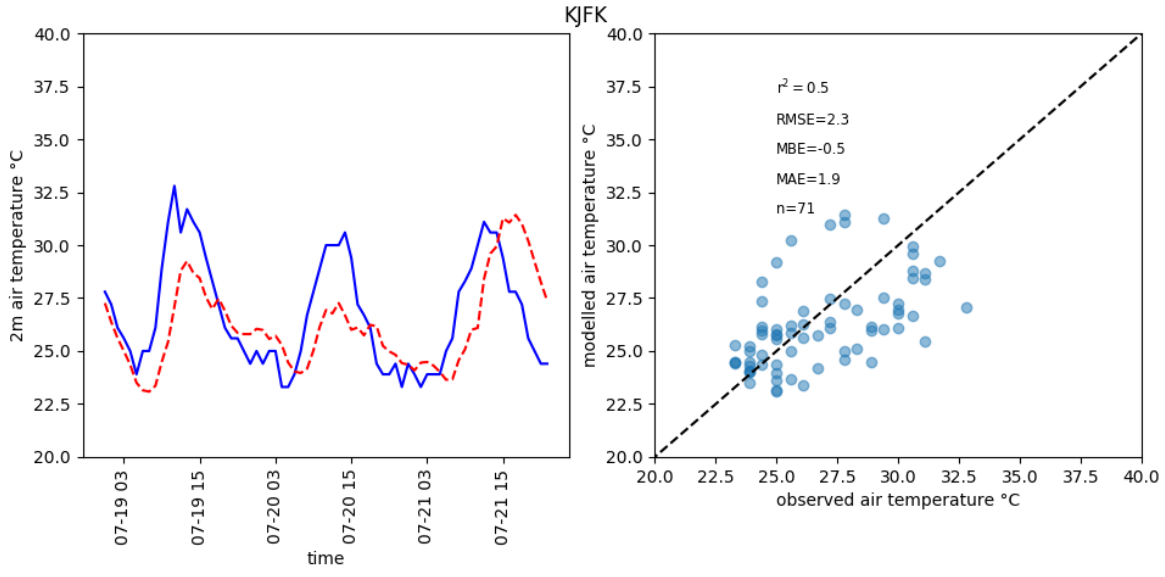

(a)

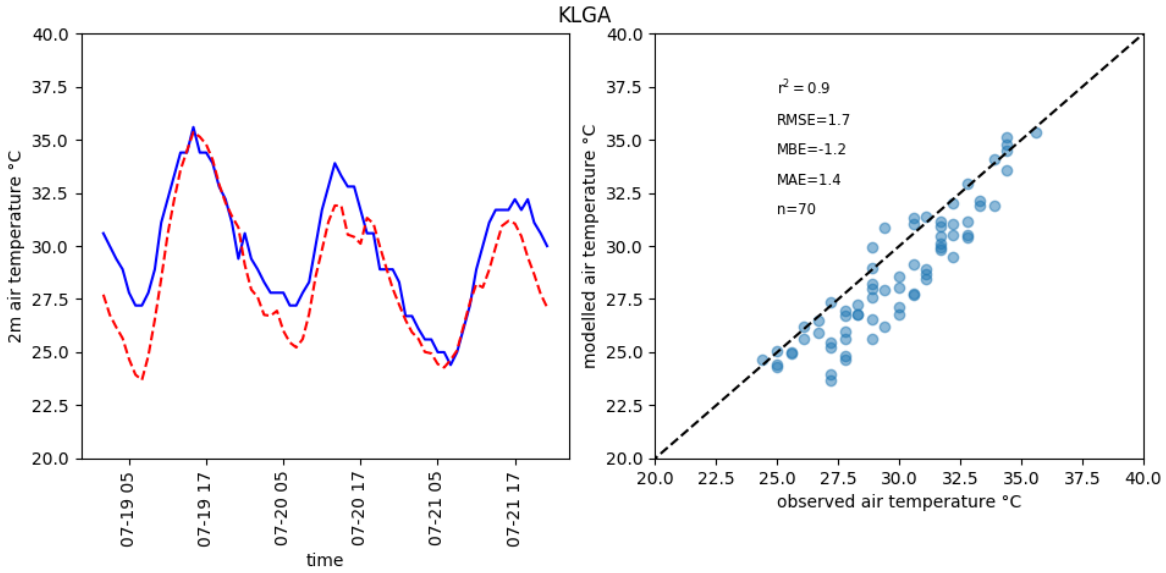

(b)

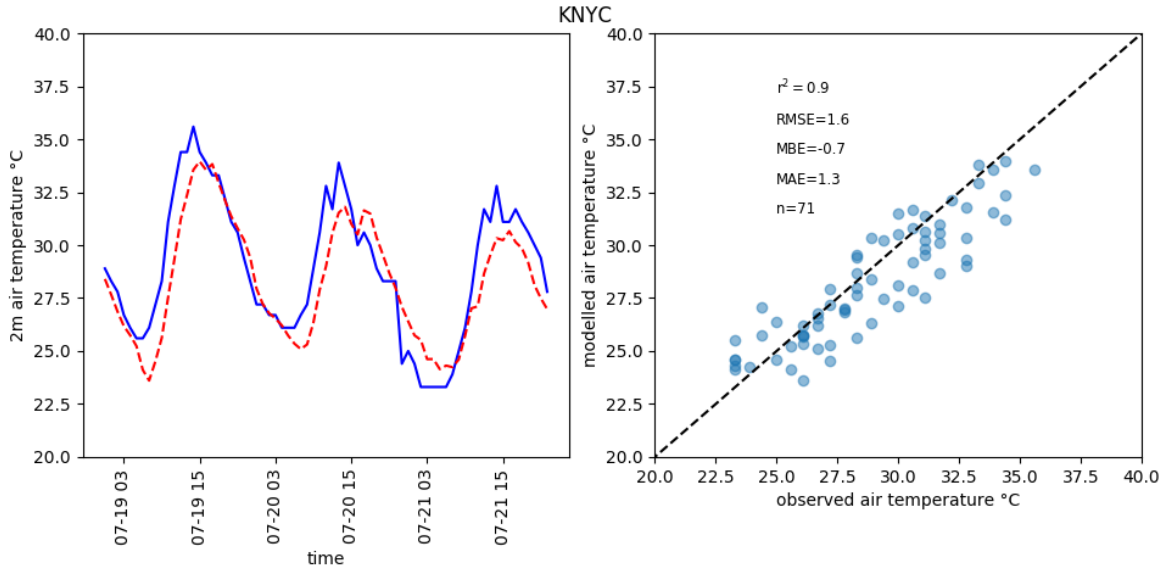

(c)

Figure 9-8: Observed (blue) vs modeled (red) air temperature for NYC at John F. Kennedy Airport (a), LaGuardia Airport (b), and NYC Central Park (c). RMSE = root mean square error, MBE = mean bias error, MAE = mean absolute error.

For New York, the weather stations analyzed were John F. Kennedy Airport (KJFK; 40.64° N, 73.76° W), LaGuardia Airport (KLGA; 40.78° N, 73.88° W), and Central Park (KNYC; 40.78° N, 73.97° W). The timing and amplitude of diurnal temperature range is less accurately captured in New York City, relative to Phoenix. The model tended to heat up too slowly when compared to observations (Figure 9-8). In particular, the daily maximum temperature at the JFK airport site was underpredicted by up to 5 °C. The reduced model skill in New York is likely due to complex sea breeze circulations and coastal

effects in New York. Overall, statistical indicators at the LaGuardia and Central Park sites are within acceptable ranges.

For Phoenix, the weather stations analyzed were Phoenix Sky Harbor (KPHX; 33.43° N, 112.00° W), Scottsdale Airport (KSDL; 33.43°, 112.00° W), and Phoenix Mesa-Gateway Airport (KIWA; 33.3°2 N, 111.65° W). Evaluation timeseries show that the timing and amplitude of diurnal temperature change is well captured in Phoenix (Figure 9-9). Statistical indicators also indicate good model skill with RMSE values of 1.4 – 2.0 K.

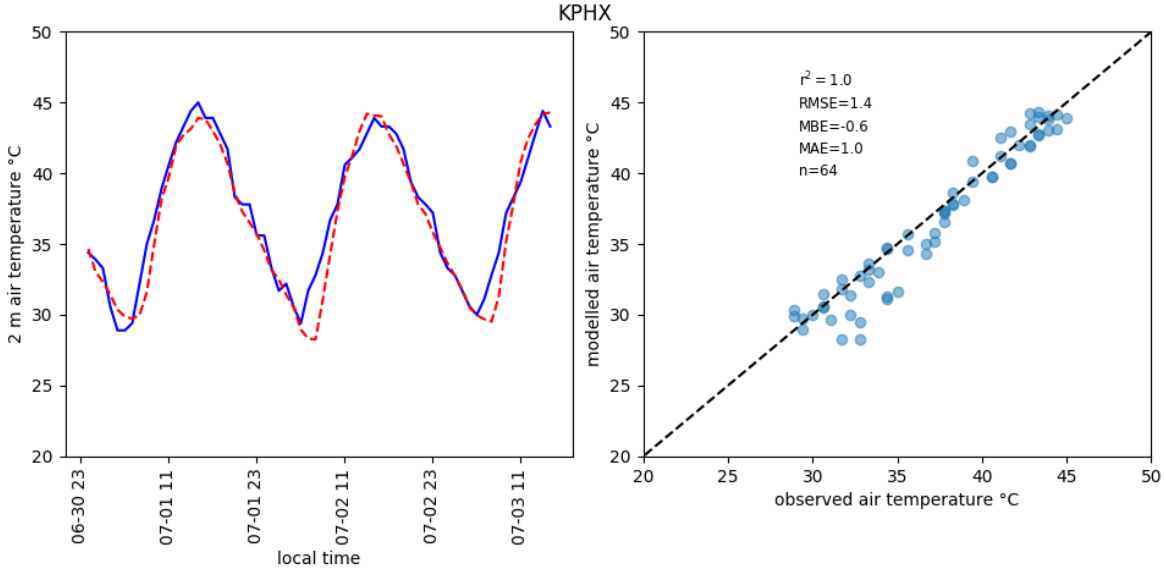

(a)

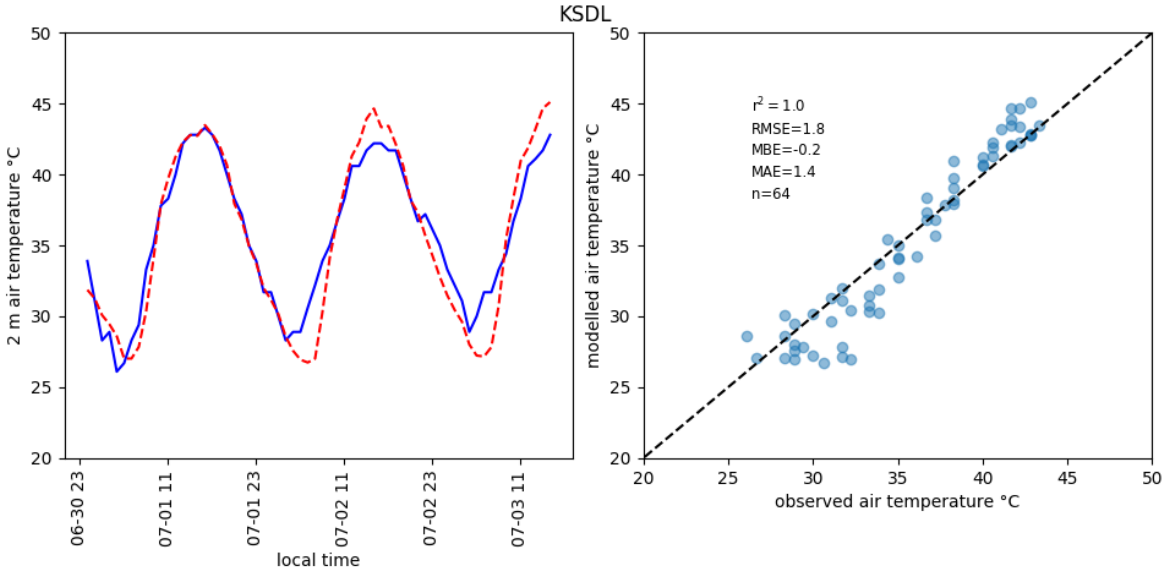

(b)

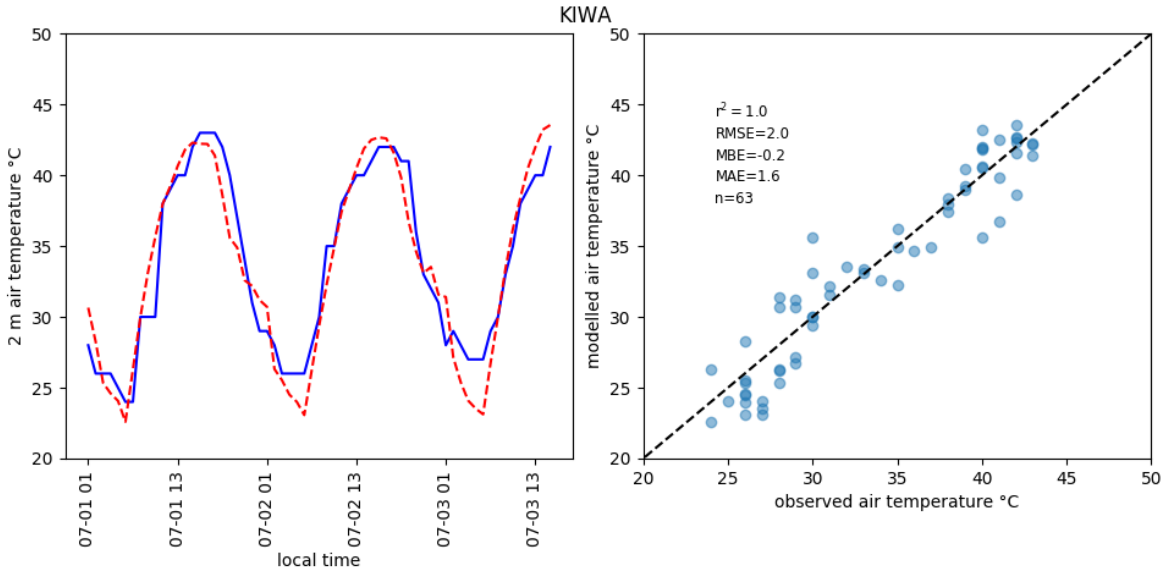

(c)

Figure 9-9: Observed (blue) vs modeled (red) air temperature for Phoenix at Sky Harbor Airport (a), Scottsdale Airport (b), and Mesa-Gateway Airport (c). RMSE = root mean square error, MBE = mean bias error, MAE = mean absolute error.

“ (Sinsel et al., 2021b).

10 Conclusion and outlook

This thesis presented a summary of extensive works with and on the microclimate model ENVI-met. By analyzing the newly developed super cool materials as a heat mitigation measure when applied on rooftops, a typical scientific application featuring the use of climate models was conducted. In two consecutive studies featuring both simple and complex urban environments, it was found that SCR could be a viable option for urban heat stress mitigation, although being limited to very hot and dry climates as well as a prevailing low-rise building morphology. Additionally, a large-scale application must be assumed as a rather hypothetical scenario, especially since SCR is competing against popular green roof solutions and photovoltaic systems that might not be improving indoor and outdoor thermal comfort but are contrastingly capable of producing renewable energy without any additional space demand. Another application study featuring the analysis of particulate matter exposition rates at child height levels yields a call for more in-depth research about air pollution concentrations on different height levels and shows the broad range of possible ENVI-met modeling tasks.

Presented model advancements featured the implementation of IVS and ACRT modules to tackle reported shortcomings in radiation flux modeling as well as the development of Lindenmeyer-system trees and a stochastic particle trajectory model as a post-processing tool for ENVI-met. All implementations were explained in detail and evaluated by proof-of-concept simulations. A presented model evaluation study in Hong Kong featuring multiple sites, simulation settings, and analyzed parameters demonstrates an important aspect in modeling as it features advice and guidelines for the application of ENVI-met on the one hand and provides validation for the current model state on the other hand. While the study found high agreement between modeled and measured values in general, deviations in predicted MRT were revealed. Such validation studies are highly necessary to find and report issues and inaccuracies that can subsequently be addressed by the developers. An example for that process is the follow-up implementation of a new MRT calculation scheme that was found to overcome the previously reported inaccuracies.

It was demonstrated that the advances presented in this thesis lead to a higher accuracy in microclimate modeling with ENVI-met. As radiative fluxes represent a major driver of climatological processes in general, improving its modeling accuracy demonstrates a cornerstone in climate modeling. Due to

ENVI-met's widespread application, it can therefore be assumed that the quality of numerous upcoming urban heat adaptation modeling studies will be improved by the presented enhancements. However, there will always be room for improvements and new developments as a model can always be refined to fit real processes even more accurately. Future validation studies will hence be required to further report any possible shortcomings. As an example, detailed rework is needed for the terrain implementation of the model that is currently not affecting the inflow boundary conditions thus possibly leading to irregularly high wind speeds and low air temperatures directly above the ground for higher terrain levels. A new algorithm might be necessary that interpolates inflow boundary conditions depending on an individual grid cell's terrain level height. Other fields of possible advancements involve the implementation of anthropogenic heat sources from air conditioning or traffic (Girgis et al., 2016) as well as a photovoltaic panel calculation module (Heusinger et al., 2021, 2020). Furthermore, a new ENVI-met module called TreePass focusing on the analysis of wind risk for trees based on the presented, newly implemented L-tree system is already in development. In order to allow a suitable analysis of the multitude of generated tree variables, the possibility to instantly analyze the simulation results by Python Scripts was also recently added to the model. An additional ongoing challenge is to open ENVI-met's file formats for input and output routines to allow an easy and interdisciplinary application (Fallmann and Emeis, 2020; Graham et al., 2020), i.e. standardize simulation input files as official XML-files and provide standardized binary output files, for example in NetCDF file format that is commonly used by climate models. These open formats can then be accessed by other platforms via common libraries to e.g. provide ENVI-met simulation files by SketchUp or Rhino plugins, respectively, or analyze output files in programs like QGIS or ParaView. Furthermore, already developed NetCDF reading and translation routines yield future publications as they can be used for automatized downscaling from mesoscale models like WRF and COSMO to ENVI-met. This work can be seen in relation to the not yet publicly available offline nesting of differently sized ENVI-met model areas, which allow the forcing of ENVI-met simulations with highly accurate, urbanized meteorological boundary conditions (Simon et al., 2018a, 2018b).

In summary, all mentioned implemented and planned advancements yield the common goal to improve microclimate modeling accuracy and further increase its application potential. Modeling studies

evaluating heat mitigation strategies as well as sustainable urban planning in general will hence benefit from these developments.

11 References

Acero, J.A., Herranz-Pascual, K., 2015. A comparison of thermal comfort conditions in four urban spaces by means of measurements and modelling techniques. Building and Environment 93, 245–257. https://doi.org/10.1016/j.buildenv.2015.06.028

Aflaki, A., Mirnezhad, M., Ghaffarianhoseini, Amirhosein, Ghaffarianhoseini, Ali, Omrany, H., Wang, Z.-H., Akbari, H., 2017. Urban heat island mitigation strategies: A state-of-the-art review on Kuala Lumpur, Singapore and Hong Kong. Cities 62, 131–145. https://doi.org/10.1016/j.cities.2016.09.003

Akbari, H., Cartalis, C., Kolokotsa, D., Muscio, A., Pisello, A.L., Rossi, F., Santamouris, M., Synnefa, A., Wong, N.H., Zinzi, M., 2016. Local climate change and urban heat island mitigation techniques – the state of the art. Journal of Civil Engineering and Management 22, 1–16. https://doi.org/10.3846/13923730.2015.1111934

Akbari, H., Levinson, R., Rainer, L., 2005. Monitoring the energy-use effects of cool roofs on California commercial buildings. Energy and Buildings 37, 1007–1016. https://doi.org/10.1016/j.enbuild.2004.11.013

Anand, J., Sailor, D.J., Baniassadi, A., 2021. The relative role of solar reflectance and thermal emittance for passive daytime radiative cooling technologies applied to rooftops. Sustainable Cities and Society 65, 102612. https://doi.org/10.1016/j.scs.2020.102612

Azarmi, F., Kumar, P., Marsh, D., Fuller, G., 2016. Assessment of the long-term impacts of PM10 and PM2.5 particles from construction works on surrounding areas. Environmental science. Processes & impacts 18, 208–221. https://doi.org/10.1039/c5em00549c

Baldauf, M., Seifert, A., Förstner, J., Majewski, D., Raschendorfer, M., Reinhardt, T., 2011. Operational Convective-Scale Numerical Weather Prediction with the COSMO Model: Description and Sensitivities. Monthly Weather Review 139, 3887–3905. https://doi.org/10.1175/MWR-D-10-05013.1

Baniassadi, A., Sailor, D.J., Ban-Weiss, G.A., 2019. Potential energy and climate benefits of supercool materials as a rooftop strategy. Urban Climate 29, 100495. https://doi.org/10.1016/j.uclim.2019.100495

Bartesaghi Koc, C., Osmond, P., Peters, A., 2018. Evaluating the cooling effects of green infrastructure: A systematic review of methods, indicators and data sources. Solar Energy 166, 486–508. https://doi.org/10.1016/j.solener.2018.03.008

Bassill, N.P., 2014. Accuracy of early GFS and ECMWF Sandy (2012) track forecasts: Evidence for a dependence on cumulus parameterization. Geophysical Research Letters 41, 3274–3281. https://doi.org/10.1002/2014GL059839

Berardi, U., Graham, J., 2020. Investigation of the impacts of microclimate on PV energy efficiency and outdoor thermal comfort. Sustainable Cities and Society 62, 102402. https://doi.org/10.1016/j.scs.2020.102402

Berardi, U., Jandaghian, Z., Graham, J., 2020. Effects of greenery enhancements for the resilience to heat waves: A comparison of analysis performed through mesoscale (WRF) and microscale (Envi-met) modeling. Science of The Total Environment 747, 141300. https://doi.org/10.1016/j.scitotenv.2020.141300

Bozonnet, E., Doya, M., Allard, F., 2011. Cool roofs impact on building thermal response: A French case study. Energy and Buildings 43, 3006–3012. https://doi.org/10.1016/j.enbuild.2011.07.017

Bröde, P., Fiala, D., Błażejczyk, K., Holmér, I., Jendritzky, G., Kampmann, B., Tinz, B., Havenith, G., 2012. Deriving the operational procedure for the Universal Thermal Climate Index (UTCI). Int J Biometeorol 56, 481–494. https://doi.org/10.1007/s00484-011-0454-1

Brousse, O., Martilli, A., Foley, M., Mills, G., Bechtel, B., 2016. WUDAPT, an Efficient Land Use Producing Data Tool for Mesoscale Models? Integration of Urban LCZ in WRF over Madrid. Urban Climate 17, 116–134. https://doi.org/10.1016/j.uclim.2016.04.001

Bruse, M., 1999. Die Auswirkungen kleinskaliger Umweltgestaltung auf das Mikroklima. Entwicklung des prognostischen numerischen Modells ENVI-met zur Simulation der Wind-, Temperatur- und Feuchteverteilung in städtischen Strukturen (PhD Thesis). Ruhr-University Bochum, Bochum.

Bruse, M., Fleer, H., 1998. Simulating Surface Plant Air Interactions inside Urban Environments with a Three Dimensional Numerical Model. Environmental Modelling & Software 13, 373–384. https://doi.org/10.1016/S1364-8152(98)00042-5

Chapman, S., Watson, J.E.M., Salazar, A., Thatcher, M., McAlpine, C.A., 2017. The impact of urbanization and climate change on urban temperatures: a systematic review. Landscape Ecol 32, 1921–1935. https://doi.org/10.1007/s10980-017-0561-4

Chen, J., Lu, L., 2020. Development of radiative cooling and its integration with buildings: A comprehensive review. Solar Energy 212, 125–151. https://doi.org/10.1016/j.solener.2020.10.013

Chen, J., Lu, L., Gong, Q., Wang, B., Jin, S., Wang, M., 2021. Development of a new spectral selectivity-based passive radiative roof cooling model and its application in hot and humid region. Journal of Cleaner Production 307, 127170. https://doi.org/10.1016/j.jclepro.2021.127170

Chen, Y., Liu, A., Cheng, X., 2020. Quantifying economic impacts of climate change under nine future emission scenarios within CMIP6. Science of The Total Environment 703, 134950. https://doi.org/10.1016/j.scitotenv.2019.134950

Coniglio, M.C., Elmore, K.L., Kain, J.S., Weiss, S.J., Xue, M., Weisman, M.L., 2010. Evaluation of WRF Model Output for Severe Weather Forecasting from the 2008 NOAA Hazardous Weather Testbed Spring Experiment. Weather and Forecasting 25, 408–427. https://doi.org/10.1175/2009WAF2222258.1

Crank, P.J., Middel, A., Wagner, M., Hoots, D., Smith, M., Brazel, A., 2020. Validation of seasonal mean radiant temperature simulations in hot arid urban climates. Science of The Total Environment 749, 141392. https://doi.org/10.1016/j.scitotenv.2020.141392

Dembski, S., Hartmann, T., Hengstermann, A., Dunning, R., 2020. Introduction Enhancing understanding of strategies of land policy for urban densification. The Town Planning Review 91, 209–216. http://dx.doi.org/10.3828/tpr.2020.12

Dornelles, K., Caram, R., Sichieri, E., 2015. Natural Weathering of Cool Coatings and its Effect on Solar Reflectance of Roof Surfaces. Energy Procedia, 6th International Building Physics Conference, IBPC 2015 78, 1587–1592. https://doi.org/10.1016/j.egypro.2015.11.216

Duque, L., Relvas, H., Silveira, C., Ferreira, J., Monteiro, A., Gama, C., Rafael, S., Freitas, S., Borrego, C., Miranda, A.I., 2016. Evaluating strategies to reduce urban air pollution. Atmospheric Environment 127, 196–204. https://doi.org/10.1016/j.atmosenv.2015.12.043

Elgheznawy, D., Eltarabily, S., 2021. The impact of sun sail-shading strategy on the thermal comfort in school courtyards. Building and Environment 202, 108046. https://doi.org/10.1016/j.buildenv.2021.108046

Falasca, S., Ciancio, V., Salata, F., Golasi, I., Rosso, F., Curci, G., 2019. High albedo materials to counteract heat waves in cities: An assessment of meteorology, buildings energy needs and pedestrian thermal comfort. Building and Environment 163, 106242. https://doi.org/10.1016/j.buildenv.2019.106242

Fallmann, J., Emeis, S., 2020. How to bring urban and global climate studies together with urban planning and architecture? Developments in the Built Environment 4, 100023. https://doi.org/10.1016/j.dibe.2020.100023

Fallmann, J., Suppan, P., Emeis, S., 2013. Modeling of the Urban Heat Island (UHI) using WRF - Assessment of adaptation and mitigation strategies for the city of Stuttgart. EGU2013-4251.

Fanger, P.O., 1972. Thermal comfort: analysis and applications in environmental engineering. McGraw-Hill, New York.

Fann, N., Roman, H.A., Fulcher, C.M., Gentile, M.A., Hubbell, B.J., Wesson, K., Levy, J.I., 2011. Maximizing Health Benefits and Minimizing Inequality: Incorporating Local-Scale Data in the Design and Evaluation of Air Quality Policies. Risk Analysis 31, 908–922. https://doi.org/10.1111/j.1539-6924.2011.01629.x

Farnham, C., Emura, K., Mizuno, T., 2015. Evaluation of cooling effects: outdoor water mist fan. Building Research & Information 43, 334–345. https://doi.org/10.1080/09613218.2015.1004844

Feng, S., Gao, D., Liao, F., Zhou, F., Wang, X., 2016. The health effects of ambient PM2.5 and potential mechanisms. Ecotoxicology and environmental safety 128, 67–74. https://doi.org/10.1016/j.ecoenv.2016.01.030

Gagge, A.P., Fobelets, A.P., Berglund, L.G., 1986. A standard predictive Index of human reponse to thermal enviroment. Transactions / American Society of Heating, Refrigerating and Air-Conditioning Engineers 92, 709–731.

Gál, C.V., Kántor, N., 2020. Modeling mean radiant temperature in outdoor spaces, A comparative numerical simulation and validation study. Urban Climate 32, 100571. https://doi.org/10.1016/j.uclim.2019.100571

Giannaros, C., Nenes, A., Giannaros, T.M., Kourtidis, K., Melas, D., 2018. A comprehensive approach for the simulation of the Urban Heat Island effect with the WRF/SLUCM modeling system: The case of Athens (Greece). Atmospheric Research 201, 86–101. https://doi.org/10.1016/j.atmosres.2017.10.015

Giorgetta, M.A., Brokopf, R., Crueger, T., Esch, M., Fiedler, S., Helmert, J., Hohenegger, C., Kornblueh, L., Köhler, M., Manzini, E., Mauritsen, T., Nam, C., Raddatz, T., Rast, S., Reinert, D., Sakradzija, M., Schmidt, H., Schneck, R., Schnur, R., Silvers, L., Wan, H., Zängl, G., Stevens, B., 2018. ICON-A, the Atmosphere Component of the ICON Earth System Model: I. Model Description. Journal of Advances in Modeling Earth Systems 10, 1613–1637. https://doi.org/10.1029/2017MS001242

Girgis, N., Elariane, S., Elrazik, M.A., 2016. Evaluation of heat exhausts impacts on pedestrian thermal comfort. Sustainable Cities and Society 27, 152–159. https://doi.org/10.1016/j.scs.2015.06.010

Graham, J., Berardi, U., Turnbull, G., McKaye, R., 2020. Microclimate Analysis as a Design Driver of Architecture. Climate 8, 72. https://doi.org/10.3390/cli8060072

Gunawardena, K.R., Wells, M.J., Kershaw, T., 2017. Utilising green and bluespace to mitigate urban heat island intensity. Science of The Total Environment 584–585, 1040–1055. https://doi.org/10.1016/j.scitotenv.2017.01.158

Habeeb, D., Vargo, J., Stone, B., 2015. Rising heat wave trends in large US cities. Nat Hazards 76, 1651–1665. https://doi.org/10.1007/s11069-014-1563-z

Hagedorn, R., Hamill, T.M., Whitaker, J.S., 2008. Probabilistic Forecast Calibration Using ECMWF and GFS Ensemble Reforecasts. Part I: Two-Meter Temperatures. Monthly Weather Review 136, 2608–2619. https://doi.org/10.1175/2007MWR2410.1

Hamill, T.M., Hagedorn, R., Whitaker, J.S., 2008. Probabilistic Forecast Calibration Using ECMWF and GFS Ensemble Reforecasts. Part II: Precipitation. Monthly Weather Review 136, 2620–2632. https://doi.org/10.1175/2007MWR2411.1

Hatvani-Kovacs, G., Bush, J., Sharifi, E., Boland, J., 2018. Policy recommendations to increase urban heat stress resilience. Urban Climate 25, 51–63. https://doi.org/10.1016/j.uclim.2018.05.001

Hellsten, A., Luukkonen, S.-M., Steinfeld, G., Kanani-Sühring, F., Markkanen, T., Järvi, L., Lento, J., Vesala, T., Raasch, S., 2015. Footprint Evaluation for Flux and Concentration Measurements for an Urban-Like Canopy with Coupled Lagrangian Stochastic and Large-Eddy Simulation Models. Boundary-Layer Meteorology 157, 191–217. https://doi.org/10.1007/s10546-015-0062-4

Heusinger, J., Broadbent, A.M., Krayenhoff, E.S., Weber, S., 2021. Adaptation of a photovoltaic energy balance model for rooftop applications. Building and Environment 192, 107628. https://doi.org/10.1016/j.buildenv.2021.107628

Heusinger, J., Broadbent, A.M., Sailor, D.J., Georgescu, M., 2020. Introduction, evaluation and application of an energy balance model for photovoltaic modules. Solar Energy 195, 382–395. https://doi.org/10.1016/j.solener.2019.11.041

Heusinger, J., Sailor, D.J., Weber, S., 2018. Modeling the reduction of urban excess heat by green roofs with respect to different irrigation scenarios. Building and Environment 131, 174–183. https://doi.org/10.1016/j.buildenv.2018.01.003

Horst, T.W., Weil, J.C., 1992. Footprint estimation for scalar flux measurements in the atmospheric surface layer. Boundary-Layer Meteorology 59, 279–296. https://doi.org/10.1007/BF00119817

Huang, J., Cedeño-Laurent, J.G., Spengler, J.D., 2014. CityComfort+: A simulation-based method for predicting mean radiant temperature in dense urban areas. Building and Environment 80, 84–95. https://doi.org/10.1016/j.buildenv.2014.05.019

Huttner, S., 2012. Further development and application of the 3D microclimate simulation ENVI-met (Dissertation). Johannes Gutenberg-University Mainz.

IPCC, 2021. Summary for Policymakers. Climate Change 2021: The Physical Science Basis. Contribution of Working Group I to the Sixth Assessment Report of the Intergovernmental Panel on Climate Change [Masson-Delmotte, V., P. Zhai, A. Pirani, S. L. Connors, C. Péan, S. Berger, N. Caud, Y. Chen, L. Goldfarb, M. I. Gomis, M. Huang, K. Leitzell, E. Lonnoy, J.B.R. Matthews, T. K. Maycock, T. Waterfield, O. Yelekçi, R. Yu and B. Zhou (eds.)].

Jacobs, C., Klok, L., Bruse, M., Cortesão, J., Lenzholzer, S., Kluck, J., 2020. Are urban water bodies really cooling? Urban Climate 32, 100607. https://doi.org/10.1016/j.uclim.2020.100607

Jahanfar, A., Drake, J., Gharabaghi, B., Sleep, B., 2020. An experimental and modeling study of evapotranspiration from integrated green roof photovoltaic systems. Ecological Engineering 152, 105767. https://doi.org/10.1016/j.ecoleng.2020.105767

Jänicke, B., Milošević, D., Manavvi, S., 2021. Review of User-Friendly Models to Improve the Urban Micro-Climate. Atmosphere 12, 1291. https://doi.org/10.3390/atmos12101291

Jasak, H., 2009. OpenFOAM: Open source CFD in research and industry. International Journal of Naval Architecture and Ocean Engineering 1, 89–94. https://doi.org/10.2478/IJNAOE-2013-0011

Johansson, E., Thorsson, S., Emmanuel, R., Krüger, E., 2014. Instruments and methods in outdoor thermal comfort studies – The need for standardization. Urban Climate, ICUC8: The 8th International Conference on Urban Climate and the 10th Symposium on the Urban Environment 10, 346–366. https://doi.org/10.1016/j.uclim.2013.12.002

Kántor, N., Chen, L., Gál, C.V., 2018. Human-biometeorological significance of shading in urban public spaces—Summertime measurements in Pécs, Hungary. Landscape and Urban Planning 170, 241–255. https://doi.org/10.1016/j.landurbplan.2017.09.030

Kántor, N., Unger, J., 2011. The most problematic variable in the course of human-biometeorological comfort assessment — the mean radiant temperature. cent.eur.j.geo. 3, 90–100. https://doi.org/10.2478/s13533-011-0010-x

Karagulian, F., Belis, C.A., Dora, C.F.C., Prüss-Ustün, A.M., Bonjour, S., Adair-Rohani, H., Amann, M., 2015. Contributions to cities' ambient particulate matter (PM): A systematic review of local source contributions at global level. Atmospheric Environment 120, 475–483. https://doi.org/10.1016/j.atmosenv.2015.08.087

Kljun, N., Calanca, P., Rotach, M.W., Schmid, H.P., 2015. A simple two-dimensional parameterisation for Flux Footprint Prediction (FFP). Geosci. Model Dev. 8, 3695–3713. https://doi.org/10.5194/gmd-8-3695-2015

Kljun, N., Rotach, M.W., Schmid, H.P., 2002. A three-dimensional backward Lagrangian footprint model for a wide range of boundary-layer stratifications. Boundary-Layer Meteorology 103, 205–226. https://doi.org/10.1023/a:1014556300021

Kormann, R., Meixner, F.X., 2001. An Analytical Footprint Model For Non-Neutral Stratification. Boundary-Layer Meteorology 99, 207–224. https://doi.org/10.1023/A:1018991015119

Kovats, S., Wolf, T., Menne, B., 2004. Heatwave of August 2003 in Europe: provisional estimates of the impact on mortality. Weekly releases (1997–2007) 8, 2409. https://doi.org/10.2807/esw.08.11.02409-en

Kravchenko, J., Abernethy, A.P., Fawzy, M., Lyerly, H.K., 2013. Minimization of Heatwave Morbidity and Mortality. American Journal of Preventive Medicine 44, 274–282. https://doi.org/10.1016/j.amepre.2012.11.015

Kumar, P., Khare, M., Harrison, R.M., Bloss, W.J., Lewis, A.C., Coe, H., Morawska, L., 2015. New directions: Air pollution challenges for developing megacities like Delhi. Atmospheric Environment 122, 657–661. https://doi.org/10.1016/j.atmosenv.2015.10.032

Lam, C.K.C., Lee, H., Yang, S.-R., Park, S., 2021. A review on the significance and perspective of the numerical simulations of outdoor thermal environment. Sustainable Cities and Society 71, 102971. https://doi.org/10.1016/j.scs.2021.102971

Lehnert, M., Tokar, V., Jurek, M., Geletič, J., 2021. Summer thermal comfort in Czech cities: measured effects of blue and green features in city centres. Int J Biometeorol 65, 1277–1289. https://doi.org/10.1007/s00484-020-02010-y

Lelieveld, J., Klingmüller, K., Pozzer, A., Pöschl, U., Fnais, M., Daiber, A., Münzel, T., 2019. Cardiovascular disease burden from ambient air pollution in Europe reassessed using novel hazard ratio functions. European heart journal 40, 1590–1596. https://doi.org/10.1093/eurheartj/ehz135

Li, D., Bou-Zeid, E., Oppenheimer, M., 2014. The effectiveness of cool and green roofs as urban heat island mitigation strategies. Environ. Res. Lett. 9, 055002. https://doi.org/10.1088/1748-9326/9/5/055002

Li, D., Liao, W., Rigden, A.J., Liu, X., Wang, D., Malyshev, S., Shevliakova, E., 2019. Urban heat island: Aerodynamics or imperviousness? Science Advances 5, eaau4299. https://doi.org/10.1126/sciadv.aau4299

Lin, B., Meyers, J., Barnett, G., 2015. Understanding the potential loss and inequities of green space distribution with urban densification. Urban Forestry & Urban Greening 14, 952–958. https://doi.org/10.1016/j.ufug.2015.09.003

Lindberg, F., Holmer, B., Thorsson, S., 2008. SOLWEIG 1.0 – Modelling spatial variations of 3D radiant fluxes and mean radiant temperature in complex urban settings. Int J Biometeorol 52, 697–713. https://doi.org/10.1007/s00484-008-0162-7

Liu, Z., Cheng, W., Jim, C.Y., Morakinyo, T.E., Shi, Y., Ng, E., 2021. Heat mitigation benefits of urban green and blue infrastructures: A systematic review of modeling techniques, validation and scenario simulation in ENVI-met V4. Building and Environment 200, 107939. https://doi.org/10.1016/j.buildenv.2021.107939

Mandal, J., Fu, Y., Overvig, A.C., Jia, M., Sun, K., Shi, N.N., Zhou, H., Xiao, X., Yu, N., Yang, Y., 2018. Hierarchically porous polymer coatings for highly efficient passive daytime radiative cooling. Science 362, 315–319. https://doi.org/10.1126/science.aat9513

Mandal, J., Yang, Y., Yu, N., Raman, A.P., 2020. Paints as a Scalable and Effective Radiative Cooling Technology for Buildings. Joule 4, 1350–1356. https://doi.org/10.1016/j.joule.2020.04.010

Manso, M., Castro-Gomes, J., 2015. Green Wall Systems: A Review of Their Characteristics. Renewable and Sustainable Energy Reviews 41, 863–871. https://doi.org/10.1016/j.rser.2014.07.203

Maronga, B., Raasch, S., Groß, G., Kanani-Sühring, F., Banzhaf, S., Büter, B., Esch, T., Forkel, R., Fröhlich, D., Gronemeier, T., Heldens, W., Lang, T., Hellsten, A., Kadasch, E., Khan, B., Ketelsen, K., Krč, P., Maamari, H., Matzarakis, A., Mauder, M., Meusel, G., Pallasch, M., Pavlik, D., Pfaffenrott, J., Resler, J., Russo, E., Salim, M.H., Schaap, M., Schneider, C., Schrempf, M., Schubert, S., Seckmeyer, G., Sieker, H., Trusliova, K., von Tils, R.H., Ward, S., Zeidler, J., 2018. Building-resolving large-eddy simulations for entire Berlin (Germany) – first results using the high-performance urban microscale model PALM-4U. Presented at the ICUC10, New York, USA.

Martilli, A., Krayenhoff, E.S., Nazarian, N., 2020. Is the Urban Heat Island intensity relevant for heat mitigation studies? Urban Climate 31, 100541. https://doi.org/10.1016/j.uclim.2019.100541

Masson, V., Bonhomme, M., Salagnac, J.-L., Briottet, X., Lemonsu, A., 2014. Solar panels reduce both global warming and urban heat island. Frontiers in Environmental Science 2, 14. https://doi.org/10.3389/fenvs.2014.00014

Mastrapostoli, E., Santamouris, M., Kolokotsa, D., Vassilis, P., Venieri, D., Gompakis, K., 2016. On the ageing of cool roofs: Measure of the optical degradation, chemical and biological analysis and assessment of the energy impact. Energy and Buildings, SI: Countermeasures to Urban Heat Island 114, 191–199. https://doi.org/10.1016/j.enbuild.2015.05.030

Matzarakis, A., Rutz, F., Mayer, H., 2010. Modelling radiation fluxes in simple and complex environments: basics of the RayMan model. Int J Biometeorol 54, 131–139. https://doi.org/10.1007/s00484-009-0261-0

Mayer, H., Höppe, P., 1987. Thermal Comfort of Man in Different Urban Environments. Theoretical and Applied Climatology 38, 43–49.

Meehl, G.A., Boer, G.J., Covey, C., Latif, M., Stouffer, R.J., 2000. The Coupled Model Intercomparison Project (CMIP). Bulletin of the American Meteorological Society 81, 313–318.

Middel, A., Turner, V.K., Schneider, F.A., Zhang, Y., Stiller, M., 2020. Solar reflective pavements—A policy panacea to heat mitigation? Environ. Res. Lett. 15, 064016. https://doi.org/10.1088/1748-9326/ab87d4

Mills, G., 2014. Urban climatology: History, status and prospects. Urban Climate, Measurement and modelling of the urban atmosphere in the present and the past 10, 479–489. https://doi.org/10.1016/j.uclim.2014.06.004

Morakinyo, T.E., Dahanayake, K.W.D.Kalani.C., Ng, E., Chow, C.L., 2017a. Temperature and cooling demand reduction by green-roof types in different climates and urban densities: A co-

simulation parametric study. Energy and Buildings 145, 226–237. https://doi.org/10.1016/j.enbuild.2017.03.066

Morakinyo, T.E., Kong, L., Lau, K.K.-L., Yuan, C., Ng, E., 2017b. A study on the impact of shadow-cast and tree species on in-canyon and neighborhood's thermal comfort. Building and Environment 115, 1–17. https://doi.org/10.1016/j.buildenv.2017.01.005

Morakinyo, T.E., Lai, A., Lau, K.K.-L., Ng, E., 2019. Thermal benefits of vertical greening in a high-density city: Case study of Hong Kong. Urban Forestry & Urban Greening, Green Infrastructures: Nature Based Solutions for sustainable and resilient cities 37, 42–55. https://doi.org/10.1016/j.ufug.2017.11.010

Morakinyo, T.E., Ouyang, W., Lau, K.K.-L., Ren, C., Ng, E., 2020. Right tree, right place (urban canyon): Tree species selection approach for optimum urban heat mitigation - development and evaluation. Science of The Total Environment 719, 137461. https://doi.org/10.1016/j.scitotenv.2020.137461

Movahhed, Y., Safari, A., Motamedi, S., Khoshkhoo, R.H., 2019. Simultaneous use of PV system and green roof: A techno-economic study on power generation and energy consumption. Energy Procedia, Renewable Energy Integration with Mini/Microgrid 159, 478–483. https://doi.org/10.1016/j.egypro.2018.12.037

Musy, M., Malys, L., Morille, B., Inard, C., 2015. The use of SOLENE-microclimat model to assess adaptation strategies at the district scale. Urban Climate, Cooling Heat Islands 14, 213–223. https://doi.org/10.1016/j.uclim.2015.07.004

Nguyen, T.T., Ngo, H.H., Guo, W., Wang, X.C., Ren, N., Li, G., Ding, J., Liang, H., 2019. Implementation of a specific urban water management - Sponge City. Science of The Total Environment 652, 147–162. https://doi.org/10.1016/j.scitotenv.2018.10.168

Nieuwenhuijsen, M.J., Khreis, H., 2016. Car free cities: Pathway to healthy urban living. Environment International 94, 251–262. https://doi.org/10.1016/j.envint.2016.05.032

Oke, T.R., 1997. Urban Environments, in: Bailey, W.G., Oke, T.R., Rouse, W.R. (Eds.), The Surface Climates of Canada. Québec: McGill-Queen's University Press, pp. 303–327.

Oke, T.R., 1988. The Urban Energy Balance. Progress in Physical Geography 12, 471–508.

Oke, T.R., 1987. Boundary Layer Climates, 2nd ed. Vancouver.

O'Malley, C., Piroozfar, P., Farr, E.R.P., Pomponi, F., 2015. Urban Heat Island (UHI) mitigating strategies: A case-based comparative analysis. Sustainable Cities and Society 19, 222–235. https://doi.org/10.1016/j.scs.2015.05.009

Ouyang, W., Sinsel, T., Simon, H., Morakinyo, T.E., Liu, H., Ng, E., 2022. Evaluating the thermal-radiative performance of ENVI-met model for green infrastructure typologies: Experience from a subtropical climate. Building and Environment 207, 108427. https://doi.org/10.1016/j.buildenv.2021.108427

Pyrgou, A., Hadjinicolaou, P., Santamouris, M., 2020. Urban-rural moisture contrast: Regulator of the urban heat island and heatwaves' synergy over a mediterranean city. Environmental Research 182, 109102. https://doi.org/10.1016/j.envres.2019.109102

Rabl, A., de Nazelle, A., 2012. Benefits of shift from car to active transport. Transport Policy 19, 121–131. https://doi.org/10.1016/j.tranpol.2011.09.008

Robine, J.-M., Cheung, S.L.K., Le Roy, S., Van Oyen, H., Griffiths, C., Michel, J.-P., Herrmann, F.R., 2008. Death toll exceeded 70,000 in Europe during the summer of 2003. Comptes Rendus Biologies, Dossier : Nouveautés en cancérogenèse / New developments in carcinogenesis 331, 171–178. https://doi.org/10.1016/j.crvi.2007.12.001

Rojas-Rueda, D., Nazelle, A. de, Tainio, M., Nieuwenhuijsen, M.J., 2011. The health risks and benefits of cycling in urban environments compared with car use: health impact assessment study. BMJ 343, d4521. https://doi.org/10.1136/bmj.d4521

Roman, L.A., Conway, T.M., Eisenman, T.S., Koeser, A.K., Ordóñez Barona, C., Locke, D.H., Jenerette, G.D., Östberg, J., Vogt, J., 2021. Beyond 'trees are good': Disservices, management costs, and tradeoffs in urban forestry. Ambio 50, 615–630. https://doi.org/10.1007/s13280-020-01396-8

Romanello, M., McGushin, A., Di Napoli, C., Drummond, P., Hughes, N., Jamart, L., Kennard, H., Lampard, P., Rodriguez, B.S., Arnell, N., Ayeb-Karlsson, S., Belesova, K., Cai, W., Campbell-Lendrum, D., Capstick, S., Chambers, J., Chu, L., Ciampi, L., Dalin, C., Dasandi, N., Dasgupta, S., Davies, M., Dominguez-Salas, P., Dubrow, R., Ebi, K.L., Eckelman, M., Ekins,

P., Escobar, L.E., Georgeson, L., Grace, D., Graham, H., Gunther, S.H., Hartinger, S., He, K., Heaviside, C., Hess, J., Hsu, S.-C., Jankin, S., Jimenez, M.P., Kelman, I., Kiesewetter, G., Kinney, P.L., Kjellstrom, T., Kniveton, D., Lee, J.K.W., Lemke, B., Liu, Y., Liu, Z., Lott, M., Lowe, R., Martinez-Urtaza, J., Maslin, M., McAllister, L., McMichael, C., Mi, Z., Milner, J., Minor, K., Mohajeri, N., Moradi-Lakeh, M., Morrissey, K., Munzert, S., Murray, K.A., Neville, T., Nilsson, M., Obradovich, N., Sewe, M.O., Oreszczyn, T., Otto, M., Owfi, F., Pearman, O., Pencheon, D., Rabbaniha, M., Robinson, E., Rocklöv, J., Salas, R.N., Semenza, J.C., Sherman, J., Shi, L., Springmann, M., Tabatabaei, M., Taylor, J., Trinanes, J., Shumake-Guillemot, J., Vu, B., Wagner, F., Wilkinson, P., Winning, M., Yglesias, M., Zhang, S., Gong, P., Montgomery, H., Costello, A., Hamilton, I., 2021. The 2021 report of the Lancet Countdown on health and climate change: Code red for a healthy future. The Lancet. https://doi.org/10.1016/S0140-6736(21)01787-6

Roth, M., Lim, V.H., 2017. Evaluation of canopy-layer air and mean radiant temperature simulations by a microclimate model over a tropical residential neighbourhood. Building and Environment 112, 177–189. https://doi.org/10.1016/j.buildenv.2016.11.026

Runnalls, K.E., Oke, T.R., 2006. A Technique to Detect Microclimatic Inhomogenities in Historical Records of Screen-Level Air Temperature 19, 959–978.

Saaroni, H., Amorim, J.H., Hiemstra, J.A., Pearlmutter, D., 2018. Urban Green Infrastructure as a tool for urban heat mitigation: Survey of research methodologies and findings across different climatic regions. Urban Climate 24, 94–110. https://doi.org/10.1016/j.uclim.2018.02.001

Santamouris, M., Fiorito, F., 2021. On the impact of modified urban albedo on ambient temperature and heat related mortality. Solar Energy 216, 493–507. https://doi.org/10.1016/j.solener.2021.01.031

Santamouris, M., Synnefa, A., Karlessi, T., 2011. Using advanced cool materials in the urban built environment to mitigate heat islands and improve thermal comfort conditions. Solar Energy, Progress in Solar Energy 2 85, 3085–3102. https://doi.org/10.1016/j.solener.2010.12.023

Santamouris, M., Yun, G.Y., 2020. Recent development and research priorities on cool and super cool materials to mitigate urban heat island. Renewable Energy 161, 792–807. https://doi.org/10.1016/j.renene.2020.07.109

Scherba, A., Sailor, D.J., Rosenstiel, T.N., Wamser, C.C., 2011. Modeling impacts of roof reflectivity, integrated photovoltaic panels and green roof systems on sensible heat flux into the urban environment. Building and Environment 46, 2542–2551. https://doi.org/10.1016/j.buildenv.2011.06.012

Schinasi, L.H., Benmarhnia, T., De Roos, A.J., 2018. Modification of the association between high ambient temperature and health by urban microclimate indicators: A systematic review and meta-analysis. Environmental Research 161, 168–180. https://doi.org/10.1016/j.envres.2017.11.004

Schrijvers, P.J.C., Jonker, H.J.J., de Roode, S.R., Kenjereš, S., 2016. The effect of using a high-albedo material on the Universal Temperature Climate Index within a street canyon. Urban Climate 17, 284–303. https://doi.org/10.1016/j.uclim.2016.02.005

Shafique, M., Kim, R., Rafiq, M., 2018. Green roof benefits, opportunities and challenges – A review. Renewable and Sustainable Energy Reviews 90, 757–773. https://doi.org/10.1016/j.rser.2018.04.006

Sharma, A., Conry, P., Fernando, H.J.S., Hamlet, A.F., Hellmann, J.J., Chen, F., 2016. Green and cool roofs to mitigate urban heat island effects in the Chicago metropolitan area: evaluation with a regional climate model. Environmental Research Letters 11, 064004. https://doi.org/10.1088/1748-9326/11/6/064004

Sharma, A., Fernando, H.J.S., Hamlet, A.F., Hellmann, J.J., Barlage, M., Chen, F., 2017. Urban meteorological modeling using WRF: a sensitivity study. International Journal of Climatology 37, 1885–1900. https://doi.org/10.1002/joc.4819

Sharmin, T., Steemers, K., Matzarakis, A., 2017. Microclimatic modelling in assessing the impact of urban geometry on urban thermal environment. Sustainable Cities and Society 34, 293–308. https://doi.org/10.1016/j.scs.2017.07.006

Simon, H., 2016. Modeling Urban Microclimate: Development, Implementation and Evaluation of New and Improved Calculation Methods for the Urban Microclimate Model ENVI-Met (PhD Thesis). Universitätsbibliothek Mainz, Mainz.

Simon, H., Bruse, M., Kropp, T., Sohni, F., 2018a. Introduction of Nesting into the Microclimate Model ENVI-Met, in: 10th International Conference on Urban Climate/14th Symposium on the Urban Environment. New York. Forthcoming.

Simon, H., Fallmann, J., Kropp, T., Tost, H., Bruse, M., 2019. Urban Trees and Their Impact on Local Ozone Concentration—A Microclimate Modeling Study. Atmosphere 10, 154. https://doi.org/10.3390/atmos10030154

Simon, H., Heusinger, J., Sinsel, T., Weber, S., Bruse, M., 2021a. Implementation of a Lagrangian Stochastic Particle Trajectory Model (LaStTraM) to Simulate Concentration and Flux Footprints Using the Microclimate Model ENVI-Met. Atmosphere 12, 977. https://doi.org/10.3390/atmos12080977

Simon, H., Kropp, T., Sohni, F., Bruse, M., 2018b. Downscaling Climate Models: Running Nested Simulations In The Microclimate Model ENVI-Met, in: 34th PLEA Conference 2018: Smart and Healthy within the 2-Degree Limit. Hongkong. In Review Process.

Simon, H., Lindén, J., Hoffmann, D., Braun, P., Bruse, M., Esper, J., 2018c. Modeling transpiration and leaf temperature of urban trees – A case study evaluating the microclimate model ENVI-met against measurement data. Landscape and Urban Planning 174, 33–40. https://doi.org/10.1016/j.landurbplan.2018.03.003

Simon, H., Sinsel, T., Bruse, M., 2021b. Advances in Simulating Radiative Transfer in Complex Environments. Applied Sciences 11, 5449. https://doi.org/10.3390/app11125449

Simon, H., Sinsel, T., Bruse, M., 2020. Introduction of Fractal-Based Tree Digitalization and Accurate In-Canopy Radiation Transfer Modelling to the Microclimate Model ENVI-met. Forests 11, 869. https://doi.org/10.3390/f11080869

Sinsel, T., Simon, H., Broadbent, A.M., Bruse, M., Heusinger, J., 2021a. Modeling the outdoor cooling impact of highly radiative "super cool" materials applied on roofs. Urban Climate 38, 100898. https://doi.org/10.1016/j.uclim.2021.100898

Sinsel, T., Simon, H., Broadbent, A.M., Bruse, M., Heusinger, J., 2021b. Modeling impacts of super cool roofs on air temperature at pedestrian level in mesoscale and microscale climate models. Urban Climate 40, 101001. https://doi.org/10.1016/j.uclim.2021.101001

Sofia, D., Gioiella, F., Lotrecchiano, N., Giuliano, A., 2020. Mitigation strategies for reducing air pollution. Environ Sci Pollut Res 27, 19226–19235. https://doi.org/10.1007/s11356-020-08647-x

Sogachev, A., Menzhulin, G.V., Heimann, M., Lloyd, J., 2002. A simple three-dimensional canopy – planetary boundary layer simulation model for scalar concentrations and fluxes. Tellus B 54, 784–819. https://doi.org/10.1034/j.1600-0889.2002.201353.x

Steuri, B., Bender, S., Cortekar, J., 2020. Successful user-science interaction to co-develop the new urban climate model PALM-4U. Urban Climate 32, 100630. https://doi.org/10.1016/j.uclim.2020.100630

Synnefa, A., Dandou, A., Santamouris, M., Tombrou, M., Soulakellis, N., 2008. On the Use of Cool Materials as a Heat Island Mitigation Strategy. Journal of Applied Meteorology and Climatology 47, 2846–2856. https://doi.org/10.1175/2008JAMC1830.1

Synnefa, A., Santamouris, M., Apostolakis, K., 2007. On the development, optical properties and thermal performance of cool colored coatings for the urban environment. Solar Energy 81, 488–497. https://doi.org/10.1016/j.solener.2006.08.005

Taylor, K.E., Stouffer, R.J., Meehl, G.A., 2012. An Overview of CMIP5 and the Experiment Design. Bulletin of the American Meteorological Society 93, 485–498. https://doi.org/10.1175/BAMS-D-11-00094.1

Theeuwes, N.E., Solcerová, A., Steeneveld, G.J., 2013. Modeling the influence of open water surfaces on the summertime temperature and thermal comfort in the city. Journal of Geophysical Research: Atmospheres 118, 8881–8896. https://doi.org/10.1002/jgrd.50704

Thomson, G., Newman, P., 2018. Urban fabrics and urban metabolism – from sustainable to regenerative cities. Resources, Conservation and Recycling 132, 218–229. https://doi.org/10.1016/j.resconrec.2017.01.010

Tsoka, S., Tsikaloudaki, A., Theodosiou, T., 2018. Analyzing the ENVI-met microclimate model's performance and assessing cool materials and urban vegetation applications–A review. Sustainable Cities and Society 43, 55–76. https://doi.org/10.1016/j.scs.2018.08.009

UN Department of Economic and Social Affairs, Population Division, 2019. World Urbanization Prospects: The 2018 Revision. New York: United Nations.

UN Human Settlements Programme, 2020. World Cities Report 2020 - The Value of Sustainable Urbanization.

Van Renterghem, T., 2018. Improving the noise reduction by green roofs due to solar panels and substrate shaping. Building Acoustics 25, 219–232. https://doi.org/10.1177/1351010X18776804

VDI, 2008. Methods for the human-biometeorological assessment of climate and air hygiene for urban and regional planning. (No. I: Climate), VDI 3787, Sheet 2. Beuth, Berlin.

Vogel, J., Afshari, A., 2020. Comparison of Urban Heat Island Intensity Estimation Methods Using Urbanized WRF in Berlin, Germany. Atmosphere 11, 1338. https://doi.org/10.3390/atmos11121338

Vogt, J., Gillner, S., Hofmann, M., Tharang, A., Dettmann, S., Gerstenberg, T., Schmidt, C., Gebauer, H., Van de Riet, K., Berger, U., Roloff, A., 2017. Citree: A database supporting tree selection for urban areas in temperate climate. Landscape and Urban Planning 157, 14–25. https://doi.org/10.1016/j.landurbplan.2016.06.005

Wallenberg, N., Lindberg, F., Holmer, B., Thorsson, S., 2020. The influence of anisotropic diffuse shortwave radiation on mean radiant temperature in outdoor urban environments. Urban Climate 31, 100589. https://doi.org/10.1016/j.uclim.2020.100589

Wang, Y., Berardi, U., Akbari, H., 2016. Comparing the effects of urban heat island mitigation strategies for Toronto, Canada. Energy and Buildings, SI: Countermeasures to Urban Heat Island 114, 2–19. https://doi.org/10.1016/j.enbuild.2015.06.046

Wania, A., Bruse, M., Blond, N., Weber, C., 2012. Analysing the influence of different street vegetation on traffic-induced particle dispersion using microscale simulations. Journal of Environmental Management 94, 91–101. https://doi.org/10.1016/j.jenvman.2011.06.036

Wong, K.V., Paddon, A., Jimenez, A., 2013. Review of World Urban Heat Islands: Many Linked to Increased Mortality. Journal of Energy Resources Technology 135. https://doi.org/10.1115/1.4023176

Yang, Y., Zhang, Y., 2020. Passive daytime radiative cooling: Principle, application, and economic analysis. MRS Energy & Sustainability 7. https://doi.org/10.1557/mre.2020.18

Zhang, Y., 2013. Urban metabolism: A review of research methodologies. Environmental Pollution 178, 463–473. https://doi.org/10.1016/j.envpol.2013.03.052

Zheng, Y., Alapaty, K., Herwehe, J.A., Genio, A.D.D., Niyogi, D., 2016. Improving High-Resolution Weather Forecasts Using the Weather Research and Forecasting (WRF) Model with an Updated Kain–Fritsch Scheme. Monthly Weather Review 144, 833–860. https://doi.org/10.1175/MWR-D-15-0005.1

Zölch, T., Rahman, M.A., Pfleiderer, E., Wagner, G., Pauleit, S., 2019. Designing public squares with green infrastructure to optimize human thermal comfort. Building and Environment 149, 640–654. https://doi.org/10.1016/j.buildenv.2018.12.051

Žuvela-Aloise, M., Koch, R., Buchholz, S., Früh, B., 2016. Modelling the potential of green and blue infrastructure to reduce urban heat load in the city of Vienna. Climatic Change 135, 425–438. https://doi.org/10.1007/s10584-016-1596-2

12 List of figures

13 List of tables

14 Index of abbreviations

ACRT	Advanced Canopy Radiation Transfer
AT	Air Temperature
AVF	Averaged View Factors
BR	Bare Roof
CFD	Computational Fluid Dynamics
CR	Cool Roof
CV	Coefficient of Variation
DEM	Digital Elevation Model
EMSD	Electronic and Mechanical Services Department Hong Kong
EPW	Energy Plus Weather
FFP	Flux Footprint Predictions model
GI	Green Infrastructure
GR	Green Roof
GT	Ground Tree
GW	Green Wall
HK	Hong Kong
HKO	Hong Kong Observatory
HTC	Human Thermal Comfort
IAGUSP	Institute of Astronomy, Geophysics and Atmospheric Sciences at the University of Sao Paulo
IDW	Inverse Distance Weighting
IVS	Indexed View Spheres
K-M	Kormann-Meixner model
KSC	Kau Sai Chau Observatory
LAD	Leaf Area Density
LaStTraM	Lagrangian Stochastic Particle Trajectory Model
LES	Large-Eddy simulations
LS	Lagrangian stochastic particle dispersion models
L-System	Lindenmeyer-system
L-Tree	Lindenmeyer-system based tree
LW	Longwave Radiation
MBE	Mean Bias Error
MRT	Mean Radiant Temperature
NetCDF	Network Common Data Form
NYC	New York City
PDRC	Passive Daytime Radiative Cooling
PET	Physiological Equivalent Temperature
PHX	Phoenix, Arizona
PM	Particulate Matter
RANS	Reynold-Averaged-Navier-Stokes equations
RH	Relative Humidity
RMSE	Root Mean Square Error
SCR	Super Cool Roof
SD	Standard Deviation
SP	Sao Paulo
SW	Shortwave Radiation
TF	Tree Free
UHI	Urban Heat Island
WRF	Weather and Research Forecast model

15 Curriculum vitae

Not available online.